

Alma Mater Studiorum - Università di Bologna

DOTTORATO DI RICERCA IN
INGEGNERIA CIVILE, CHIMICA, AMBIENTALE E DEI MATERIALI

Ciclo 34

Settore Concorsuale: 09/D2 - SISTEMI, METODI E TECNOLOGIE DELL'INGEGNERIA CHIMICA
E DI PROCESSO

Settore Scientifico Disciplinare: ING-IND/24 - PRINCIPI DI INGEGNERIA CHIMICA

DESIGN AND EVALUATION OF AEROSOL AND LIQUID SEPARATION
SYSTEMS

Presentata da: Riccardo Onesti

Coordinatore Dottorato

Alessandro Tugnoli

Supervisore

Cristiana Boi

Co-supervisore

Matteo Minelli

Esame finale anno 2022

Abstract

Conventional chromatographic columns are packed with porous beads by the universally employed slurry-packing method. The difficulties in column packing, the lack of precise control of the particle size distribution, shape and position inside the column, and the intraparticle diffusion as primary mass transport phenomena have dramatic effects on the separation efficiency. In the last decades most of the efforts aimed to reduce the particle size and their size distribution. Other efforts have been made towards unconventional supports, such as membranes and monoliths. Currently, one of the most promising solutions is represented by homogeneous beds with a perfectly ordered structure, but their application is limited to two-dimensional devices for analytical applications due to limitations of the manufacturing techniques.

In the first part of the thesis an ordered, three-dimensional, pillar-array structure was designed by a CAD software. Several columns, characterized by different fluid distributors and bed length, were produced by a stereolithographic 3D printer and compared in terms of pressure drop and height equivalent to a theoretical plate (HETP). To prevent the release of unwanted substances and to provide a surface for immobilizing a ligand, pillars were coated with one or more of the following materials: titanium dioxide, nanofibrillated cellulose (NFC) and polystyrene. The external NFC layer was functionalized with Cibacron Blue and the dynamic binding capacity of the column was measured by performing three chromatographic cycles, using bovine serum albumin (BSA) as target molecule.

The second part of the thesis deals with Covid-19 pandemic related research activities. In early 2020, due to the pandemic outbreak, surgical face masks became an essential non-pharmaceutical intervention to limit the spread of the disease and their request skyrocketed to unprecedented levels. To address the consequent shortage and to support the reconversion of the Italian industry, in late March 2020 a multidisciplinary group of the University of Bologna created the first Italian laboratory able to perform all the tests required for the evaluation and certification of surgical masks.

More than 1200 tests were performed on about 350 prototypes, to evaluate their bacterial filtration efficiency, breathability and resistance against splashes of synthetic blood, according to the standard EN 14683:2019. The results were analyzed to define the best material properties and masks composition for the production of masks with excellent efficiency. To optimize the usage of surgical masks and to reduce their environmental burden, the variation of their performance over time of usage were investigated as to determine the maximum lifetime. To make the lifetime evaluation possible in any laboratory, the BFE apparatus was upgraded to recreate real conditions of usage and a protocol to simulate BFE and breathability variations over time of usage was developed.

CONTENTS

Structure and aim of the work	1
PART I: 3D pillar-array support for chromatography	3
Introduction to chromatography	5
CHAPTER 1: Conventional packed-bed columns: limitations and alternatives	11
1.1 Causes of limited column efficiency	15
1.1.1 <i>Height equivalent to a theoretical plate</i>	19
1.2 Unconventional support	22
1.2.1 <i>Support requirements</i>	23
1.2.1.1 <i>Chemical inertness</i>	23
1.2.1.2 <i>Chemical and mechanical stability</i>	24
1.2.1.3 <i>Pore size</i>	25
1.2.1.4 <i>Particle size</i>	26
1.2.2 Support materials and structures	27
1.2.2.1 <i>Non-porous supports</i>	28
1.2.2.2 <i>Perfusion media</i>	29
1.2.2.3 <i>Expanded-bed adsorbent</i>	30
1.2.2.4 <i>Membranes</i>	31
1.2.2.5 <i>Monoliths</i>	32
1.3 Recent developments in HPLC	33
1.3.1 <i>Fully porous particles</i>	34
1.3.2 <i>Core-shell particles</i>	36
1.3.3 <i>Monoliths</i>	38
1.3.4 <i>Micropillar array columns</i>	39
1.3.5 <i>3D printing</i>	40
References	43

CHAPTER 2: Column design and fluid dynamic characterization	49
2.1 Column design and manufacturing	50
2.1.1 <i>Pillars</i>	51
2.1.2 <i>Distributors</i>	54
2.1.3 <i>Column shell</i>	55
2.1.4 <i>Designed columns overview</i>	56
2.2 3D printing: Original Prusa SL1	57
2.3 Pillar coating	60
2.3.1 <i>Nanofibrillated cellulose and titanium dioxide spray coatings</i>	63
2.3.1.1 <i>Experimental apparatus for spray coating</i>	64
2.3.2 <i>Polystyrene coating by phase inversion</i>	65
2.4 Fluid dynamic characterization	65
2.4.1 <i>Fast Protein Liquid Chromatography apparatus</i>	65
2.4.2 <i>Pressure drop test</i>	67
2.4.3 <i>Pulse test</i>	68
2.4.3.1 <i>Determination of the HETP</i>	69
2.5 Results	72
2.5.1 <i>Fluid dynamic characterization</i>	73
2.5.2 <i>Coatings</i>	77
2.5.2.1 <i>Spray coating apparatus set-up</i>	77
2.5.2.2 <i>Definition of the best type of coating</i>	80
References	83
CHAPTER 3: Functionalization and affinity adsorption	87
3.1 Theory of chromatographic cycles.....	87
3.2 NFC layer functionalization with Cibacron Blue F3GA.....	90
3.3 Dynamic adsorption test.....	91
3.4 Results	92
References	95
CHAPTER 4: Conclusions of Part I.....	97

PART II: Surgical masks test and durability evaluation.....	101
Introduction to surgical masks.....	103
CHAPTER 5: COVID-19 pandemic and the role of face masks.....	111
5.1 SARS-CoV-2 modes of transmission	112
5.2 Non-pharmaceutical measures to prevent transmission.....	118
5.3 Role and types of face masks	120
References	127
CHAPTER 6: Surgical face masks	133
6.1 European regulation, tests and classification	134
6.1.1 <i>Differential pressure</i>	136
6.1.2 <i>Bacterial filtration efficiency in vitro (BFE)</i>	137
6.1.3 <i>Resistance against splashes of synthetic blood – Splash test</i>	142
6.2 Mechanisms of filtration	146
6.3 Materials, properties and manufacturing processes	149
6.3.1 <i>Nonwoven fabrics properties and raw materials</i>	150
6.3.2 <i>Manufacturing processes</i>	152
6.3.3 <i>Meltblowing</i>	153
6.3.4 <i>Spunbonding</i>	154
6.3.5 <i>Electrospinning</i>	155
References	157
CHAPTER 7: UniBo Laboratory tests and apparatus.....	159
7.1 Test apparatus and protocols.....	161
7.1.1 <i>Breathability</i>	163
7.1.2 <i>Bacterial filtration efficiency</i>	166
7.1.3 <i>Splash test</i>	172
7.2 Results	174
References	184

CHAPTER 8: Durability of surgical masks	187
8.1 Real usage evaluation.....	190
8.1.1 <i>Results of real usage evaluation</i>	192
8.2 Parameters affecting the durability	197
8.2.1 <i>Results of parameters affecting the durability</i>	199
8.3 Protocol for lifetime estimation	201
8.3.1 <i>Results of protocol for lifetime estimation</i>	204
References	208
CHAPTER 9: Conclusions of Part II	211

Structure and aim of the work

The research activities resumed in the present work started in October 2018, with the aim of developing an innovative chromatographic column with a perfectly ordered morphology, able to overcome the main limitations of conventional packed bed columns for preparative applications.

In early 2020, due to the Covid-19 pandemic outbreak, several activities experienced a sharp slowdown, others a radical change. Since the beginning of the pandemic, surgical masks played a key role in the containment of SARS-CoV2 and for the protection of frontline healthcare workers. Unfortunately, their request skyrocketed to unprecedented levels and China, the world's leading manufacturer, was overwhelmed with orders, leading to a severe shortage of these medical devices. In March 2022, to face the shortage and to support the reconversion of the Italian industry towards surgical masks, a multidisciplinary group of volunteers of the University of Bologna, led by prof. Cristiana Boi¹ and prof. Francesco Saverio Violante², created in less than a week the first Italian laboratory able to verify the efficiency of surgical masks, according to the EU regulation. The author of this work was involved from the beginning in the design and set-up of the test lines and served as laboratory operations manager, diverting the research efforts on the characterization of surgical mask.

Therefore, this work will be divided in two distinct parts.

The first part reports the results obtained in the development of the first regular pillar-array column for preparative protein chromatography, with a detailed analysis of the design and of the manufacturing techniques.

The second part reports the efforts of the Unibo Surgical Masks laboratory. From March 2022, the laboratory supported more than one-hundred public and private companies, in Italy and abroad, towards the production of high-performing and compliant surgical mask. In addition, it assisted several hospitals in the selection of masks available on the market and the national committed for Covid-19 Italian task force, for the production of surgical masks at a national scale.

¹ Associate professor at the Department of Civil, Chemical, Environmental and Materials Engineering (DICAM) of the University of Bologna.

² Full professor at Department of Medical and Surgical Science (DIMEC) of the University of Bologna.

The huge number of data collected allowed to determine the relationships between materials and performance. In parallel with the test activity, to optimize the usage of surgical masks and to reduce their environmental burden, the variation of their performance over time of usage were investigated as to determine the maximum lifetime.

PART I

3D PILLAR-ARRAY SUPPORT FOR CHROMATOGRAPHY

Introduction to chromatography

The high level of purity of the final product required by the biotech industry, especially for food and pharmaceutical applications, is typically achieved by the combination of several separation and purification techniques. An example is provided in figure 1. Due to the capital and operative costs of each step, downstream processing usually represents the major cost of biopharmaceuticals manufacturing and the possibility to isolate the desired product in single-step is very attractive [1].

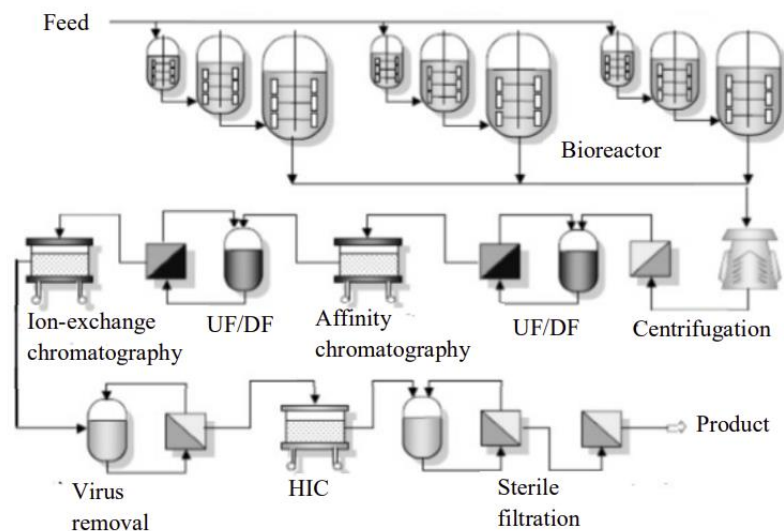


Figure 1: Schematic representation of an antibody purification process

In this context, chromatography is the most widely used technique in the final purification stages, when a high purity should be achieved, because of its high versatility, selectivity and efficiency [2]: it is the only technology able to identify and separate femtomoles of substances in a complex matrix and, at the same time, to purify industrial products in the ton

range [3]. In a chromatographic process the liquid mixture (mobile phase) is fed to a column where the molecules are retained and separated according to their properties and their behaviour with respect to the stationary phase. Based on the nature of the interactions between the two phases (such as electrical or chemical affinity), different chromatographic techniques can be identified. One of the most versatile is affinity chromatography, which is based on highly specific and reversible interactions between a ligand immobilized on the stationary phase and the target molecule that is retained inside the column, while all other substances flow through. At the end of the process the product is recovered by changing the process conditions. Its high specificity makes affinity chromatography an irreplaceable technique in the purification of some components, despite its high cost that, in cases like the capture of monoclonal antibodies, may represent 50-80% of the total downstream processing costs [4 – 6].

The stationary phase of conventional chromatographic columns is constituted by small porous particles, packed by the universally employed slurry-packing method. The consequent difficulties in column packing, the lack of precise control of the particle size distribution, their shape and position inside the column and the intraparticle diffusion as primary mass transport phenomena of the target molecule to the binding site, represent the main limitations that have dramatic effects on the separation efficiency [7, 8]. In the last decades most of the efforts aimed to reduce the particles size and its distribution, with the main drawbacks of increasing the pressure drops and the frictional heating to values close to the tolerable limits [9]. Currently, particles sizes in the range 1.7-2.5 μm and 10-30 μm are frequently used for analytical and preparative applications, respectively. Other efforts have been made towards unconventional supports able to reduce the pressure drops and the contribution of diffusion, such as membranes and monoliths. Currently, one of the most promising solutions is represented by homogeneous beds with a perfectly ordered structure,

that have shown a surprising ability both to increase the column efficiency and to reduce pressure drops. These structures have been extensively studied and tested in the last decade, but their application was limited to two-dimensional devices for analytical applications of micro and nano-volume samples [10, 11], mainly due to limitations of the manufacturing techniques [12, 13].

Recent development of 3D-printers able to combine a high resolution with an acceptable manufacturing velocity allow the creation of regular 3D structures with a fine control over the particle size, shape and position. However, some constraints limit the diffusion of this technology in chromatography, above all the poor compatibility of the available materials.

In this part of the thesis an ordered, three-dimensional, pillar-array structure designed by a CAD software and produced by a stereolithographic 3D-printer will be presented, underlining the advantages and disadvantages belonging to this manufacturing technique. Moreover, a complete fluid dynamic characterization of the column will be provided and a coating solution to overcome the drawbacks of commercially available resins will be studied.

References

- [1] P. A. Marichal-Gallardo and M. M. Álvarez, “State-of-the-art in downstream processing of monoclonal antibodies: process trends in design and validation,” *Biotechnol Prog*, vol. 28, no. 4, pp. 899–916, Jul. 2012, doi: 10.1002/BTPR.1567.
- [2] S. di Martino, “Studio sperimentale e modellazione della separazione di proteine con membrane di affinità,” Ph.D. thesis, University of Bologna, 2009.
- [3] H. Schmidt-Traub, M. Schulte, and A. Seidel-Morgenstern, *Preparative Chromatography*, 3rd ed. 2020.
- [4] “Comparing Performance of New Protein A Resins for Monoclonal Antibody Purification | American Pharmaceutical Review - The Review of American Pharmaceutical Business & Technology.” <https://www.americanpharmaceuticalreview.com/Featured-Articles/347357-Comparing-Performance-of-New-Protein-A-Resins-for-Monoclonal-Antibody-Purification/> (accessed Apr. 26, 2022).
- [5] B. Kelley, “Very large scale monoclonal antibody purification: the case for conventional unit operations,” *Biotechnol Prog*, vol. 23, no. 5, pp. 995–1008, Sep. 2007, doi: 10.1021/BP070117S.
- [6] A. A. Shukla, B. Hubbard, T. Tressel, S. Guhan, and D. Low, “Downstream processing of monoclonal antibodies--application of platform approaches,” *J Chromatogr B Analyt Technol Biomed Life Sci*, vol. 848, no. 1, pp. 28–39, Mar. 2007, doi: 10.1016/J.JCHROMB.2006.09.026.
- [7] F. Svec and Y. Lv, “Advances and recent trends in the field of monolithic columns for chromatography,” *Analytical Chemistry*, vol. 87, no. 1, pp. 250–273, Jan. 2015, doi: 10.1021/AC504059C/ASSET/IMAGES/AC504059C.SOCIAL.JPEG_V03.
- [8] M. F. Wahab, D. C. Patel, R. M. Wimalasinghe, and D. W. Armstrong, “Fundamental and Practical Insights on the Packing of Modern High-Efficiency Analytical and Capillary Columns,” *Analytical Chemistry*, vol. 89, no. 16, pp. 8177–8191, Aug.

- 2017, doi:
10.1021/ACS.ANALCHEM.7B00931/SUPPL_FILE/AC7B00931_SI_001.PDF.
- [9] J. de Vos, K. Broeckhoven, and S. Eeltink, “Advances in Ultrahigh-Pressure Liquid Chromatography Technology and System Design,” *Analytical Chemistry*, vol. 88, no. 1, pp. 262–278, Jan. 2016, doi: 10.1021/ACS.ANALCHEM.5B04381/ASSET/IMAGES/ACS.ANALCHEM.5B04381.SOCIAL.JPEG_V03.
- [10] H. Eghbali, V. Verdoold, L. Vankeerberghen, H. Gardeniers, and G. Desmet, “Experimental Investigation of the Band Broadening Arising from Short-Range Interchannel Heterogeneities in Chromatographic Beds under the Condition of Identical External Porosity,” *Analytical Chemistry*, vol. 81, no. 2, pp. 705–715, Jan. 2008, doi: 10.1021/AC802124P.
- [11] J. op de Beeck, W. de Malsche, P. de Moor, and G. Desmet, “Hydrodynamic chromatography separations in micro- and nanopillar arrays produced using deep-UV lithography,” *Journal of Separation Science*, vol. 35, no. 15, pp. 1877–1883, Aug. 2012, doi: 10.1002/JSSC.201200076.
- [12] A. Daneyko, A. Hölzel, S. Khirevich, and U. Tallarek, “Influence of the particle size distribution on hydraulic permeability and eddy dispersion in bulk packings,” *Analytical Chemistry*, vol. 83, no. 10, pp. 3903–3910, May 2011, doi: 10.1021/AC200424P/SUPPL_FILE/AC200424P_SI_001.PDF.
- [13] M. R. Schure and R. S. Maier, “How does column packing microstructure affect column efficiency in liquid chromatography?,” *Journal of Chromatography A*, vol. 1126, no. 1–2, pp. 58–69, Sep. 2006, doi: 10.1016/J.CHROMA.2006.05.066.

CHAPTER 1

Conventional packed-bed columns: limitations and alternatives

In an affinity chromatographic cycle, the target molecule contained in a mixture is fed to a column where it is retained by highly specific and reversible interactions (similar to those occurring in many biological systems, such as the ones between an antigen and an antibody or an enzyme and its substrate [1]) with a ligand immobilized on the stationary phase, while all the other substances flow through unbound. The product is recovered from the column by changing the process conditions, so that the complex dissociates. Figure 1.1 shows a qualitative concentration profile of the target molecule at the column outlet as a function of fed volume in a typical affinity chromatographic cycle, while the process will be described more in detail in chapter 3.

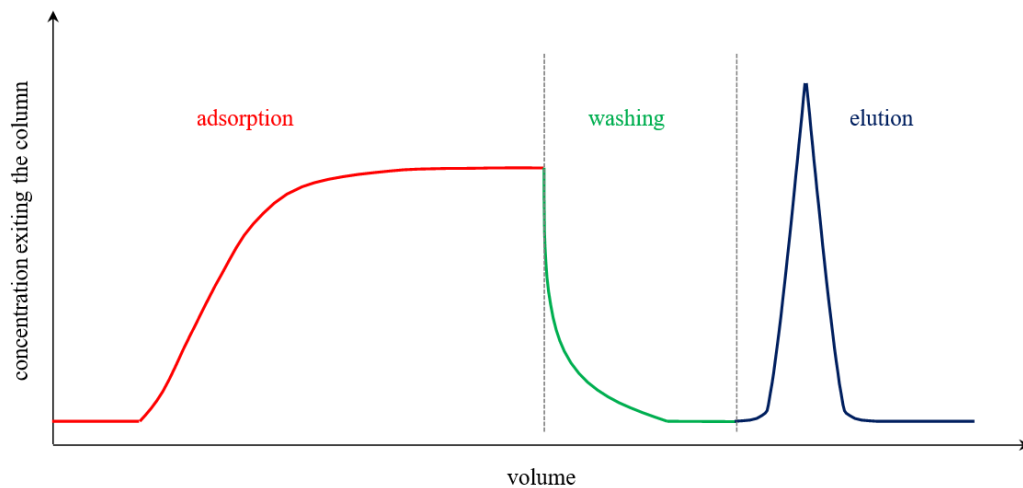


Figure 1.1: Qualitative concentration profile of the target molecule in a complete affinity chromatographic cycle [3]

Thanks to its high specificity, affinity chromatography is the most widely used separation process for the recovery of recombinant proteins, monoclonal antibodies, enzymes, vaccines, gene therapy vectors and other high valuable molecules [2].

The red curve in figure 1.1 is called *breakthrough curve* (BTC). It represents the concentration of the target molecule in the mobile phase exiting the column during the adsorption step and provides important information about the performance of the process, such as the binding capacity and the time required for the separation [3]. The BTC is shown in detail in figure 1.2.

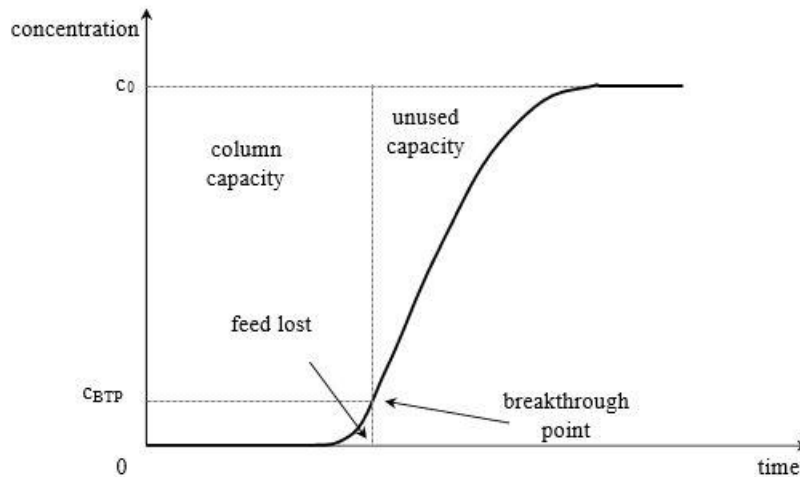


Figure 1.2: Breakthrough curve [3]

From a quantitative point of view, the area under the BTC represents the amount of target molecule that has not been retained by the column, thus representing the product loss, while the area above the curve is the amount adsorbed, indicating the dynamic binding capacity, DBC. It is worth noting that the DBC depends on process conditions, such as flow rate and feed concentration. To achieve an acceptable compromise between amount of product lost and unexploited binding capacity of the column, in industrial processes the adsorption step is stopped when the concentration in the flow through reaches a value that is normally in the range 5-10% of the feed concentration, called breakthrough point [4]. Therefore, it is of primary importance to have chromatographic supports able to provide not only a high binding capacity, but also a very steep breakthrough curve.

The position of the breakthrough is affected by the binding capacity of the column and by the concentration of the solute in the feed. If the latter is kept constant, a higher binding

capacity shifts the breakthrough curve to the right, while, if the former is kept constant, a lower concentration of the solute in the feed moves the breakthrough to the left [1].

About the shape, ideally the BTC should be a step and not a curve, as shown in figure 1.3.

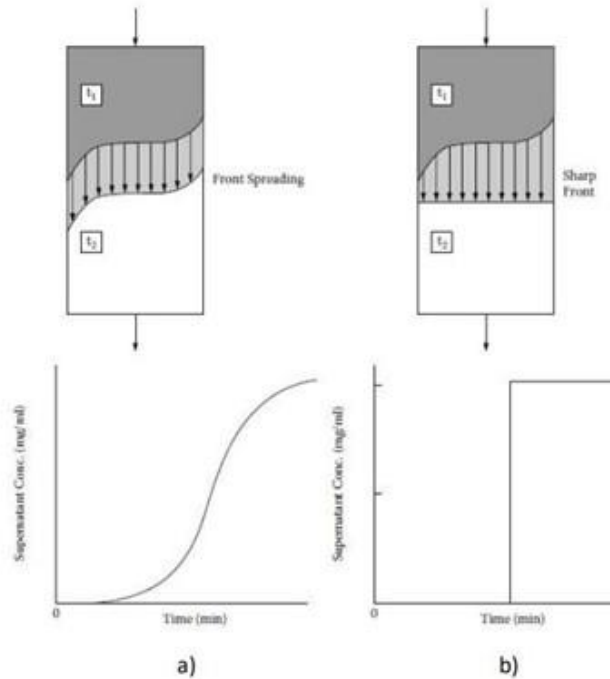


Figure 1.3: BTC in a) real case, b) ideal case [1]

However, as will be shown in Chapter 2 for pulse tests, a step distribution cannot be observed in real applications due to poor flux distribution and slow adsorption phenomena. At a molecular scale, the adsorption takes place because of the formation of binding forces between the surface of the adsorbent and the target molecule in the mobile phase. The binding forces can be distinguished in two types, depending on their nature and strength [5]:

- Physisorption, based on Van der Waals forces ($\hat{H}_{ad} < 50 \text{ kJ/mol}$);
- Chemisorption, based on strong valence forces ($\hat{H}_{ad} \geq 60 - 450 \text{ kJ/mol}$).

Chromatographic adsorption processes must be completely reversible and the adsorbed molecules should maintain their chemical identity. Therefore, only physisorption can be exploited. The energy of this phenomenon is sufficient to increase the temperature of gases

while the effects are irrelevant in liquid chromatography, which can be indeed considered isothermal [5].

In addition to the thermodynamics of the distribution of the target molecule between the two phases, the efficiency of a chromatographic process is influenced by other parameters, the fluid dynamics inside the packed bed and the rate of mass transfer in and around the particles above all.

Conventional affinity chromatography columns are packed with porous beads or resins. They offer a large surface area for the affinity adsorption, but they suffer from several limitations that limit their efficiency and increase the cost of the separation process, such as:

- intraparticle diffusion as primary transport phenomenon of the target molecule to the binding site;
- high operational costs, due to the high pressure drop even at low flow rates;
- difficulties in column packing;
- high material costs;

Indeed, it has become necessary to develop and characterize cheaper and more efficient materials for the stationary phase.

In this chapter, the origins of the main limitations affecting the performance of chromatographic columns will be described, along with the main recent adopted solutions, highlighting their advantages, disadvantages and the constraints that should be met for this separation technology.

1.1 Causes of limited column efficiency

A powerful instrument for the characterization of a chromatographic column and for the determination of its efficiency are pulse tests. In a pulse test, a known volume with a known concentration of an inert tracer is fed to the column and its concentration is recorded at the outlet, as shown in figure 1.4. When molecules contained in the mobile phase enter the top of the column they form a narrow line ($x = 0$). Ideally, a rectangular outlet profile with a width similar to the injected pulse is desired. However, this behaviour cannot be observed in reality: while flowing, molecules spread over a much wider portion of the column due to nonidealities of fluid flow, that cause broadenings of the residence time distribution of the solute and, therefore, undesired dilution of the target component in the axial direction [6].

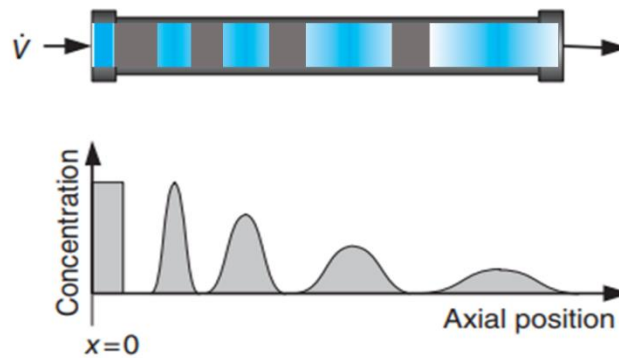


Figure 1.4: Axial dispersion of the tracer

Several transport mechanisms contribute to molecular spreading [7]:

- Longitudinal diffusion;
- Eddy diffusion;
- Mobile-phase mass transfer;
- Stationary-phase mass transfer.

Longitudinal diffusion expresses the influence of back-mixing to band broadening due to axial diffusion of the solute molecules. It becomes relevant in case of large voids among the adsorbent particles (which increase with particle size), especially when the column is

operated at low flow rates [8, 9]. In addition, this term depends on the diffusion coefficient of the solute that, in turn, can be tuned by working on the composition of the mobile phase. From this perspective, reducing the viscosity of the solvents would lead to higher diffusion coefficients and lower pressure drops [7].

The term *mobile-phase mass transfer* refers to the local different velocity and path length of the molecules following the same streamline, as shown in figure 1.5: the portion of the liquid adjacent to a solid particle moves very slowly or not at all, while that in the centre of the streamline move faster and travel for a longer distance per unit time [7, 10]. It results that this contribution to band broadening increases with flow rate. This phenomenon can be more pronounced in the wall region, due to local uniformities of the void space between the particles.

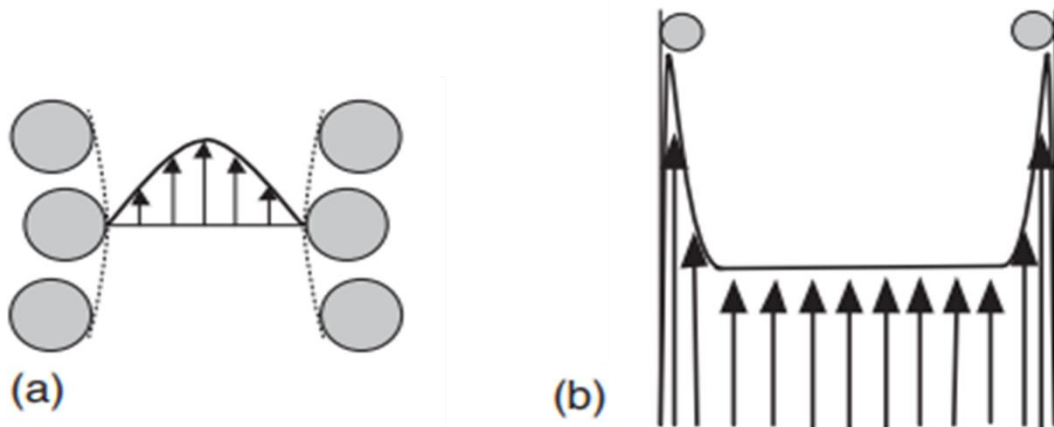


Figure 1.5: velocity profile: a) among particles inside the column, b) in case of a large void in the wall region [6].

The presence of porous particles is another source of spreading, the *stationary-phase mass transfer*, which considers different phenomena as reported in figure 1.6. Molecules in the bulk of the mobile phase are transported by convection and diffusion towards the surface of the porous beads and enter the pores by diffusing through a film of stagnant liquid that surround the particles (film diffusion). Within the small pores, the mobile phase is stagnant

or unmoving, indeed the molecules move inside and outside the pores by restricted Fickian diffusion only, a significantly slower mass transport phenomena compared to convection [1].

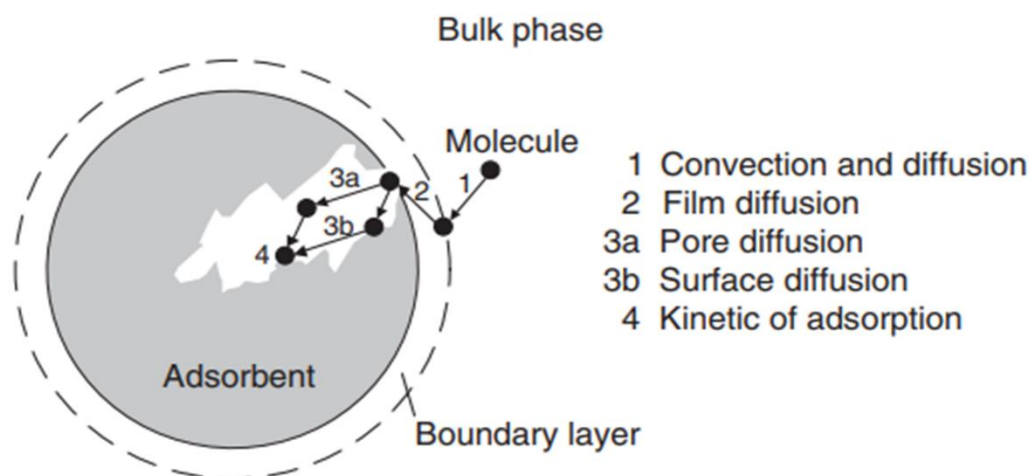


Figure 1.6: mass-transfer phenomena involved in case of porous beads [6].

Some molecules diffuse inside the particles for a short distance, but they are not influenced by the attraction forces of the adsorbent surface and return to the mobile phase quickly (pore diffusion). Other molecules diffuse further into the pores due to the interactions with the solid surface and require more time to exit the column (surface diffusion). Inside the pores, the adsorption on free binding sites takes place. The result is a different residence time inside the pores and, indeed, greater band broadening, which increases with the velocity of the mobile-phase. Band broadening is also strongly promoted by wide pore size distributions, since the residence time of molecules in larger pores is shorter than that in smaller pores. According to Guiochon et al., the kinetics of adsorption and mass transfer from the bulk of the mobile phase to the film surrounding the particles are relatively fast and the limiting processes are film diffusion and transport inside the pores [15]. In preparative chromatography, where the particle size is usually greater than 5 μm , film and surface diffusion are considered not very relevant and pore diffusion is regarded as the dominant mass transfer resistance [16]–[18].

Eddy diffusion arises from the so called “multipath effect”. A perfect hexagonal dense packing is not achievable due to imperfections of the packing material (particles are unavoidably manufactured with a size distribution) and packing procedures, which often cause unequal space between the particles and uneven packing density, especially at the column walls. Therefore, each molecule follows its own streamline inside the column, passes through paths of different dimensions that affect its velocity and arrives at the end of the column at different times, as shown in figure 1.7.

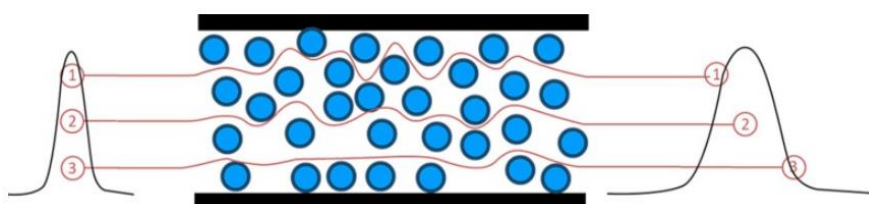


Figure 1.7: Multipath effect [7].

This phenomenon is approximately independent of flow rate and depends on the arrangement and sizes of the solid particles within the column. In the last decades, the improvements of chromatographic column efficiency have been based predominantly on the reduction of particles size [11]. This is true especially for analytical HPLC applications, where particles smaller than 2 μm are currently in use. However, a further reduction is limited by the consequent increase of pressure drops and frictional heating [12, 13]. In addition, this approach had limited effects on the current poor control of the size distribution, shape and uniform arrangement of the particles inside the column, that are the primary causes of bed inhomogeneity and, indeed, of the reduced efficiency [14].

The distributor and the collector, placed respectively at the inlet and at the outlet of the column, represents additional critical points. The former is particularly important to achieve a uniform distribution of the mobile phase, especially in case of low-pressure chromatography, for which specific distributors have been designed [19].

Another contribution to band broadening is provided by every *volume external to the column* that belong to the process plant, such as the volumes of pipes, connections and detectors. Their influence can be reduced by the optimization of the design (i.e. by minimizing the tube lengths and by avoiding dead space) but cannot be eliminated [10].

1.1.1 Height equivalent to a theoretical plate

The efficiency of a chromatographic column is strongly associated to the way the stationary-phase influences the motion of the mobile-phase. All the processes described in the previous paragraph have deleterious effects on the separation efficiency of a chromatographic column that can be quantified with the height equivalent to a theoretical plate (HETP). The HETP can be expressed by the Van Deemter equation (equation 1.1) [7]:

$$H = \underbrace{A}_{\text{Eddy diffusion}} + \underbrace{\frac{B}{u}}_{\text{Longitudinal diffusion}} + \underbrace{C \cdot u}_{\text{Mobile-phase and stationary-phase mass transfer}} \quad (1.1)$$

Where u is the superficial velocity of the mobile phase, usually expressed in cm/h, while A, B and C are three constants that express the contributions to band broadening and are specific for a particular solute, column and set of experimental conditions. Figure 1.8 shows a graphical representation of the Van Deemter equation.

The A-term is related to the Eddy dispersion, is typically constant over the entire velocity range and can be described by equation 1.2 [20]:

$$A = \lambda \cdot d_p \quad (1.2)$$

Where " d_p " is the particle diameter and " λ " is a parameter that describes the bed inhomogeneity.

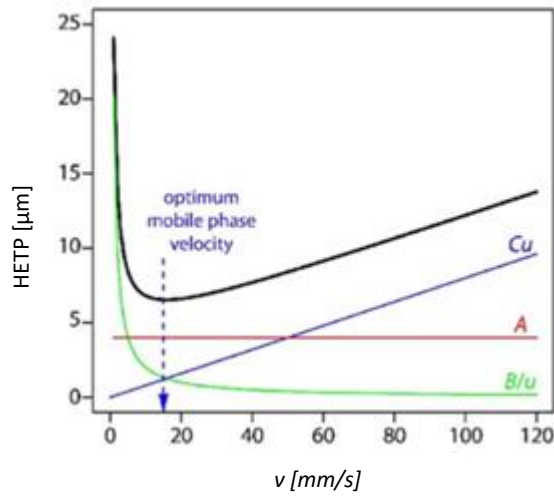


Figure 1.8: Example of the Van Deemter equation reporting the HETP versus the mobile phase velocity [7].

Therefore, the efficiency of a chromatographic column can be improved by reducing the particle diameter and distribution and by improving the packing procedure. Regarding the particle diameter, its reduction causes a proportional increase of the pressure drop, as described by equation 1.3 [15]:

$$\Delta p = 150 \frac{(1 - \varepsilon_e)^2 \mu u_0 L_c}{\varepsilon_e^3 d_p^2} \quad (1.3)$$

Where ε_e is the external void fraction, μ is the kinematic viscosity, u_0 is the superficial velocity, L_c is the length of the column and d_p is the particles average diameter. An optimal diameter average value with respect to pressure drop and plate height in preparative chromatography is typically in the range 10-15 μm [6]. To obtain a narrow size distribution of the particle diameter, a sizing process is usually performed to achieve a ratio $\frac{d_{p\ 90}}{d_{p\ 10}} < 2.5$, where $d_{p\ 90}$ and $d_{p\ 10}$ are the average diameter at 90% and 10% of the cumulative size distribution, respectively, as shown in figure 1.9.

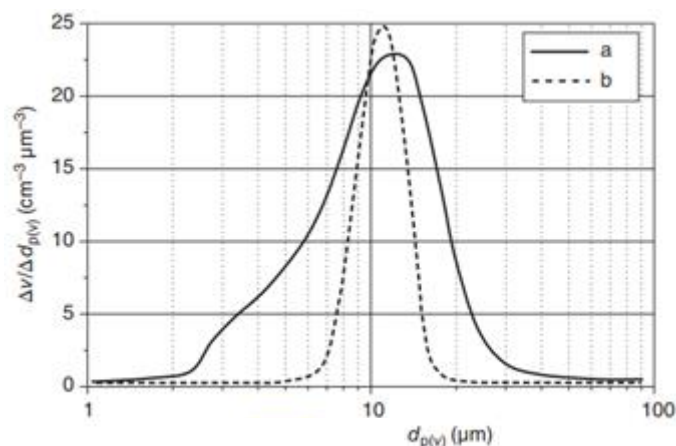


Figure 1.9: size distribution of porous beads (a) before and (b) after the sizing process [6].

The B-term is related to longitudinal diffusion and on the mobile phase composition and velocity. Typically, it is not relevant in preparative chromatography, where the velocity of the mobile phase is sufficiently high [6]. On the contrary, the contribution to the overall band broadening of the C-term, which is related to the mass transfer resistance, increases with the velocity of the solvent, due to a higher influence of the mass transfer resistance inside the pores. In addition, its slope (and, indeed, the plate height) can be reduced by optimizing the pore accessibility and the diffusional path length.

It can be inferred that the HETP initially decreases with the velocity, up to a certain velocity value, then begins to increase again. Indeed, a minimum exists (H_{min}) and, for a column with a perfectly homogeneous bed, its value is given by the cross-point of the curves B/u and Cu. The corresponding value of the mobile phase velocity is the optimal one and can be calculated by equation 1.4 [8]:

$$u_{opt} = \sqrt{B/C} \quad (1.4)$$

However, conventional columns packed with porous beads have beds that are far from being perfectly homogeneous. In this case the A-term cannot be neglected and its magnitude determines the minimum HETP achievable, that can be determined by equation 1.5 [8]:

$$H_{min} = A + \sqrt{B C} \quad (1.5)$$

The Van Deemter equation assumes that all contributions are independent of each other. However, whenever two interparticle streams meet and combine, the resulting remixing causes the loss of the velocity profile created by the mobile-phase mass transfer. On the basis on experimental data, Knox proposed a similar relationship (equation 1.6), in which Eddy diffusion and mobile-phase mass transfer are treated as a single band-broadening event [21]:

$$h = A v^{0.33} + \frac{B}{v} + C \cdot v \quad (1.6)$$

Eddy diffusion and mobile- Longitudinal stationary-phase
phase mass transfer diffusion mass transfer

Where h is the reduced plate height and v is the reduced velocity, which can be calculated by equations 1.7 and 1.8, respectively:

$$h = \frac{H}{d_p} \quad (1.7)$$

$$v = \frac{u d_p}{D_m} \quad (1.8)$$

Where d_p is the particles average diameter and D_m is the molecular diffusion coefficient of the solute.

1.2 Unconventional supports

To overcome the limitations of packed-bed columns, several alternatives have been proposed, mainly aimed to reduce the effects of the diffusion as primary mass transport phenomena. However, their potential is limited due to the inability to meet all the requirements of a chromatographic process, often in direct conflict with each other.

1.2.1 Support requirements

The selection of the proper material is typically the first step in the development of a support for affinity chromatography. Several requirements must be met and many of them are in direct conflict with each other. Therefore, the chosen support should be a compromise that depends on the specific application.

Ideally, the support should, at the same time, play a completely passive role and be able to couple the target molecule. In addition, it should be compatible with the chemical modifications required to immobilize the ligand and allow a rapid and unhindered access of the target molecule to the affinity ligand [22]. Moreover, a great stability over a wide range of pH, temperature, pressure and solvent conditions is required. These properties can be summarized and classified as:

- chemical inertness;
- chemical and mechanical stability;
- pore size;
- particle size.

Finally, especially for large-scale preparative applications, the cost of the support is another important factor to consider [6].

1.2.1.1 Chemical inertness

The base material should be inert to any molecule contained in the mobile phase except for the target molecule, to avoid the reduction of free binding sites and the presence of undesired substances in the product. Almost all affinity separations are performed in aqueous solutions with low ionic strength, therefore the support should be as hydrophilic as possible and

should have few charges to prevent ionic interactions [1]. Polysaccharide agarose is one of the most common suitable materials, because of its polymeric chains (whose repeating unit is shown in figure 1.10) that form a porous hydrophilic network. Cellulose is another example.

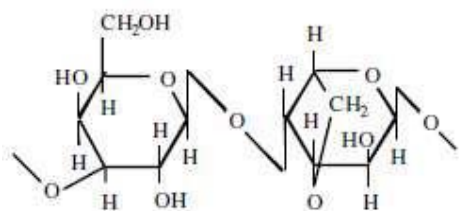


Figure 1.10: Repeating unit of Agarose

Other materials are not suitable in their original form but can be adapted by chemical or coating treatments. Silica support is certainly hydrophilic, but due to the presence of silanol groups its surface possesses a strong negative charge at neutral pH that causes irreversible adsorption of some solutes, such as proteins. This phenomenon can be prevented by coating its surface with a polymer, or by reaction with alcohols or trialkoxysilanes [22, 23]. On the contrary, polystyrene is highly hydrophobic but can be rendered hydrophilic by surface coating. The interest for other supports, based on metal oxides, alumina and zirconia is growing [1].

1.2.1.2 Chemical and mechanical stability

The support should be stable towards all the substances that will be used in the process, such as proteolytic enzymes, microbes, elution buffers and regenerating agents. In addition, the support must be stable to strong sodium hydroxide solutions, used for regular sanitization in cleaning in place (CIP) mode in the biomanufacturing industry as bactericide and for the removal of irreversibly deposited materials, such as denatured proteins and lipids, that can contaminate and clog the column.

From this point of view, the cross-linked form of agarose-based supports easily withstands sanitation with 0.5 M sodium hydroxide and autoclaving at 120 °C. On the contrary, silica can be damaged at pH above 8 [24], but its resistance to alkaline environment can be improved by surface coating or by incorporating zirconium or aluminium [25].

The mechanical resistance is another important parameter, since an adsorption process requires specific speed and flow rate. Often, this translates in high pressure inside the column that can cause severe modifications and damages to the support structure. Some supports, like high cross-linked polymers or silica, have a high mechanical resistance. Others, like standard agarose beds, compress and cause a further increase of the pressure, up to the collapse [26].

1.2.1.3 Pore size

Both the size of the pores and the dimensions of the target molecule affect the accessibility of the target molecule to the ligand and their relationship can be expressed in terms of effective diffusion coefficient. According to Renkin, the effective diffusion coefficient can be expressed as a function of the ratio between the radius of the molecule, R_s , and the radius of the pore, R_p [27] (equation 1.9):

$$D_{eff} = D K_D \varepsilon_p \frac{\left[1 - 2.10 \left(\frac{R_s}{R_p} \right) + 2.09 \left(\frac{R_s}{R_p} \right)^3 - 0.95 \left(\frac{R_s}{R_p} \right)^5 \right]}{\tau} \quad (1.9)$$

where D is the molecular diffusion coefficient for the solute in free solution, K_D is the distribution coefficient for the solute, τ is the tortuosity factor and ε_p is the support porosity and. The analysis of different ratios between the molecule and the pore radius leads to the conclusion that, to avoid too small diffusion rates, a value of at least $R_p = 5 R$ for the

pore radius should be preferred [1]. However, large pores cause the reduction of the surface area per unit volume of support and, in turn, a lower binding capacity. Typically, a pore size in the range 300 - 700 Å is a good compromise for packed-bed columns [1].

1.2.1.4 Particle size

In preparative chromatography, a wide variety of particles dimension in the range 10 - 400 μm are available [28]. Small particles reduce the distance between the bulk of the solution and the ligand inside the pores, because of the shorter pores and the thinner stagnant mobile phase layer around, thus reducing the time required for diffusion, both in adsorption and elution, with positive effects on the column efficiency. According to Einstein (equation 1.10) [29] the time required by the target molecule to reach the ligand, t_d , is directly proportional to the square of the mean distance, d , and inversely proportional to twice the effective diffusion coefficient, D_{eff} :

$$t_d = \frac{d^2}{2 D_{\text{eff}}} \quad (1.10)$$

However, the reduction of the particle size below 10 μm does not give a proportional improvement of the column performance in preparative applications, since the adsorption and desorption kinetics of the target molecule to the ligand become the limiting factors [16]. In addition, the reduction of particle size is the main cause of high pressure drop, ΔP , which are inversely proportional to the square power of the particle diameter, d_p , as shown by the Carman-Kozeny equation 1.11 [1]:

$$\frac{\Delta P}{L} = \mu C \frac{u}{d_p^2} \quad (1.11)$$

Where L is the column height, μ is the mobile phase viscosity, C is a constant that depends on the column porosity and u is the linear flow velocity. A reduction of the particle size by

a factor 5 leads to a rise of the pressure drop of a factor 25, causing in higher operative costs and higher mechanical resistance required by the material [1]. Moreover, the danger of fouling increases as particle size decreases, due to a reduction of the interstitial spaces available to the flowing solution.

Indeed, the particle size should be carefully chosen for each specific application, considering the mechanical resistance of the support and defining the best compromise between performance and operating costs.

1.2.2 Support materials and structures

Conventional columns, packed with porous beads, show a limited efficiency due to the relatively high distance between the bulk of the solution and the ligand inside the pores that should be covered by the target molecule by diffusion. In addition, these columns suffer of high pressure drops, which increase with time due to bed compaction and plugging. The use of smaller particles allows a more efficient use of the adsorptive surface but, as highlighted in the previous paragraphs, it increases the pressure drop and, thus, the operative costs.

With the aim of improving the performance and reduce the costs, several new and innovative support materials have been developed over the last decades and can be classified as follow:

- Non-porous supports;
- Perfusion media;
- Expanded bed adsorbents;
- Membranes;
- Monoliths (or continuous supports).

The main difference between these configurations is the predominant mass transport phenomena, schematically represented in figure 1.11, that drives the target molecule to the binding site: diffusion and convection.

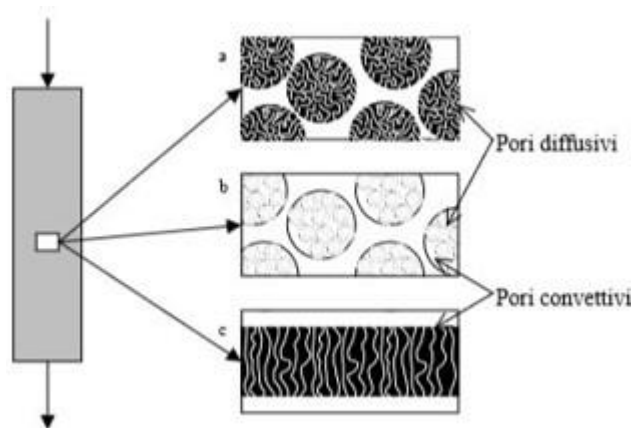


Figure 1.11: diffusive and convective pores [1]

Each solution has advantages and disadvantages with respect to the others, therefore the best compromise should be identified depending on the specific application and on the process requirements.

1.2.2.1 Non-porous supports

Non-porous supports are constituted by dense rigid particles in which the absence of pores, as can be observed in figure 1.12, virtually eliminates the contribution of stationary-phase mass transfer resistance to band broadening. In addition, these supports allow to reduce the pressure drop related to bed compaction and plugging. A further reduction can be achieved by using monodisperse particles instead of polydisperse [30]. The main drawback is the lower surface area due to the absence of the pores and, as a consequence, the lower binding capacity: a bed made of $1 \mu\text{m}$ non-porous particles has a surface area of about 5 m^2 per mL of column, while the corresponding value in case of porous silica beads with 300 \AA pores is almost ten times higher [1]. Typically, these beads have a diameter in the range $1 - 3 \mu\text{m}$ and are used for fast analytical or micro-preparative separations.

Non-porous submicron fibers have a very high dynamic binding capacity and a low backpressure fall and are considered non-porous supports [1].

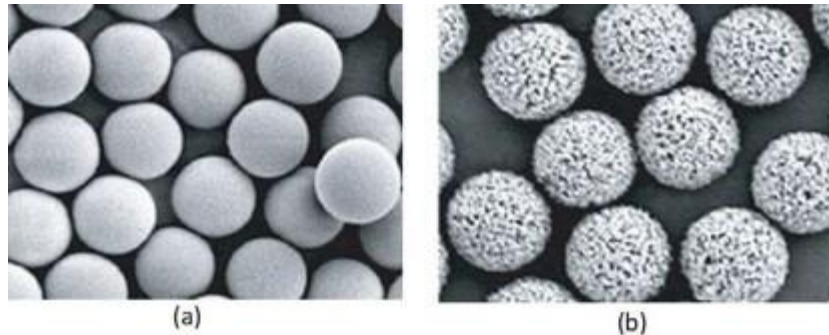


Figure 1.12: non-porous (a) and porous (b) beads for affinity chromatographic support [1]

1.2.2.2 Perfusion media

Perfusion media are columns packed with particles with a bimodal pore size distribution, as shown in figure 1.13. The large flow-through pores allow the transport of the target molecule to the interior of each particle by convection, thus reducing the distance to be covered by diffusion in the small diffusion pores, that increase the surface area. As consequence, a significant improvement of the performance compared with standard particles of the same size is observed, especially for large molecules and high flow rates, where slow diffusion is the limiting factor. Often, these supports present equal or even higher static binding capacity compared to conventional packing with particles of the same size [31, 32]. This is observed especially in case of large molecules binding to large ligands (i.e. IgG to protein A), when the resulting complex can be so large to block small pores reducing the binding capacity of the support [33]. This phenomenon is less frequent in perfusion media, where the length to be covered by diffusion is much shorter and it decreases the statistical likelihood for a ligand to become unreachable [1].

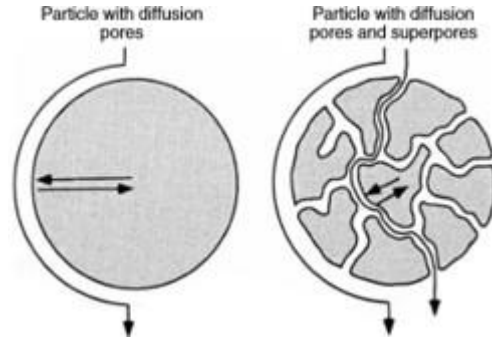


Figure 1.13: comparison of particles with normal diffusion pores versus particles with diffusion and flow-through pores

1.2.2.3 Expanded-bed adsorbents

The use of expanded-bed adsorbent is recommended in case of high risk of column clogging [22], due to the presence of solid contaminants (such as cells and cell debris) in viscous solutions. In this type of affinity chromatography, the upward flow of the mobile phase through the column expands the bed, as shown in figure 1.14, creating larger interstitial spaces where the contaminants can flow through, avoiding column clogging. The dimension of the interstitial space can be controlled by varying the fluid velocity.

To facilitate the control of the expansion, particles with a high density are recommended, such as porous mineral oxides [34]. Conventional particles can be made denser by adding dense material, like quartz. An example are the Streamline adsorbents from Cytiva and the UFC-agarose from UpFront Chromatography.

Expanded-bed adsorbent allow to reduce the number of pre-treatments, such as filtration and centrifugation and enables a significant reduction of the pressure drop, at the expense of performance.

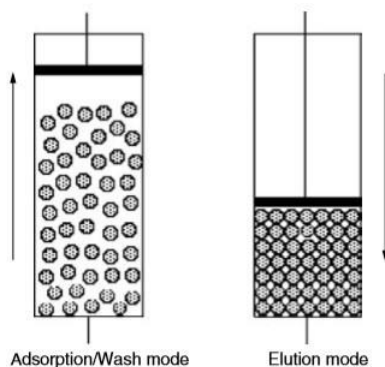


Figure 1.14: Expanded-bed chromatography. The bed expands during adsorption-wash step and compacts during elution

1.2.2.4 Membranes

Membranes were originally designed to overcome the limitations of packed-bed columns, by reducing the pressure drop and reducing the effects of diffusion.

In membrane systems, mass transfer occurs primarily by convection and the porosity is in the range 0.6 - 0.8, while the average pore sizes is $0.4 - 3.0 \mu\text{m}$ [35]. These characteristics allow to hold the pressure drop to low values, even at high flow rates, and to reduce the time required for adsorption, washing and elution steps. Therefore, membranes are particularly adequate for the separation of vulnerable and large biomolecules, such as proteins. The main drawback of membranes is the low binding surface due to the absence of small diffusive pores, as for non-porous beads [36]. To overcome this problem, multilayer supports can be created by stacking membranes sheets one over the other. This solution allows also to reduce the intrinsic membrane inhomogeneity, due to a non-homogeneous pore distribution, and to easily scale-up the process compared to other materials and configurations. It is noteworthy that, even for high multilayer systems, the longitudinal dimension is always much lower compared to the lateral one, leading to problems of uniform flow distribution.

Membranes can be produced in several geometries, such as disks, layered sheets, rolled geometries or hollow fibers. The most common materials are cellulose, polysulfone or

polyamide [36]. Depending on the application, different functional particles, such as silica, can be incorporated into a porous polymeric matrix, generating mixed matrix membrane adsorbers with superior performance. These membranes are widely used in lab-scale operations for the isolation of peptides, nucleic acid and other organic compounds from complex liquid mixtures [36]. The production of affinity membranes has been based from that of beads and is performed in three steps:

- Choice of appropriate support;
- Activation of the surface
- Immobilization of the ligand.

The properties required for affinity chromatography applications (such as mechanical resistance to high pressure and wide range of pH, easily functionalization, highest possible surface area, etc) are difficult to find in a single membrane and, for this reason, they have not reach commercial maturity up to now [35].

1.2.2.5 Monoliths

Monoliths are supports consisting of a single continuous piece of material and are characterized by an easy preparation with good reproducibility, versatile surface chemistry, low backpressure and fast mass transport. Their advantages are similar to those of membranes, from which they differ in terms of material, preparation and morphology.

As for perfusion media, monoliths are characterized by a bimodal pore size distribution [7] that provides high separation and good fluid dynamics characteristics:

- large micrometre-size through-pores, allow the target molecule to reach faster the ligands by convection and with low pressure drop, even at high flow rates;

- smaller diffusive pores, in the 10 nm range, contribute significantly to the overall surface area.

Monoliths can be produced from organic (polystyrene, acrylamides, acrylates, methacrylates or imprinted polymers) or inorganic materials (silica, titanium, zirconia or aluminium oxide) by three methods [24]: polymerization of an organic monomer in the presence of additives, formation of silica-based network via sol-gel process and by a sintering process, that allows to fuse the porous packing material inside the column shell. Therefore, for lab scale or analytical application monolith can be prepared directly in the chromatographic column, avoiding the time-consuming step of column packing. However, their production, especially for industrial application, is not straightforward [37, 38]. Monoliths are typically disk or rod shaped, with the longitudinal dimension exceeding the lateral one. Therefore, they are considered closer to packed-bed columns than to membrane adsorbers.

1.3 Recent developments in HPLC

Nonporous and fully porous particles are the two main types of packing materials used for high performance liquid chromatography (HPLC) so far. The major difference is that porous particles are affected by the mobile-phase mass transfer resistance of the stagnant liquid inside the pores, but offer much greater surface area and higher loading capacity. Over the last years, the advances in packed bed columns have been focused mainly on the reduction of the particles size of fully porous particles and on the development of core-shell superficially porous particles [39]. However, the advantages provided by sub-2 μm particles are not large as expected, mainly due to frictional heating caused by the higher pressure drop and radially inhomogeneity of packing density [40, 41]. Indeed, several research focused the attention on other unconventional products, like monoliths. In the early 20th century, the

importance of the homogeneity of the packing was recognized by Knox, that postulated that the efficiency of a chromatographic column can be approximately doubled by the use of a perfectly ordered packing [20, 21]. By following this approach, in the last decade two-dimensional pillar-array columns with very ordered and precise structure were fabricated by silicone etching, achieving surprising performance of separation. However, their use is limited to the analytical research, due to the small volume and the low operative flow rates, both in the micro-scale range. Today, the recent development of 3D printers gives the opportunity to explore new complex morphologies and particles shapes and to potentially produce stationary phase with perfect ordered structure in three dimensions.

In this section an overview of the advances of columns for analytical application will be provided.

1.3.1 Fully porous particles

Currently, columns packed with fully porous particles having a diameter in the range 1.5-2.0 μm are commercially available and used in the pharmaceutical and biotech industry for analytical applications [42, 43]. The higher efficiency of smaller particles has been demonstrated by several research, but their use is limited by the higher pressure drops and more difficulties in the column packing [44, 45]. Compared to nonporous particles, this kind of packing offers higher surfaces areas and sample loading capacity from 16.5 to 50 times greater [46, 47].

The advances in fully porous packed bed column have been focused on the improvement of column packing techniques, on the reduction of the particles size distribution (PSD) and on the development of new materials. Gritti and Guiochon demonstrated the higher performance achievable by a narrow PSD, by testing columns packed with 1.9 μm Titan-

C18 particles (relative standard deviation, RSD, of about 10%), measuring a minimum reduced plate height $h_{min} = 1.6$, thanks to the very low intraparticle diffusivity (B-term) [48]. Armstrong *et al.* investigated the use of amorphous polycondensed aluminosilicate ceramic particles, a class of geopolymers with a great mechanical and chemical stability, even at high pH. They produced particle with a mean particles size (MPS) of 6.1 μm ($D_{90}/D_{10} = 2.9$, RSD = 7.6%), with a specific surface area of 385 m^2/g , comparable to that of the commercially available silica particles (200-450 m^2/g) [49].

Table 1.1 provides a list of recent commercially available columns packed with fully porous beads and of their efficiency [50].

Table 1.1: Summary of different fully porous fine particles packing [50].

Stationary phase	Column dimension	h_{min}	H_{min} (μm)	N_{max}	Solute
1.5 μm Grace Vision HT C18	2.0 mm \times 50 mm	3.1	4.6	10,870	Ethinylestradiol
	2.0 mm \times 50 mm	3.1	4.6	10,870	Bicalutamide
	2.0 mm \times 50 mm	4.6	6.9	7246	Ivermectin
1.7 μm BEH C18	2.1 mm \times 50 mm	2.6	4.4	11,364	Butyrophenone
	2.1 mm \times 50 mm	3.3	5.6	8990	Acenaphthene
	2.1 mm \times 50 mm	2.8	4.8	10,500	Butylparaben
	2.1 mm \times 50 mm	2.8	4.7	10,638	Ethinylestradiol
	2.1 mm \times 50 mm	2.8	4.8	10,417	Bicalutamide
	2.1 mm \times 50 mm	3.8	6.5	7692	Ivermectin
	2.1 mm \times 100 mm	2.9	4.9	20,408	Phenol
	2.1 mm \times 100 mm	2.5	4.2	23,810	Propylparaben
2.1 mm \times 150 mm	2	3.4	44,118	Naphtho[2,3-a]pyrene	
1.7 μm BEH Shield RP18	2.1 mm \times 50 mm	2.3	3.9	12,800	Butylparaben
1.8 μm Zorbax Eclipse XDB C18	2.1 mm \times 50 mm	3	5.4	9300	Butylparaben
1.8 μm Zorbax Extend C18	2.1 mm \times 50 mm	2.5	4.5	11,100	Butylparaben
1.8 μm Zorbax Stable Bond C18	2.1 mm \times 50 mm	3.2	5.8	8700	Butylparaben
	2.1 mm \times 50 mm	2.8	4.8	10,417	Ethinylestradiol
	2.1 mm \times 50 mm	2.72	4.9	10,204	Bicalutamide
	2.1 mm \times 50 mm	3.8	6.9	7246	Ivermectin
1.9 μm Hypersil GOLD C18	2.1 mm \times 50 mm	2.6	4.9	10,100	Butylparaben
	2.1 mm \times 50 mm	3.7	7.1	7042	Ivermectin
1.9 μm Restek Pinnacle DB C18	2.1 mm \times 50 mm	2.9	4.9	10,204	Ethinylestradiol
	2.1 mm \times 50 mm	2.6	4.9	10,204	Bicalutamide
	2.1 mm \times 50 mm	3.2	6.1	8197	Ivermectin
2.0 μm YMC UltraHT Pro C18	2.0 mm \times 50 mm	2.5	5.0	10,000	Ethinylestradiol
	2.0 mm \times 50 mm	2.5	5.0	10,000	Bicalutamide

1.3.2 Core-shell particles

In core-shell particles a nonporous core is coated with a porous layer of stationary phase, as shown in figure 1.15. The columns packed with these particles show a 20-30% lower longitudinal diffusion (B-term) and 40% lower Eddy dispersion (A-term), compared to those packed with fully porous particles. In addition, a more favourable C-term has been measured in case of large molecules, such as proteins [51]. As consequence, core-shell particles provide smaller HETP compared to totally porous particles of the same size and, indeed, the same separation can be achieved with larger particles and consequent lower pressure drops.

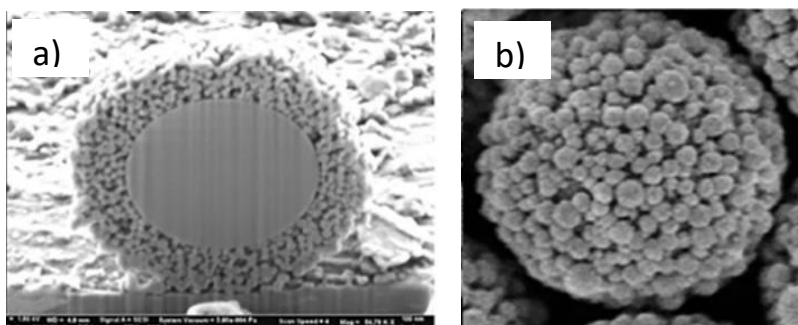


Figure 1.15: TEM analysis of a core-shell particles: a) section, b) porous layer [50]

As for fully porous articles, most of core-shell beads are made from silica. The core is typically produced using the Stober process, while the shell is built up by a layer-by-layer approach until the desired shell thickness is achieved [52, 53]. However, other materials have been used to create the core or the porous layer. Deng and Marlow coated polystyrene particles with an organo-silicone shell, while Hung *et al.* synthesized carbon core particles that are more stable to pH and temperature compared to silica [54, 55].

The actual generation of commercial products has particles with a porous zone that constitutes roughly $3/4^{\text{th}}$ of the total particle volume. On the basis of the particles size, they can be divided in two categories, namely 1.6-2 μm 4-5 μm [39]. Table 1.2 provides a list of recent commercially available columns packed with core-shell particles, along with their efficiency [50].

Table 1.2: Summary of different core-shell particles packings [50]

Stationary phase	Column dimension	h_{\min}	H_{\min} (μm)	N_{\max}	Solute
2.7 μm Poroshell 120	2.1 mm \times 100 mm	2.5	6.8	14,706	Naphthalene
	2.1 mm \times 50 mm	2.0	5.4	9259	Naphthalene
	4.6 mm \times 150 mm	1.4	3.8	39,474	Naphthalene
	4.6 mm \times 100 mm	1.6	4.3	23,256	669 Da compound
2.7 μm Halo	2.1 mm \times 150 mm	1.8	4.9	30,612	Naphthalene
	4.6 mm \times 150 mm	1.6	4.3	34,883	Naphthalene
	4.6 mm \times 150 mm	1.7	4.6	32,609	Anthracene
	4.6 mm \times 150 mm	2.0	5.4	27,778	Bradykinin, lys-bradykinin
	4.6 mm \times 150 mm	\sim 2.0	\sim 5.4	\sim 28,000	Insulin
	4.6 mm \times 150 mm	\sim 2.0	\sim 5.4	\sim 28,000	Lysozyme
	4.6 mm \times 150 mm	\sim 4.0	\sim 10.8	\sim 13,900	BSA
	4.6 mm \times 150 mm	1.8	4.9	30,612	β -Lipotropin
		1.7	4.6	10,870	Virginiamycin
	4.6 mm \times 50 mm	2.0	5.4	9259	Insulin
	2.1 mm \times 50 mm	3.4	9.2	5435	Polypeptide 4.1 kDa
	2.1 mm \times 50 mm	1.6	4.3	11,628	Levonorgestrel
	4.6 mm \times 100 mm	1.5	4.1	24,390	669 Da compound
	2.1 mm \times 100 mm	1.8	4.9	20,408	Butyrophenone
2.6 μm Kinetex	2.1 mm \times 150 mm	1.5	3.9	38,462	Naphthalene
	4.6 mm \times 150 mm	1.3	3.4	44,118	Naphthalene
	2.1 mm \times 50 mm	1.9	4.9	10,204	Estradiol
	2.1 mm \times 100 mm	1.9	4.9	20,408	Estradiol
	3.0 mm \times 100 mm	1.3	3.4	29,412	Estradiol
	4.6 mm \times 100 mm	1.2	3.1	32,258	Estradiol
	4.6 mm \times 100 mm	1.2	3.1	32,258	Naphthopyrene
	2.1 mm \times 100 mm	1.5	3.9	25,641	Naphthopyrene
	4.6 mm \times 100 mm	1.4	3.6	27,778	669 Da compound
1.7 μm Kinetex	2.1 mm \times 150 mm	2.9	4.9	30,612	Naphthalene
	4.6 mm \times 100 mm	2.1	3.6	27,778	Naphthalene
	2.1 mm \times 50 mm	3.7	6.3	7937	Polypeptide 4.1 kDa
	2.1 mm \times 50 mm	1.5	2.6	19,231	Estradiol
	2.1 mm \times 50 mm	2.5	4.3	11,628	Naphthopyrene
Eiroshell 150-C18	2.1 mm \times 50 mm	1.9	3.2	15,625	Naphthopyrene
Eiroshell 250-C18	2.1 mm \times 50 mm	2.2	3.7	13,514	Naphthopyrene
Eiroshell 350-C18	2.1 mm \times 50 mm	2.5	4.3	11,628	Naphthopyrene
2.7 μm HALO-ES	4.6 mm \times 150 mm	1.4	3.8	39,474	β -Lipotropin
	4.6 mm \times 150 mm	\sim 2	\sim 5.4	\sim 28,000	Insulin

1.3.3 Monoliths

The main advantage of monolithic column is the higher porosity, that can be tuned up to 90%, compared to the typical 40% of particles packed column, resulting in a higher permeability but, also, on a higher diffusional distance in the flow-through pores that negatively affect the mobile phase mass transfer C-term [39]. Therefore, research on monolithic media mainly focused on the reduction of the skeleton size.

Dores-Sousa *et al.* synthesized a poly(styrene-co-divinylbenzene) monolithic support, demonstrating that the optimal monolithic structure is characterized by high homogeneity of the structure and high external porosity, with polymer globules size in the submicron range and macropores whose dimension can be tuned by changing the porogen to monomer ratio towards speed (100-500 nm) or efficiency (500 nm – 1 μ m) [56, 57]. Simone *et al.* created a methacrylated-based monoliths by γ -ray polymerization that showed more than $1 \cdot 10^6$ plates per metre of column, at a mobile phase velocity of 0.5 mm/s [58]. In silica monoliths, Hara *et al.* achieved an average domain size in the sub-2 μ m range, obtaining a minimal plate height of 4 μ m. However, it was observed that the smaller is the domain size, the worse is the homogeneity of the structures [59]. Currently, the limit of monolithic column is the radial heterogeneity, that is caused by the inherent shrinkage that pulls away the mass from the centre towards the sides during the production process, leading to high Eddy dispersion terms.

Table 1.3 provides a list of literature examples of monolithic columns.

Table 1.3: examples of monolithic columns from literature

type	H (μm)
silica monolith capillary (1st gen)	6.90
silica monolith capillary (2nd gen)	4.80
silica monolith capillary (3rd gen)	4.00
silica monolith-normal bore (2nd gen)	6.50
silica monolith-normal bore (2nd gen)	6.00
low aspect ratio silica monolith	4.60
low aspect ratio silica monolith	4.40
polymer monolith	8.70
polymer monolith	16.00
polymer monolith	9.80
porous layer open tubular	5.50
micropillar array (radially elong. pillar)	0.77
micropillar array (radially elong. pillar)	0.74
micropillar array (radially elong. pillar)	0.56
micropillar array (cylindrical pillar)	3.15

1.3.4 Micropillar array columns

These columns consist of regular arrays of silicon pillars, constructed by microlithographic etching to be perpendicular to the mobile phase flow and to provide an absolute regularity and homogeneity of the stationary phase inside the column, thereby eliminating the contribution of Eddy dispersion A-term [60]. Currently, a series of commercial products (μPAC) are manufactured by Thermo Fisher Scientific. μPAC columns have pillars with a diameter of $5\ \mu\text{m}$, height of $20\ \mu\text{m}$, an interpillar distance of $2.5\ \mu\text{m}$ and an external porous layer of deactivated silica having a width of $0.3\ \mu\text{m}$ and created by anodic oxidation in dilute hydrofluoric acid [7]. According to Desmet *et al.*, μPAC can be regarded as columns packed with $5\ \mu\text{m}$ or $7.5\ \mu\text{m}$ particles, compared to which they provide lower reduced plate height (as shown in figure 1.16) and much higher permeability, that allows to connect several columns in series, achieving a number of theoretical plates between 1 and 1.6 million for a 2 m column [7, 61]. Both the volume and the flow rate are in the micrometres, therefore requiring nanoflow HPLC instruments and highly skilled staff. The maximum operating

pressure is around 300 bars. The production techniques do not allow to produce larger volume columns, limiting their application to single-cell proteomics research [7].

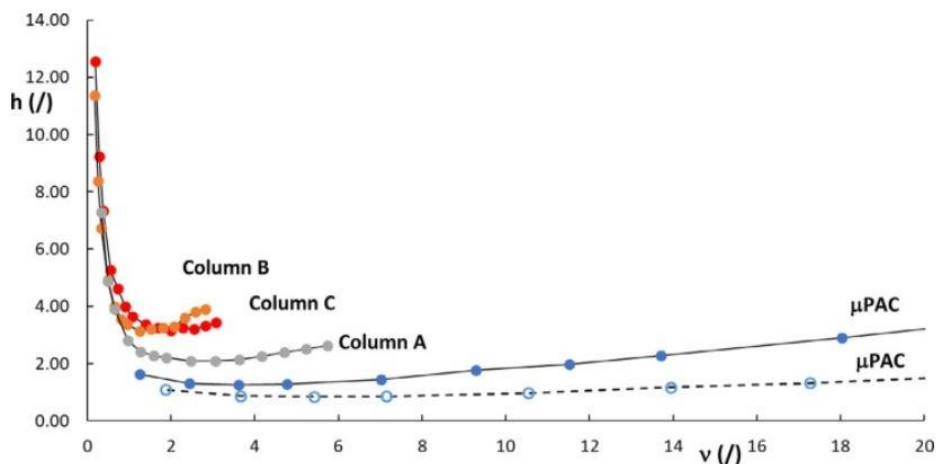


Figure 1.16: reduced plate height curves vs mobile phase velocity. A, B and C are columns packed with 3, 2 and 1.7 μm particles, respectively. uPAC dashed curve and continuous curve are the values obtained considering particles of 5 and 7 μm , respectively [7].

1.3.5 3D printing

Today, the recent development of 3D printers with high resolution and relatively fast layer-by-layer production processes enables the creation of any desired three-dimensional structure. Therefore, 3D printing gives the opportunity to explore new complex morphologies and particles shapes and to potentially produce stationary phases with perfect ordered structure, eliminating Eddy dispersion [62, 63]. In 2017, Nawada *et al.* used a 3D printer to produce, for the first-time, beds with a perfectly ordered structure and particles of different shapes (tetrahedra, octahedra, truncated icosahedra and stella octangulae, showed in figure 1.17). Notably, the best results in terms of HETP were obtained with tetrahedral particles, questioning the universally accepted superiority of spherical beads [64].

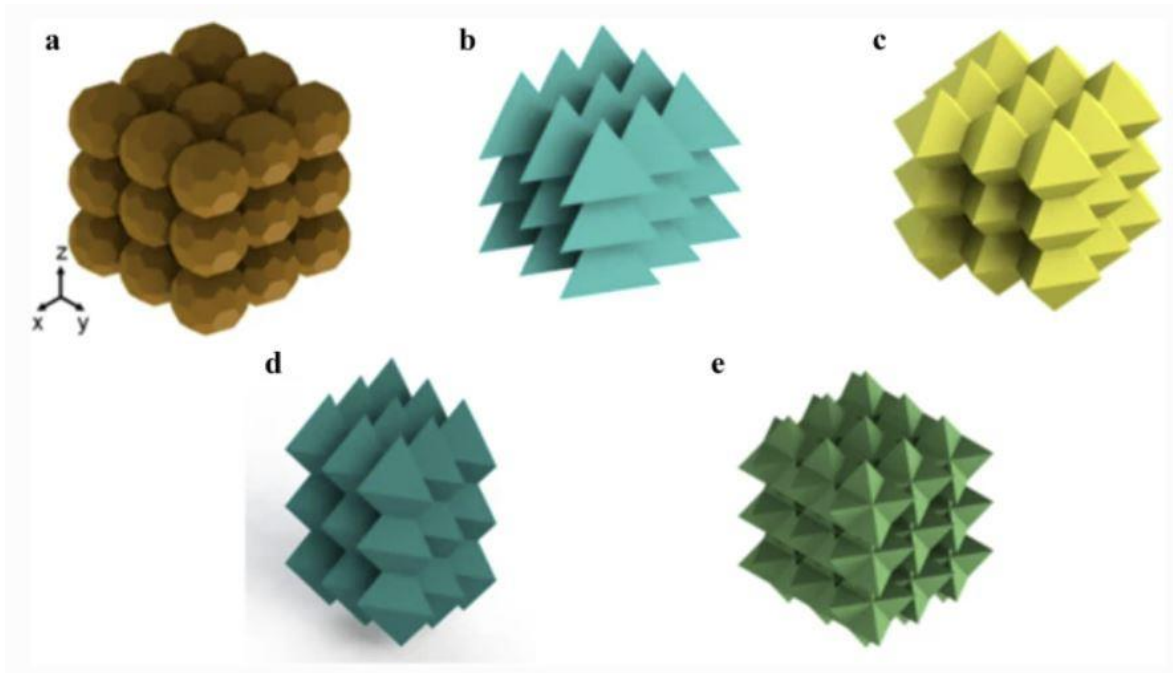


Figure 1.17: particles shapes and arrangement of the beds printed by Nawada *et al.*: a) spheres, b) tetrahedra, c) octahedra, d) triangular bipyramids, and e) stella octangulae. [64]

In another work, Nawada *et al.* tested the effects of several arrangements of spheres: simple cubic (SC), body-centred cubic (BCC) and face-centred cubic (FCC), showing the narrower range of flow velocities of the FCC arrangement compared to the others and, indeed, higher efficiency [65].

Currently, several prototypes have been designed and produced by 3D printing, showing its potential to offer several solutions for chromatographic applications, such as [10]:

- Creation of any desired morphology;
- Rapid prototyping;
- Manufacture of complex bespoke equipment and ancillary column elements;
- Creation of columns cartridge, eliminating the problem related to column packing.

However, several restrictions for the 3D printing of stationary phase for chromatographic separations exist. The current biggest hurdle is represented by the absence of suitable materials. Despite a wide range of 3D printable materials are on the market, including metals,

ceramics and polymers, they are universally designed to create dense components (instead of porous structures that are of interest for chromatography) and without considering the possibility to bear specific functional groups [63]. In addition, the 3D printing process requires the addition to the raw materials of plasticizers, fillers and additives that may be partially released, causing the contamination of the mobile phase. Furthermore, the formulations of the materials are proprietary, thus limiting their optimization for the separation sciences by external research groups [10]. Currently, several approaches have been followed to overcome these limitations. One approach is based on the use of commercial materials with some properties that meet the chromatography requirements: MacDonald *et al.* used Veroclear (by Stratasys), a material with negative charges on the surface that were exploited for proteins separation [66]. Another approach is similar to that used for conventional resin and is based on the post-printing coating and functionalization of the materials [67, 68]. A third approach was followed by Simon and Di Martino, that formulated a material with a bifunctional monomer (bearing quaternary amine groups as anion exchange ligands) and demonstrated for the first time the possibility to 3D print functional stationary phases with a binding capacity similar to commercial resins [63].

A further limitation is related to the resolution, the speed and the printable size. The best additive manufacturing techniques able to print samples with acceptable dimensions and printing time have a resolution around 100 μm , whereas values in the nanometres scale would be required for the production of chromatographic columns. On the contrary, two-photon polymerization has a resolution of 50 nm, but suffers of very high printing time, even for small volumes: the creation of a (1000 x 100 x 10) μm columns with 1.5 μm pores and 80% porosity requires about 24 hours [10], [69].

References

- [1] "Handbook of Affinity Chromatography," *Handbook of Affinity Chromatography*, Jul. 2005, doi: 10.1201/9780824751982.
- [2] P. C. Wankat, "A Review of: 'SEPARATION AND PURIFICATION TECHNIQUES IN BIOTECHNOLOGY' Frederick J. Dechow Noyes Publications, Park Ridge, NJ, August 31, 1989, hardbound, 490 pages, \$72.00.," <http://dx.doi.org/10.1080/03602549008050932>, vol. 19, no. 1, pp. 119–120, Jan. 2006, doi: 10.1080/03602549008050932.
- [3] S. di Martino, "Studio sperimentale e modellazione della separazione di proteine con membrane di affinità," Ph.D. thesis, University of Bologna, 2009.
- [4] P. R. Gavara, N. S. Bibi, M. L. Sanchez, M. Grasselli, and M. Fernandez-Lahore, "Chromatographic Characterization and Process Performance of Column-Packed Anion Exchange Fibrous Adsorbents for High Throughput and High Capacity Bioseparations," *Processes 2015, Vol. 3, Pages 204-221*, vol. 3, no. 1, pp. 204–221, Mar. 2015, doi: 10.3390/PR3010204.
- [5] Y. Grillet, P. L. Llewellyn, H. Reichert, J. P. Coulomb, N. Pellenq, and J. Rouquerol, "Confinement in micropores and enthalpies of physisorption," *Studies in Surface Science and Catalysis*, vol. 87, no. C, pp. 525–533, Jan. 1994, doi: 10.1016/S0167-2991(08)63114-8.
- [6] H. Schmidt-Traub, M. Schulte, and A. Seidel-Morgenstern, *Preparative Chromatography*, 3rd ed. 2020.
- [7] G. Rozing, "Micropillar array columns for advancing nanoflow HPLC," *Microchemical Journal*, vol. 170, p. 106629, Nov. 2021, doi: 10.1016/J.MICROC.2021.106629.
- [8] J. J. van Deemter, F. J. Zuiderweg, and A. Klinkenberg, "Longitudinal diffusion and resistance to mass transfer as causes of nonideality in chromatography," *Chemical Engineering Science*, vol. 50, no. 24, pp. 3869–3882, Dec. 1995, doi: 10.1016/0009-2509(96)81813-6.
- [9] J. op de Beeck, W. de Malsche, P. de Moor, and G. Desmet, "Hydrodynamic chromatography separations in micro- and nanopillar arrays produced using deep-UV lithography," *Journal of Separation Science*, vol. 35, no. 15, pp. 1877–1883, Aug. 2012, doi: 10.1002/JSSC.201200076.
- [10] C. Salmean and S. Dimartino, "3D-Printed Stationary Phases with Ordered Morphology: State of the Art and Future Development in Liquid Chromatography," *Chromatographia 2018 82:1*, vol. 82, no. 1, pp. 443–463, Dec. 2018, doi: 10.1007/S10337-018-3671-5.
- [11] J. H. Knox and M. Saleem, "Kinetic Conditions for Optimum Speed and Resolution in Column Chromatography," *Journal of Chromatographic Science*, vol. 7, no. 10, pp. 614–622, Oct. 1969, doi: 10.1093/CHROMSCI/7.10.614.
- [12] J. de Vos, K. Broeckhoven, and S. Eeltink, "Advances in Ultrahigh-Pressure Liquid Chromatography Technology and System Design," *Analytical Chemistry*, vol. 88, no. 1, pp. 262–278, Jan. 2016, doi: 10.1021/ACS.ANALCHEM.5B04381/ASSET/IMAGES/ACS.ANALCHEM.5B04381.SOCIAL.JPEG_V03.

- [13] D. T. T. Nguyen, D. Guillarme, S. Rudaz, and J. L. Veuthey, "Fast analysis in liquid chromatography using small particle size and high pressure," *Journal of Separation Science*, vol. 29, no. 12, pp. 1836–1848, Aug. 2006, doi: 10.1002/JSSC.200600189.
- [14] F. Svec and Y. Lv, "Advances and recent trends in the field of monolithic columns for chromatography," *Analytical Chemistry*, vol. 87, no. 1, pp. 250–273, Jan. 2015, doi: 10.1021/AC504059C/ASSET/IMAGES/AC504059C.SOCIAL.JPEG_V03.
- [15] G. Guiochon, A. Felinger, D. G. Shirazi, and A. M. Katti, "Fundamentals of Preparative Chromatography," p. 990, 2006.
- [16] O. Ludemann-Hombourger, R. M. Nicoud, and M. Bailly, "The 'VARICOL' process: A new multicolumn continuous chromatographic process," *Separation Science and Technology*, vol. 35, no. 12, pp. 1829–1862, 2000, doi: 10.1081/SS-100100622.
- [17] O. Ludemann-Hombourger, M. Bailly, and R. M. Nicoud, "Design of a Simulated Moving Bed: Optimal Particle Size of the Stationary Phase," <http://dx.doi.org/10.1081/SS-100100225>, vol. 35, no. 9, pp. 1285–1305, Jun. 2006, doi: 10.1081/SS-100100225.
- [18] F. G. Helfferich, "Principles of adsorption & adsorption processes, by D. M. Ruthven, John Wiley & Sons, 1984, xxiv + 433 pp," *AIChE Journal*, vol. 31, no. 3, pp. 523–524, Mar. 1985, doi: 10.1002/AIC.690310335.
- [19] C. Johnson, V. Natarajan, and C. Antoniou, "Evaluating two process scale chromatography column header designs using CFD," *Biotechnology Progress*, vol. 30, no. 4, pp. 837–844, Jul. 2014, doi: 10.1002/BTPR.1902.
- [20] J. H. Knox, "Band dispersion in chromatography – a new view of A-term dispersion," *Journal of Chromatography A*, vol. 831, no. 1, pp. 3–15, Jan. 1999, doi: 10.1016/S0021-9673(98)00497-X.
- [21] J. H. Knox, "Band dispersion in chromatography—a universal expression for the contribution from the mobile zone," *Journal of Chromatography A*, vol. 960, no. 1–2, pp. 7–18, Jun. 2002, doi: 10.1016/S0021-9673(02)00240-6.
- [22] "(PDF) New synthetic ways for the preparation of high-performance liquid chromatography supports | Michael Buchmeiser - Academia.edu." https://www.academia.edu/22724884/New_synthetic_ways_for_the_preparation_of_high_performance_liquid_chromatography_supports (accessed Apr. 26, 2022).
- [23] R. Arshady, "Beaded polymer supports and gels. II. Physico-chemical criteria and functionalization," *Journal of Chromatography A*, vol. 586, no. 2, pp. 199–219, Nov. 1991, doi: 10.1016/0021-9673(91)85125-Y.
- [24] D. S. Hage *et al.*, "PHARMACEUTICAL AND BIOMEDICAL APPLICATIONS OF AFFINITY CHROMATOGRAPHY: RECENT TRENDS AND DEVELOPMENTS," *J Pharm Biomed Anal*, vol. 69, p. 93, Oct. 2012, doi: 10.1016/J.JPBA.2012.01.004.
- [25] F. Gu *et al.*, "Silica-based strong anion exchange media for protein purification," *J Chromatogr A*, vol. 1376, pp. 53–63, Jan. 2015, doi: 10.1016/J.CHROMA.2014.11.082.
- [26] W. C. Li, "Protein separation using non-porous sorbents," *J Chromatogr B Biomed Sci Appl*, vol. 699, no. 1–2, pp. 29–45, Oct. 1997, doi: 10.1016/S0378-4347(97)00179-5.

CHAPTER I

- [27] J. Thömmes, "Fluidized bed adsorption as a primary recovery step in protein purification," *Adv Biochem Eng Biotechnol*, vol. 58, pp. 185–230, 1997, doi: 10.1007/BFB0103305.
- [28] W. C. Li, "Protein separation using non-porous sorbents," *J Chromatogr B Biomed Sci Appl*, vol. 699, no. 1–2, pp. 29–45, Oct. 1997, doi: 10.1016/S0378-4347(97)00179-5.
- [29] P. C. Wankat, "Large-scale adsorption and chromatography," 1986.
- [30] "(PDF) Affinity chromatography with triazine dyes immobilized onto activated non-porous monodisperse silicas | Milton Hearn - Academia.edu."
https://www.academia.edu/32291400/Affinity_chromatography_with_triazine_dyes_immobilized_onto_activated_non_porous_monodisperse_silicas (accessed Apr. 28, 2022).
- [31] P. E. Gustavsson, A. Axelsson, and P. O. Larsson, "Superporous agarose beads as a hydrophobic interaction chromatography support," *J Chromatogr A*, vol. 830, no. 2, pp. 275–284, Jan. 1999, doi: 10.1016/S0021-9673(98)00899-1.
- [32] P. E. Gustavsson, K. Mosbach, K. Nilsson, and P. O. Larsson, "Superporous agarose as an affinity chromatography support," *Journal of Chromatography A*, vol. 776, no. 2, pp. 197–203, Aug. 1997, doi: 10.1016/S0021-9673(97)00348-8.
- [33] B. J. Horstmann, C. N. Kenny, and H. A. Chase, "Adsorption of proteins on sepharose affinity adsorbents of varying particle size," *Journal of Chromatography A*, vol. 361, no. C, pp. 179–190, Jan. 1986, doi: 10.1016/S0021-9673(01)86905-3.
- [34] J. ZHAO, S. YAO, and D. LIN, "Adsorbents for Expanded Bed Adsorption: Preparation and Functionalization," *Chinese Journal of Chemical Engineering*, vol. 17, no. 4, pp. 678–687, Jan. 2009, doi: 10.1016/S1004-9541(08)60263-3.
- [35] C. Boi, "Membrane chromatography for biomolecule purification," in *Current trends and future developments on (bio-) membranes*, 2019, pp. 151–166.
- [36] "Handbook of Membrane Separations : Chemical, Pharmaceutical, Food, and Biotechnological Applications," *Handbook of Membrane Separations*, Jul. 2008, doi: 10.1201/9781420009484.
- [37] E. Lalli, J. S. Silva, C. Boi, and G. C. Sarti, "Affinity Membranes and Monoliths for Protein Purification," *Membranes 2020, Vol. 10, Page 1*, vol. 10, no. 1, p. 1, Dec. 2019, doi: 10.3390/MEMBRANES10010001.
- [38] E. Lalli, "Purification of antibodies through convective chromatography," University of Bologna, Bologna, 2018.
- [39] K. Broeckhoven and G. Desmet, "Advances and Innovations in Liquid Chromatography Stationary Phase Supports," *Analytical Chemistry*, vol. 93, no. 1, pp. 257–272, Jan. 2021, doi: 10.1021/ACS.ANALCHEM.0C04466/ASSET/IMAGES/ACS.ANALCHEM.0C04466.SOCIAL.JPEG_V03.
- [40] K. D. Patel, A. D. Jerkovich, J. C. Link, and J. W. Jorgenson, "In-depth characterization of slurry packed capillary columns with 1.0- μm nonporous particles using reversed-phase isocratic ultrahigh-pressure liquid chromatography," *Analytical Chemistry*, vol. 76, no. 19, pp. 5777–5786, Oct. 2004, doi: 10.1021/AC049756X.

- [41] L. A. Colón, J. M. Cintrón, J. A. Anspach, A. M. Fermier, and K. A. Swinney, "Very high pressure HPLC with 1 mm id columns," *Analyst*, vol. 129, no. 6, pp. 503–504, 2004, doi: 10.1039/B405242K.
- [42] H. K. Mayer, G. Fiechter, and E. Fischer, "A new ultra-pressure liquid chromatography method for the determination of biogenic amines in cheese," *Journal of Chromatography A*, vol. 1217, no. 19, pp. 3251–3257, May 2010, doi: 10.1016/J.CHROMA.2009.09.027.
- [43] R. Toporišič, A. Mlakar, J. Hvala, I. Prislán, and L. Zupančič-Kralj, "Identification of new impurities of enalapril maleate on oxidation in the presence of magnesium monoperoxyphthalate," *Journal of Pharmaceutical and Biomedical Analysis*, vol. 52, no. 2, pp. 294–299, Jun. 2010, doi: 10.1016/J.JPBA.2009.12.018.
- [44] J. S. Mellors and J. W. Jorgenson, "Use of 1.5- μm porous ethyl-bridged hybrid particles as a stationary-phase support for reversed-phase ultrahigh-pressure liquid chromatography," *Analytical Chemistry*, vol. 76, no. 18, pp. 5441–5450, Sep. 2004, doi: 10.1021/AC049643D.
- [45] Y. S. Li, B. Li, N. Y. Han, and B. J. Xu, "Studies on a poly(styrene-divinylbenzene)-encapsulated sub-micrometer sized organic–inorganic hybrid silica packing, its synthesis, some of its characteristics and applications," *Journal of Chromatography A*, vol. 1021, no. 1–2, pp. 183–189, Dec. 2003, doi: 10.1016/J.CHROMA.2003.09.011.
- [46] N. Wu, Y. Liu, and M. L. Lee, "Sub-2 μm porous and nonporous particles for fast separation in reversed-phase high performance liquid chromatography," *Journal of Chromatography A*, vol. 1131, no. 1–2, pp. 142–150, Oct. 2006, doi: 10.1016/J.CHROMA.2006.07.042.
- [47] R. M. Seifar, J. C. Kraak, W. T. Kok, and H. Poppe, "Capillary electrochromatography with 1.8- μm ODS-modified porous silica particles," *Journal of Chromatography A*, vol. 808, no. 1–2, pp. 71–77, May 1998, doi: 10.1016/S0021-9673(98)00142-3.
- [48] F. Gritti and G. Guiochon, "The rationale for the optimum efficiency of columns packed with new 1.9 μm fully porous Titan-C18 particles—a detailed investigation of the intra-particle diffusivity," *J Chromatogr A*, vol. 1355, pp. 164–178, Aug. 2014, doi: 10.1016/J.CHROMA.2014.05.076.
- [49] R. M. Wimalasinghe, C. A. Weatherly, M. F. Wahab, N. Thakur, and D. W. Armstrong, "Geopolymers as a New Class of High pH Stable Supports with Different Chromatographic Selectivity," *Analytical Chemistry*, vol. 90, no. 13, pp. 8139–8146, Jul. 2018, doi: 10.1021/ACS.ANALCHEM.8B01426/ASSET/IMAGES/LARGE/AC-2018-014267_0005.JPEG.
- [50] S. Fekete, E. Oláh, and J. Fekete, "Fast liquid chromatography: The domination of core–shell and very fine particles," *Journal of Chromatography A*, vol. 1228, pp. 57–71, Mar. 2012, doi: 10.1016/J.CHROMA.2011.09.050.
- [51] G. Guiochon and F. Gritti, "Shell particles, trials, tribulations and triumphs," *Journal of Chromatography A*, vol. 1218, no. 15, pp. 1915–1938, Apr. 2011, doi: 10.1016/J.CHROMA.2011.01.080.
- [52] W. Chen *et al.*, "Synthesis and optimization of wide pore superficially porous particles by a one-step coating process for separation of proteins and monoclonal antibodies," *J Chromatogr A*, vol. 1414, pp. 147–157, Oct. 2015, doi: 10.1016/J.CHROMA.2015.08.043.

- [53] W. Stöber, A. Fink, and E. Bohn, "Controlled growth of monodisperse silica spheres in the micron size range," *Journal of Colloid and Interface Science*, vol. 26, no. 1, pp. 62–69, Jan. 1968, doi: 10.1016/0021-9797(68)90272-5.
- [54] C. H. Hung *et al.*, "Improved efficiency of reversed-phase carbon/nanodiamond/polymer core-shell particles for HPLC using carbonized poly(divinylbenzene) microspheres as the core materials," *J Sep Sci*, vol. 36, no. 24, pp. 3821–3829, Dec. 2013, doi: 10.1002/JSSC.201300988.
- [55] T. S. Deng, H. J. Bongard, and F. Marlow, "A one-step method to coat polystyrene particles with an organo-silica shell and their functionalization," *Materials Chemistry and Physics*, vol. 162, pp. 548–554, Jul. 2015, doi: 10.1016/J.MATCHEMPHYS.2015.06.027.
- [56] J. L. Dores-Sousa, A. Fernández-Pumarega, J. de Vos, M. Lämmerhofer, G. Desmet, and S. Eeltink, "Guidelines for tuning the macropore structure of monolithic columns for high-performance liquid chromatography," *J Sep Sci*, vol. 42, no. 2, pp. 522–533, Jan. 2019, doi: 10.1002/JSSC.201801092.
- [57] J. L. Dores-Sousa, H. Terryn, and S. Eeltink, "Morphology optimization and assessment of the performance limits of high-porosity nanostructured polymer monolithic capillary columns for proteomics analysis," *Anal Chim Acta*, vol. 1124, pp. 176–183, Aug. 2020, doi: 10.1016/J.ACA.2020.05.019.
- [58] P. Simone *et al.*, "Capillary methacrylate-based monoliths by grafting from/to γ -ray polymerization on a tentacle-type reactive surface for the liquid chromatographic separations of small molecules and intact proteins," *Journal of Chromatography A*, vol. 1498, pp. 46–55, May 2017, doi: 10.1016/J.CHROMA.2016.11.039.
- [59] T. Hara, H. Kobayashi, T. Ikegami, K. Nakanishi, and N. Tanaka, "Performance of Monolithic Silica Capillary Columns with Increased Phase Ratios and Small-Sized Domains," *Analytical Chemistry*, vol. 78, no. 22, pp. 7632–7642, Nov. 2006, doi: 10.1021/AC060770E.
- [60] W. de Malsche, H. Eghbali, D. Clicq, J. Vangeloooven, H. Gardeniers, and G. Desmet, "Pressure-Driven Reverse-Phase Liquid Chromatography Separations in Ordered Nonporous Pillar Array Columns," *Analytical Chemistry*, vol. 79, no. 15, pp. 5915–5926, Aug. 2007, doi: 10.1021/AC070352P.
- [61] M. Baca, G. Desmet, H. Ottevaere, and W. de Malsche, "Achieving a Peak Capacity of 1800 Using an 8 m Long Pillar Array Column," *Analytical Chemistry*, vol. 91, no. 17, pp. 10932–10936, Sep. 2019, doi: 10.1021/ACS.ANALCHEM.9B02236/ASSET/IMAGES/MEDIUM/AC9B02236_M006.GIF.
- [62] Z. X. Low, Y. T. Chua, B. M. Ray, D. Mattia, I. S. Metcalfe, and D. A. Patterson, "Perspective on 3D printing of separation membranes and comparison to related unconventional fabrication techniques," *Journal of Membrane Science*, vol. 523, pp. 596–613, Feb. 2017, doi: 10.1016/J.MEMSCI.2016.10.006.
- [63] U. Simon and S. Dimartino, "Direct 3D printing of monolithic ion exchange adsorbers," *Journal of Chromatography A*, vol. 1587, pp. 119–128, Feb. 2019, doi: 10.1016/J.CHROMA.2018.12.017.

- [64] S. Nawada, S. Dimartino, and C. Fee, "Dispersion behavior of 3D-printed columns with homogeneous microstructures comprising differing element shapes," *Chemical Engineering Science*, vol. 164, pp. 90–98, Jun. 2017, doi: 10.1016/J.CES.2017.02.012.
- [65] M. R. Schure, R. S. Maier, D. M. Kroll, and H. T. Davis, "Simulation of ordered packed beds in chromatography," *Journal of Chromatography A*, vol. 1031, no. 1–2, pp. 79–86, Mar. 2004, doi: 10.1016/J.CHROMA.2003.12.030.
- [66] N. P. Macdonald, S. A. Currivan, L. Tedone, and B. Paull, "Direct Production of Microstructured Surfaces for Planar Chromatography Using 3D Printing," *Analytical Chemistry*, vol. 89, no. 4, pp. 2457–2463, Feb. 2017, doi: 10.1021/ACS.ANALCHEM.6B04546/SUPPL_FILE/AC6B04546_SI_001.PDF.
- [67] C. Cheng and M. Gupta, "Surface functionalization of 3D-printed plastics via initiated chemical vapor deposition," *Beilstein J. Nanotechnol*, vol. 8, pp. 1629–1636, 2017, doi: 10.3762/bjnano.8.162.
- [68] T. Wang, L. Cao, W. Yang, Q. Feng, W. Chen, and Y. Zhang, "Adaptive patch-based POCS approach for super resolution reconstruction of 4D-CT lung data," *Physics in Medicine & Biology*, vol. 60, no. 15, p. 5939, Jul. 2015, doi: 10.1088/0031-9155/60/15/5939.
- [69] S. Waheed *et al.*, "3D printed microfluidic devices: enablers and barriers," *Lab on a Chip*, vol. 16, no. 11, pp. 1993–2013, May 2016, doi: 10.1039/C6LC00284F.

CHAPTER 2

Column design and fluid dynamic characterization

Conventional chromatographic columns are packed with porous beads, whose diameter is typically in the range 1.7-2.5 mm for analytical separations and 10-20 μm for preparative columns [1]. In affinity preparative chromatography, the particle size increases up to 50-100 μm , since smaller beads would cause higher pressure drops and, in turn, poor ligand utilization and higher separation costs [2, 3]. The use of large porous beads, where diffusion becomes the predominant mass transport phenomena, and the lack of control during the universally employed slurry-packing method have a dramatic adverse effect on the process efficiency.

In the last two decades, 2D homogeneous beds with a perfectly ordered internal morphology have shown an impressive ability to increase the efficiency of a chromatographic column, but their extension to three-dimensional columns was impeded by manufacturing techniques limitations. The recent development of 3D printers with a good compromise between resolution and production speed offers the possibility to design and produce three dimensional columns with the desired geometry and the necessary ancillary components. However, some drawbacks need to be addressed, especially the limited variety of compatible materials and their adverse effects on the mobile phase.

In this chapter, an innovative three-dimensional column with an ordered pillar-array structure will be presented. The column was designed by means of a 3D CAD software, 3D printed by masked-stereolithography and characterized in terms of pressure drops and

HETP. In addition, a coating procedure able to prevent the release of undesired substances in the mobile phase and, at the same time, to offer an external surface that can be easily functionalized was developed.

2.1 Column design and manufacturing

The bed of the chromatographic column presented in this work is constituted by pillar-like shaped elements that, placed in specific positions inside a properly designed shell (the equivalent of the glass or stainless steel tubes used in conventional columns), create a series of well-defined flow paths, having a rectangular 0.1 x 10 mm cross-section. The aim is to minimize the mobile phase velocity and residence time differences inside the column, by creating flow paths of similar shape, length and dimensions. A graphical representation is shown in figure 2.1.

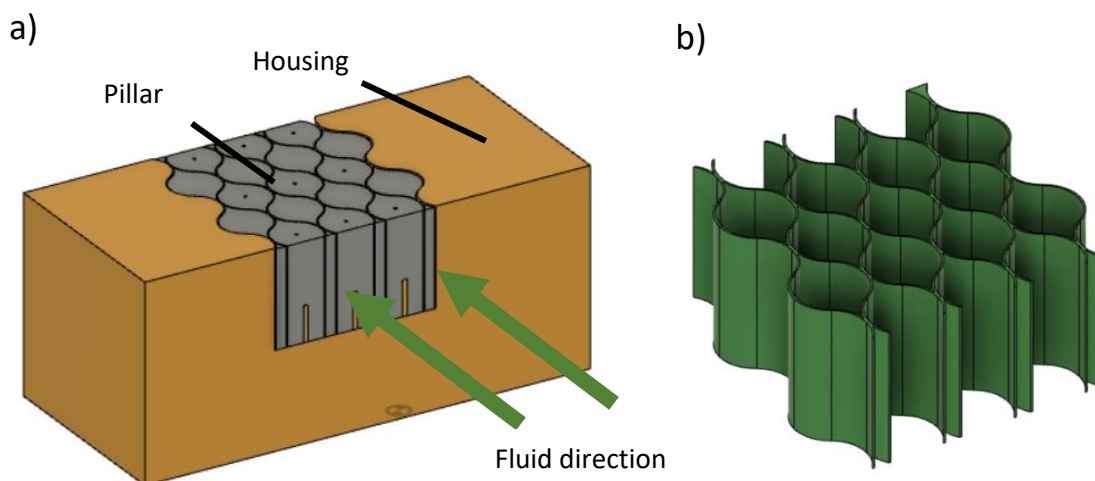


Figure.2.1: CAD representation of: a) pillars inside cell holder, b) fluid flow path created by the pillars

In addition to the pillars and to the shell, other key components are the fluid distributors and collectors, located at the inlet and at the outlet of the column, respectively. Two types of fluid distributors, presented in chapter 2.1.2, were compared: one incorporated in the shell, while the other is constituted by special pillars. Depending on the number of pillars that

make up the bed and on the type of distributors, several columns were designed by the 3D CAD software “Autodesk Fusion 360”, developed by Autodesk Inc. (California, USA), and printed by a masked-stereolithographic process. The different columns designed and manufactured are resumed in chapter 2.1.3.

Ideally, the best solution would have been to print each entire column in a single print job. However, this was not possible due to the insufficient resolution in the x-y plane of the 3D-printer used, which is not able to successfully create voids between two solid surfaces when the distance between them is smaller than 0.35 mm. Since the design distance between the pillars themselves, and the pillars and the walls, was significantly smaller (0.1 mm), the columns were broken down into two components that were individually printed and subsequently assembled by hand:

- the shell;
- the pillars.

This solution allowed to apply and test different types of coatings on the pillars surface, before their insertion inside the column, as reported in chapter 2.3.

2.1.1 Pillars

Pillars, shown in figure 2.2, represent the stationary phase of the column and have the aim to define a precise flow path for the mobile phase and to offer the surface for the adsorption. They have a ring-like base, with internal and external diameter of 2.9 mm and 5.0 mm respectively, and two tapered ends. The height of the pillar is 10.0 mm. The shape and the dimensions of the pillar were chosen to meet several constraints. Since the pillars should be individually manufactured and then placed inside the column, a push-in grafting system for

their precise positioning and orientation was designed, made by a properly shaped void inside the pillar that tightly fit to a seat printed inside the shell.

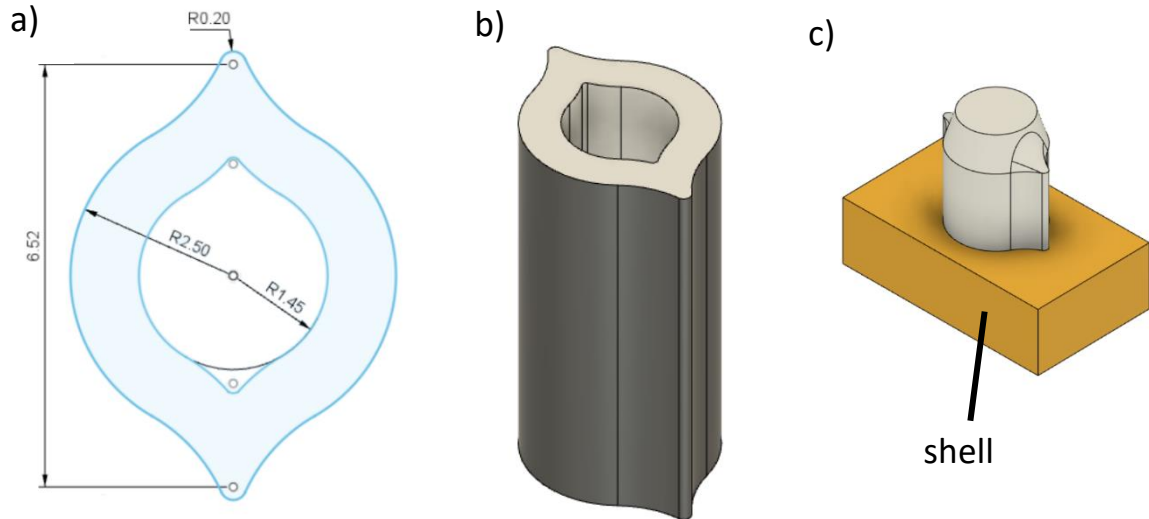


Figure 2.2: CAD representation of: a) pillar basis, b) entire pillar, c) graft for proper positioning of the pillar inside the holder. Only the black surfaces are in contact with the liquid, while the white surfaces are in contact with other solid components

The dimensions of the grafts and the width of the pillar walls, set equal to 1 mm to provide a sufficient mechanical resistance over a wide range of pressures, led to an external pillar diameter of 5 mm, from which two consequences arose:

- i. as shown in figure 2.3, the adoption of cylindrical pillars would have caused, in case of an interpillar distance equal to 0.1 mm, the formation of a large void area (1.45 mm^2), where mixing phenomena take place and mobile-phase mass transfer resistance becomes the most limiting parameter in terms of column efficiency. The adoption of cylindrical pillars with two tapered ends allowed to reduce of about 1/3 the voids area (0.56 mm^2);
- ii. the second issue is related to the surface available for adsorption: for a fixed height, larger pillars turn in lower number of pillars per unit area and, indeed, smaller

surface for the chromatographic process. The area in contact with the mobile-phase of one pillar, having the mentioned dimension, was of 178.52 mm².

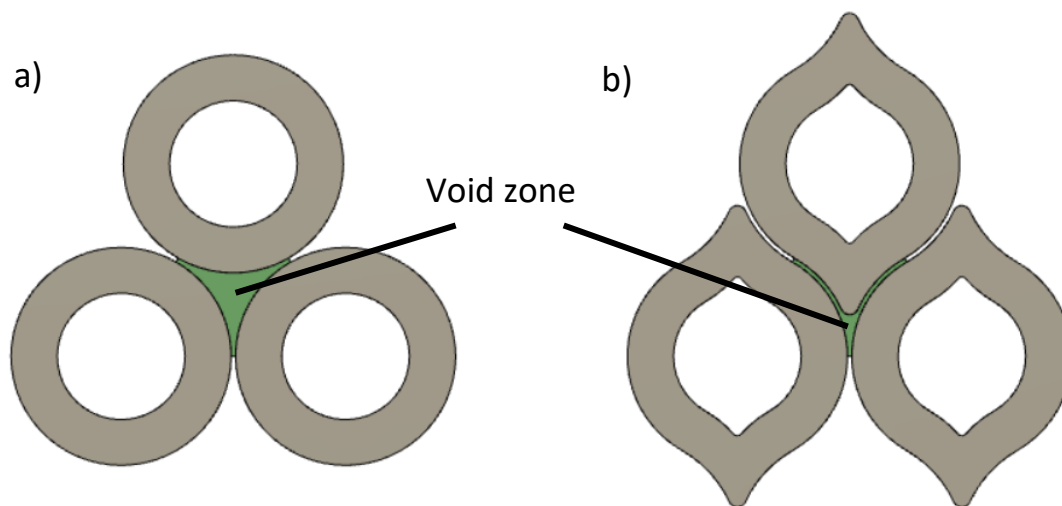


Figure 2.3: Presence of larger inter-pillar voids in case of a) cylindrical pillars, b) cylindrical pillars with tapered ends

The column was designed to obtain an interpillar spacing of 0.1 mm at any point. This value was chosen on the basis of two considerations:

- the expansion of the resin during the printing process would have reduced the gap;
- the application of coating layers would have caused a further reduction of the inter-pillar distance.

The arrangement of pillars inside the column allows to identify a repetitive unit, consisting of two rows, as shown in figure 2.4. Two types of columns can be distinguished on the basis of the repetitive unit, namely 3x3 and 3x4, where the numbers indicate the quantity of pillars in the first and in the second row, respectively.

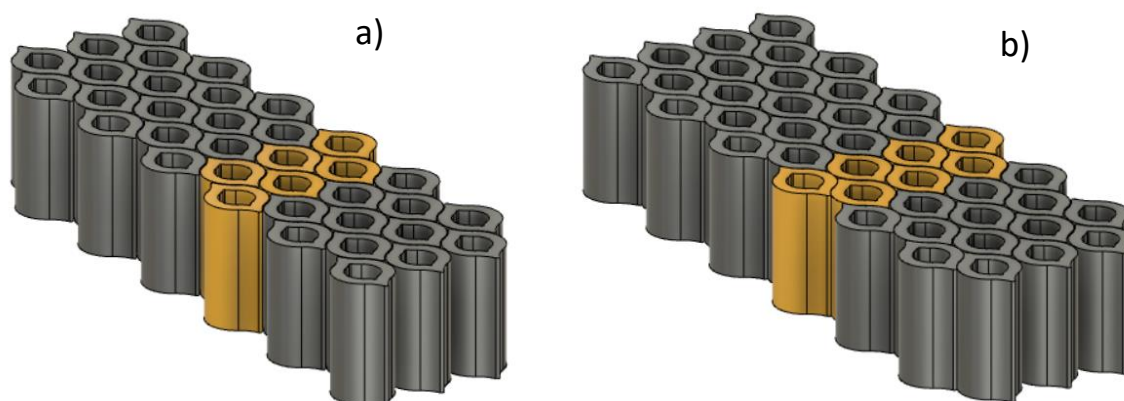


Figure 2.4: CAD representation of the repetitive unit in a) 3x3 column, b) 3x4 column.

2.1.2 Distributors

The mobile phase is fed to the column through a small tube, for instance in the Fast Protein Liquid Chromatography apparatus used in this work and presented in chapter 2.3, the internal tube diameter is 0.75 mm. For a good flow distribution, the liquid feed should spread evenly in the space between the pillars at the column inlet and finally collected at the outlet. In lab scale conventional cylindrical columns, this goal is achieved by using porous disks, called “frits”, which spread the fluid in the radial direction over the entire column cross-sectional area. In this work, two different distributors and collectors were designed, namely L and V. The V distributor and collector, shown in figure 2.5, were made by pillars with a specifically designed shape, size and arrangement. In L distributors (represented in figure 2.6), the fluid was distributed and then collected by 3 pipes with an internal diameter of 0.5 mm, following a Z-pathway inside the column that resulted to be very efficient in membrane modules [4].

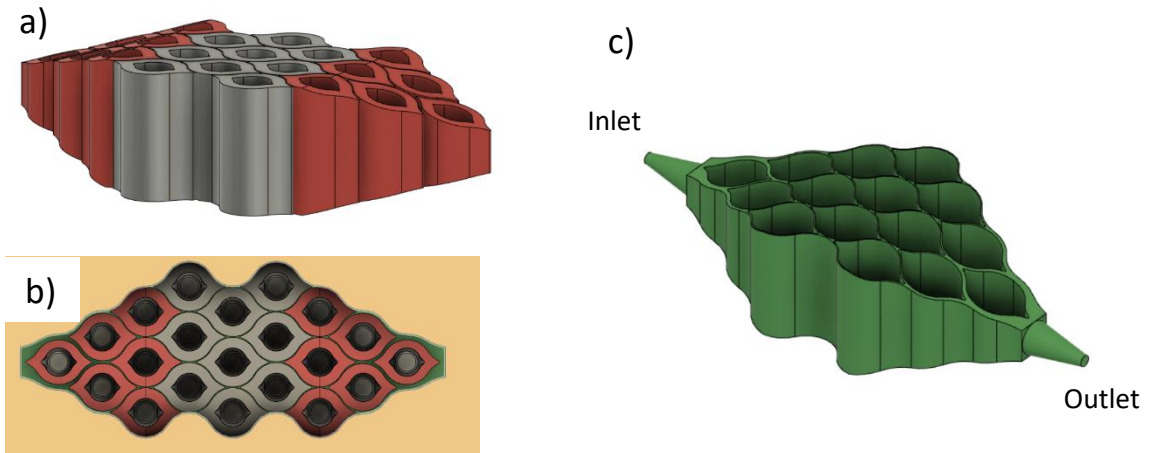


Figure 2.5: CAD representation of V distributor and collector in a 3x3 column: a) Lateral view of pillar only, b) Top view of pillar inside the housing, c) mobile phase profile.

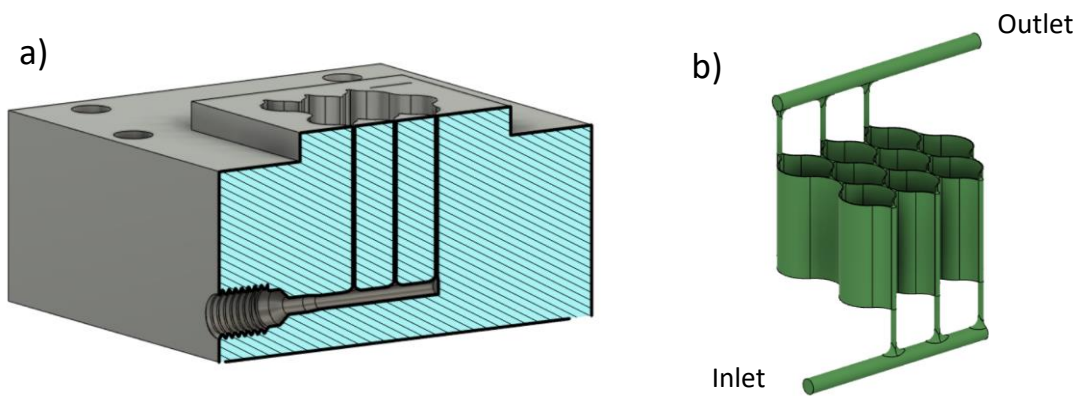


Figure 2.6: CAD representation of L distributor and collector in a 3x3 column: a) Lateral view of the distributor included in the housing, b) mobile phase profile.

2.1.3 Column shell

The shell of the column, represented in figure 2.7, is constituted by two parts: the housing and the cover. The housing consists of a rectangular base (in which are located the seats for the engagement of the pillars) and appropriately shaped walls with a height equal to that of the pillars. The housing includes also joints specific for the connections of tubes and, in the case of columns with the L distributors, the inlet distributor. The cover consists of a rectangular base in which are located the seats for the top-engagement of the pillars.

The housing, the pillars and the cover are printed separately and then assembled.

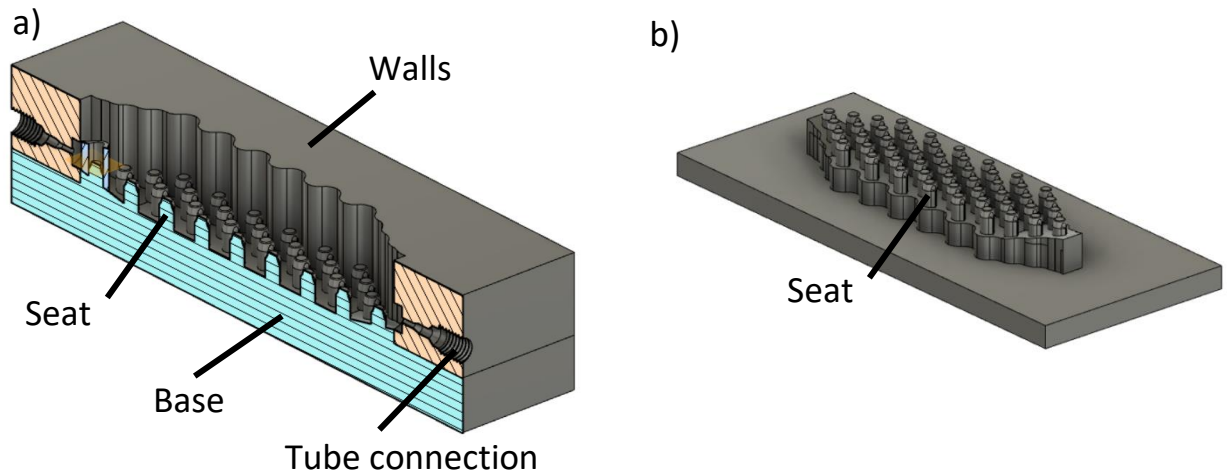


Figure 2.7: CAD representation of the components of the shell: a) Housing, b) Cover

2.1.4 Designed columns overview

Several columns were designed, printed and tested, to evaluate the effects of the repetitive pillar units, of the bed length (number of pillar rows) and of the distributors on column efficiency.

Each column was identified by an alphanumeric code, as described in figure 2.8, and it is reported in table 2.1 along with its properties.

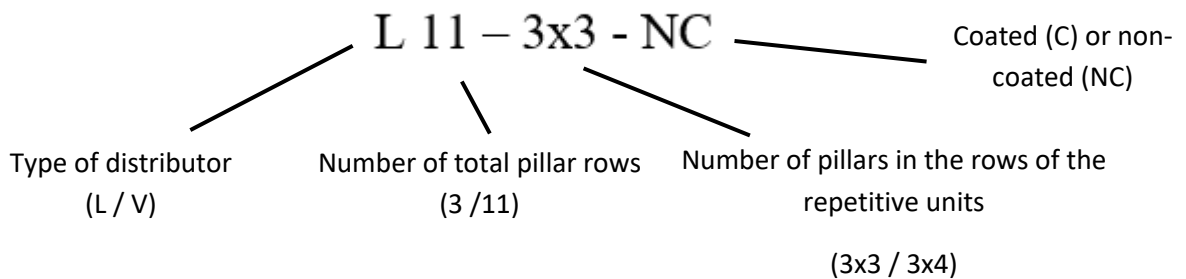


Figure 2.8: Example of alphanumeric code for a column with a 3x3 repetitive unit, 11 rows of pillars in total, L distributor

Table 2.1: Properties of the columns and test performed

Column	Column length [mm]	Adsorption area [mm ²]	Liquid volume [mm ³]	Type of test
V3-3x3-NC	52.87	1606.7	329.9	Pressure drop Pulse test
L3-3x3-NC	16.3	1606.7	233.7	Pressure drop Pulse test
V11-3x3-NC	88.1	5891.2	1073.3	Pressure drop Pulse test
V11-3x4-NC	88.1	6782.8	1212.4	Pressure drop Pulse test
L11-3x3-NC	59.77	5891.2	980.2	Pressure drop Pulse test
V11-3x4-C	88.1	6782.8	1212.4	Pressure drop Pulse test Chrom. cylce

2.2 3D-Printing: Original Prusa SL1

The columns were manufactured by the “Original Prusa SL-1”, a M-SLA (Masked Stereolithographic Apparatus) 3D printer by Prusa Research a.s. (Prague, Czech Republic).

M-SLA is a light-assisted printing process in which a photosensitive resin is cured (polymerized) by exposure to UV-light in a layer-by-layer process [5]. Figure 2.9 provides a schematic representation of this type of 3D printer. The built platform is submerged in the resin, contained in a tank having the base made of a transparent polymeric film. Immediately below the film, a Liquid Crystal Display (LCD) and a UV-lamp are placed, in sequence.

The LCD screen, by the activation of specific pixels, allows the passage of the light and the polymerization of a layer of resin on the built platform, according to the design. The width of the layer depends on the time of exposure to the UV-light (typically in the range 3-60 s). At the end of the exposure time, the built platform moves up for a distance equal to desired layer height and the process starts again [6].

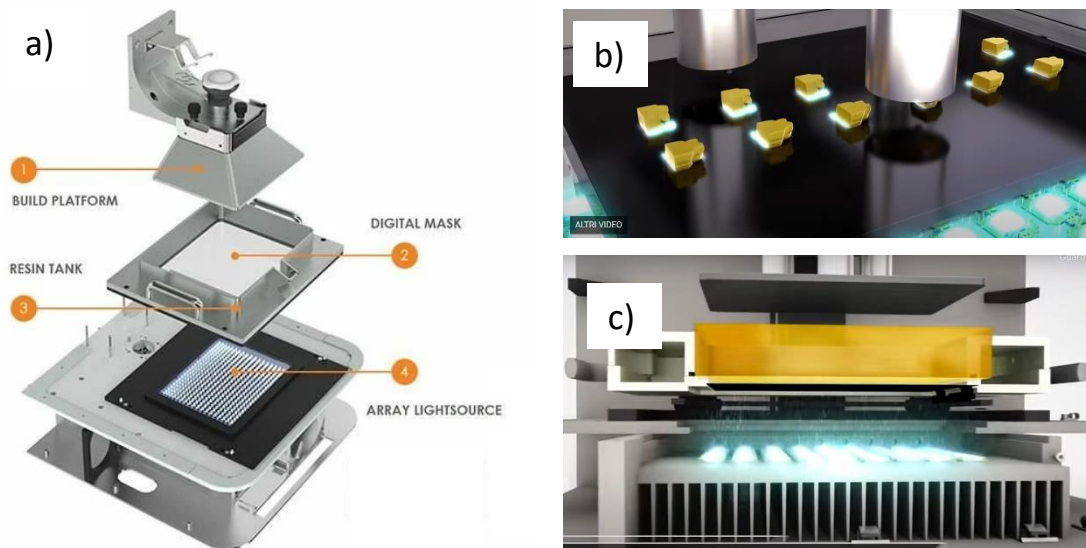


Figure 2.9: Representation of: a) main components of a M-SLA 3D printer, b) Light emission by the UV lamp, c) LCD activated pixels and printing process

The Original Prusa SL-1 is equipped with a 2560x1440 pixels, 5.5'' LCD screen, able to provide a resolution of 0.047 mm per pixel on the horizontal x-y plane and of 0.01 mm in the vertical z-axis [7].

All the columns were printed using the phenolic epoxy “Transparent tough” resin, purchased at Prusa Research a. s., whose composition is indicated in table 2.2 [8]. The two components of the shell of the columns were printed with an initial exposure time of 35 s, which steadily decreased over the first ten layers to an operative exposure time of 8 s, corresponding to a layer height of 0.1 mm. A higher initial exposure time is typically used to provide a stronger adhesion of the first layer to the built plate, a key parameter for the successfully manufacturing of large components. On the other hand, it causes the formation of layers that are larger than desired in the x-y plane, due to a reduced resolution and a higher expansion of the polymerized resin.

Table 2.2: Composition of the Transparent tough resin by Prusa Research a. s.

Chemical name	CAS number	Composition (wt%)
Epoxy resin	61788-97-4	40-50%
Monomer	13048-33-4	20-40%
Photoinitiators	947-19-3	3-5%

Since this phenomenon depends on the exposure time, which decreases over the first ten layers, the expansion of the layer reduces accordingly from layer 1 to layer 10, creating the so called “Elephant foot shape”, showed in figure 2.10. However, the Elephant foot effect affected only the first millimetre of the base of the two shell components and, therefore, the fluid dynamics of the column was not influenced.

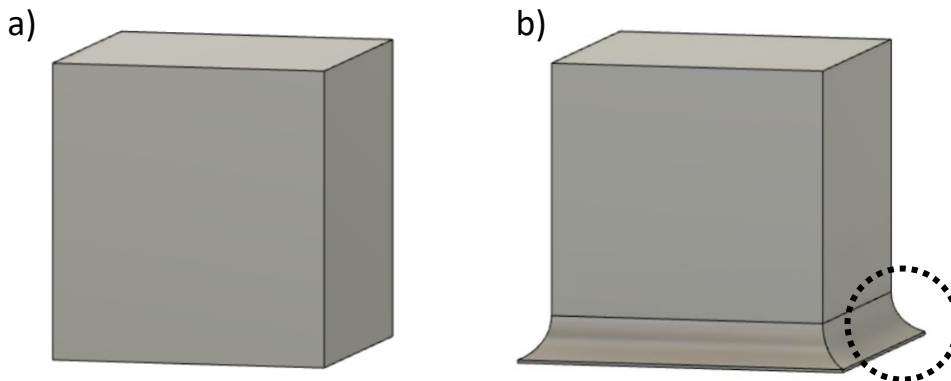


Figure 2.10: difference between: a) 3D CAD-model and b) 3D printed components with elephant foot shape

Instead, the pillars were printed with an operative exposure time of 6 s, corresponding to a layer height of 0.025 mm, in absence of a different initial exposure time. This setting allowed to successfully produce the pillars without the Elephant foot shape.

After the 3D printing step, all the components were soaked in a 2-propanol bath under magnetic stirring for 5 minutes, to remove the liquid resin residues, then dried with compressed air and cured under UV-light. These steps were performed using the Original

Prusa Washing and Curing Machine CW1S, manufactured by Prusa Research a. s., while the 2-propanol was purchased by Sigma-Aldrich (Milan, Italy). Figure 2.11 shows the surface of a pillar, after the washing and curing procedure, obtained by Scanning Electron Microscope (SEM) analysis, where the layers can be clearly distinguished.

The inter-pillar distance inside the real columns, after the printing and assembling processes, was measured by means of a feeler gauge (typically used to measure intervals of engine mechanical elements). In all the columns, an effective inter-pillar distance of 0.05 mm was observed, indicating that the positioning of the pillars was sufficiently precise and that the reduction compared to the CAD design (0.1 mm) was due to the expansion of the resin during the pillar printing process.

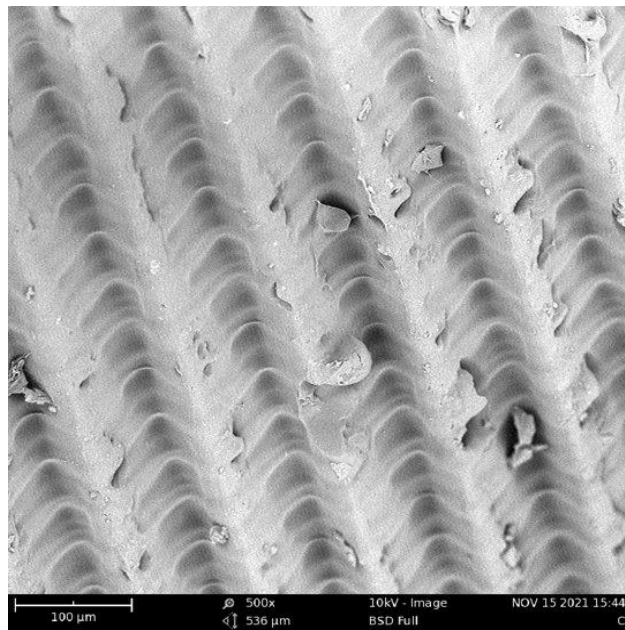


Figure 2.11: SEM analysis at 500x magnification of the pillar surface, after washing and curing

2.3 Pillar coating

SLA offers many advantages with respect to other 3D printing techniques, higher resolution and smooth surfaces above all. However, the main drawbacks are the limited number of

printable materials and the presence of additives within the resins, which lead to two important consequences in chromatography: difficulties in binding the desired ligand on the stationary phase and release in the liquid phase of unwanted material, as described in paragraph 1.3.5. To overcome these limitations, three different materials were used to coat the pillars:

- Nanofibrillated cellulose (NFC);
- Titanium dioxide (TiO₂);
- Polystyrene (PS);

NFC and TiO₂ particles, dissolved in specific solutions, were applied on the pillar surface by cold-spray coating, a process in which the solution is sprayed onto the desired surface by means of a pressure spray gun [9, 10]. A specific apparatus for making NFC and TiO₂ coatings was set-up and tuned by several experiments and is described in chapter 2.3.1.1. Instead, PS layers were created by phase inversion, a process widely used in membrane manufacturing in which the polymer solution is immersed in a non-solvent bath that promotes precipitation of the polymer [11].

Several pillars were coated by NFC, TiO₂, polystyrene or a combination of them, to evaluate the best type of coating. Table 2.3 summarizes all the coatings produced.

Table 2.3: List of produced coatings.

Coating type	Coating layers	Internal layer	Mid-layer	External layer
A	1	NFC	-	-
B	1	TiO ₂		
C	2	TiO ₂	NFC	
D	1	PS		
E	2	PS	NFC	
F	3	TiO ₂	PS	NFC

C, E, and F coating types consisted of the stratification of layers, produced one at time, as shown in figure 2.12 in case of F coating: the internal layer was applied on the pillar surface, then covered by the mid-layer that was finally coated by the external layer. NFC and TiO₂ layers for the coating presented in table 2.3 were produced at a rotation velocity of 1000 rpm (more details are provided in chapter 2.3.1.1).

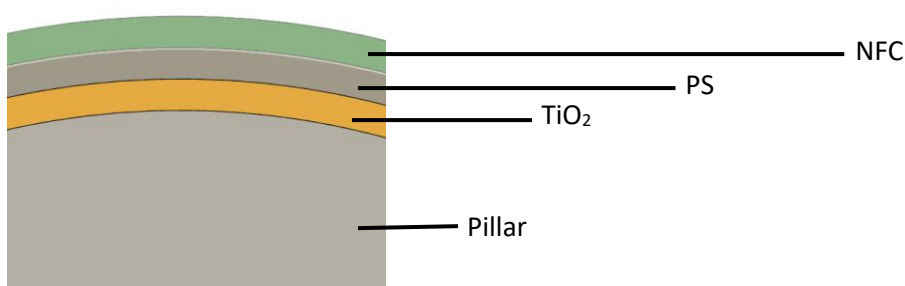


Figure 2.12: graphical representation of type F coating

Two pillars per each coating type were tested for adsorption and for fluid flow resistance. In particular, a static adsorption test was performed to evaluate the performance of the coating in terms of barrier between the solid resin surface and the mobile phase (to avoid the release of undesired material) and to measure its contribution to non-specific adsorption of dissolved proteins. Whereas a qualitative test in flow was made to evaluate the resistance and the adhesion of the coating layers during operative real condition.

In the static adsorption test, each pillar was soaked in 2 mL of 0.3 mg/mL bovine serum albumin, BSA, (Sigma-Aldrich) solution in 20mM PBS, under gentle agitation for 24 hours. The BSA concentration of each solution was measured before and after the test by UV readings at 280nm using a spectrophotometer Nanodrop One (Thermo Fisher Scientific, Milan, Italy). Control experiments were performed using a noncoated pillar, to differentiate the effect of the coatings, and on pure BSA solutions, to verify the stability of the protein over the entire time of investigation.

In the fluid flow resistance test, the pillars were placed in a shell properly designed to reproduce the same fluid dynamics condition of the prototype columns presented in chapter 2.1 and exposed to a demineralized water flow rate of 60 mL/min, for 1 hour. The coating condition after the test was evaluated by SEM analysis.

The best solution was found with the F-type coating that was used to coat all the pillars to produce a complete V11-3x4 column (V11-3x4-C).

2.3.1 Nanofibrillated cellulose and titanium dioxide spray coatings

Cellulose-based supports are largely used in chromatography, because of the cellulose hydrophilic nature that leads to a low non-specific protein binding [12]. In addition, as shown in figure 2.13, cellulose has three active sites (-OH groups in position 2, 3 and 5) that can be used for the functionalization and immobilization of affinity ligands.

NFC consists in agglomerates of microfibril units with diameters smaller than 100 nm and length in the order of micrometers, obtained by mechanical disintegration (fibrillation) of cellulose fibers, compared to which the accessibility of hydroxyl groups in a network is higher [13, 14]. A free sample of NFC was provided by Exilva (Sarpsborg, Norway) and homogeneously dispersed in pure acetone (Sigma-Aldrich) to reach a concentration of 0.25% wt/wt, to get a low viscosity of the solution.

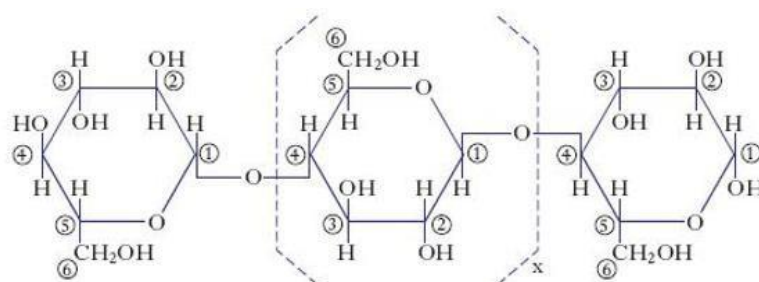


Figure 2.13: Cellulose structure

Titanium dioxide is another material used in affinity chromatography, mainly for the separation of phosphorylated biomolecules, since it has a good stability towards pH and temperature [15]. It is also the main component of primers, preparatory coatings used to increase the adhesion of paints to surfaces.

2.3.1.1 Experimental apparatus for spray coating

The pillars were stuck between two nuts in a threaded rod. The rod was inserted into the chuck of a mechanical stirrer, which allowed the pillars to rotate at the desired speed, up to 1000 rpm. The solution was sprayed for 1 second on the rotating pillars by a HVLP (High Volume, Low Pressure) airbrush, placed at a distance of 25 cm and set at a pressure of 2.5 bar, as suggested by the manufacturer, Shenzhen Deshunke Technology Co. (Guandong, China). The coating was then dried by compressed air emitted by the airbrush for 20 s. Figure 2.14 provides a representation of the coating process. To make the experiment replicable and to ensure the correct time of spraying, the airbrush was activated by a pressure-driven piston, in turn automatically operated by a solenoid valve and a Programmable Logic Computer (PLC).

To set-up the apparatus and to evaluate the effects of the rotation speed on the coating quality, several tests were performed with the NFC solution at pillar speeds, namely 250, 500 and 1000 rpm. For the TiO₂ solution, the tests were performed at 1000 rpm only. Ten pillars per each experiment were coated, to verify if the procedure was replicable. All the pillars were weighted before and after the coating process, to determine the mass of NFC or TiO₂ settled on the solid surface. A qualitative analysis of the surface was performed by a Scanning Electron Microscope (SEM) Phenom ProX (ThermoFisher scientific, Waltham, USA).

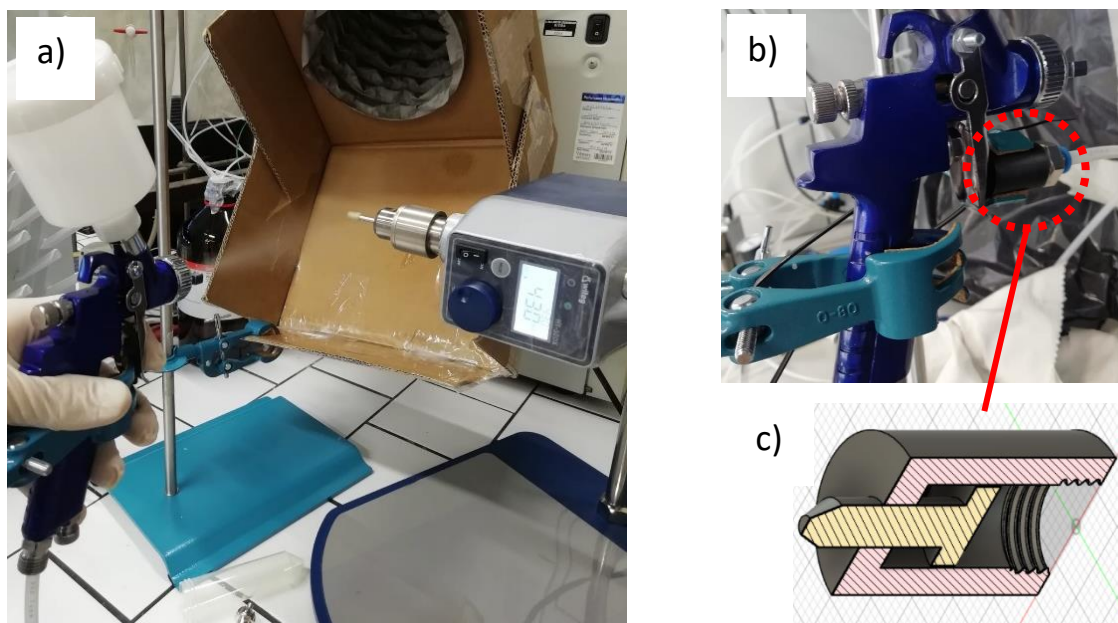


Figure 2.14: Coating experimental apparatus: a) spraying of solution on rotating pillar, b) activation of the airbrush by a pressure-driven piston, c) CAD representation of the piston

2.3.2 Polystyrene coating by phase inversion

PS is a waterproof material, resistant to many acids and bases and chemically inert. PS coating was created by phase inversion. Recycled PS hemispheric pellets, provided by AirPol Italia (Marcianise, CE, Italy) with a 99% purity, were dissolved in N-methyl-2-pyrrolidone (NMP), with a polystyrene to NMP ratio of 1:4 in mass, as suggested by Gao et al. [16]. The pillars were rapidly soaked in the PS-NMP solution and then left in a demineralized water bath for 1 hour, to promote the precipitation of the polymer and to obtain a dense layer.

2.4 Fluid dynamic characterization

All the columns presented in chapter 2.1 were characterized in pressure drop tests, aimed to find a relationship between flow rate and backpressure caused by the column, and in pulse tests, to determine the efficiency in terms of height equivalent to a theoretical plate (HETP).

All fluid dynamic characterization tests were performed with the Fast Protein Liquid Chromatography (FPLC) instrument AKTA Purifier100, by GE Healthcare (Milan, Italy).

2.4.1 Fast Protein Liquid Chromatography apparatus

The apparatus is schematically represented in figure 2.15. Two piston pumps, A and B, withdraw the desired solution from 4 different lines (namely A1, A2, B1 and B2), two per each pump. The solution is pumped to the sample injection valve, which can assume three different positions: *Load*, *Inject* and *Waste*. When the valve is in the *Load* position, the fluid, entering from port 7, exits from port 1 and is directly fed to the column. In this situation, it is possible to prepare an injection sample, by connecting a tube of a known and desired volume (loop) to port 2 and 6 and injecting the sample by a syringe through the port 3: the tube fills and the excess is wasted through port 4. By switching the valve in the *Inject* position, the solution entering the valve is connected to the loop and pushes the injection sample to the column. In the *Waste* position the column is by-passed and the solution is directly wasted. This option is typically used only for cleaning operations of the instrument.

Downstream the column, three detectors for the measure of the UV-absorbance, pH and conductivity of the mobile phase exiting the column are placed in order. These values are continuously recorded and elaborated by the software Unicorn, which in addition allows to set the desired flow rate at any time and to record the real-time backpressure caused by all the components of the instrument, column included.

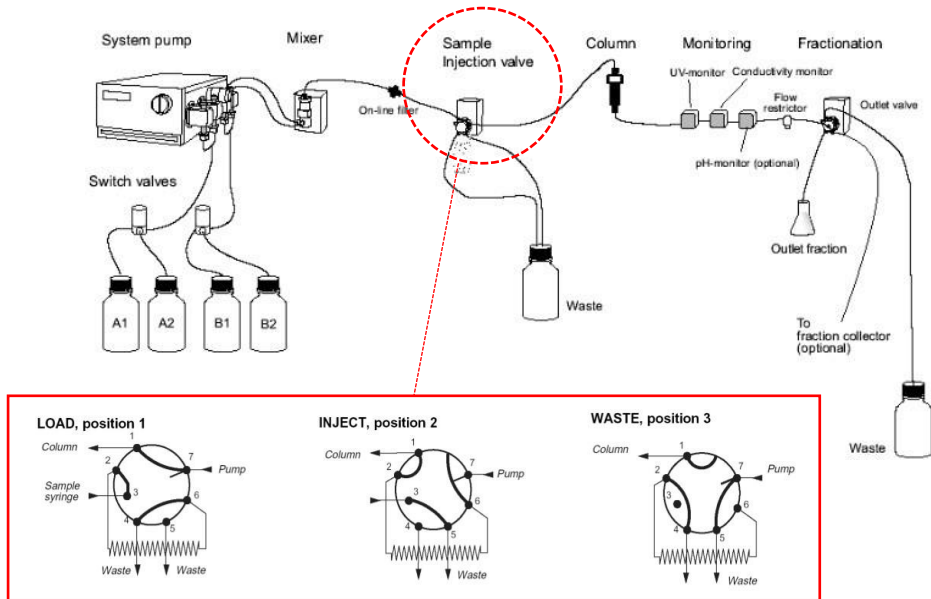


Figure 2.15: schematic representation of the FPLC AKTA Purifier100

2.4.2 Pressure drop test

Knowledge of pressure drop at a given flow rate is a key factor in the evaluation of a chromatographic column, because of its strong influence on several process parameters, such as operating time, maximum flow rate tolerated by the stationary phase, ligand utilization and productivity [10, 13].

For a given fluid that flows through an incompressible porous material, the pressure drop grows linearly with flow rate, as stated by Darcy's law, reported in equation 2.1 [17]:

$$\Delta p = \frac{A Q}{\mu L k} \quad (2.1)$$

Where:

- Δp is the pressure drop, in Pa ;
- L is the length of the porous material, in m ;
- A is the cross-sectional area, in m^2 ;

- k is the permeability, in m^2
- μ is the dynamic viscosity, in $Pa \cdot s$;
- Q is the flow rate, in m^3/s .

Pressure drop tests were executed with demineralized water at 25 °C ($\mu = 1 \cdot 10^{-3} Pa \cdot s$) in the flow rate range 0-60 mL/min, with a step- increment of 2.5 mL/min. To take into account that a portion of the measured pressure drops were caused by all the other volumes of the apparatus external to the columns, the test was repeated for the FPLC system alone and its contribution was subtracted.

2.4.3 Pulse test

Pulse tests consist in the injection of a known volume with a known concentration of an inert tracer and in the analysis of its concentration at the outlet of the column. The absence of interactions between the mobile and the stationary phase allows to evaluate the distribution of the liquid inside the column due to convective and diffusive mass transport phenomena and to evaluate their effects in terms of column efficiency.

A pulse test is performed after column equilibration in which the buffer solution is fed to the column for a time sufficient to create uniform conditions and to remove air bubbles or any trace of other substances. During column equilibration, the injection valve is set to the *load* position and the loop can be filled with the injection sample. After the equilibration, the injection valve switches to the *inject* position, the sample is pushed through the column and its concentration is recorded by the downstream detectors.

In the pulse test performed, bovine serum albumin (BSA) was used as inert tracer with an initial concentration of 4 mg/mL in a 20 mM phosphate buffer containing 250 mM sodium

chloride and 5% v/v ethanol, to reduce any possible interactions between the tracer and the pillar surface. The concentration of the tracer at the column outlet was recorded every 0.05 s by the UV-detector, at a wavelength of 280 nm. Other tracers typically used for pulse tests, such as NaCl and NaOH, were not considered due to the lower resolution of the specific detector that records the measured value every 0.5 s. Each column was tested at different flow rates, ranging from 5 to 60 mL/min with step increments of 2.5 mL/min, and applying an injection volume of 196 mL. All tests were performed in triplicates, to reduce the error due to a single measurement. The same experiments were performed for the instruments only (without the column), to exclude the influence of the external volumes.

2.4.3.1 Determination of the HETP

Figure 2.16 shows two examples of the shape of a tracer distribution (peak) recorded during a typical pulse test. Ideally, a symmetric peak following a Gaussian distribution should be observed. However, it is common to see peaks with an unusual profile, such as tailing asymmetric peaks that can be caused by secondary interactions between the tracer and the stationary phase or by the use of an injection volume too large (column overloading) [18]. In addition, the characterization of a peak is a powerful instrument for the determination of the efficiency of a column.

For a chromatographic peak expressed as concentration profile, $c(t)$, versus time, t , (or eluted volume, V), several moments can be calculated by using standard moment definitions [19]:

zero order moment, which corresponds to the area under the peak, as in equation 2.2;

$$M_0 = \int_a^b c(t) dt \quad (2.2)$$

n-th order moment, equation 2.3;

$$M_n = \int_a^b c(t) t^n dt \quad (2.3)$$

n-th absolute moment, equation 2.4;

$$\mu_n = \frac{M_n}{M_0} = \frac{\int_a^b c(t) dt}{\int_a^b c(t) dt} \quad (2.4)$$

n-th absolute central moment, by equation 2.5.

$$\bar{\mu}_n = \frac{\int_a^b c(t) (t - \mu_1)^n dt}{\int_a^b c(t) dt} \quad (2.5)$$

Where a and b are the peak start and end points. Several peak parameters can be determined by the knowledge of the moments of the distribution:

- the average retention time of the solute, t_R , which is equal to the first order moment;
- the peak variance, σ^2 , which is equal to the second order moment;
- the peak skew can be calculated by equation 2.6

$$P_s = \frac{M_3}{M_2^{3/2}} \quad (2.6)$$

The first absolute moment and the second absolute central moment are related to the number of theoretical plates of a chromatographic column, according to equation 2.7:

$$N = \frac{\mu_1^2}{\bar{\mu}_2} = \frac{t_R^2}{\sigma^2} \quad (2.7)$$

From N, it is possible to determine the HETP with equation 2.8:

$$HETP = \frac{L_c}{N} \quad (2.8)$$

Where L_c is the column length.

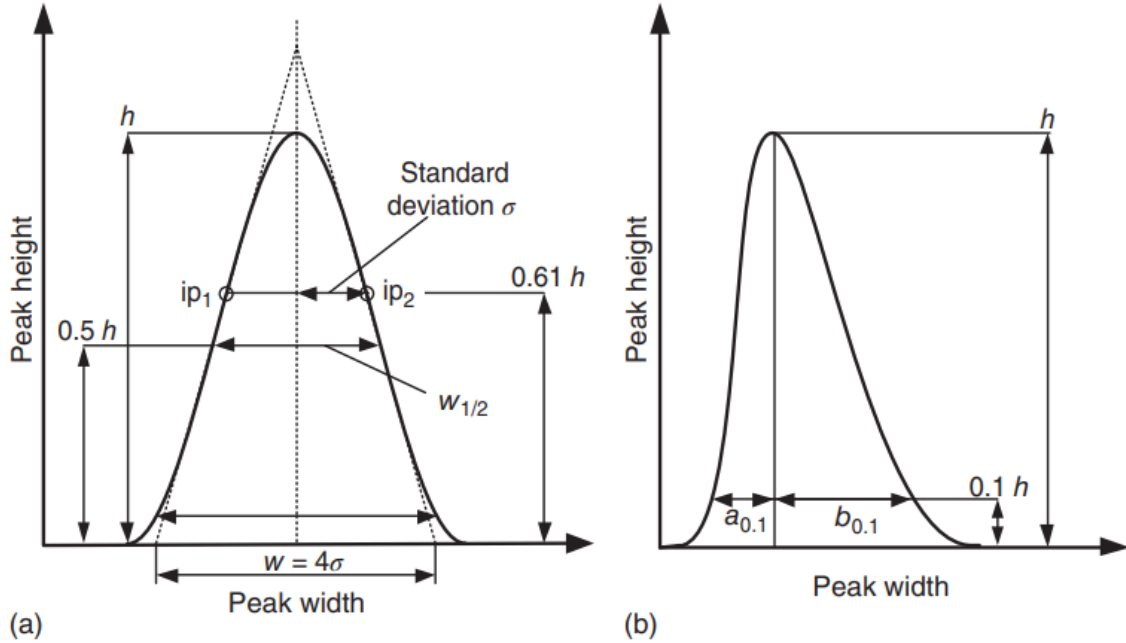


Figure 2.16: example of tracer distribution at the column outlet: a) symmetric gaussian peak, b) asymmetric tailing peak

In case of a highly efficient column, a peak with a shape very close to a symmetric Gaussian distribution can be observed. In this case the retention time corresponds to the peak maximum and the variance can be easily evaluated by the peak width [20]. The simplest and most used technique consist in the calculation of the peak width at half height, $w_{1/2}$ (corresponding to $2.354 \sigma^2$) and in the estimation of the number of plates by equation 2.9:

$$N \approx 5.54 \left(\frac{t_R}{w_{1/2}} \right)^2 \quad (2.9)$$

As an alternative, the variance can be calculated at the inflection points (ip_1 and ip_2 in figure 15) and the estimated value of N is given by equation 2.10:

$$N \approx 16 \left(\frac{t_R}{w} \right)^2 \quad (2.10)$$

However, equations 2.9 and 2.10 are highly inaccurate when dealing with non-symmetric peaks and usually overestimate the efficiency [21]. Indeed, usually the estimation of the HETP is performed by integrating the moments equations.

The moments are highly influenced by the numerical integration method used for their calculation. Misra *et al.* showed that the integration of the moments equations by the Simpson's rule leads to one order reduction of the error compared to trapezoidal rule and two order reduction compared to rectangular integration method [22]. Therefore, the Simpson's rule was used to integrate the equations for the evaluation of the HETP.

2.5 Results

Six chromatographic columns were designed and manufactured by M-SLA 3D printing. All the columns were designed to have cylindrical-shaped pillars with an external diameter of 5 mm. In the CAD design, the pillars were positioned in a way to create a series of vertical channels in the core of the column, having a height of 10 mm (equal to that of the pillars) and a width of 0.1 mm, to offer a constant free cross-sectional area for the mobile phase equal to 7 mm². The width of the channels was measured after printing and assembling processes by a feeler gauge and a constant average value of 0.05 mm was observed for all the columns, indicating that the reduction was ascribable to a uniform expansion of the resin during the printing process and not to an imprecise positioning of the pillar inside the column. The channel shrinking can be seen as a positive effect, since it reduces the contribution of the stationary-phase mass transfer resistance. In addition, it affected the external porosity of the column, that decreased from 0.07 in the CAD design to 0.04 for the real columns. This porosity refers to the core of the column, where the repetitive units are placed. For columns L3-3x3-NC and L11-3x3-NC, the L distributors are placed in the shell

and do not affect the porosity, that remains constant over the entire column volume. For non-coated columns, the V distributors are placed inside the column and their influence on the total porosity cannot be excluded. The porosity of all the columns is reported in table 2.4.

Table 2.4: Design and Real external porosity of the columns

Column	CAD external porosity	Real external porosity
	$\epsilon_{e,CAD}$	$\epsilon_{e,Real}$
L3-3x3-NC	0.072	0.041
L11-3X3-NC	0.072	0.041
V3-3x3-NC	0.083	0.056
V11-3X3-NC	0.081	0.054
V11-3x4-NC	0.081	0.054
V11-3X4-C	0.085	0.057

2.5.1 Fluid dynamic characterization

The type of distributor influenced also the pressure drop of the columns, that were plotted against the superficial velocity in figure 2.17, where slightly higher pressure drops were observed for the non-coated columns with the L-type distributors, compared to those with the V-type.

Instead, the coated V11-3x4-C column is affected by the highest pressure drop, likely due to a lack of control of the coating thickness or due to a further swelling of the NFC coating layer, both effects cause a reduction of the flow paths. However, all the columns were characterized by very low pressure drops, even at high superficial velocity, especially if

compared to conventional packed-bed columns for which, in case of bed height of 1 meter, the pressure at a typical superficial velocity of 800 cm/h may exceed 100 bar [18].

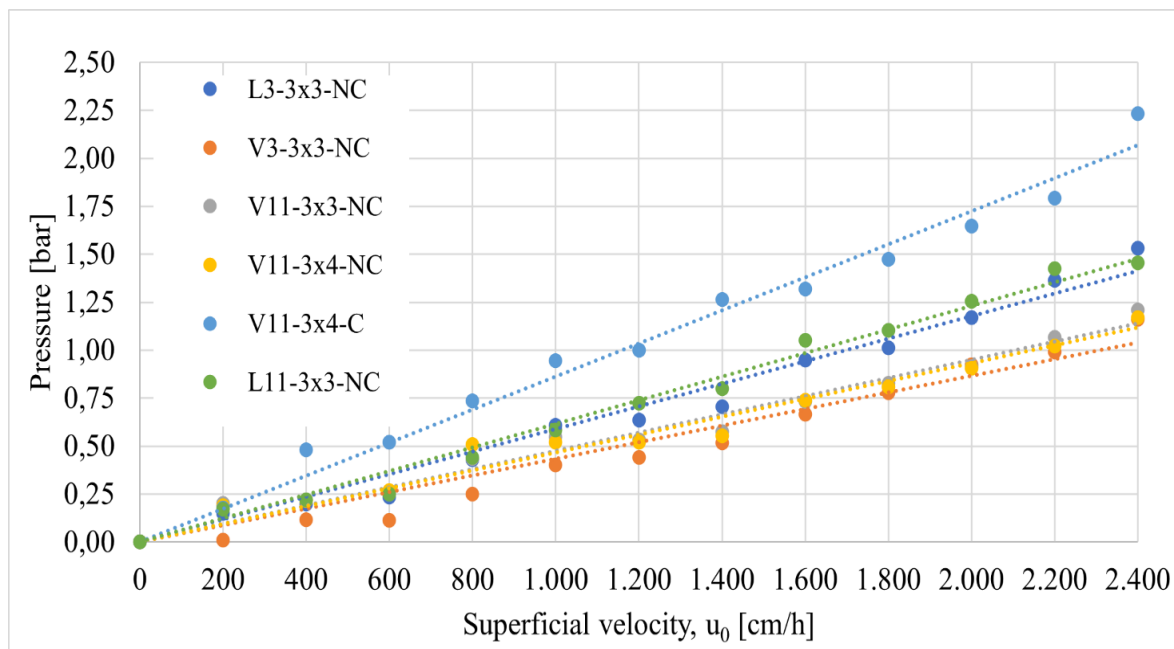


Figure 2.17: pressure drop of the columns as a function of the superficial velocity

Notably, short columns, whose bed was made by only 3 pillar rows (L3-3x3-NC and V3-3x3-NC), exhibited pressure drops almost identical to the corresponding long columns (L11-3x3-NC and V11-3x3-NC) made with 11 pillar rows. This phenomenon suggests that the pressure drops are mainly caused by the elements in the shell, such as the very small channels and joints designed to connect the FPLC instruments (indicated in figure 2.7), and not by the pillars surface. Consequently, the bed of the column can be largely extended to increase the surface available for the adsorption process without the drawback of too high pressure drops.

In addition, during these tests, backpressures up to 20 bars were recorded by the instruments due to the effects of pipes, connections and detectors downstream the column. In one case, the pressure rose up to 67 bars, when the formation of cracks in the holder was first observed. These results confirmed the mechanical resistance of the prototypes to moderate pressure, compatible with some preparative chromatography applications.

Figure 2.18 shows the HETP variation with flow rate for non-coated columns, calculated by the integration of the moments with the Simpson's method. As expected, for all the columns, the HETP initially decreases with the flow rate down to a certain value and then it remains constant. This behaviour is due to the absence of small diffusive pores, that lead to a value of the C-constant in the Van Deemter equation equal to zero.

Significant information can be derived about the efficiency of both, the distributors and the bed of the columns. About the distributors, the two columns with the L distributors provided the best results: the lowest HETP values observed were 0.085 mm for the L3-3x3-NC and 0.178 mm for the L11-3x3-NC, corresponding to 11.8 and 5.6 plates per mm of column, respectively. These results suggests that, in case of columns with the L distributors, the efficiency halves by a 3 time increase of the bed length. For the three non-coated columns with the V distributors, the lowest HETP values observed were 0.0419 mm for the V3-3x3-NC, 0.157 mm for the V11-3x3-NC and 0.162 mm for the V11-3x4-NC, corresponding to 2.4, 0.64 and 0.62 plates per mm of column, respectively. Therefore, in case of columns with the V distributors, the different bed configurations, 3x3 and 3x4, do not provide any advantage in terms of performance, which decreases 4 times when the bed length triplicates. However, better results could be obtained by increasing the flowrate.

Figure 2.19 shows the variation of HETP with the flow rate for the coated columns. In this case the C-term of the Van Deemter equation cannot be neglected, due to the presence of the NFC layers inside which the molecules move by diffusion. The significantly lower efficiency of the coated column, compared to the non-coated ones, is probably caused by the synergy of several elements:

- the contribution of the mobile-phase mass transfer resistance, due to the presence of large (10 mm) cellulose layers around the pillars;

- the difficulties in creating precise and replicable stratification of coatings on the pillars;
- the presence of the V distributors.

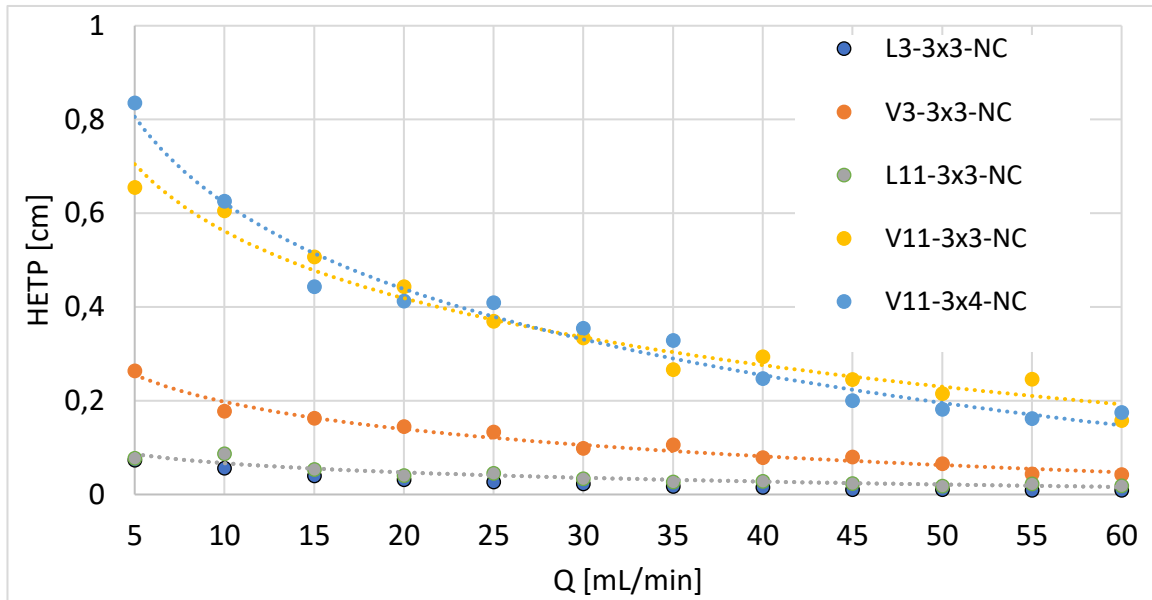


Figure 2.18: HETP vs Q for the non coated columns

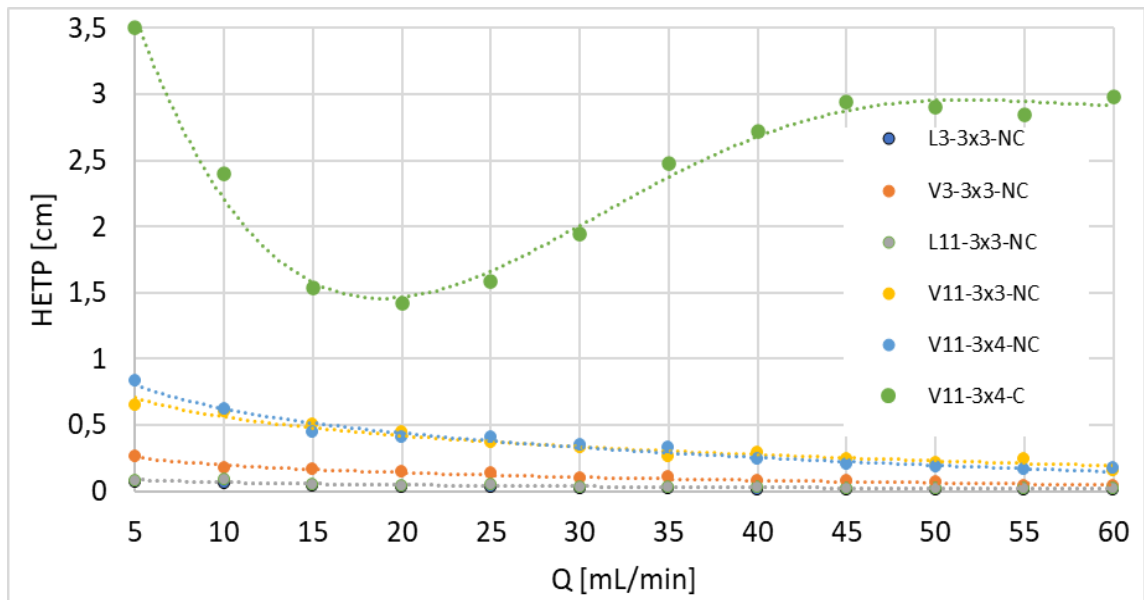


Figure 2.19: HETP vs Q for all the columns

2.5.2 Coatings

3 types of coatings were examined, alone or in combination, with the aim of screening the pillars to avoid the release of undesired substances in the mobile phase and of providing a surface for ligand immobilization:

- NFC layer by cold spray coating;
- TiO₂ particles layer by cold spray coating;
- Polystyrene layer by phase inversion.

Several experiments were performed to set-up and tune the experimental apparatus for the spray coating.

2.5.2.1 Spay coating apparatus set-up

For the NFC coating, different rotation velocities of the pillar were tested and qualitatively evaluated by a SEM analysis. An example of the results is reported in figure 2.20.

At the lowest rotation speed, 250 rpm, the pillar performed only four complete revolutions over the spray time (1 second). In addition, the velocity was not sufficient to force the alignment of the fibers. The result was a poor distribution of the cellulose and the formation of macro-aggregates and macro-voids. At 500 rpm, a more uniform distribution of the material and the reduction of macro-voids were observed, but still macro-aggregates were present. The best result was obtained at 1000 rpm, the highest velocity of the mechanical stirrer, thanks to the high number of revolutions accomplished by the pillars over the spray time (16) and the shear forces applied by the rotating surface on the impacting fibers.

CHAPTER 2

All the pillars coated with the NFC were weighted before and after the coating process but, due to the low density of the cellulose fibers and the small amount of material settled on the pillar surface, it was not possible to determine the mass of NFC layers.

Two pillars coated at 1000 rpm were tested under operative conditions to verify the resistance and the behaviour of the NFC layer. The results of the SEM analysis performed on these pillars is shown in figure 2.21.

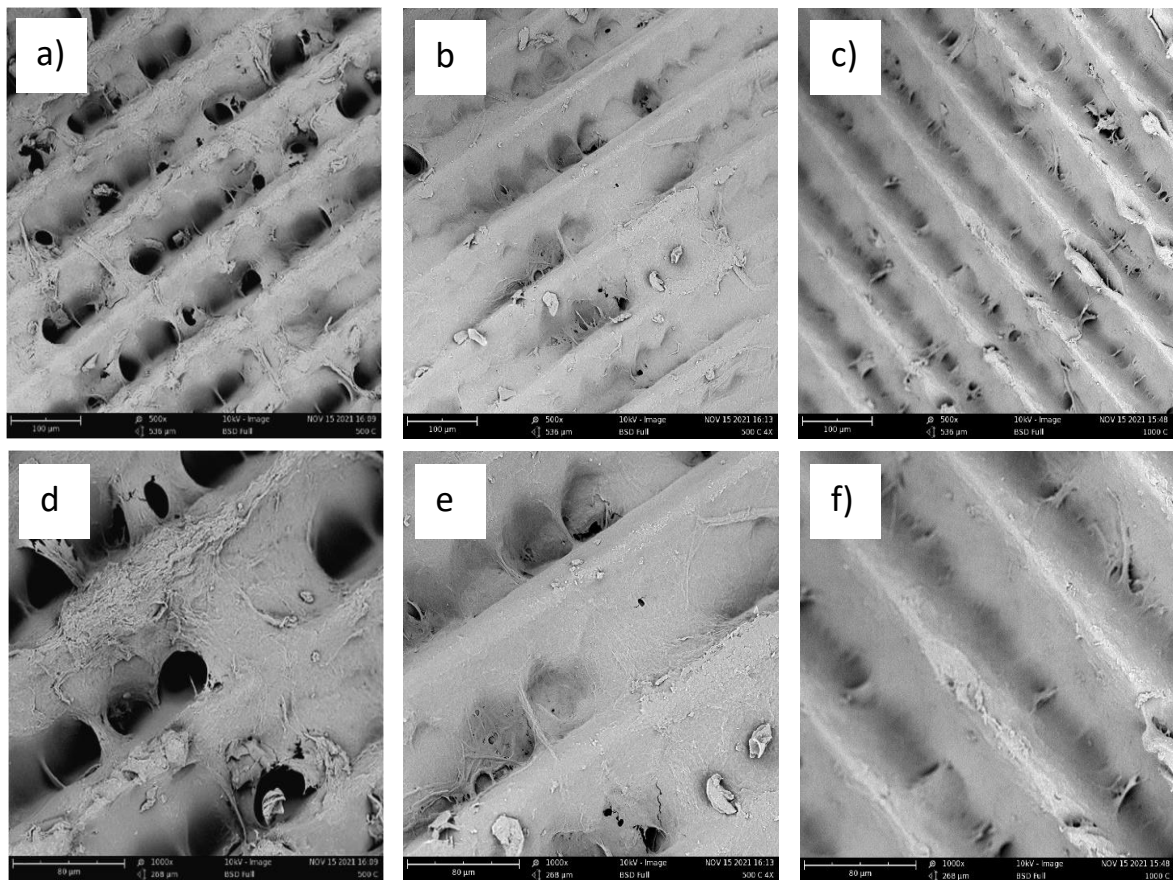


Figure 2.20: NFC spray coated pillars at different rotation speed and magnifications: a) $v=250$ rpm, magn.=500x, b) $v=500$ rpm, magn.=500x, c) $v=1000$ rpm, magn.=500x, d) $v=250$ rpm, magn.=1000x, e) $v=500$ rpm, magn.=1000x, f) $v=1000$ rpm, magn.=1000x

The NFC coating showed a good resistance to the shear forces applied by the mobile phase flowing at high velocity. However, again it was not possible to measure the mass of material present before and after the test to determine if a portion was lost during the process. As

expected, a certain swelling degree of the cellulose coating was observed and the peaks of the resin surface appeared less pronounced.

On the basis of the results obtained for the NFC, the TiO_2 spray coating was tested only at a 1000 rpm speed. The results of the SEM analysis are reported in figure 2.22, where a uniform distribution of a matrix containing TiO_2 particles can be observed. The aim of the TiO_2 was only to increase the adhesion to the pillar surface of other materials (NFC or polystyrene) that, settled on it, shield the TiO_2 particles from the shear forces applied by the mobile phase. Therefore, the test to verify the resistance to the operative conditions was not performed.

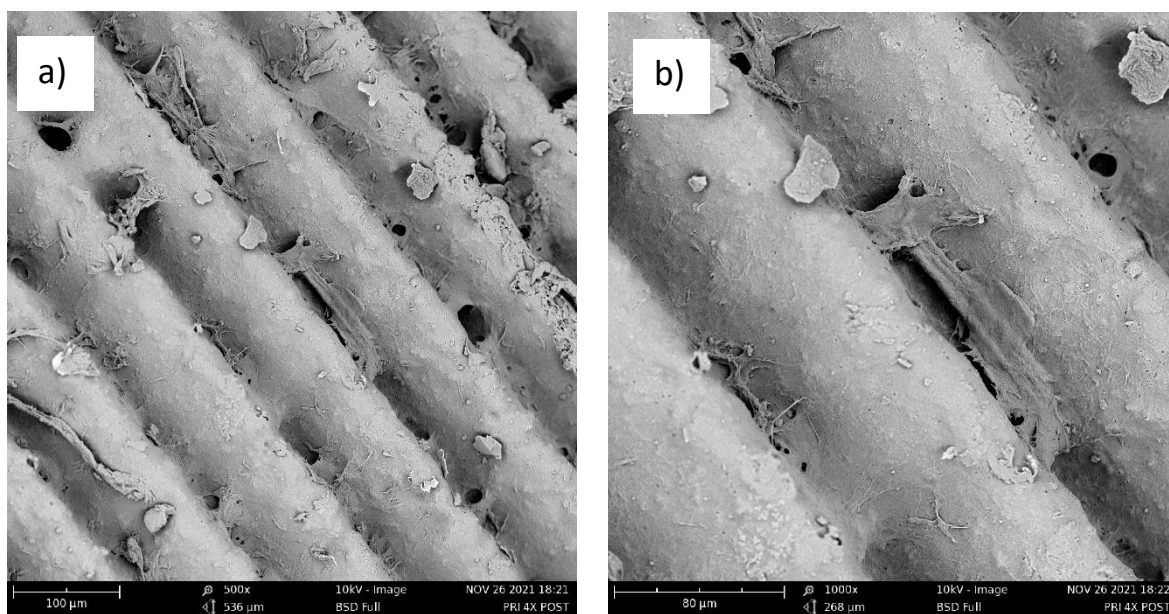


Figure 2.21: NFC coating after the test at operative conditions: a) magn.=500x, b) magn.=1000x

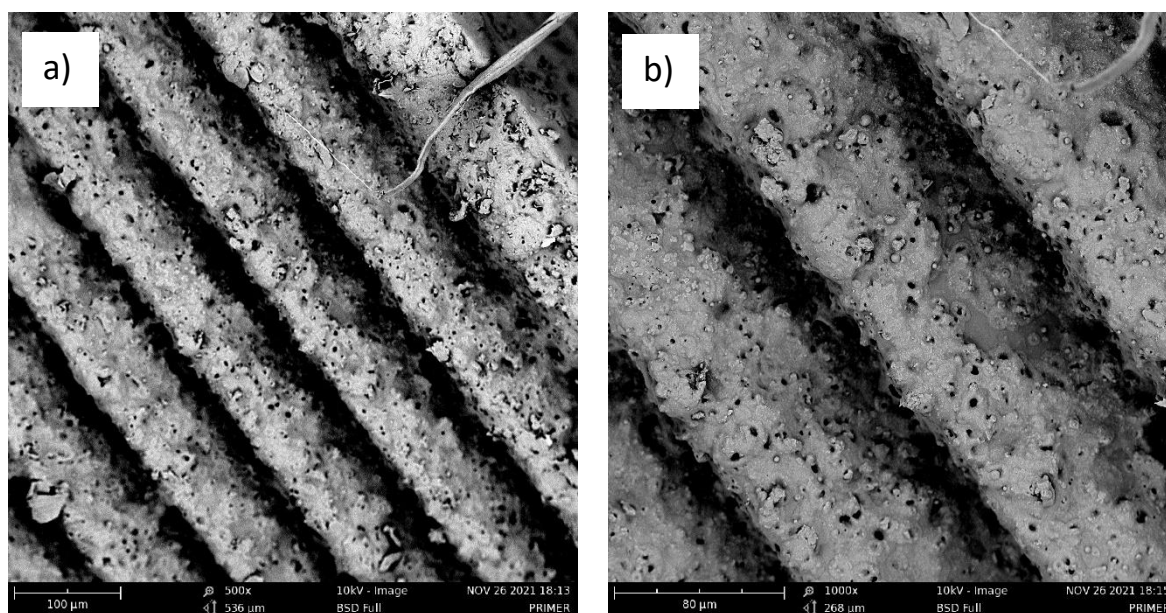


Figure 2.22: TiO_2 layer applied by spray coating at a) magn.=500x, b) magn.=1000x

2.5.2.2 Definition of the best type of coating

In this work the pillars coating has two goals: avoid the release of material by the resin in the mobile phase and provide a surface that can be functionalized. Six types of coating, presented in chapter 2.3, were created and subjected to two tests:

- static adsorption test;
- resistance to fluid flow.

Two samples per each coating type and test were analysed.

Table 2.5 shows the results of the static adsorption test, where the final concentration for each coating is the average value of the two samples tested. As expected, the concentration measured by UV readings at 280nm for the non-coated pillar is significantly higher than the initial BSA concentration, indicating the release of unknown and undesired components in solution. Both NFC and TiO_2 coatings, alone or combined (Coating A, B and C), were not able to successfully screen the BSA solution from the pillars surface, since a lower, but non

negligible increase of the absorbance at 280 nm was observed. Polystyrene (Coating C) was the only material able to create an impermeable, dense coating, preventing the release of any substance from the solid resin. Unfortunately, the polystyrene layer showed a very low adhesion to the pillars and detached almost immediately during the resistance to fluid flow test. The application of a NFC coating on the PS layer (Coating E) solved partially the problem by creating a self-standing network. However, the detachment of the PS layer in some points was always observed. The best solution was offered by Coating F. The solution used to create the TiO₂ layer was originally designed by the manufacturer to work as primer, a preparatory coating that increases the adhesion between the surface and the final paint. As shown in figure 2.22, it creates a matrix into which a large amount of TiO₂ particles are nested and that offers a surface with a high grip for the polystyrene layer. In addition, the external NFC coating provides a further support.

Table 2.5: Results of the static adsorption test, showing the mass of BSA in the different solutions

	Pure BSA	Non-coated Pillar	Coating A	Coating B	Coating C	Coating D	Coating E	Coating F
			NFC	TiO ₂	TiO ₂ +NFC	PS	PS+NFC	TiO ₂ +PS+NFC
C_i [mg/mL]	0.361	0.361	0.361	0.361	0.361	0.361	0.361	0.361
C_f [mg/mL]	0.365	1.358	1.126	0.894	0.677	0.346	0.371	0.323
m_f - m_i [mg]	0.008	1.994	1.530	0.533	1.066	-0.030	0.020	-0.076

Type F coating was used to coat all the pillars of the V11-3x4-C column. This column was specifically designed taking into account the additional thickness of the pillar diameter caused by the coating. The thickness of the layers were measured by several SEM analysis, from which it was concluded that the sum of the thickness of the first two layers (TiO₂ and PS) is typically in the range $64 \pm 5 \mu\text{m}$, while the NFC layer is in the range $12 \pm 3 \mu\text{m}$. Figure

2.23 shows the SEM analysis of an experiment in which a pillar was coated by 1 layer of TiO_2 , 1 layer of polystyrene and 7 layers of NFC, in sequence. The TiO_2 layer cannot be observed, since it is completely covered by the polystyrene or its thickness is lower than the peak that characterizes the surface of the pillars. On the contrary, the large polystyrene layers and the 7 NFC layers can be clearly distinguished. In addition, figure 2.23 shows that a small but non negligible variation of the NFC layer thickness is present, indicating the need to optimize the coating procedures, spray coating above all.

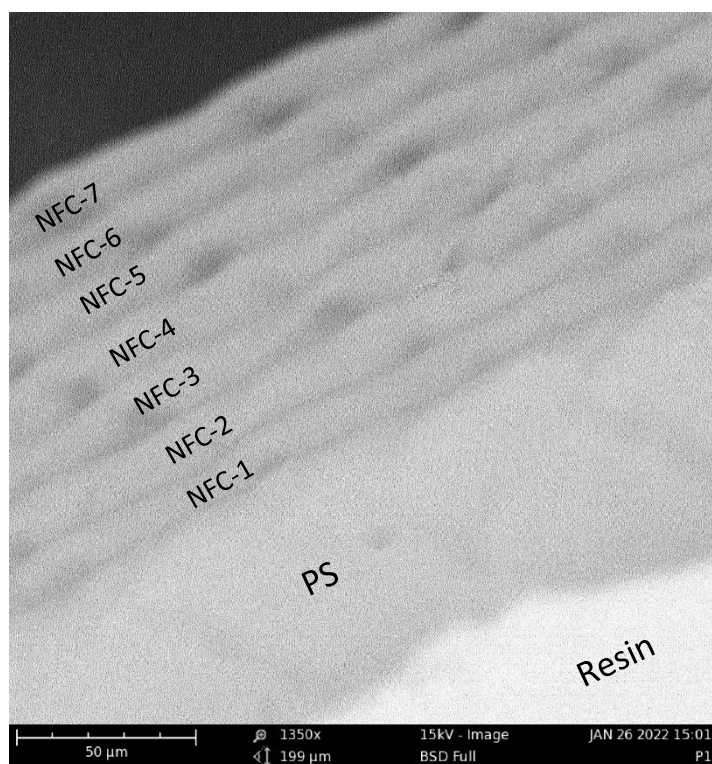


Figure 2.23: pillar coated by 1 layer of TiO_2 , 1 layer of polystyrene and 7 layers of NFC

References

- [1] H. Schmidt-Traub, M. Schulte, and A. Seidel-Morgenstern, *Preparative Chromatography*, 3rd ed. 2020.
- [2] C. Boi, “Membrane adsorbers as purification tools for monoclonal antibody purification,” *J Chromatogr B Analyt Technol Biomed Life Sci*, vol. 848, no. 1, pp. 19–27, Mar. 2007, doi: 10.1016/J.JCHROMB.2006.08.044.
- [3] “Studio Sperimentale e Modellazione della Separazione di Proteine con Membrane di Affinità.” <http://amsdottorato.unibo.it/1815/> (accessed Apr. 24, 2022).
- [4] G. Chen, J. Pagano, D. Yu, S. Ghose, Z. Li, and R. Ghosh, “Fast and high-resolution purification of a PEGylated protein using a z2 laterally-fed membrane chromatography device,” *Journal of Chromatography A*, vol. 1652, p. 462375, Aug. 2021, doi: 10.1016/J.CHROMA.2021.462375.
- [5] D. Mondal *et al.*, “mSLA-based 3D printing of acrylated epoxidized soybean oil - nano-hydroxyapatite composites for bone repair,” *Materials Science and Engineering: C*, vol. 130, p. 112456, Nov. 2021, doi: 10.1016/J.MSEC.2021.112456.
- [6] “3D Printing Basics: What Is MSLA 3D Printing? - Technipages.” <https://www.technipages.com/3d-printing-basics-what-is-msla-3d-printing> (accessed Apr. 22, 2022).
- [7] “Original Prusa 3D printers directly from Josef Prusa.” <https://www.prusa3d.com/> (accessed Apr. 22, 2022).
- [8] “Resin | Original Prusa 3D printers directly from Josef Prusa.” <https://www.prusa3d.com/category/resin/> (accessed Apr. 23, 2022).
- [9] T. A. Sherazi, “Spray Coating,” *Encyclopedia of Membranes*, pp. 1–2, 2014, doi: 10.1007/978-3-642-40872-4_552-1.
- [10] S. Mirmehdi, M. Luiza Cafalchio de Oliveira, P. Ricardo Gherardi Hein, M. Vilela Dias, C. Isabel Grígoli de Luca Sarantópoulos, and G. Henrique Denzin Tonoli, “Spraying Cellulose Nanofibrils for Improvement of Tensile and Barrier Properties of Writing & Printing (W&P) Paper, Journal of Wood Chemistry and Technology,” *Journal of Wood Chemistry and Technology*, vol. 0, pp. 1–13, 2018, doi: 10.1080/02773813.2018.1432656.

- [11] A. Basile, S. Mozia, and R. Molinari, *Current Trends and Future Developments on (Bio-) Membranes: Photocatalytic Membranes and Photocatalytic Membrane Reactors*. Elsevier Inc., 2018.
- [12] K. K. Unger, C. D. F. von Hohenesche, and M. Schulte, “Columns, Packings and Stationary Phases,” *Preparative Chromatography: of Fine Chemicals and Pharmaceutical Agents*, pp. 51–105, Apr. 2005, doi: 10.1002/3527603484.CH3.
- [13] K. Missoum, M. N. Belgacem, and J. Bras, “Nanofibrillated Cellulose Surface Modification: A Review,” *Materials*, vol. 6, no. 5, p. 1745, 2013, doi: 10.3390/MA6051745.
- [14] “What is Exilva | Exilva, a product by Borregaard.” <https://www.exilva.com/about/what-is-exilva> (accessed Apr. 24, 2022).
- [15] K. Engholm-Keller and M. R. Larsen, “Titanium dioxide as chemo-affinity chromatographic sorbent of biomolecular compounds — Applications in acidic modification-specific proteomics,” *Journal of Proteomics*, vol. 75, no. 2, pp. 317–328, Dec. 2011, doi: 10.1016/J.JPROT.2011.07.024.
- [16] “Factors controlling surface morphology of porous polystyrene membranes prepared by thermally induced phase separation - Gao - 2000 - Polymer International - Wiley Online Library.” [https://onlinelibrary.wiley.com/doi/10.1002/\(SICI\)1097-0126\(200004\)49:4%3C323::AID-PI369%3E3.0.CO;2-7](https://onlinelibrary.wiley.com/doi/10.1002/(SICI)1097-0126(200004)49:4%3C323::AID-PI369%3E3.0.CO;2-7) (accessed Apr. 24, 2022).
- [17] “Les fontaines publiques de la ville de Dijon: exposition et application ... - Henry Darcy - Google Books.” https://books.google.it/books?id=DOWbgyt_MzQC&printsec=frontcover&hl=de&source=gbs_ge_summary_r&cad=0#v=onepage&q&f=false (accessed Apr. 24, 2022).
- [18] D. A. Barrett, V. A. Brown, P. N. Shaw, M. C. Davies, H. Ritchie, and P. Ross, “Characterization of a Range of Alkyl-Bonded Silica HPLC Stationary Phases: Chromatographic Behavior of Neutral, Acidic, and Basic Test Solutes,” *Journal of Chromatographic Science*, vol. 34, 1996, Accessed: Apr. 25, 2022. [Online]. Available: <https://academic.oup.com/chromsci/article/34/3/146/291371>
- [19] W. W. Yau, “Characterizing Skewed Chromatographic Band Broadening,” *Analytical Chemistry*, vol. 49, no. 3, pp. 395–398, Mar. 1977, doi: 10.1021/AC50011A017/ASSET/AC50011A017.FP.PNG_V03.

- [20] E. Stauffer, J. A. Dolan, and R. Newman, “Gas Chromatography and Gas Chromatography—Mass Spectrometry,” *Fire Debris Analysis*, pp. 235–293, Jan. 2008, doi: 10.1016/B978-012663971-1.50012-9.
- [21] M. F. Wahab, D. C. Patel, and D. W. Armstrong, “Total peak shape analysis: detection and quantitation of concurrent fronting, tailing, and their effect on asymmetry measurements,” *J Chromatogr A*, vol. 1509, pp. 163–170, Aug. 2017, doi: 10.1016/J.CHROMA.2017.06.031.
- [22] S. Misra, M. F. Wahab, D. C. Patel, and D. W. Armstrong, “The utility of statistical moments in chromatography using trapezoidal and Simpson’s rules of peak integration,” *Journal of Separation Science*, vol. 42, no. 8, pp. 1644–1657, Apr. 2019, doi: 10.1002/JSSC.201801131.

CHAPTER 2

CHAPTER 3

Functionalization and affinity adsorption

The aim of any affinity chromatography column is to separate the largest amount of a target molecule from a complex liquid mixture as economically as possible, with the highest possible purity and in the lowest time. The separation is achieved by highly specific interactions between the ligand immobilized on the stationary phase and the target molecule, that is retained inside the column. To recover the product, the interaction should be reversible.

In this chapter the column L11-3x3-C, whose pillars were coated with the coating type F, presented in paragraph 2.3, was functionalized by immobilizing Cibacron Blue F3GA, a triazine dye affinity ligand commonly used for protein purification [1], to the external NFC layer of the pillars. To evaluate the result of the functionalization, the ability of the column to bind and retain bovine serum albumin (BSA) and the reversibility of their interactions, three complete chromatographic cycle were performed on the column before and after the functionalization.

3.1 Theory of Chromatographic cycles

A chromatographic cycle can be divided in three consecutive steps, as shown in chapter 1:

- Adsorption;
- Washing;
- Elution.

In the adsorption step the target molecule in equilibration buffer is fed to the column. Initially the target molecule is completely adsorbed by the affinity support and its concentration in the liquid stream exiting the column (generally called flow through) is zero. As the process continues, the target molecule concentration increases due to the saturation of the active sites and the consequent reduced adsorption capacity of the column. When the column reaches its maximum binding capacity, the target molecule is no more retained in the column and its concentration in the outlet equals that of the feed. From a quantitative point of view, the area under the BTC represents the amount of target molecule that has not been retained by the column, while the area above is the column operative capacity. In real experiments the system is constituted by a series of instruments (pumps, pipes, detectors, valves, etc.) that represent additional volumes external to the column [2]. The influence of these volumes can be measured by performing a chromatographic cycle in non-binding conditions. This can be achieved in different ways, among those is to perform an adsorption cycle in elution buffer or to use a non-functionalized column (with exactly the same geometry and volumes) in absence of specific interactions between the stationary phase and the target molecule. The result is the dispersion curve (DC). Therefore, the mass of product retained by the column is represented by the area above the BTC and below the DC, as shown in figure 3.1, and it can be calculated by equation 3.1:

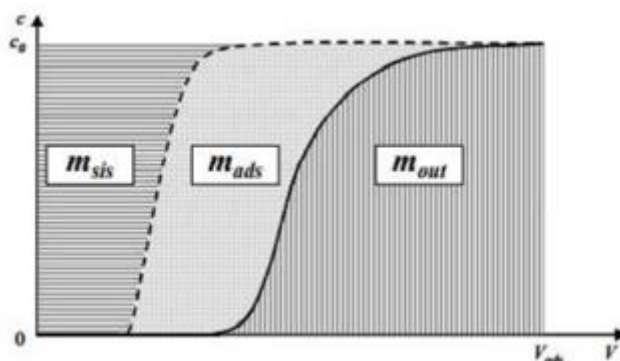


Figure 3.1: qualitative profile of the BTC and of the DC, during the adsorption step

$$m_{ads} = \left(\int_0^{V_{ads}} c(V) dV \right)_{DC} - \left(\int_0^{V_{ads}} c(V) dV \right)_{BTC} \quad (3.1)$$

Similar considerations can be done for the washing step, shown in figure 3.2, during which only equilibration buffer is fed to the column, to remove the mass of target molecule retained inside the column by non-specific interactions, that can be calculated by equation 3.2:

$$m_{des} = \left(\int_{V_{ads}}^{V_{ads+lav}} c(V) dV \right)_{BTC} - \left(\int_{V_{ads}}^{V_{ads+lav}} c(V) dV \right)_{DC} \quad (3.2)$$

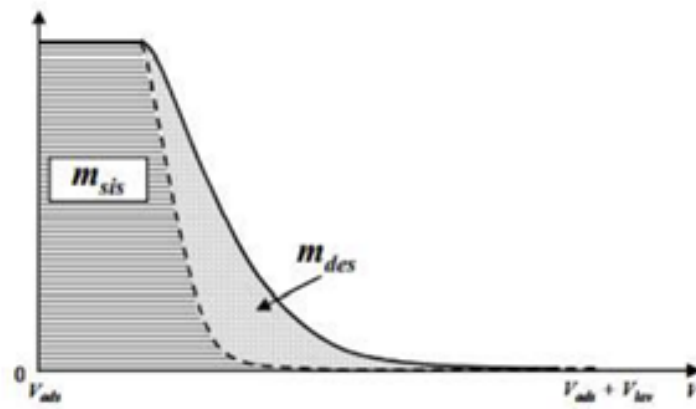


Figure 3.2: Qualitative profile of the concentration of the target molecule at the column outlet, during the washing step

In the desorption step a specific buffer, elution buffer, is fed to the column, with the aim of changing the operative conditions inside the column and promote the elution of the target molecule. The mass of eluted molecule can be calculated by equation 3.3, while the mass irreversibly adsorbed by the support by equation 3.4:

$$m_{el} = \left(\int_{V_{ads+lav}}^{V_{ads+lav+el}} c(V) dV \right)_{BTC} \cdot V_{el} \quad (3.3)$$

$$m_{imm} = m_{ads} - m_{des} - m_{el} \quad (3.4)$$

3.2 NFC layer functionalization with Cibacron Blue F3GA

The functionalization was achieved by following the procedure suggested by Lalli et. al. [3]. All the chemicals were purchased from Sigma-Aldrich (Milan, Italy).

The dye was added to 20 mL of demineralized filtered water to achieve a concentration of 10 mg/mL. The solution was continuously recirculated through the column for 60 min at 5 mL/min, by means of a peristaltic pump. The temperature of the system was kept at a constant temperature of 60°C by submerging the column, the reservoir and the tubes connecting the column to the pump and to the reservoir in a thermostatic water bath. After one hour, 5 mL of 20 wt% NaCl aqueous solution were added into the reservoir. After one hour, the temperature of the water bath was set to 80°C and 2 mL of 25 wt% Na₂CO₃ were added to the reservoir, to modify the pH and accelerate the reaction between the NFC fibers and the dye, as indicated in figure 3.3 [4 – 6]. The solution was continuously recirculated through the column for additional 4 hours.

The column was then washed by pumping 5 mL of the following solutions at a flow rate of 0.5 mL/min by means of a piston syringe pump. The different solutions were pumped in this order:

1. hot water (60°C);
2. 20% v/v methanol;
3. 2 M NaCl aqueous solution;
4. 0.05 M Tris-HCl solution containing 0.05 M NaCl (pH 8.0);
5. 0.5 M NaSCN (pH 8.0);
6. 20% v/v methanol;
7. 2 M NaCl aqueous solution.

The washing procedure was repeated until no dye could be detected.

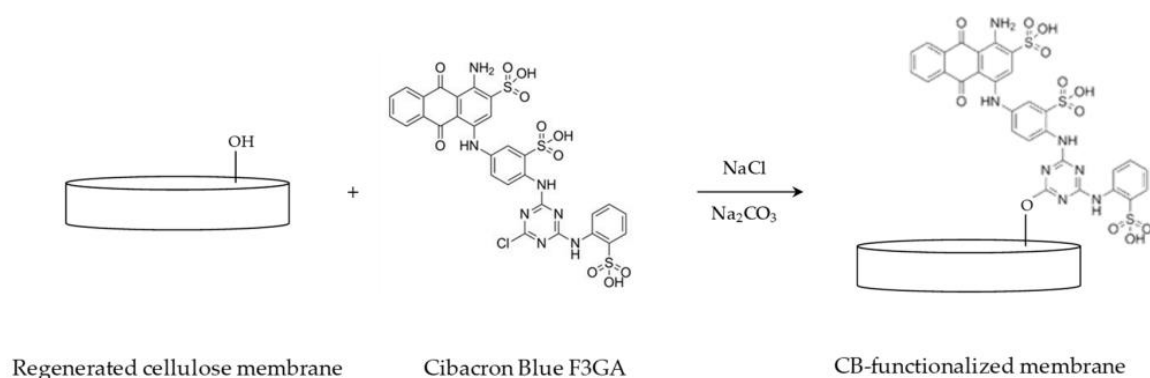


Figure 3.3: Immobilization reaction on cellulose support [3].

3.3 Dynamic adsorption test

Four chromatographic cycles were executed on the column V11-3x4-C, one before functionalization as to obtain the dispersion curve and three after the immobilization of Cibacron Blue. The tests were performed at 20 mL/min, chosen since it was the flow rate at which the column showed the best performance during the pulse tests, using pure BSA as target molecule at a concentration of 0.5 mg/mL in equilibration buffer. The composition of the buffer solutions and the volume fed to the system in each step are reported in table 3.1.

The tests were performed using the FPLC apparatus:

- Column equilibration: the instrument, with the valve A set in the load position, feeds the application buffer to the column by using line 1 of pump A, with the aim of creating homogeneous conditions inside the column and to remove any trace of other substances used in the previous tests;
- Adsorption: at the end of the equilibration step, valve A switch to inject position and the buffer solution flow into the loop, forcing the sample through the column;

- Washing: valve A switch again to load position, so that the buffer solution flows through the column, removing the portion of BSA non-specifically bound present in the column;
- Elution: pump A stops and pump B, from line 1, starts to feed to the column the elution buffer.

Table 3.1: overview of the chromatographic cycles.

Target molecule	Bovine Serum Albumin (BSA)
Equilibration buffer	0.05 M Tris-HCl solution + 0.05 M NaCl pH 8.0
Elution buffer	0.05 M Tris-HCl solution + 0.05 M NaCl + 0.5 M NaSCN pH 8.0
Column	V11-3x3-C
Flow rate	20 mL/min
Column equilibration	10 mL of equilibration buffer
Adsorption	25 mL of 0.5 mg/mL BSA in equilibration buffer
Washing	20 mL of equilibration buffer
Elution	10 mL of elution buffer

3.4 Results

Figure 3.4 shows the DC and the BTC obtained during the adsorption step of the three chromatographic cycles. From equations 3.2, 3.3 and 3.4, an adsorbed mass of 0.34 mg of BSA per mL of column was calculated for the first cycle. In absolute terms, this value is very low. Three different causes can be identified to explain such a low binding capacity:

- Poor column performance: as shown in paragraph 2.5.1, column V11-3x3-C was characterized by a very low efficiency, that may have affected the dynamic binding capacity of the column;
- Failure of the functionalization procedure and, therefore, absence of available sites for adsorption;
- The high mobile phase velocity led to a too short residence time of the BSA molecule inside the column, preventing the adsorption on active sites;
- Diffusion limitation in the coating layer: due to the high mobile phase velocity and the relatively low corresponding pressure drops, few molecules penetrated inside the external cellulose layers and most of them were attached only on the very external surface, that is quantitatively very small and was immediately saturated.

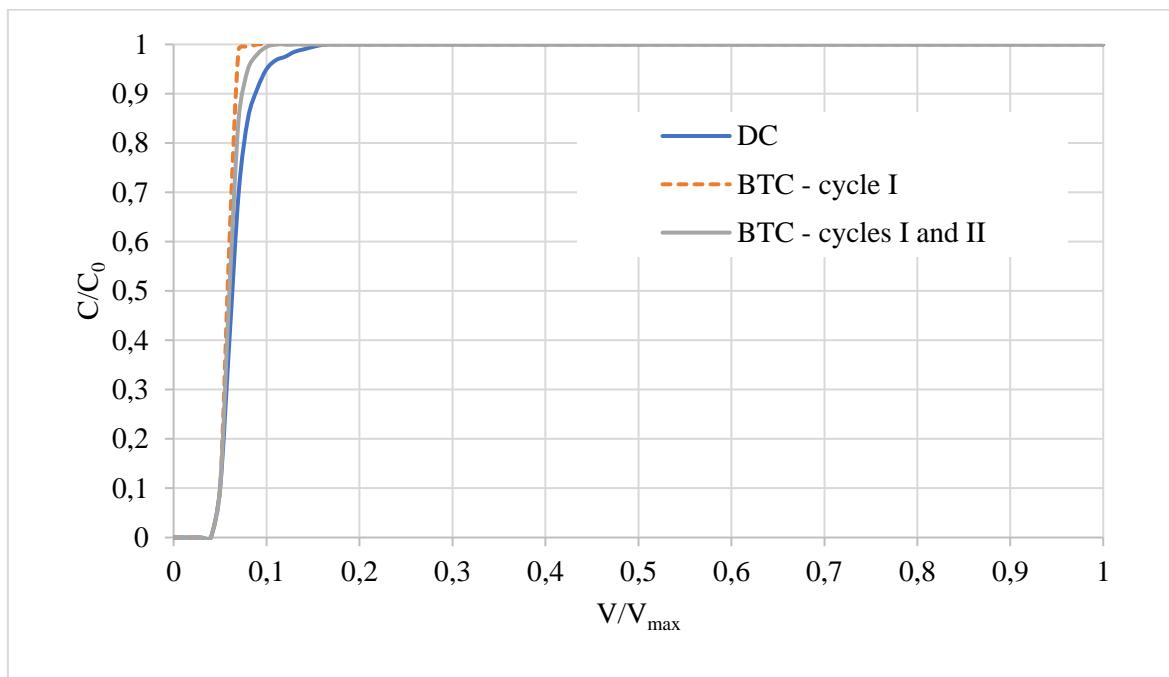


Figure 3.4: Dimensionless BTC and DC for the three chromatographic cycles

About the failure of the functionalization procedure, additional details can be obtained by the mass of BSA eluted during the first chromatographic cycle, that was equal to 0.04 mg/mL. The absence of BSA in the eluted fraction suggests that the elution buffer was not

effective in recovering the target molecule. A further confirmation was given by the results of the subsequent two chromatographic cycles, where nearly 0 mg/mL BSA were adsorbed, indicating the absence of free active sites. However, the very low efficiency of the column should be considered. Compared to non-coated columns, V11-3x3-C column showed a high HETP value, significantly affected by the Eddy diffusion (A-term). Since A-term is a measure of the packing uniformity, the presence of preferential pathways may have reduced the effective exploited portion of the column for the adsorption. Therefore, it cannot be excluded that the present results are the consequence of the combination of all the causes previously identified.

References

- [1] A. Denizli and E. Pişkin, "Dye-ligand affinity systems," *Journal of Biochemical and Biophysical Methods*, vol. 49, no. 1–3, pp. 391–416, Oct. 2001, doi: 10.1016/S0165-022X(01)00209-3.
- [2] S. di Martino, "Studio sperimentale e modellazione della separazione di proteine con membrane di affinità," Ph.D. thesis, University of Bologna, 2009.
- [3] E. Lalli, J. S. Silva, C. Boi, and G. C. Sarti, "Affinity Membranes and Monoliths for Protein Purification," *Membranes 2020, Vol. 10, Page 1*, vol. 10, no. 1, p. 1, Dec. 2019, doi: 10.3390/MEMBRANES10010001.
- [4] C. Y. Wu, S. Y. Suen, S. C. Chen, and J. H. Tzeng, "Analysis of protein adsorption on regenerated cellulose-based immobilized copper ion affinity membranes," *Journal of Chromatography A*, vol. 996, no. 1–2, pp. 53–70, May 2003, doi: 10.1016/S0021-9673(03)00531-4.
- [5] A. Kassab, H. Yavuz, M. Odabaşı, and A. Denizli, "Human serum albumin chromatography by Cibacron Blue F3GA-derived microporous polyamide hollow-fiber affinity membranes," *Journal of Chromatography B: Biomedical Sciences and Applications*, vol. 746, no. 2, pp. 123–132, Sep. 2000, doi: 10.1016/S0378-4347(00)00311-X.
- [6] H. L. Nie and L. M. Zhu, "Adsorption of papain with Cibacron Blue F3GA carrying chitosan-coated nylon affinity membranes," *International Journal of Biological Macromolecules*, vol. 40, no. 3, pp. 261–267, Feb. 2007, doi: 10.1016/J.IJBIOMAC.2006.08.005.

CHAPTER 3

Conclusions of Part I

In this part of the work, a three-dimensional, regular pillar-array chromatographic column was designed, produced and tested for preparative affinity protein separation. The column design has been done with a 3D CAD software and then 3D printed by masked-stereolithography (M-SLA). The core of the column consisted of a series of pillar-like shaped elements that, placed in a precise position inside a housing, create a series of identical flow paths with a rectangular cross-section for the mobile phase. The dimensions of the flow path were 0.1x10 mm by design, while in the printed columns an average value of 0.05x10 mm was measured due to the expansion of the resin. Several specimens were produced to evaluate the effects of the bed length and of the fluid distributors and collectors. In particular, two distributors were designed: the V distributor, consisting of a series pillars integrated in the column bed, and the L distributors, consisting of a series of pipes integrated in the column shell. The columns were characterized in terms of pressure drops and HETP. The latter characterization was performed by injecting small volumes of an inert tracer and by calculating the moments of their distribution at the column outlet by the Simpson's rule.

Significant information can be derived about the efficiency of both, the distributors and the bed of the columns. About the distributors, the best performance was obtained by the columns with the L distributors, for which the lowest HETP value observed was 0.085 mm for the L3-3x3-NC and 0.178 mm for the L11-3x3-NC, corresponding to 11.8 and 5.6 plates per mm of column, respectively. These results suggests that, in case of columns with the L distributors, the efficiency halves by increasing of 3 times the bed length. For the three non-coated columns

with the V distributors, the lowest HETP values observed were 0.0419 mm for the V3-3x3-NC, 0.157 mm for the V11-3x3-NC and 0.162 mm for the V11-3x4-NC, corresponding to 2.4, 0.64 and 0.62 plates per mm of column, respectively. Therefore, in case of columns with the V distributors, the different bed configurations, 3x3 and 3x4, do not provide any advantages in terms of performance, that decreases 4 times when the bed length triplicates. Even if better results could be obtained by increasing the flowrate, especially for the columns with the V distributors, they indicate that this column is still far from the separation efficiency obtained by commercial columns. Since diffusive pores are not present in the column, the mobile-phase mass transfer resistance (C-term in the Van-Deemter equation) is zero and the main limitations arise from the presence of defects, that cause flow paths with different length and width increasing the contribution of Eddy dispersion (A-term), and by the large voids between pillars, that promote longitudinal diffusion (B-term). The use of a 3D printer with an higher resolution should allow to reduce the interpillar distance and to achieve a more homogeneous structure.

One of the main drawbacks of 3D printing for chromatographic applications is the lack of appropriate materials. To produce the column, a phenolic epoxy resin specifically designed for the 3D printer was chosen, to obtain the best possible results in terms of resolution. Unfortunately, it was observed a release of undesired substances in the liquid phase due to leachable present in the resin. To overcome this limitation and to provide a surface to attach the ligand, three different materials were used to coat the portion of the pillars in contact with the mobile phase: nanofibrillated cellulose (NFC), titanium dioxide (TiO₂) and polystyrene (PS). NFC and TiO₂ coating layers were created by cold spray coating, while the polystyrene layers were applied by phase inversion. Several pillars were coated, by a single layer of these materials or by a stratification of them, and tested to measure their adhesion to the pillar surface under operative fluid flow conditions and to evaluate their ability to prevent the release of substances from the resin. The single layers of NFC and TiO₂ showed a good adhesion to the pillars, but a

certain degree of contamination of the mobile phase was observed, while an opposite behaviour was detected for the PS. The best results were obtained by the application of three different layers, in order TiO₂, PS, NFC: the TiO₂ particles increase the adhesion of the PS coating that avoid the direct contact between the resin and the liquid and it is enveloped by a network of NFC. A set of pillars were coated with this method and used to assembly a complete column. Unfortunately, this column was affected by significant mobile-phase mass transfer, with deleterious effects on its performance. Part of the lower efficiency of the column was caused by the poor coating uniformity within the pillars.

To test the ability of the column to bind proteins by affinity interactions, the external NFC coating of the pillars was functionalized with Cibacron Blue and the column was tested in three complete chromatographic cycles, using bovine serum albumin (BSA) as target molecule in non-competitive conditions. Only a small amount of proteins was retained by the column in the first cycle and none in the second and in the third. This unsatisfactory result seemed to be caused by the failure of the functionalization procedure, but the synergy of other factors, especially the low efficiency of the column and the low residence time caused by the high velocity of the mobile phase, cannot be excluded.

PART II

SURGICAL MASKS TESTING AND DURABILITY EVALUATION

Introduction to surgical masks

Surgical masks are loose-fitting medical devices that act as a physical barrier between the airways (mouth and nose) of the wearer and the environment, preventing infective agents contained in large-particle droplets, splashes, sprays or splatter emitted during respiration to spread in the surrounding area [1, 2].

Before 2020, the use of surgical masks in Western countries was mainly limited to the healthcare field, they were worn by workers to protect the patients from infective agents and, in some circumstances, to protect themselves against splashes of contaminated biological fluids, or worn by patients to reduce the risk of spread of infections. Instead, in some Eastern Asian countries, especially China, South Korea and Japan, surgical masks were daily worn by the general public to reduce the risk of spreading airborne diseases during allergy and flu season and to prevent the inhalation of airborne irritants, like pollens or dust particles generated by air pollution [3]. In 2019, the surgical masks market was estimated at 2141.3 million dollars [4]. Because of the low manufacturing costs and high and fast production capacity, with which foreign manufactures could not compete, China has established itself as the main surgical masks' producer, accounting for approximately half of the world production [5], as reported in figure 1.1. On the other hand, several countries decided to reduce their stocks and to rely more on supplies from China and on just-in-time logistic, to reduce acquisitions and storage costs. That has been the case of France, whose former strategic masks producer closed in 2018 and strategic stockpile dropped from one billion in 2010 to 150 million in early 2020 [6, 7]. A similar approach was followed by the United States, whose strategic stockpile of surgical masks, used against the 2009 flu pandemic, was

Introduction to surgical masks

not replenished [8]. Unfortunately, in the early 2020, the request for surgical masks skyrocketed to unprecedented levels due to the Covid-19 pandemic outbreak and the world's leading manufacturer was overwhelmed with orders, leading to a severe shortage of these medical devices [5].

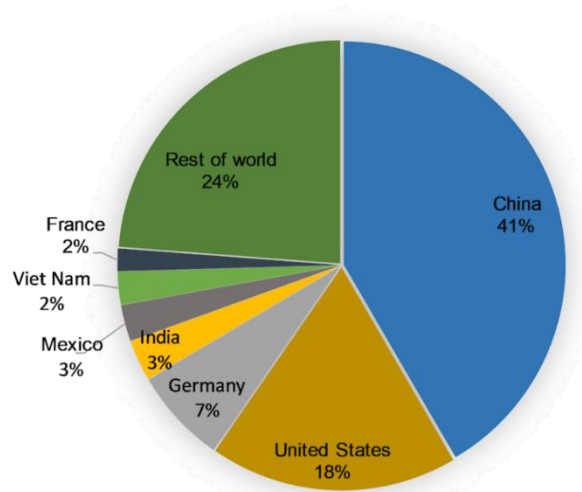


Figure 1: Share of export of face masks, by country, 2017 [5]

Coronavirus disease 2019 (COVID-19) is a viral respiratory illness causing moderate to severe effects: most people recover without requiring special treatment, but sometimes, it can lead to potentially lethal respiratory insufficiency requiring intensive care. COVID-19 is caused by a new strain of coronavirus, named Severe Acute Respiratory Syndrome Coronavirus-2 (SARS-CoV-2). These viruses usually circulate among animals and the precise way in which SARS-CoV-2 was transmitted to humans is currently under investigation. The virus mainly spreads via respiratory droplets and aerosols, generated by an infected subject (while speaking, breathing, sneezing or coughing), that are inhaled by other people. Sometimes infection may occur when susceptible subjects, having contaminated hands, touch their nose, eyes or mouth. More rarely, the infection may occur due to contact with contaminated surfaces, on which the viable virus declines over time and rarely it is present in sufficient amount to cause infection [9].

COVID-19 appeared in late 2019 in Wuhan (China) and spread very quickly across the entire globe according to asynchronous patterns. On March 11th, it was declared a global pandemic

by WHO and, in a matter of weeks, it affected over 100 countries. The disease appeared in Italy for the first time on 30 January 2020 and progressively grew over the national territory: on 27 March 2020, with 80589 reported cases, Italy was the third country in the world in terms of total number of cases, after China and USA, despite its smaller population [10, 11]. Within the first 20 months, 36 million cases of COVID-19 were reported in Europe, 208 million worldwide, numbers that do not consider asymptomatic undiagnosed cases [8].

The velocity and the routes of transmission caused an unpredicted immediate worldwide demand of personal protective equipment (PPE) in early 2020, in particular surgical face masks and respirators for the protection of the healthcare workers facing the disease in the hospitals. China, the world's leading manufacturer was overwhelmed with orders and in January 2020, with a productivity of 20 million masks per day, was not even able to meet its own internal demand of 240 million per day [5]. This situation, further exacerbated by the absence of sufficient strategic stocks and secure supplies, led to a dramatic shortage of surgical masks for healthcare workers, who were in direct contact with infected patients.

To address domestic shortages, many countries put in place restrictions on exports and other measures, like the compulsory purchase by governments of all available stocks. Table 1 reports some examples. On March 3rd 2020, the World Health Organization (WHO) called for industry and governments to increase manufacturing to meet global demands and, on April 6th 2020, released recommendations for their rational use [12, 13]. Several companies, private and public organizations all around the world started reconverting their production towards surgical masks or to search for channels to import them, but their efforts were partially nullified by several bottlenecks in the masks' value chain. Even if surgical masks are basic and relatively cheap products, their production requires the assembly of different parts in a relatively sophisticated process, along with several types of inputs, as reported in figure 1.2 [5]. The main and most influent bottleneck was the production of polypropylene

Introduction to surgical masks

electret melt-blown, a specialized nonwoven fabric responsible of the majority of the filtration efficiency of a surgical mask. Manufacturing of this material requires very high capital investment for the purchase of heavy machinery (such as hoppers, extruders and melt spinning systems), making the switch to this production expensive and very difficult within a reasonable time.

Table 1: Economies with COVID-19 export restrictions covering face masks [5].

Economy	Date (effective)	Type of restriction
<i>Chinese Taipei</i>	24/01/2020	Export ban
<i>India</i>	31/01/2020	Export ban
<i>Oman</i>	26/02/2020	Export ban
<i>Kazakhstan</i>	30/02/2020	Export ban
<i>Turkey</i>	28/02/2020	Export licenses
<i>Kazakhstan</i>	30/02/2020	Export ban
<i>Russia</i>	03/03/2020	Export ban
<i>Germany</i>	04/03/2020	Export ban
<i>France</i>	06/03/2020	Requisition order
<i>EU</i>	15/03/2020	Export licenses
<i>U.S.A.</i>		Export ban, exemptions for pre-existing commercial relationship

In terms of process, further and less serious bottlenecks were present:

- *Assembly line*: ultrasonic welding, the technique used to assembly the nonwoven surgical masks layers, is widely used in the textile and automotive industry, making the conversion of existing production line easier;

Introduction to surgical masks

- *Distribution*: COVID-19 created several problems also to domestic transport and logistic infrastructure, making difficult the delivery to hospitals on the basis of real-time need.

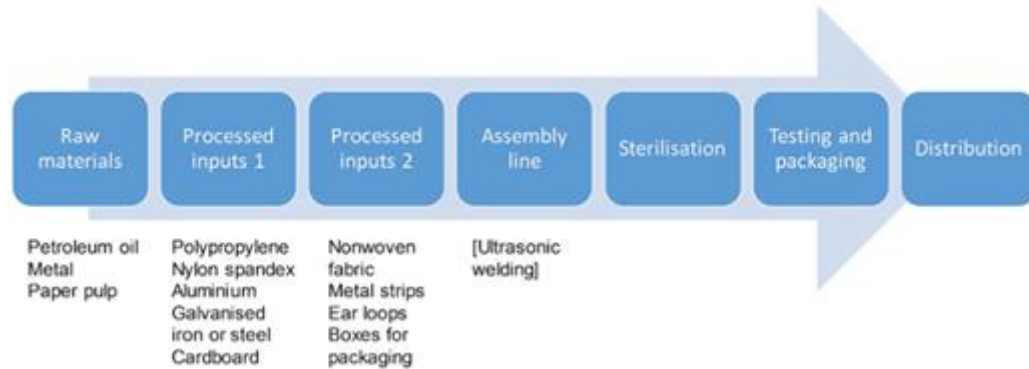


Figure 2: Surgical masks value chain [5].

The above-mentioned bottlenecks, along with several companies' lack of knowledge about surgical masks characteristics and production process, created quality issues exacerbating the shortages. For example, in mid-May, the European Commission suspended an order of 10 million Chinese masks after two countries reported having received sub-standard products [14]. Surgical masks dedicated to the European market, whether they are produced or imported, should comply to the European regulation EN 14683:2019, "*Medical face masks – Requirements and test methods*", which specifies construction, design, performance requirements and test methods [2]. In Italy, the absence of laboratories able to perform all the test provided by the European regulation EN 14683:2019 for the evaluation of surgical masks appeared to be an additional bottleneck [15]. On 17 March 2020, a decree-law of the Italian government allowed the validation of not CE-marked surgical masks, produced or imported in the national territory, by the National Institute of Health (ISS), which evaluates the masks quality on the basis of the results of any laboratory (even if not credited) able to perform the tests required by the EN standard [16].

To support the Italian industrial reconversion to the production of surgical masks, in late March 2020 a multidisciplinary team of the University of Bologna, driven by the expertise

Introduction to surgical masks

of chemical engineers, microbiologists, and occupational physicians, created the first Italian laboratory able to perform all the test required by the European regulation [15]. Four different test lines were set-up:

- *Breathability*: for the measure of the resistance caused by a surgical mask to respiration and, indeed, an indirect evaluation of the comfort offered to the wearer;
- *Bacterial filtration efficiency (BFE)*: to quantify the efficiency of the mask in filtrating exhaled respiratory droplets and aerosols;
- *Splash test*: for the qualitative analysis of the protection offered against splashes of blood and body fluids;
- *Bioburden*: for the evaluation of the microbial cleanliness.

The laboratory started its activity on late March 2020 and, after one year of activity, more than 600 surgical mask prototypes were tested (with nearly 1200 tests performed in total) for private and public companies and organization.

In this work, an analysis of the apparatuses indicated by the EN standard is presented, pointing out strengths and weakness of the protocols, for which additional improvements are proposed. In addition, the results obtained from the tests will be analyzed, to provide useful correlations between surgical masks performance, materials and manufacturing processes. To address the shortage of surgical masks and to mitigate their environmental impact, the lifetime of two surgical masks was evaluated by measuring how their performance vary over time of usage. Since a deterioration of the bacterial filtration efficiency was observed, the BFE apparatus was used to investigate the causes. To allow the execution of experiments aimed to evaluate the lifetime of a surgical masks in any laboratory equipped with a BFE apparatus, an experimental protocol able to simulate the real use will be presented.

References

- [1] “N95 Respirators, Surgical Masks, Face Masks, and Barrier Face Coverings | FDA.” <https://www.fda.gov/medical-devices/personal-protective-equipment-infection-control/n95-respirators-surgical-masks-face-masks-and-barrier-face-coverings> (accessed Jan. 20, 2022).
- [2] *BS EN 14683:2019: Medical face masks - Requirements and test methods*. European Committee for standardization.
- [3] “A quick history of why Asians wear surgical masks in public — Quartz.” <https://qz.com/299003/a-quick-history-of-why-asians-wear-surgical-masks-in-public/> (accessed Jan. 20, 2022).
- [4] “Surgical, Face, and Respiratory Mask Market Size, Share | Industry Report, 2030.” <https://www.psmarketresearch.com/market-analysis/facial-surgical-mask-market> (accessed Jan. 20, 2022).
- [5] “The face mask global value chain in the COVID-19 outbreak: Evidence and policy lessons.” <https://www.oecd.org/coronavirus/policy-responses/the-face-mask-global-value-chain-in-the-COVID-19-outbreak-evidence-and-policy-lessons-a4df866d/> (accessed Jan. 20, 2022).
- [6] “Pénurie de masques : une responsabilité partagée par les gouvernements successifs | Public Senat.” <https://www.publicsenat.fr/article/politique/penurie-de-masques-une-responsabilite-partagee-par-les-gouvernements-successifs> (accessed Jan. 20, 2022).
- [7] “How France Lost the Weapons to Fight a Pandemic - The New York Times.” <https://web.archive.org/web/20200711054403/https://www.nytimes.com/2020/05/17/world/europe/france-coronavirus.html> (accessed Jan. 20, 2022).
- [8] “Opinion | How the World’s Richest Country Ran Out of a 75-Cent Face Mask - The New York Times.” <https://www.nytimes.com/2020/03/25/opinion/coronavirus-face-mask.html> (accessed Jan. 20, 2022).
- [9] “Questions and answers on COVID-19: Basic facts.” <https://www.ecdc.europa.eu/en/covid-19/questions-answers/questions-answers-basic-facts> (accessed Jan. 20, 2022).

- [10] A. Remuzzi and G. Remuzzi, “COVID-19 and Italy: what next?,” *The Lancet*, vol. 395, no. 10231, pp. 1225–1228, Apr. 2020, doi: 10.1016/S0140-6736(20)30627-9.
- [11] F. Ortenzi, E. Albanese, and M. Fadda, “A Transdisciplinary Analysis of COVID-19 in Italy: The Most Affected Country in Europe,” *International Journal of Environmental Research and Public Health*, vol. 17, no. 24, pp. 1–12, Dec. 2020, doi: 10.3390/IJERPH17249488.
- [12] “Advice on the use of masks in the context of COVID-19: interim guidance, 6 April 2020.” <https://apps.who.int/iris/handle/10665/331693> (accessed Jan. 20, 2022).
- [13] “Shortage of personal protective equipment endangering health workers worldwide.” <https://www.who.int/news/item/03-03-2020-shortage-of-personal-protective-equipment-endangering-health-workers-worldwide> (accessed Jan. 20, 2022).
- [14] “EU suspends delivery of 10 million masks over quality issues - SFGate.” <https://web.archive.org/web/20200521081946/https://www.sfgate.com/news/article/EU-suspends-delivery-of-10-million-masks-over-15269498.php> (accessed Jan. 20, 2022).
- [15] “Il business delle mascherine e i laboratori che fanno i test: molte non sono a norma - Il Sole 24 ORE.” <https://www.ilsole24ore.com/art/il-business-mascherine-e-laboratori-che-fanno-test-molte-non-norma-ADqkm8F> (accessed Jan. 20, 2022).
- [16] “Gazzetta Ufficiale.” <https://www.gazzettaufficiale.it/eli/id/2020/03/17/20G00034/sg> (accessed Jan. 20, 2022).

CHAPTER 5

COVID-19 pandemic and the role of face masks

COVID-19 appeared in late 2019 in Wuhan, China, and spread very quickly across the entire globe according to asynchronous patterns. Within the first 20 months, 36 million cases of COVID-19 were reported in Europe, 208 million worldwide [1]. During the first twelve months, virus-specific pharmaceutical interventions such as vaccines and therapeutics were not available, making non-pharmaceutical measures the only weapon to reduce SARS-CoV-2 transmission. Among these, face masks have played, and still do, a primary role.

Due to the lack of knowledge about the modes of transmission of the virus and its ability to be spread also by asymptomatic and pre-symptomatic individuals, the importance of universal masking was initially underestimated and their use recommended only to symptomatic patients and healthcare workers dealing with them. At present, the use of face masks is strongly recommended in all circumstances in which physical distancing is not possible and in indoor settings. However, different types of face masks offering a different degree of protection exist. Indeed, the knowledge of the modes of transmission of COVID-19 and that of the efficiency of the different types of face masks in filtrating infectious respiratory droplets and aerosols are fundamental to grant the highest possible protection to the wearer.

5.1 SARS-CoV-2 modes of transmission

The knowledge of the specific mechanisms of transmission of SARS-CoV-2 is a key factor for the evaluation of the effectiveness and the suitability of non-pharmaceutical intervention in mitigating the virus spreading [2]. In general, the transmission of a respiratory virus starts whenever an infected individual (infecter) breathes, talks, sneezes, coughs or laughs, spreading in the environment globs of mucus, saliva and water, in which viral particles are encapsulated. The dimension of the globs depends on the exhalation event and affect both, their behaviour and their potential dangerousness. Bigger globs, hereinafter referred to as “droplets”, are too heavy to remain in the air and splash down nearby, causing the contamination in the immediate surroundings of air, bodily surfaces (i.g. skin and clothes) and objects. Smaller globs, or droplets reduced due to evaporation, linger in the air and can potentially contaminate a larger area [3]. Henceforth, small globs will be called “aerosol”, while in literature also the terms “bioaerosol” and “droplet nuclei” are used with the same meaning.

The scenarios with respect to the generation of droplets and aerosol have not been adequately understood and the situation is further complicated by the lack of standardized terminology and features [4]. The World Health Organization (WHO) and the Centers for Disease Control and Prevention (CDC) look at airborne and droplet transmission as discrete categories, with the former occurring almost exclusively during medical aerosol generating procedures [5 – 7]:

- droplets are particles with a diameter greater than 5 μm , which settle on the ground within seconds to minutes depending on their size following a ballistic trajectory and are transmitted over distances usually lower than 2 metres;
- Aerosols are particles with a diameter smaller than 5 μm which remain in the air for minutes to hours and can be transmitted over longer distances.

The 5 μm threshold used to dichotomise aerosols and droplets has never been supported theoretically or experimentally and, recently, aerosol scientists indicate in 100-200 μm the correct size threshold to differentiate these particles [8–10].

As a result of this approach, a 2 metres safe exclusion zone has been accepted to prevent possible host-to-host droplet transmission, but this notion is not supported by any comprehensive study. Xie *et al.* analysed the effects of droplet size, exhaled air velocity and relative humidity on droplets dispersion and evaporation by numerical computations. The results, shown in figure 5.1, confirmed in general the behaviour of droplets and aerosols, but also demonstrated that droplets can penetrate a longer distance: 1 metre in case of exhaling (1 m/s), 2 meters in case of coughing (10 m/s) and 6 meters in case of sneezing (50 m/s) [11].

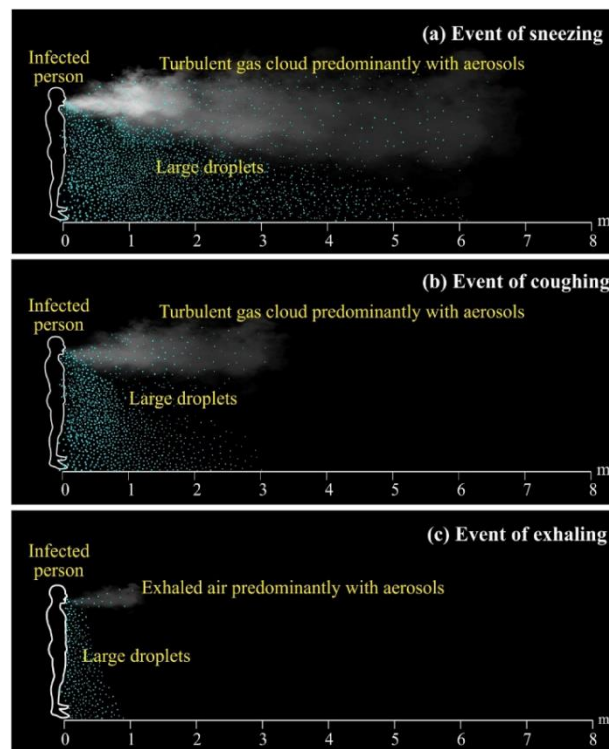


Figure 5.1: trajectory of droplets and aerosols emitted: a) in case of sneezing, at 50 m/s, with droplets travelling for 6 m; b) in case of coughing, at 10 m/s, with droplets travelling for 2 m; c) in case of exhaling, at 1 m/s, with droplets travelling for 1 m [3].

CHAPTER 5

However, this study does not consider several phenomena occurring in real scenarios, such as turbulence due to inhalation and exhalation, cloud dynamics and interaction between droplets, presence of ventilation and air distribution design in a room.

To better describe the behaviour of respiratory particles, recent studies suggest to avoid dichotomization and to look at the exhaled particles as a continuum of aerosols and droplets of all sizes, which constitute a multiphase turbulent gas cloud (“puff”), as shown in figure 5.2. This approach leads to important practical implications in defining recommendations to minimize the risk for disease transmission: the gas cloud not only carries within it clusters of droplets but, thanks to its locally moist and warm atmosphere, also prevent their evaporation, increasing in turn their lifetime [12]. The results obtained in case on sneeze confirm the penetration of 7-8 meters of droplets, reported by Xie *et al.* and by other more recent studies [13].

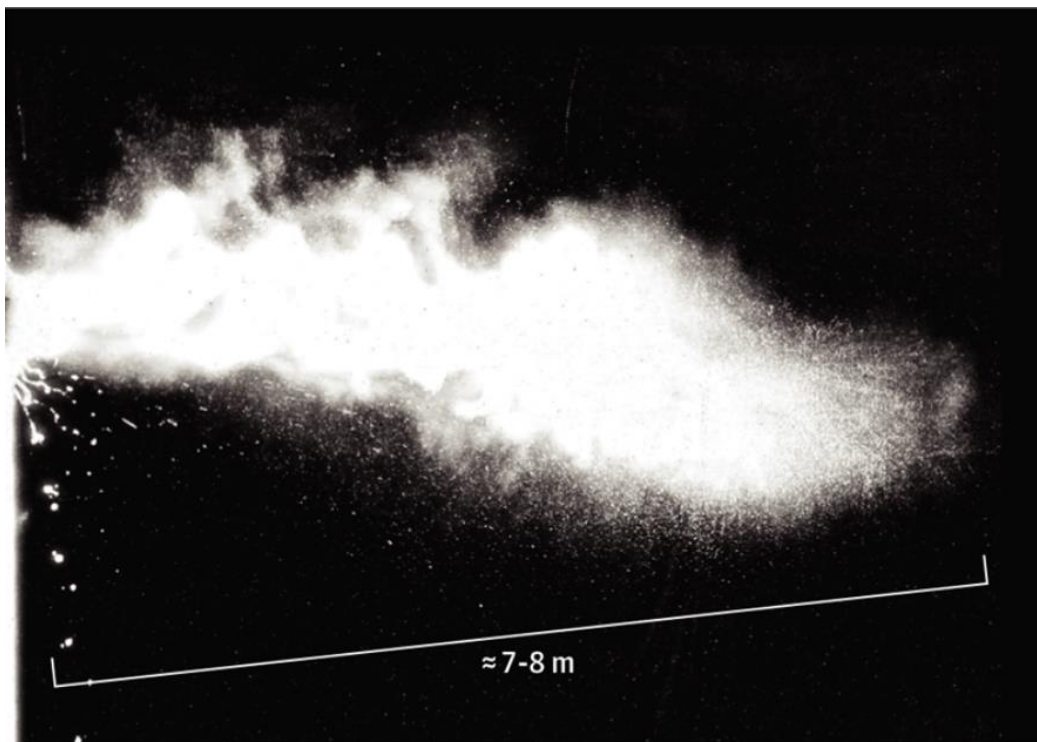


Figure 5.2: multiphase turbulent gas clouds emitted in case of sneezing [12].

The release in the environment of infectious droplets and aerosols leads to the contamination of the surrounding air, bodily surfaces (i.g. skin and clothes) and objects. The transmission of the virus to a susceptible individual (infectee) may occur via several biologically plausible, individual or simultaneous, routes, as reported in figure 5.3. Again, the lack of standardized terminology and features causes confusion [14]. WHO indicates three main modes of transmission [7]:

- *Respiratory droplet transmission* can occur when the droplets released by the infector, following a ballistic trajectory, reach the mouth, nose or eyes of an infectee in close contact (within 1 meter);
- *Direct and indirect (fomite) contact transmission* occur as mucous membranes are infected when the infectee touches its mouth, eyes and nose with hands contaminated due to the direct physical contact with the infector or with a contaminated surface (fomite);
- *Airborne transmission* may occur due to the inhalation of infectious aerosols in the air.

Three main transmission routes are also proposed by the CDC [15]:

- *Inhalation* of infectious droplets and aerosol particles present in the air;
- *Deposition* of exhaled droplets and particles onto exposed mucous membranes (i.g. due to coughing);
- *Direct or indirect (fomite) contact*.

The quantification of the relative contribution of all these transmission modes is a challenging task and is still unquantified, since they are complex phenomena affected by several factors, mainly relative to the virus (infection dose, viability, time and distance during exposure), to the host (breathing rate, morphology of the respiratory tract, target

tissue, receptor distribution, immune response and barriers) and to the environmental conditions (temperature and relative humidity, precipitation, pH, presence and flowrate of the ventilation, solar ultraviolet radiation and presence of chemicals) [3, 16 – 18].

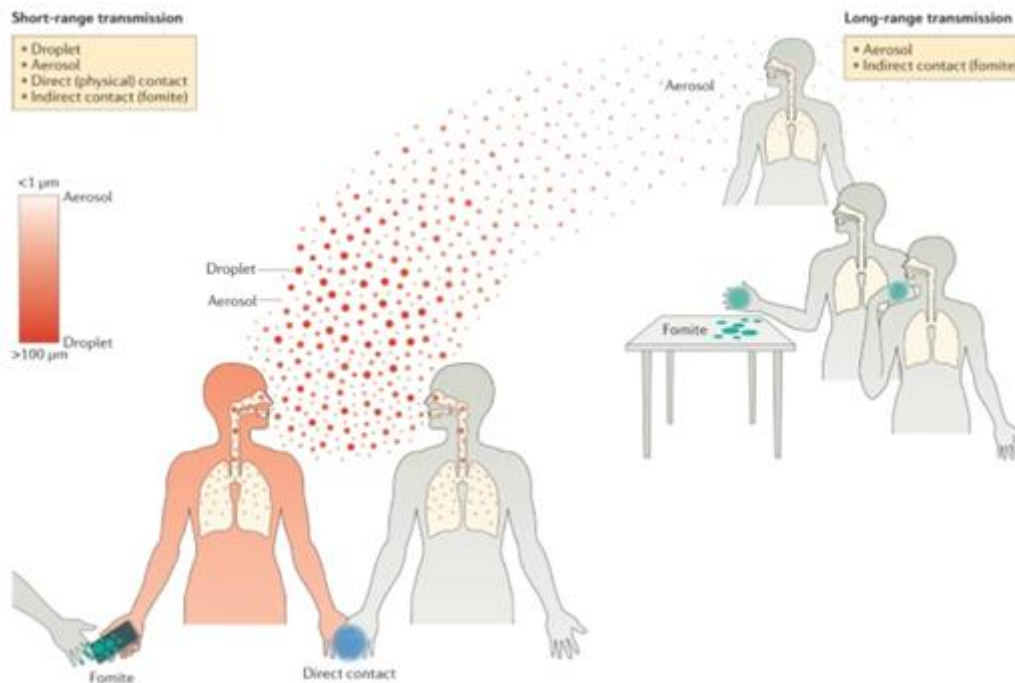


Figure 5.3: Primary modes of transmission of respiratory viruses [2].

Several theoretical modelling, laboratory-based and *in silico* studies have been performed to determine the frequency of transmission mode, but their specific controlled conditions make them not reflective of the physiological host process and real-world environmental conditions. Some droplet dispersion experiments and simulations have found that respiratory particles floating in the air can travel for long distances [19 – 21]. However, this does not necessarily support long-range aerosol transmission of infectious viral particles since the dilution and the progressively lower virus concentration and viability under dynamic environmental conditions were not considered [7]. Two hospital-based studies collected aerosol samples around patients admitted into medical wards and assessed the presence of infectious viable virus in different particle size [21, 22]. In particular, Lednicky *et al.* detected a small amount of airborne virus, ranging from 6 to 74 median tissue culture

infectious dose (TCID₅₀). However, the low presence of viable SARS-CoV-2 in air samples of hospital settings (where robust ventilation, air filtration, PPE and others transmission-based precautions are present) does not provide straightforward information about aerosols transmission frequency in the community [24]. This similarly applies to fomite transmission. Despite several laboratory-based studies reported SARS-CoV-2 surface contamination and stability, there are no specific reports which have directly demonstrated fomite transmission, mainly due to the difficulties to discern it from respiratory droplet [7, 25].

Although laboratory and theoretical studies can be useful only as complementary source of knowledge, substantial epidemiological evidence exists in support of specific transmission modes in real-world conditions. Koh *et al.* conducted a systematic review on the secondary attack rate, SAR, (the probability that an infection occurs among susceptible people within a specific group) in household, non-household and healthcare settings [26]:

- *Household SAR*: estimated at 18.1%, suggests the importance of high frequency and intensity of contacts, usually occurring between family members;
- *Healthcare SAR*: usually lower than 2%, can reach higher values in absence of proper precautions, as occurred in Wuhan (China) in early January 2020 due to inadequate acknowledgment of the pathogens and PPE shortage;
- *Non-household SAR*: usually ranged between 0-5% in workplace, school and social settings, can be significantly higher in mass gatherings, as occurred at a meeting in Germany (84.6%) or at a sky chalet in France (73.3%).

The results show that a rapid person-to-person transmission is usually observed in crowded, closed and poor-ventilated environments, especially in the absence of proper PPE (such as in shared eating environments), supporting the close-contact respiratory transmission, via short-range aerosols and droplets, and direct contact as primary modes of SARS-CoV-2

transmission. This study, along with others that analysed outbreak in different settings (such as restaurants, churches, flights, bus and indoor fitness) suggests that long-range aerosols transmission can contribute to spread the infection only under certain conditions, including prolonged exposure in enclosed spaces with inadequate ventilation [1, 26]. However, infection due to inhalation at distances greater than 2 metres is less likely to occur than at close distance and long-range aerosols transmission has not been officially recognized by the WHO [7]. Similarly occurs for fomite transmission. Despite consistent studies have demonstrated the contamination of surfaces and the survival of the virus from hours to days, depending on the type of surface and on the environmental conditions, the fomite transmission has not been directly demonstrated [7].

5.2 Non-pharmaceutical measures to prevent transmission

Current mitigation strategies for SARS-CoV-2 rely on population-wide adoption of both, pharmaceutical (PIs) and non-pharmaceutical interventions (NPIs), reported in figure 5.4.

During the first twelve months of the COVID-19 pandemic, virus-specific pharmaceutical interventions such as vaccines and therapeutics were not available, making NPIs the most important (and only) public health measures to reduce respiratory virus transmission. The first mass vaccination programme (pharmaceutical intervention) started in early December 2020 and, on January 12th 2022, almost 4 billion people have been fully vaccinated with one of the several vaccines validated by the WHO [28]. COVID-19 vaccines are highly effective against serious illness (bringing to hospitalization and death), but the maximum level of protection is not reached until several weeks after full vaccination and, even if there is some evidence that being vaccinated reduces the probability of contagion, breakthrough infections (infection and illness inspite of being fully vaccinated) is however possible. In addition, new

virus mutations and variants affect the effectiveness of the different vaccines [29]. Indeed, it arises the necessity to still apply NPIs, which play a key role in mitigating virus spread and will likely remain the mainstay of preventive measure against COVID-19, even in the post-vaccination era.

The importance of using multiple preventive interventions to reduce the risk of infection is recognized by the “Emmentaler Cheese Respiratory Pandemic Defence Model”, illustrated in figure 5.4 [2].

EMMENTALER CHEESE RESPIRATORY PANDEMIC DEFENSE MODEL

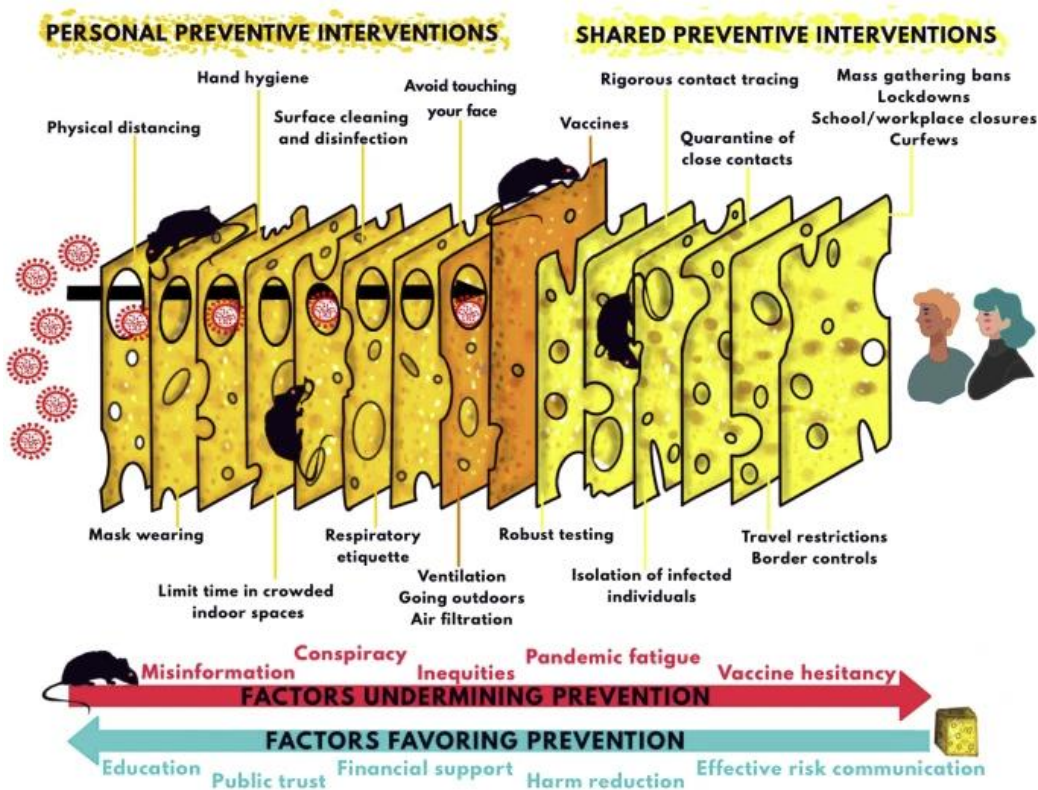


Figure 5.4: Emmentaler cheese respiratory pandemic defense model [2].

SARS-CoV-2 infection occurs when multiple holes align, permitting a trajectory of successful transmission. Each measure, taken individually, is not sufficient at preventing the spread of the virus due to the presence of vulnerabilities or limitations (holes), while when several measures are used the weaknesses in any of them could be offset by the strengths of

the others. There are also external factors which are able to undermine (black rats) or favour (additional cheese) prevention efforts.

NPIs can be divided into personal and shared public health interventions, although some of them can be both. Shared interventions consist in a series of national measures taken by governments to identify and isolate infectious individuals, to reduce the probability to import or export the virus and its new mutations from and to abroad (travel restrictions), and to reduce the possibility of superspreading events (i.g. mass gatherings ban, workplace closure). Personal preventive interventions are a series of recommendations (and sometimes national laws) to be followed by everyone, acting on each mode of transmission to reduce its contribution to the virus spread. These measures, suggested by the WHO, can be grouped as follows [30]:

- Keep social distance of at least 1 metre and avoid crowds and close contact;
- Use of face masks or coverings in poorly ventilated settings and when physical distancing is not possible;
- Hand and environment hygiene to reduce direct contact and fomite transmission.

5.3 Role and types of face masks

The term “face masks” usually refers to a broad variety of devices used in several fields (also sport, cosmetics and art). However, here this term will be used with exclusive reference to devices that primarily guard the airways by creating a physical barrier that separates the mouth and the nose of the wearer from the immediate environment, preventing the inhalation or the spreading of contaminants. Depending on the intended aim, the protection offered (intended as the efficiency in filtrating particles), the fit of the design and the compliance to specific regulations, face masks can be classified as follows and as reported in figure 5.5:

- Cloth masks;
- Surgical masks;
- Respirators;
- Elastomeric respirators.

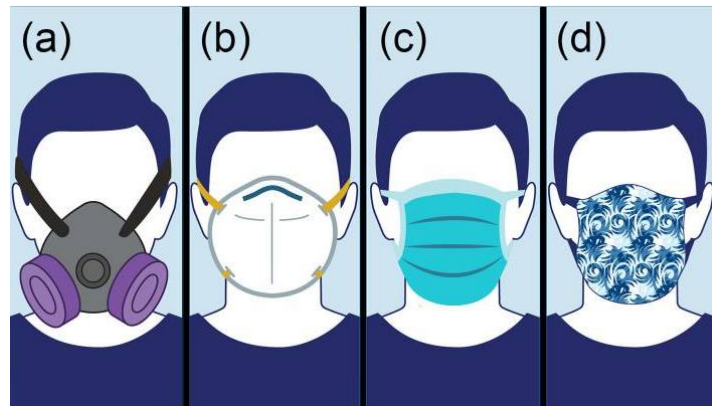


Figure 5.5: Representation of the different face masks: a) Elastomeric respirators with replaceable filters; b) respirators; c) surgical mask; d) cloth mask [3].

Cloth masks, also called non-medical or fabric masks, are hygienic devices that should not comply to any regulation and can be homemade or industrially produced. The only requirement is that they should be able to cover both, mouth and nose, while there is no indication about the fitting or the material. The WHO indicates that cloth masks should be ideally made of 3 layers: a water-resistant outer layer (like polyester), a filtering nonwoven fabric mid-layer to enhance filtration and a water absorbent inner layer (like cotton) to absorb droplets exiting the airways. It is also suggested to wash the mask at least once a day, by using a detergent in hot water [31]. Due to the absence of specific regulations and mandatory tests verifying their composition and performances, the ability of these device to filter droplets and aerosols exiting the wearer airways or coming from the environment may drastically vary from device to device (the difference between two cloth masks is shown in figure 5.6). Indeed, the protection offered to the wearer and to close susceptible individuals cannot be estimated. Similarly, the breathability, intended as the resistance to the respiration

caused by the mask, is undetermined. The advantage of these devices is that they can be washed and re-used, but the effect of these operations on the filtration efficiency is unstudied. Surgical masks, also called procedural masks, are medical loose-fitting disposable devices, designed mainly to prevent the spread of splashes and respiratory droplets exhaled from the wearer, while they are less effective against fine airborne particles. To a certain extent, they also protect the wearer from external infectious contaminants [31]. The protection offered is also limited by the loose fit between the mask edge and the wearer's face, which leads to leakage in the range 12-25% [32]. Surgical masks should comply to specific regulations, which slightly vary from country to country. The European regulation is the EN14683:2019, along with the respective references. It provides for a series of tests, primary aiming to verify the filtration efficiency of particles with a mean size (MPS) of $3\ \mu\text{m}$ and the comfort in terms of breathability [33]. These masks are rectangular-shaped and usually composed by three polypropylene layers: a spunbond water-repellent outer layer, a filtering melt-blown (mostly electret) mid-layer and a spunbond absorbent layer [34].

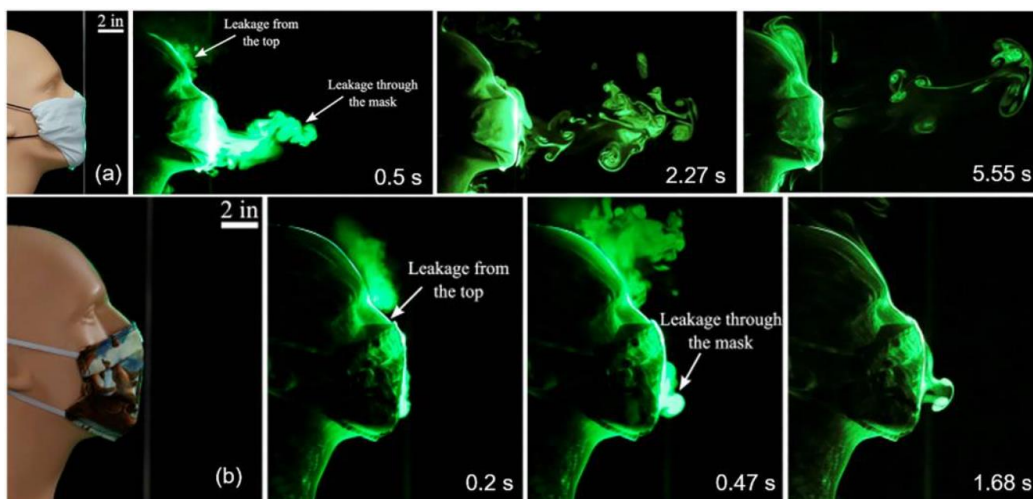


Figure 5.6: Effect of a cloth masks on the propagation of respiratory droplets and aerosols: a) mask made following the recommendation of the United States Surgeon General; b) two cotton-layers homemade mask [35].

Respirators have a similar composition (with usually the addition of a further filtering meltblown layer) but, unlike surgical masks, they are designed to be fitted and to have a tight seal, which dramatically reduces the leakage. Compared to surgical masks, respirators offer a greater protection also thanks to the high filtration efficiency for particles larger than 300 nm. These characteristics allows the protection of the wearer and of close susceptible individuals against respiratory droplets, fine aerosols and splashes [36]. However, several studies found that respirators are not significantly superior to surgical masks for preventing the spread of influenza, even if the experiment were conducted in healthcare settings and in presence of other NPIs, whose contribution was not quantified [37]. Cheng *et al.* came to similar results by measuring the size distribution of respiratory particles emitted during different respiratory activities, with and without face masks. The results, reported in figure 5.7, led to the conclusion that surgical masks are as effective as respirators in preventing the diffusion in the environment of respiratory droplets and aerosols exhaled by the wearer in any circumstances [38]. This behaviour can be ascribed to the efficiency of both mask types in removing larger particles, and freshly generated droplets and aerosols are usually larger at the source since they have not time to evaporate. These results are a further demonstration of the importance of controlling the virus spread at the source, by wearing surgical masks or respirators. On the contrary, some studies have shown that cloth masks are up to 50-folds less effective than respirators and 25-folds than surgical masks in reducing the virus spread [39], but these values can vary according to the cloth mask quality.

Respirators are disposable devices and should comply to specific regulations, which slightly vary from country to country. The European regulation is the EN 149:2001 + A1:2009. Some respirators are equipped with a one-way exhalation valve that allows exhaled airflow out, along with respiratory droplets and aerosols. Therefore, the use of such devices has been discouraged for the purpose of controlling COVID-19 spread [40].

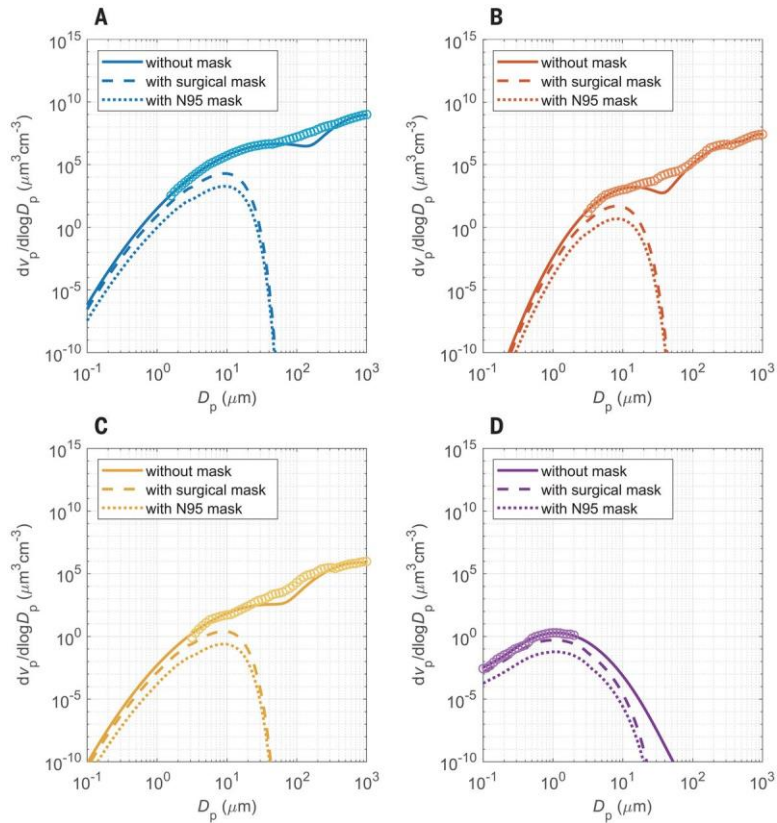


Figure 5.7: Volume size distribution of respiratory particles emitted during different activities, with and without mask: a) sneezing; b) coughing; c) speaking; d) breathing. The symbols v_p and D_p are the volume concentration and the diameter of respiratory particles, respectively, and $dv_p/d\log D_p$ represents the volume distribution function [38].

Elastomeric respirators are reusable well-fitting devices that offer protection to the wearer depending on the replaceable filters employed. Since they are scarcely used by the community or healthcare workers, as they require maintenance and a supply of replaceable expensive components, these devices will be not further discussed.

In early 2020, the importance of universal masking of the population, including the healthy, in mitigating the COVID-19 spread was not officially recognized and the use of masks was recommended only to healthcare workers operating with symptomatic patients and the patients themselves [37 – 39]. Some months later, given the evidence that COVID-19 can be spread also by pre-symptomatic and asymptomatic individuals, universal face masking has been recommended as a low-cost and efficient non-pharmaceutical intervention. On 8 April 2020, the European Centre for Disease Prevention and Control (ECDC), recommended

the use of face masks also in the community in closed, poor-ventilated and crowded environment and in general in all that circumstances in which a physical distancing was not possible [39]. To alleviate personal protective equipment shortages among healthcare workers, ECDC also suggested the use non-medical face masks among the asymptomatic general public. On 5 June 2020 the WHO released a similar interim guidance, recommending the use of surgical masks and respirators also by vulnerable people (over 60 or with underlying health risks) [44]. These recommendations were followed by several policy makers. In Italy the universal masking of the population became mandatory on May 4th [45]. According to #Mask4All, 95% of the world population lives in countries where the use of masks in public places is recommended or required by the government and leading experts [46].

The effectiveness of masks in mitigating the virus transmission is still under debate and has not been recognized by the WHO, since all the studies performed were conducted in closed environment with specific conditions and the authors were not able to exclude or to quantify the contribution of other factors (environmental condition, quality and correct use of the masks, type of the virus and minimal dose leading to the infection, presence of other NPIs, etc.) [44]. However, epidemiological studies have demonstrated the efficacy of wearing face masks in the community observing the resulting reduction of the reproduction number R_0 , which is the expected number of cases directly generated by one infectious subject in a population where all the individuals are susceptible to infection. Tian *et al.* [47] state the efficacy strongly depends on the quality of the masks and on the adherence, as reported in figure 5.8, and that the universal use of performant face masks could lead to a drastic reduction of the virus spread.

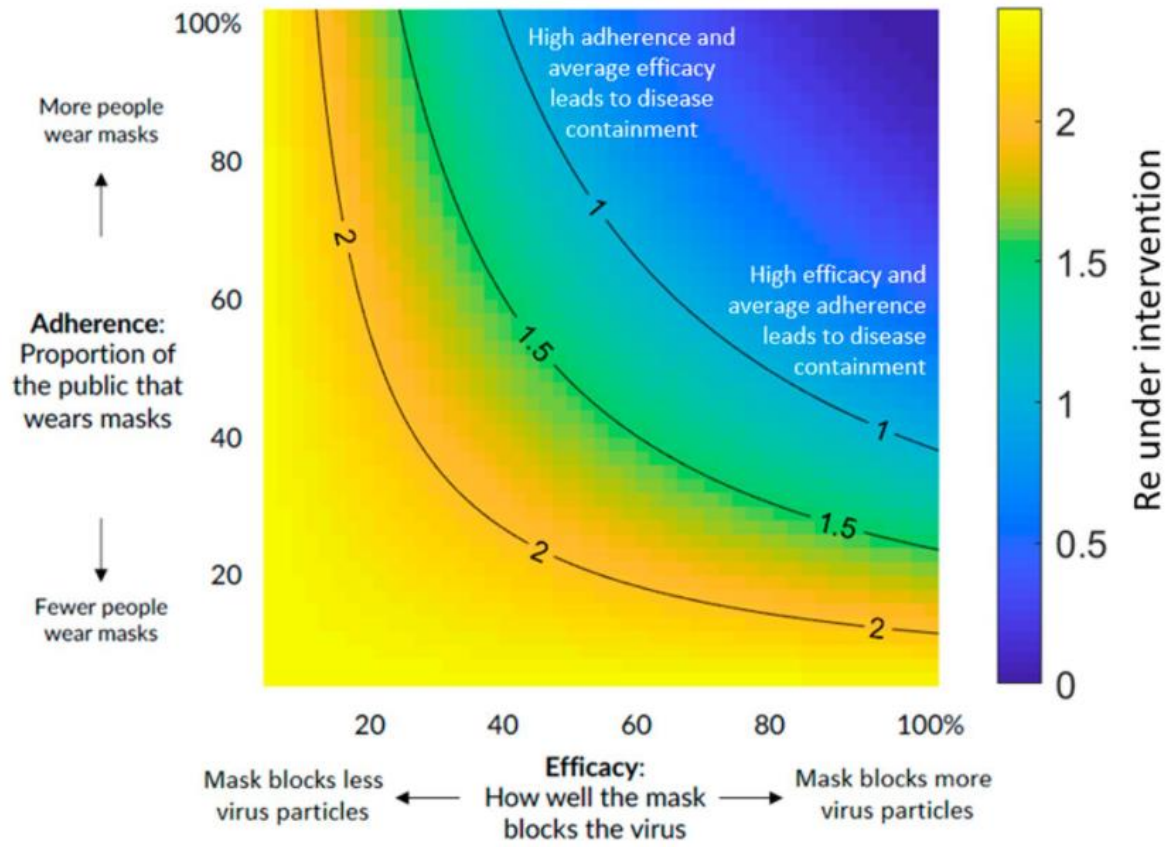


Figure 5.8: Impact of public mask wearing on the reproduction number (initial value $R_0=2.4$), under the full range of mask adherence and efficacy scenario [47].

References

- [1] “Questions and answers on COVID-19: Basic facts.” <https://www.ecdc.europa.eu/en/covid-19/questions-answers/questions-answers-basic-facts> (accessed Jan. 15, 2022).
- [2] K. Escandón *et al.*, “COVID-19 false dichotomies and a comprehensive review of the evidence regarding public health, COVID-19 symptomatology, SARS-CoV-2 transmission, mask wearing, and reinfection,” *BMC Infectious Diseases* 2021 21:1, vol. 21, no. 1, pp. 1–47, Jul. 2021, doi: 10.1186/S12879-021-06357-4.
- [3] M. Jayaweera, H. Perera, B. Gunawardana, and J. Manatunge, “Transmission of COVID-19 virus by droplets and aerosols: A critical review on the unresolved dichotomy,” *Environmental Research*, vol. 188, p. 109819, Sep. 2020, doi: 10.1016/J.ENVRES.2020.109819.
- [4] H. Tada, A. Nohara, and M. A. Kawashiri, “Controversy around airborne versus droplet transmission of respiratory viruses: implication for infection prevention,” *Curr Opin Infect Dis*, vol. 32, no. 4, pp. 300–306, Aug. 2019, doi: 10.1097/QCO.0000000000000563.
- [5] “Infection Prevention and Control of Epidemic and Pandemic Prone Acute Respiratory Infections in Healthcare – WHO Guidelines,” *World Health Organization (WHO)*, 2014.
- [6] “Guideline for Isolation Precautions: Preventing Transmission of Infectious Agents in Healthcare Settings.,” *Centers for Disease Control and Prevention (CDC)*, 2007.
- [7] “Transmission of SARS-CoV-2: implications for infection prevention precautions,” *World Health Organization (WHO)* , 2020.
- [8] E. and M. National Academies of Sciences, “Airborne Transmission of SARS-CoV-2: Proceedings of a Workshop—in Brief,” *Airborne Transmission of SARS-CoV-2*, Oct. 2020, doi: 10.17226/25958.

- [9] K. A. Prather, L. C. Marr, R. T. Schooley, M. A. McDiarmid, M. E. Wilson, and D. K. Milton, “Airborne transmission of SARS-CoV-2,” *Science* (1979), vol. 370, no. 6514, pp. 303–304, Oct. 2020, doi: 10.1126/SCIENCE.ABF0521.
- [10] N. Zhang, W. Chen, P. T. Chan, H. L. Yen, J. W. T. Tang, and Y. Li, “Close contact behavior in indoor environment and transmission of respiratory infection,” *Indoor Air*, vol. 30, no. 4, pp. 645–661, Jul. 2020, doi: 10.1111/INA.12673.
- [11] X. Xie, Y. Li, A. T. Y. Chwang, P. L. Ho, and W. H. Seto, “How far droplets can move in indoor environments--revisiting the Wells evaporation-falling curve,” *Indoor Air*, vol. 17, no. 3, pp. 211–225, Jun. 2007, doi: 10.1111/J.1600-0668.2007.00469.X.
- [12] L. Bourouiba, “Turbulent Gas Clouds and Respiratory Pathogen Emissions: Potential Implications for Reducing Transmission of COVID-19,” *JAMA*, vol. 323, no. 18, pp. 1837–1838, May 2020, doi: 10.1001/JAMA.2020.4756.
- [13] N. H. W. Loh *et al.*, “The impact of high-flow nasal cannula (HFNC) on coughing distance: implications on its use during the novel coronavirus disease outbreak,” *Canadian journal of anaesthesia = Journal canadien d’anesthésie*, vol. 67, no. 7, pp. 893–894, Jul. 2020, doi: 10.1007/S12630-020-01634-3.
- [14] N. H. L. Leung, “Transmissibility and transmission of respiratory viruses,” *Nature Reviews Microbiology* 2021 19:8, vol. 19, no. 8, pp. 528–545, Mar. 2021, doi: 10.1038/s41579-021-00535-6.
- [15] “Scientific Brief: SARS-CoV-2 Transmission | CDC.” <https://www.cdc.gov/coronavirus/2019-ncov/science/science-briefs/sars-cov-2-transmission.html> (accessed Jan. 15, 2022).
- [16] L. Zhou, S. K. Ayeh, V. Chidambaram, and P. C. Karakousis, “Modes of transmission of SARS-CoV-2 and evidence for preventive behavioral interventions,” *BMC Infectious Diseases*, vol. 21, no. 1, pp. 1–9, Dec. 2021, doi: 10.1186/S12879-021-06222-4/PEER-REVIEW.
- [17] P. Mecnas, R. T. da Rosa Moreira Bastos, A. C. Rosário Vallinoto, and D. Normando, “Effects of temperature and humidity on the spread of COVID-19:

- A systematic review,” *PLOS ONE*, vol. 15, no. 9, p. e0238339, Sep. 2020, doi: 10.1371/JOURNAL.PONE.0238339.
- [18] N. H. L. Leung, “Transmissibility and transmission of respiratory viruses,” *Nature Reviews Microbiology* 2021 19:8, vol. 19, no. 8, pp. 528–545, Mar. 2021, doi: 10.1038/s41579-021-00535-6.
- [19] V. Stadnytskyi, C. E. Bax, A. Bax, and P. Anfinrud, “The airborne lifetime of small speech droplets and their potential importance in SARS-CoV-2 transmission,” *Proceedings of the National Academy of Sciences*, vol. 117, no. 22, pp. 11875–11877, Jun. 2020, doi: 10.1073/PNAS.2006874117.
- [20] P. Anfinrud, V. Stadnytskyi, C. E. Bax, and A. Bax, “Visualizing Speech-Generated Oral Fluid Droplets with Laser Light Scattering,” *New England Journal of Medicine*, vol. 382, no. 21, pp. 2061–2063, May 2020, doi: 10.1056/NEJMC2007800/SUPPL_FILE/NEJMC2007800_DISCLOSURES.PDF.
- [21] P. Bahl, C. Doolan, C. de Silva, A. A. Chughtai, L. Bourouiba, and C. R. MacIntyre, “Airborne or Droplet Precautions for Health Workers Treating Coronavirus Disease 2019?,” *The Journal of Infectious Diseases*, Apr. 2020, doi: 10.1093/INFDIS/JIAA189.
- [22] J. A. Lednicky *et al.*, “Viable SARS-CoV-2 in the air of a hospital room with COVID-19 patients,” *International Journal of Infectious Diseases*, vol. 100, pp. 476–482, Nov. 2020, doi: 10.1016/J.IJID.2020.09.025/ATTACHMENT/621CA6E7-EEC4-4C08-998A-9C3C997A3FB4/MMC1.DOCX.
- [23] J. L. Santarpia *et al.*, “The Infectious Nature of Patient-Generated SARS-CoV-2 Aerosol,” *medRxiv*, p. 2020.07.13.20041632, Jul. 2020, doi: 10.1101/2020.07.13.20041632.
- [24] M. A. Baker *et al.*, “Low Risk of Coronavirus Disease 2019 (COVID-19) Among Patients Exposed to Infected Healthcare Workers,” *Clinical Infectious Diseases*, vol. 73, no. 7, pp. e1878–e1880, Oct. 2021, doi: 10.1093/CID/CIAA1269.

- [25] N. Bedrosian *et al.*, “A Systematic Review of Surface Contamination, Stability, and Disinfection Data on SARS-CoV-2 (Through July 10, 2020),” *Environmental Science and Technology*, vol. 55, no. 7, pp. 4162–4173, Apr. 2021, doi: 10.1021/ACS.EST.0C05651/SUPPL_FILE/ES0C05651_SI_004.XLSX.
- [26] W. C. Koh *et al.*, “What do we know about SARS-CoV-2 transmission? A systematic review and meta-analysis of the secondary attack rate and associated risk factors,” *PLOS ONE*, vol. 15, no. 10, p. e0240205, Oct. 2020, doi: 10.1371/JOURNAL.PONE.0240205.
- [27] X. S. Zhang and C. Duchaine, “SARS-CoV-2 and health care worker protection in low-risk settings: A review of modes of transmission and a novel airborne model involving inhalable particles,” *Clinical Microbiology Reviews*, vol. 34, no. 1, pp. 1–29, Oct. 2020, doi: 10.1128/CMR.00184-20/ASSET/B9C4EA72-E5B3-4DC1-A66E-624CD35CA594/ASSETS/GRAPHIC/CMR.00184-20-F0001.JPEG.
- [28] “WHO Coronavirus (COVID-19) Dashboard | WHO Coronavirus (COVID-19) Dashboard With Vaccination Data.” <https://covid19.who.int/> (accessed Jan. 15, 2022).
- [29] “COVID-19 Vaccines Advice.” <https://www.who.int/emergencies/diseases/novel-coronavirus-2019/covid-19-vaccines/advice> (accessed Jan. 15, 2022).
- [30] “Advice for the public.” <https://www.who.int/emergencies/diseases/novel-coronavirus-2019/advice-for-public> (accessed Jan. 15, 2022).
- [31] “Coronavirus disease (COVID-19): Masks.” <https://www.who.int/emergencies/diseases/novel-coronavirus-2019/question-and-answers-hub/q-a-detail/coronavirus-disease-covid-19-masks> (accessed Jan. 15, 2022).
- [32] T. Oberg and L. M. Brosseau, “Surgical mask filter and fit performance,” *Am J Infect Control*, vol. 36, no. 4, pp. 276–282, May 2008, doi: 10.1016/J.AJIC.2007.07.008.

- [33] *BS EN 14683:2019: Medical face masks - Requirements and test methods.* European Committee for standardization.
- [34] “How Surgical Masks are Made, Tested and Used.” https://www.thomasnet.com/articles/other/how-surgical-masks-are-made/#_Types_of_Masks (accessed Jan. 15, 2022).
- [35] S. Verma, M. Dhanak, and J. Frankenfield, “Visualizing the effectiveness of face masks in obstructing respiratory jets,” *Physics of Fluids*, vol. 32, no. 6, Jun. 2020, doi: 10.1063/5.0016018.
- [36] J. T. J. Ju, L. N. Boisvert, and Y. Y. Zuo, “Face masks against COVID-19: Standards, efficacy, testing and decontamination methods,” *Advances in Colloid and Interface Science*, vol. 292, p. 102435, Jun. 2021, doi: 10.1016/J.CIS.2021.102435.
- [37] L. J. Radonovich *et al.*, “N95 Respirators vs Medical Masks for Preventing Influenza Among Health Care Personnel: A Randomized Clinical Trial,” *JAMA*, vol. 322, no. 9, pp. 824–833, Sep. 2019, doi: 10.1001/JAMA.2019.11645.
- [38] Y. Cheng *et al.*, “Face masks effectively limit the probability of SARS-CoV-2 transmission”, Accessed: May 01, 2022. [Online]. Available: www.freeicons.io,
- [39] “Using face masks in the community - Reducing COVID-19 transmission from potentially asymptomatic or pre-symptomatic people through the use of face masks.” <https://web.archive.org/web/20200408134120/https://www.ecdc.europa.eu/en/publications-data/using-face-masks-community-reducing-covid-19-transmission> (accessed Jan. 15, 2022).
- [40] “Types of Masks and Respirators | CDC.” <https://www.cdc.gov/coronavirus/2019-ncov/prevent-getting-sick/types-of-masks.html> (accessed Jan. 15, 2022).
- [41] “Advice on the use of masks in the context of COVID-19: interim guidance, 6 April 2020.” <http://apps.who.int/iris/handle/10665/331693> (accessed Jan. 15, 2022).

CHAPTER 5

- [42] “Advice on the use of masks in the community, during home care, and in health care settings in the context of COVID-19: interim guidance, 19 March 2020.” <http://apps.who.int/iris/handle/10665/331493> (accessed Jan. 15, 2022).
- [43] “Advice on the use of masks in the community, during home care and in health care settings in the context of the novel coronavirus (2019-nCoV) outbreak: interim guidance, 29 January 2020.” <http://apps.who.int/iris/handle/10665/330987> (accessed Jan. 15, 2022).
- [44] “Advice on the use of masks in the community, during home care and in healthcare settings in the context of the novel coronavirus (COVID-19) outbreak.” [https://www.who.int/publications/i/item/advice-on-the-use-of-masks-in-the-community-during-home-care-and-in-healthcare-settings-in-the-context-of-the-novel-coronavirus-\(2019-ncov\)-outbreak](https://www.who.int/publications/i/item/advice-on-the-use-of-masks-in-the-community-during-home-care-and-in-healthcare-settings-in-the-context-of-the-novel-coronavirus-(2019-ncov)-outbreak) (accessed Jan. 15, 2022).
- [45] “Gazzetta Ufficiale.” <https://www.gazzettaufficiale.it/eli/id/2020/04/27/20A02352/sg> (accessed Jan. 15, 2022).
- [46] “#Masks4All: Cloth masks can help stop the spread of COVID-19, save lives and restore jobs.” <https://masks4all.co/> (accessed Jan. 15, 2022).
- [47] L. Tian *et al.*, “Calibrated Intervention and Containment of the COVID-19 Pandemic,” Mar. 2020, Accessed: Jan. 20, 2022. [Online]. Available: <https://arxiv.org/abs/2003.07353v6>

CHAPTER 6

Surgical face masks

Surgical masks, also called procedural masks, are rectangular-shaped, medical, loose-fitting, disposable devices, designed to:

- mainly protect the patients from infectious splashes and respiratory droplets emitted by healthcare workers;
- protect the wearer against splashes of potentially contaminated liquid;
- be worn by patients to reduce the risk of spread of infections.

Before 2020, the use of surgical masks in Western countries was mainly limited to the healthcare field and half of the total production was accountable to China. In the early 2020, due to the Covid-19 pandemic outbreak, surgical face masks became an essential non-pharmaceutical intervention to limit the spread of the disease and their request skyrocketed to unprecedented levels. To address the consequent shortage, several private and public companies started reconverting their production towards surgical masks, but their efforts were partially nullified mainly by the shortage of raw materials, the absence of appropriate production plants and the poor knowledge about surgical masks properties and requirements. Even if surgical masks are basic and relatively cheap products, their production requires the assembly of different parts in a relatively sophisticated process, along with several types of inputs. In addition, they should comply to specific regulations. In Europe, the regulation EN

14683:2019 provides for all the tests that should be performed for the certification of these devices.

In this chapter the tests stated by the EN standard will be analysed in detail, to understand which are the most important parameters that should be taken into account in evaluating the performance of a surgical mask and how they are measured. Finally, these parameters will be related to the materials and to the production processes typically employed in surgical masks fabrication, to evaluate their influence on the performance.

6.1 European regulation, tests and classification

Surgical masks for the European market, whether they are produced or imported, should comply to the European regulation EN 14683:2019, “*Medical face masks – Requirements and test methods*”, which specifies construction, design, performance requirements and test methods [1]. This regulation refers also to other documents:

- EN ISO 10993-1:2009, “*Biological evaluation of medical devices – Part 1: Evaluation and testing within a risk management*”;
- EN ISO 11737-1:2018, “*Sterilization of health care products – Microbiological methods – Part 1: Determination of a population of microorganisms on products*” [2];
- ISO 22609:2004, “*Clothing for protection against infectious agents – Medical face masks – Test method for resistance against penetration by synthetic blood (fixed volume, horizontally projected)*” [3].

Table 6.1 summarizes all the tests prescribed.

The differential pressure test, also called “breathability test”, is a measure of the resistance to respiration caused by the surgical mask, which affects the comfort of the end user. Indeed,

the regulation establishes that the maximum pressure drop caused by a surgical mask sample should be lower than 60 Pa/cm².

Table 6.1: Performance requirements for medical face masks [1].

Test	Type I ^a	Type II	Type IIR
Bacterial filtration efficiency (BFE), (%)	≥ 95	≥ 98	≥ 98
Differential pressure (Pa/cm ²)	< 40	< 40	< 60
Splash resistance pressure (kPa)	Not required	Not required	≥ 16,0
Microbial cleanliness (cfu/g)	≤ 30	≤ 30	≤ 30

The bacterial filtration efficiency test (BFE) evaluates its performance in filtering infectious droplets and aerosols that may be spread on inhaled by the wearer. According to the BFE, surgical masks can be classified as [1]:

- Type I: with a BFE between 95% and 98%, should only be used for patients and other persons to reduce the risk of spread of infections;
- Type II and type IIR: have a BFE not lower than 98% and are intended for use by healthcare professionals.

Healthcare workers involved in treating individuals injured or sick, can be exposed to biological liquids (blood or body fluids) capable of transmitting diseases, such as blood-borne viruses that can cause hepatitis and acquired immune deficiency syndrome (AIDS). In case of potential danger, Type IIR surgical masks should be used. These masks shall be subjected to an additional test, the splash resistance, that is a qualitative estimation of the protection of the healthcare worker lips and nose from exposure to blood and body fluids.

The microbial cleanliness is a quantitative evaluation of the microbes present on the masks before the first use and not a quantitative evaluation of their performance as a non-pharmaceutical measure to limit the spread of respiratory infections. Indeed, the microbial cleanliness will be no further discussed.

6.1.1 Differential pressure

The differential pressure, also called “breathability” or “breathing resistance”, is a test used to determine the resistance of airflow through the facemask: the lower is the value, the easier is the breathing by the end user, which turns in a higher confort level.

Figure 6.1 shows the apparatus for the test. A circular sample with a diameter of 25 mm is crossed by a constant airstream of 8 L/min, with the airflow direction from the inner layer to the outer layer of the masks. A differential manometer (or two manometers, M1 and M2) measures the difference in airflow pressure expressed in Pa, $X_{M1} - X_{M2}$, at the inlet and at the outlet of the sample. The breathability of the samples is obtained by dividing the differential pressure for the area of the sample, equal to 4.9 cm²:

$$\Delta P = \frac{X_{M1} - X_{M2}}{4.9} \quad (6.1)$$

For each mask specimen, 5 differet areas should be tested and the readings averaged. The average value for each test specimen is then used to determine the final classification. At least 5 specimens should be tested, or a greater number allowing for an Acceptable Quality Level (AQL) of 4%. In addition, all the specimens should be conditioned by exposure to a room temperature of $(21 \pm 5)^{\circ}C$ and a relative humidity of $(85 \pm 5)\%$ for at least 4 hours before the tests, to simulate the conditions of use when the wearer breath through the mask.

Type I and type II surgical masks should cause a pressure drop lower than 40 Pa/cm², while for type IIR a higher pressure drop is granted, to allow the use of thicker layers which increases the protection against blood splashes.

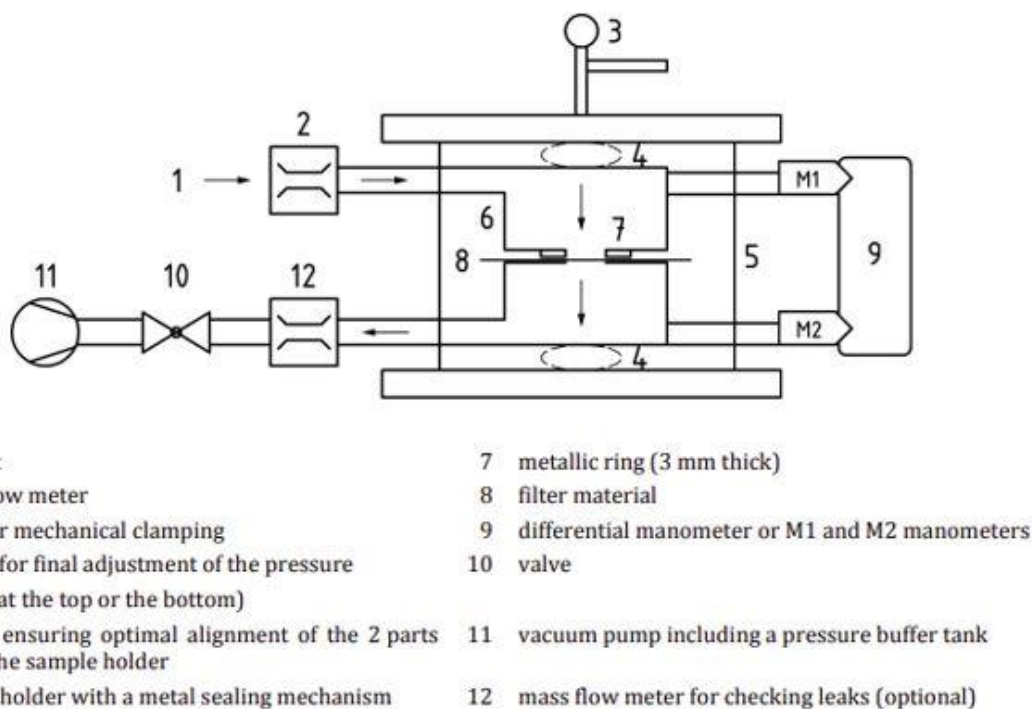


Figure 6.1: test apparatus for measuring the differential pressure [1].

6.1.2 Bacterial filtration efficiency in vitro (BFE)

This test method is designed for measuring the ability of surgical masks to filtrate infectious droplets and aerosols. Figure 6.2 illustrates the test apparatus.

The use of *Staphylococcus Aureus* as challenge organism is based on its clinical relevance as a leading cause of nosocomial infections [4]. The bacterial challenge aerosol mixes with an airstream flowing inside the cylinder at 28.3 L/min. Mask specimen (minimum dimension 100 mm x 100 mm) is placed at the end of a cylindrical glass tube, having an internal diameter of 80 mm and a length of 600 mm. A pressure driven nebulizer injects at the top of the glass chamber a *Staphylococcus Aureus* solution aerosol with a mean particle size (MPS) of $3.0 \pm 0.3 \mu\text{m}$.

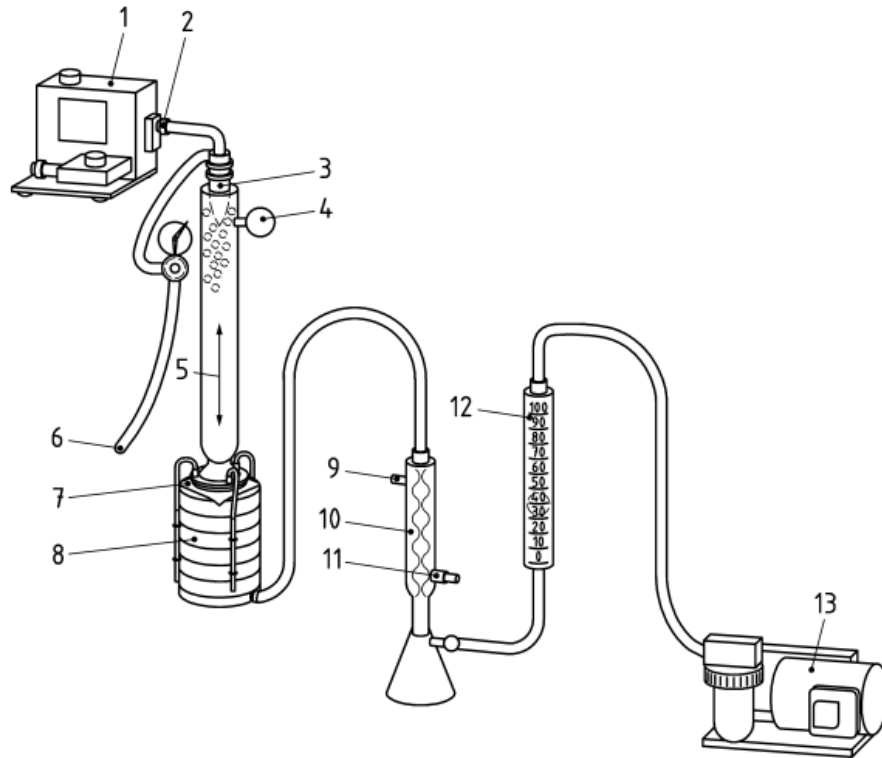


Figure 6.2: Apparatus for the evaluation of the BFE [1].

The resulting two-phase mixture flows through the specimen, which retain a fraction of the droplets and aerosols depending on its filtration efficiency. The permeating particles are then collected in a 6-stages Andersen cascade impactor. Each stage, characterized by its nominal cut-off diameter, is constituted by a tryptic soy agar culture plate placed under a stainless steel 316L surface with 400 drilled holes. It collects particles according to their aerodynamic diameter, as shown in figure 6.3. The dimensions of the holes set the velocity of the airstream transporting the particles: if the liquid particle diameter is larger than the stage cut-off size, the particle is not able to follow the airstream and impacts on the culture plate, if it is smaller it is carried to the next stage. Particles smaller than $0.65 \mu m$ cannot be collected by the impactor indeed, to avoid the dispersion of these fine particles in the environment, the air stream is cooled down by the means of a condenser and is forced to pass through a vacuum trap.

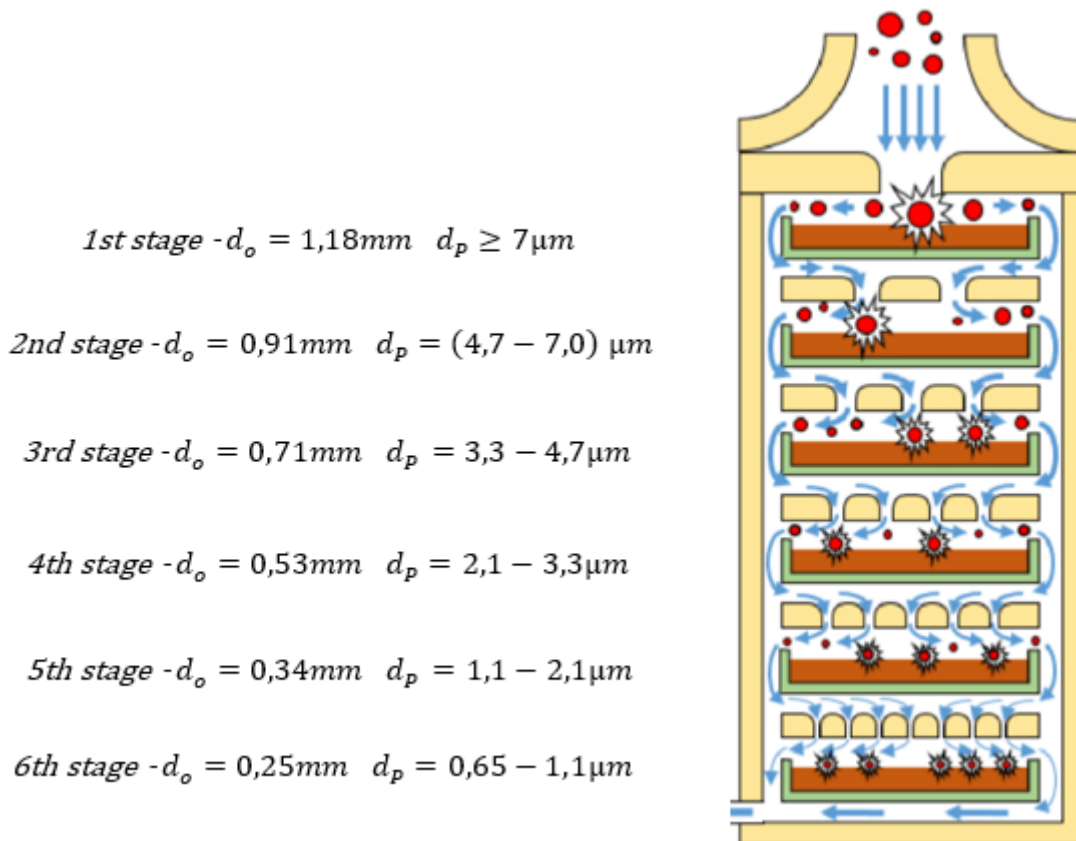


Figure 6.3: Andersen 6-stages impactor

The test of each specimen takes two minutes: the bacterial challenge is delivered inside the apparatus, along with the airflow, for 1 minute and then only air is fluxed for an additional minute, to remove all the particles present in the system. At the end, the culture plates are removed from the impactor and incubated at $(37 \pm 2) ^\circ\text{C}$ for (20 to 52) h. During the incubation the collected cells multiply into colonies, as shown in figure 6.4. After the incubation the resulting colonies (colonies forming units, CFU) present on each plate are counted. To start a new test, the culture plates should be replaced with new ones.

The observed number of CFU of each plate “i” ($\text{CFU}_{c,i}$), should be adjusted for the probability that more than one viable particle was collected through a sampling hole and merged with other microorganisms at an impaction site to produce a single colony [5].

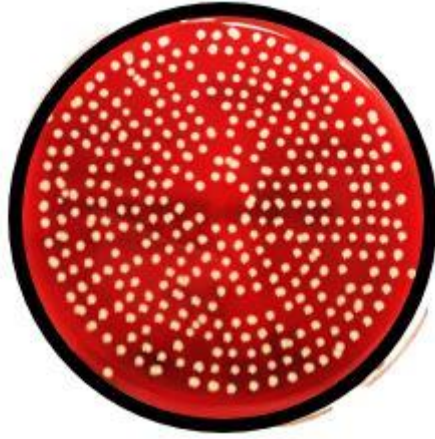


Figure 6.4: Example of culture plate from stage 4th of the impactor, after 24 h of incubation

This is done by using a “positive-hole correction table” (provided by Andersen [6]), which is based on the principle that as the number of viable particles impacting on a plate increases, the probability of particles entering unoccupied holes decreases. For each counted CFU number ($CFU_{c,i}$), the table provides the number of the most probable real number of CFU ($CFU_{r,i}$). The values were calculated using the equation 6.2, where N is the total number of holes per stage (400):

$$CFU_{r,i} = N \left[\frac{1}{N} + \frac{1}{N-1} + \frac{1}{N-2} + \dots + \frac{1}{N - CFU_{c,i} + 1} \right] \quad (6.2)$$

A graphical representation of the positive-hole conversion table is provided in figure 6.5. According to the regulation, the positive-hole conversion should be applied only to stages from 3 to 6 and the total number of colonies collected by the impactor during a test (CFU_T) is given by the sum of the number of CFU on each plate, as reported in equation 6.3:

$$CFU_T = \sum_{i=3}^6 CFU_{r,i} \quad (6.3)$$

To completely test a surgical mask, 5 specimens are needed and the procedure illustrated in table 6.2 should be followed. All the specimens should be conditioned by exposure to a room

temperature of $(21 \pm 5)^\circ\text{C}$ and a relative humidity of $(85 \pm 5)\%$ for at least 4 hours before the test, to simulate the conditions of use when the wearer breaths through the mask.

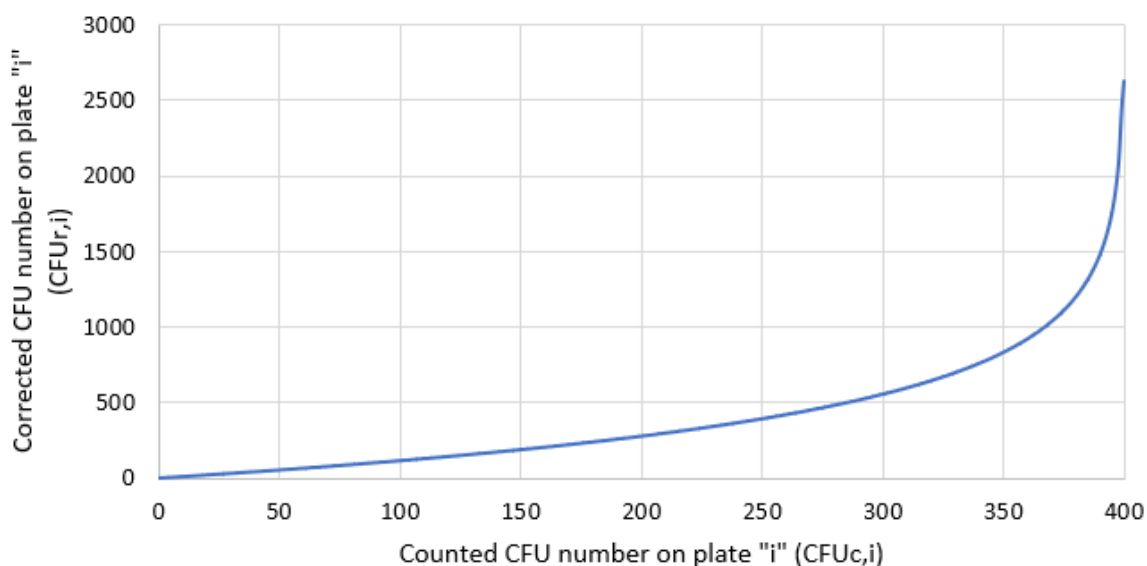


Figure 6.5: graphical representation of the positive-hole conversion table.

In the positive control runs the test is performed in absence of the mask specimen. Indeed, due to the absence of filtering media, all the infectious particles entering the glass chamber reach the impactor and are collected. The aim of positive control runs is to evaluate the number of CFU entering the system and to verify that it is constant over the entire procedure. This number, CFU_{PC} , is the mean of the two positive control runs:

$$CFU_{T,PC} = \frac{CFU_{T,PC1} + CFU_{T,PC2}}{2} \quad (6.4)$$

The dilution of the bacterial challenge should be adjusted to have a number of CFU in the two positive control runs between 1700 and 3000. From these values is also possible to verify the mean particle size.

In the negative control run the test is performed in absence of the mask specimen and of the bacterial challenge. The aim is to verify the absence of contaminations in the system, which may invalidate the results. Since no bacteria are delivered to the system, the number of CFU

should be zero. The aim of the test is to verify the mask bacterial filtration efficiency (BFE), indeed the portion of CFU permeated through the sample compared to those collected by the impactor in the absence of the filtering media. This value is calculated as:

$$BFE_j = \frac{CFU_{T,PC} - CFU_{T,j}}{CFU_{T,PC}} \cdot 100 \quad (6.5)$$

For type I surgical masks, the BFE of all the 5 specimens should be equal or higher than 95%, while for type II and type IIR, it should be equal or higher than 98%.

Table 6.2: Procedure for testing a surgical mask. BC: nebulized bacterial challenge; AF: airflow at 28.3 L/min.

Test n°	Test name	Procedure	Specimen n°
1	Positive control run 1 (PC1)	1 min (BC+AF) + 1 min. (AF)	No specimen
2	Test specimen 1 (S1)	1 min (BC+AF) + 1 min. (AF)	Specimen 1
3	Test specimen 2 (S2)	1 min (BC+AF) + 1 min. (AF)	Specimen 2
4	Test specimen 3 (S3)	1 min (BC+AF) + 1 min. (AF)	Specimen 3
5	Test specimen 4 (S4)	1 min (BC+AF) + 1 min. (AF)	Specimen 4
6	Test specimen 5 (S5)	1 min (BC+AF) + 1 min. (AF)	Specimen 5
7	Positive control run 2 (PC2)	1 min (BC+AF) + 1 min. (AF)	No specimen
8	Negative control run (NC)	2 min. (AF)	No specimen

6.1.3 Resistance against splashes of synthetic blood – Splash test

The splash test evaluates the resistance of medical masks to the penetration by 2 mL of synthetic blood hitting the mask external surface at high velocity [3]. To help simulate the density and the wetting characteristics of blood and fluids, the surface tension of the

synthetic blood should be $(0.042 \pm 0.002) N/m$ and its density $1.005 g/mL$. The apparatus for the splash test is shown in figure 6.6.

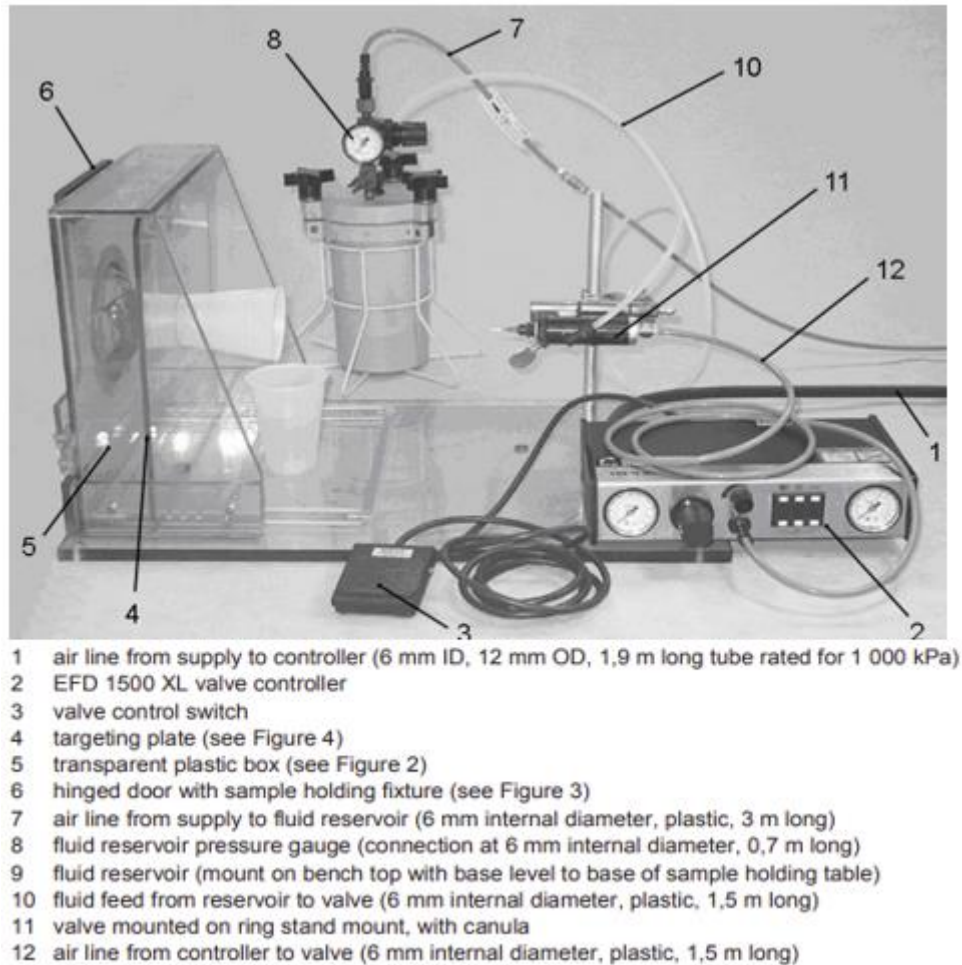


Figure 6.6: Splash test apparatus [1, 3].

A pressure-driven syringe, equipped with a 12.7 mm long canula having an inside diameter of 0.84 mm, is placed at 300 mm from the surgical mask and it squirts on the mask 2 mL of synthetic blood. An instrument (EFD 1500 XL valve controller in figure 6.6) allows to set the desired pressure and splash time. The regulation indicates three test relative pressures (10.6 kPa, 16.0 kPa and 21.3 kPa) while the splash time should be properly set to deliver the required amount of synthetic blood. The knowledge of these values allows the calculation of the velocity of the fluid, that simulate that of blood exiting an artery in a clinical setting, by

applying the Bernoulli equation at the inside of the blood vessel (location 1) and at the exit of the canula (location 2):

$$\frac{p_1}{\rho_1} + \frac{v_1^2}{2g} + z_1 = \frac{p_2}{\rho_1} + \frac{v_2^2}{2g} + z_2 \quad (6.6)$$

Where:

- p_1 and p_2 are the pressures;
- ρ_1 is the density of the synthetic blood;
- v_1 and v_2 are the velocities;
- z_1 and z_2 are the heights respect to a plane;
- g is the gravitational acceleration.

Several assumptions are made to simplify the Bernoulli equation and its application to this situation:

- The velocity of the fluid inside the vessel (v_1) is much lower compared to the one at the end of the canula (v_2), thus v_1 can be neglected;
- The height of the fluid inside the vessel (z_1) and at the exit of the canula (z_2) are the same, thus the terms for height can be both neglected;
- The frictional losses between the inside and the outside of the syringe can be neglected;
- Because of the short distances (300 mm), the frictional loss of the stream in air can be neglected, therefore the velocity at which the fluid hits the mask surface can be considered equal to that at which it exits the canula.

By rearranging the equation 6.6 and considering the gauge pressure in a free stream of fluid in air equal to zero, the velocity at which the synthetic blood impacts the masks can be calculated by equation 6.7:

$$v_2 = 137.59 \sqrt{p_1} \quad (6.7)$$

The resulting velocity for each test pressure is reported in table 6.4.

Table 6.4: velocity of the synthetic blood ejected from the syringe

Pressure [kPa]	Velocity [cm/s]	Velocity rounded to nearest 5 cm/s [cm/s]
10.6	447.96	450
16.0	550.36	550
21.3	635.00	635

The velocity of the fluid can be written also as:

$$v_2 = \frac{Q}{t \cdot A} \quad (6.8)$$

Where:

- Q is the volume of synthetic blood that should be splashed;
- t is the splash time;
- A is the cross-sectional area of the canula orifice.

The cross-sectional area of the orifice is given by:

$$A = \frac{\pi \cdot d^2}{4} \quad (6.9)$$

Where d is the diameter of the orifice. Equations 6.8 and 6.9 can be combined and rearranged to calculate the splash time:

$$t = \frac{4Q}{v \cdot \pi \cdot d^2} \quad (6.10)$$

Table 6.5 reports the splash time and the velocity of the fluid corresponding to each test pressure indicated by the regulation.

Table 6.5: Pressure and splash time.

Pressure (kPa)	Fluid velocity (cm/s)	Splash time (s)
10.6	447.96	450
16.0	550.36	550
21.3	635.00	635

The splash test should be performed on a number of specimens sufficient to achieve an acceptable quality limit (AQL) of 4.0 %. All the specimens should be conditioned by exposure to a room temperature of $(21 \pm 5)^{\circ}\text{C}$ and a relative humidity of $(85 \pm 5)\%$ before the tests, to simulate the conditions of use when the wearer breaths through the mask. After the test, the samples undergo to a visual analysis and results are reported as “pass/fail”: any evidence of synthetic blood penetration on the inner layer constitutes failure. The mask is finally rated at the highest corresponding blood pressure for which its specimens demonstrated an AQL of 4.0. Type IIR surgical mask should be rated for a pressure of at least 16 kPa.

6.2 Mechanism of filtration

Surgical masks use nonwoven fibrous filter media, made by micrometric fibres that crisscross to form a web with a porosity high enough to grant a sufficient breathability [7]. The most of respiratory droplets and aerosols have a dimension much smaller compared to the pores of the filter. Indeed, the filtration of these particles is achieved not only by sieving, but mainly through the combination of other mechanisms, which are reported in figure 6.7 and can be classified as follows [8]:

- Gravity sedimentation
- Inertial impaction;

- Interception
- Diffusion
- Electrostatic attraction.

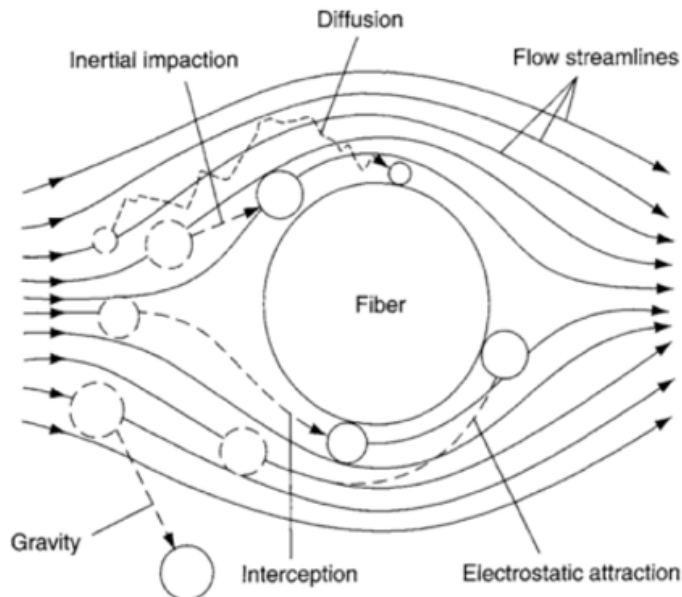


Figure 6.7: Main mechanisms of filtration [8].

Gravity sedimentation is a phenomenon affecting larger respiratory droplets. The motion of these particles, due to their size, is mostly governed by the ballistic energy or by the gravity force which prevents them to follow the airstream. As a consequence, they settle onto the filter fibres [8]. According to Konda *et al.* inertia and gravity can be the dominant mechanisms for size larger than $1\ \mu\text{m}$ [9]. Particles of around $1\ \mu\text{m}$ or grater may be effectively removed also by inertial impaction [10]. While flowing with the airstream around the mask fibres, the inertia of these particles becomes too large inducing changes in the direction with respect to the airflow. As consequence, the particles stray from the air streamlines, collide with the fibres and adhere to them [11]. However, the effect of inertial impaction in capturing ultrafine and nanoparticles is negligible [12]. Interception occurs when a particle following the primary streamline passes close to a fibre. If the distance between the centre of the particle and the fibre surface is lower than the particle radius, the

particle is intercepted. This method is successful in filtering particles from $0.2\ \mu\text{m}$ up to $0.6\ \mu\text{m}$ [13].

For particles smaller than $0.2\ \mu\text{m}$, diffusion is the prevailing trapping mechanism. These particles follow a random Brownian motion, bouncing into the filter media. The abnormal motion raises the probability of collision between particles and fibre [13]. The rate of diffusion increases as particle size and superficial velocity decrease: a lower velocity means a higher residence time and, in turn, a higher probability of collision [11]. Of the above-mentioned mechanical filtration mechanisms, diffusion and interception are the most dominant for sub-micrometre particles. However, there is a range of particles size of $0.2\text{--}0.5\ \mu\text{m}$ in which these two mechanisms are less effective. This is true in particular for $300\ \text{nm}$ particles, that represents the most penetrating particle size (MPPS) [14], as shown in figure 6.8a. To fill in this gap, most of the nonwoven filters for surgical masks are electrically charged and are called electrets.

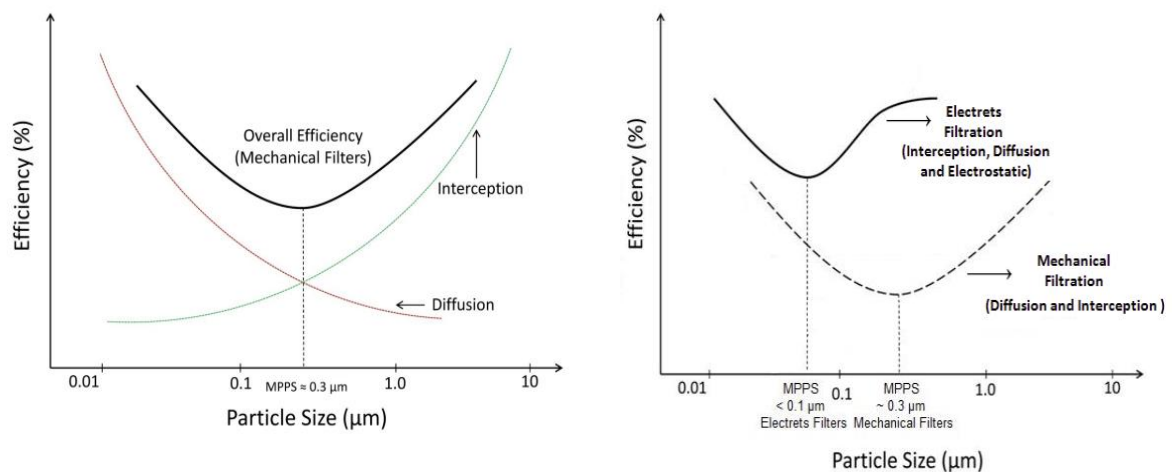


Figure 6.8: MPPS and qualitative variation of the filtration efficiency as a function of the particle size. a) mechanical filter; b) electrets [16].

As for diffusion, high velocity negatively affects the filtration efficiency of electrostatic attraction. Richardson *et al.* analysed the effect of the flow rate on the percentage of penetration of particles of different size for an electret. The results, shown in figure 6.9, confirm that the penetration rate increases with the air velocity. However, the experiments

were performed at constant flow and do not reflect the real conditions in which the human breathing follows a cyclic pattern [15].

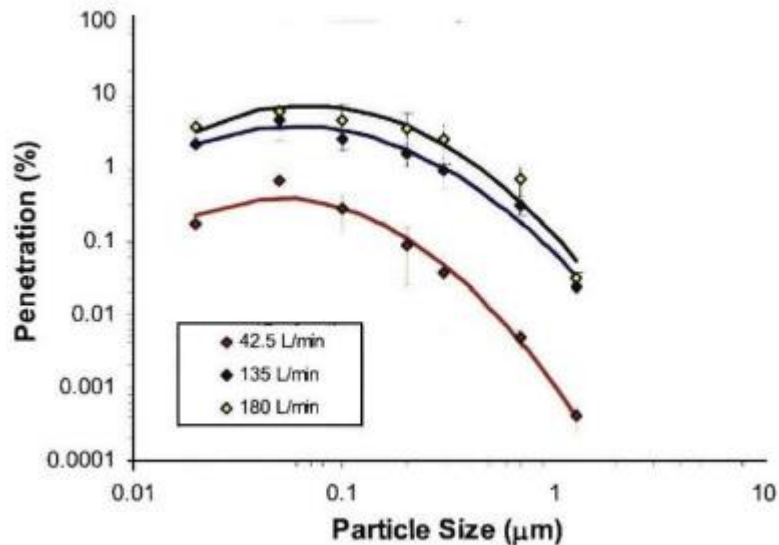


Figure 6.9: Penetration of particles through an electret according to their size and air flowrate [15].

6.3 Materials, properties and manufacturing processes

Surgical masks are rectangular-shaped devices usually composed by three layers: an inner absorbent layer, an external hydrophobic layer and a highly efficient filter placed between the two. To be classified as surgical mask, the materials employed should provide to the device all the characteristics required by the corresponding regulation [1]:

- High bacterial filtration efficiency;
- Low pressure drops;
- Resistance against liquid body splashes;
- Mechanical, thermal and chemical resistance high enough that it shall not disintegrate, split or tear during the intended use;

- Non-toxic and non-flammable.

Medical face masks layers are usually made of nonwoven fabrics, which are preferred to woven or knit fabrics. This is due to their natural randomness and three-dimensional structure that increases for the particles both the probability of being caught and the distance to travel, leading to higher filtration efficiency [16]. Indeed, the required characteristics of the masks entirely depends on the nonwoven layers properties (such as the fibres size and the web structure), which in turn are affected by the raw materials and the manufacturing techniques. Meltblowing and spunbonding are the most widely used processes to manufacture the nonwoven fabric used for surgical masks [17]. The resulting fabrics, called meltblown and spunbond respectively, are usually made of polypropylene: the former is employed as filter while the latter as external layers.

6.3.1 Nonwoven fabrics properties and raw materials

The properties of a nonwoven fabric mainly depend on the characteristics of the fibres and in the way they are produced and arranged to form the filter [18].

Among all the fibre characteristics, the parameters that mainly affect the bacterial filtration efficiency and the breathability of a nonwoven fabric is the fibre diameter. Fibres with the smallest diameter possible have a high area to volume ratio. In addition, they lead to a more compact web structure and to a more tortuous pathway through which the particles should flow, enhancing the probability to capture also fine droplets and aerosols by diffusion and interception [17]. However, the resulting fabric structure increases not only the filtration efficiency of the fabric, but also the resistance to the air flow (breathability).

The fibres diameter, along with their density, also affect two parameters that are widely used to characterize a nonwoven fabric: the porosity decreases with the diameter, while the bulk density increases. The bulk density, also called packing density, is the mass per unit volume of the fabric and is usually expressed in g/m^3 . By dividing the bulk density for the fabric thickness another parameter, called basis weight or grammage, can be calculated. The porosity is the fraction of void volume and can be estimated as the ratio between the density of the package and that of the fibres.

Two additional important characteristics of a nonwoven fabric for surgical masks production are the wettability and mechanical resistance. The former mainly depends on the fibres surface chemistry, which should provide the highest possible hydrophobicity to protect the wearer from large droplets and splashes. The inner layer represents an exception, since it should be able to absorb expelled fluid and helps to reduce the humidity inside the mask [19]. The mechanical resistance depends on the fibre diameter and, indeed, on the manufacturing process.

Depending on the desired properties, the nonwoven fabrics can be made by natural fibres (such as cotton or silk), synthetic fibres or by a mixture of the two. Synthetic fibres are usually preferred, since they are cheaper and provide a more homogeneous final product. Common polymers for the production of synthetic fibres are rayon, polyolefins, polyesters and nylon. Among those, isotactic polypropylene is the most used because it is cheap, highly hydrophobic and lightweight. Moreover, it provides the highest yields (fibres per kilogram) and has a melting temperature and a melt viscosity low enough to be easily processed into fibres of different size for the fabrics production [17], [20]. To achieve different properties, a mixture of synthetic and natural fibres is used. This is the case of the inner fabric layer that, unlike the external and mid layers, should be able to absorb large respiratory droplets exhaled by the wearer.

6.3.2 Manufacturing processes

There is a large number of processes for the manufacturing of nonwoven fabrics. The most used are meltblowing and spunbonding. The resulting fabrics originate their name from the production process and have different properties. Meltblowns are usually employed as filters because of their high filtration efficiency, which mostly derives from the smaller fibres. Spunbonds have larger fibres, a lower filtration efficiency and a higher breathability compared to meltblowns, indeed they are usually employed as external layers. Figure 6.10a shows the fibres diameter difference between internal and external layers. Spunbonds and meltblowns can be thermally bonded to form a composite web that combine good mechanical resistance and high filtration efficiency. The most typical combination for surgical masks is the SMS, reported in figure 6.10b.

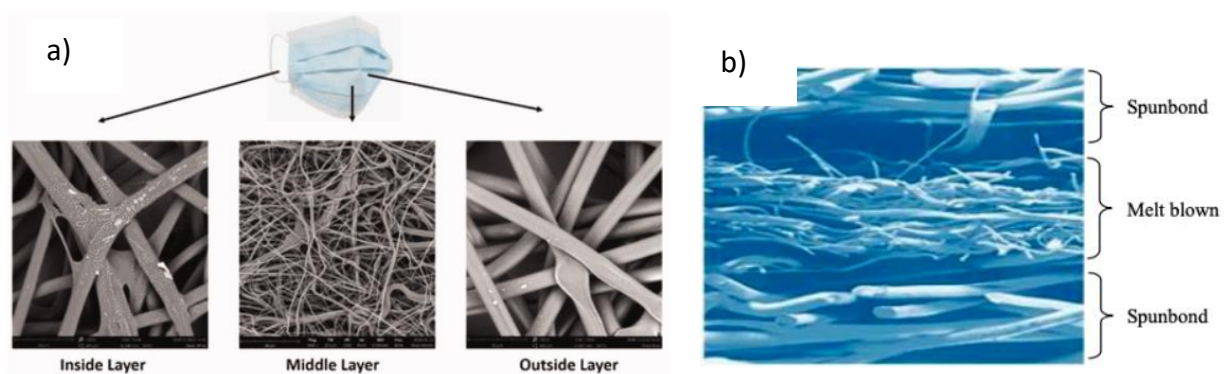


Figure 6.10: a) typical surgical masks composition; b) SMS composite web

To enhance the filtration efficiency without affecting the breathability, nonwoven fabric involved in surgical masks production can be electrostatically charged by additional processes, among which the most used is the Corona discharge method. These products, called “electrets”, are mainly meltblown.

Electrets can be directly produced by electrospinning, a technique able to produce nonwoven fabric with nanometric charged fibres.

6.3.3 Meltblowing

The meltblown process is shown in figure 6.11. The polymer is fed to a rotating single-screw heated extruder where it is melted. The molten polymer is then filtered and pumped to a die assembly, where hot and high-velocity air blows the fibres extruded by hundreds of small nozzles. Depending on the nozzles' diameter, on the polymer viscosity and on the temperature and velocity of the air, fibres with diameter in the range $(0.5 - 30) \mu\text{m}$ can be obtained. Those for surgical masks fabrics typically have a diameter in the range $(0.5 - 30) \mu\text{m}$. The resulting fibres, still kept in the molten state by the primary air, starts to entangle and are than rapidly cooled down by a secondary high-velocity turbulent airstream which also increases the degree of entanglement. The solid fibres are then collected on screen or on a rotating drum, where they form a low-crystallinity web that is finally wind-up. However, for some applications, the fabric can be further treated. A typical additional treatment for the fabrics used as filters of surgical masks is the electrical charge to form electrets. Pu *et al.* tried to apply an electrostatic field directly to the meltblown spinning head. The process, called electrostatic-assisted meltblown (ESAMB), led to smaller fibres and, as consequence, to higher filtration efficiency and pressure drops.

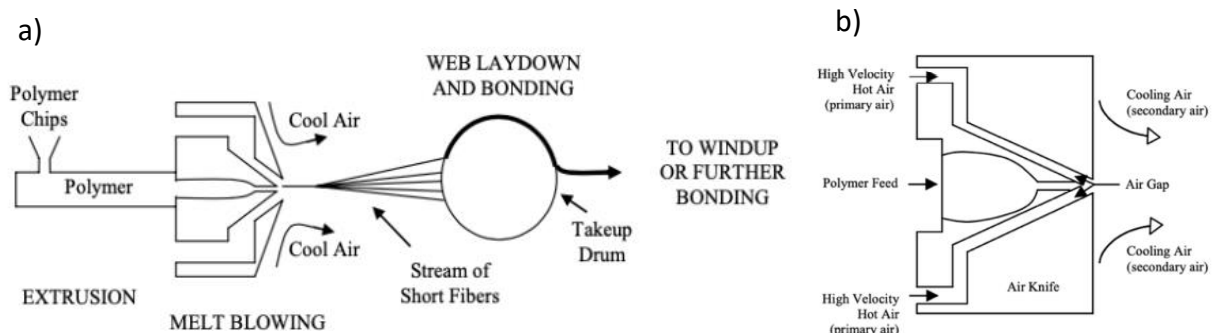


Figure 6.11: a) meltblown process b) die assembly in a meltblown process

The fabric resulting from meltblowing is characterized by a high filtration efficiency, because of the random orientation and the small diameter of the fibres, which in turn increase the pressure drops. Indeed, it is mostly used as filtering mid-layer. However, it possesses

poor mechanical properties that require the combination with more resistant fabrics. Typically, the basis weight of meltblowns is in the range $(20 - 200) \text{ g/m}^2$.

6.3.4 Spunbonding

In the spunbond process, represented in figure 6.12, the polymer is fed to a rotating single-screw heated extruder where it is melted. The molten polymer is then filtered and pumped to a die head, where it is extruded by hundreds of capillaries. The resulting fibres pass through two consecutive airstreams. The former cools down, flowing perpendicularly to the fibres, cools down the molten fibres and determines their density. The latter attenuates the fibres and influences their final diameter. Typical values of the obtained fibres diameter are in the range $(15 - 35) \mu\text{m}$. Finally, a system controls the way the fibres lay down on the collector, affecting their mechanical strength.

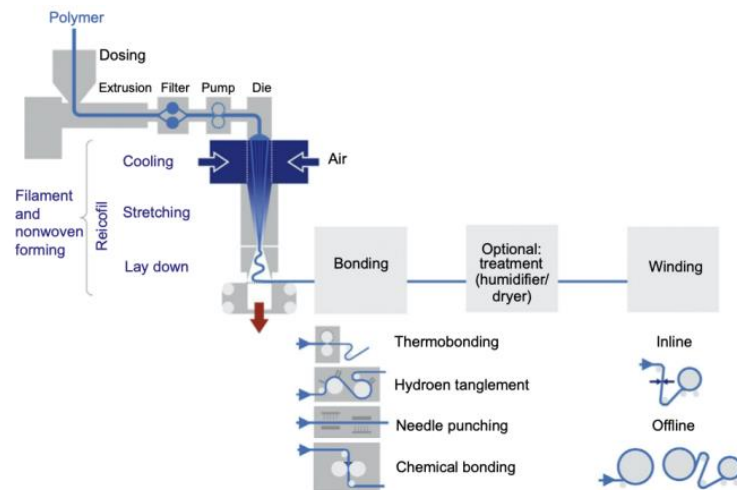


Figure 6.12: Spunbonding process

The fabrics resulting from spunbonding are characterized by a lower filtration efficiency compared to meltblowns, because of the larger diameter of the fibres, but causes lower pressure drops. In addition, they possess good mechanical properties. Indeed, spunbonds are

mostly used as inner or outer layer, supporting and shielding the filtering mid-layer. Typically, the basis weight of spunbonds is in the range (10 – 20) g/m^2 .

6.3.5 Electrospinning

The electrospinning process is able to produce nanometric fibres by means of a high voltage electric field, created by applying a high electric potential difference (typically in the range 5-30 kPa) between the needles (positively charged) and the collector (negatively charged). The solution containing the desired polymer is pumped to the needle where it gets charged. Once ejected, the jet accelerates and splits into multiple filaments due to the electrostatic repulsion, in a process called “splaying”). While blowing towards the collector, the solvent evaporates and the filaments solidify creating the fibres, which are finally collected. The result is a very thin web which, however, is extremely weak and soft. To override this limitation, the fibres are collected on a nonwoven support able to provide a sufficient mechanical resistance. The resulting fabric is constituted by charged fibres with a typical diameter of 250 nm, that provides a filtration efficiency higher than that of spunbonds and meltblowns. Unfortunately, this efficient technique is available at laboratory-scale at the moment.

Even if surgical masks are basic and relatively cheap products, their production requires the assembly of different parts in a relatively sophisticated process, along with several types of inputs, as reported in figure 6.13. The main and most influent bottleneck has been the production of polypropylene electret melt-blown, a specialized nonwoven fabric responsible of the majority of the filtration efficiency of a surgical mask. The manufacturing of this material requires very high capital investment for the purchase of heavy machinery (such as

hoppers, extruders and melt spinning systems), making the switch to this production expensive and very difficult within a reasonable time.

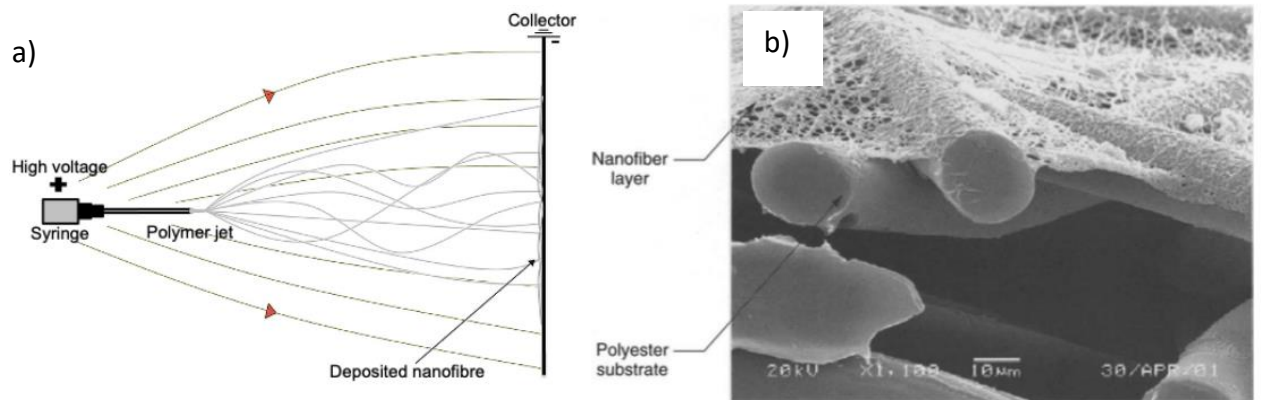


Figure 6.13: a) electrospinning process; b) electrospun nanofibers on spunbond layer

References

- [1] *BS EN 14683:2019: Medical face masks - Requirements and test methods*. European Committee for standardization.
- [2] "ISO - ISO 10993-1:2018 - Biological evaluation of medical devices — Part 1: Evaluation and testing within a risk management process." <https://www.iso.org/standard/68936.html> (accessed Jan. 22, 2022).
- [3] "ISO - ISO 22609:2004 - Clothing for protection against infectious agents — Medical face masks — Test method for resistance against penetration by synthetic blood (fixed volume, horizontally projected)." <https://www.iso.org/standard/35055.html> (accessed Jan. 22, 2022).
- [4] K. P. Chellamani, D. Veerasubramanian, and R. S. Vignesh Balaji, "Surgical Face Masks: Manufacturing Methods and Classification," *Journal of Academia and Industrial Research*, vol. 2, no. 6, p. 320, 2013.
- [5] J. M. Macher, "Positive-Hole Correction of Multiple-Jet Impactors for Collecting Viable Microorganisms," *American Industrial Hygiene Association Journal*, vol. 50, no. 11, pp. 561–568, Nov. 1989, doi: 10.1080/15298668991375164.
- [6] A. A. ANDERSEN, "NEW SAMPLER FOR THE COLLECTION, SIZING, AND ENUMERATION OF VIABLE AIRBORNE PARTICLES," *Journal of Bacteriology*, vol. 76, no. 5, p. 471, Nov. 1958, doi: 10.1128/jb.76.5.471-484.1958.
- [7] G. Sun *et al.*, "Overview of the Fiber Dynamics during Melt Blowing," *Industrial & Engineering Chemistry Research*, vol. 61, no. 2, pp. 1004–1021, Jan. 2022, doi: 10.1021/ACS.IECR.1C03972.
- [8] A. Tcharkhtchi, N. Abbasnezhad, M. Zarbini Seydani, N. Zirak, S. Farzaneh, and M. Shirinbayan, "An overview of filtration efficiency through the masks: Mechanisms of the aerosols penetration," *Bioactive Materials*, vol. 6, no. 1, pp. 106–122, Jan. 2021, doi: 10.1016/J.BIOACTMAT.2020.08.002.
- [9] A. Konda, A. Prakash, G. A. Moss, M. Schmoltdt, G. D. Grant, and S. Guha, "Aerosol Filtration Efficiency of Common Fabrics Used in Respiratory Cloth Masks," *ACS Nano*, vol. 14, no. 5, pp. 6339–6347, May 2020, doi: 10.1021/ACSNANO.0C03252/SUPPL_FILE/NNOC03252_SI_001.PDF.
- [10] A. Tcharkhtchi, N. Abbasnezhad, M. Zarbini Seydani, N. Zirak, S. Farzaneh, and M. Shirinbayan, "An overview of filtration efficiency through the masks: Mechanisms of the aerosols penetration," *Bioactive Materials*, vol. 6, no. 1, pp. 106–122, Jan. 2021, doi: 10.1016/J.BIOACTMAT.2020.08.002.
- [11] Y. Qian, K. Willeke, S. A. Grinshpun, J. Donnelly, and C. C. Coffey, "Performance of N95 Respirators: Filtration Efficiency for Airborne Microbial and Inert Particles," <http://dx.doi.org/10.1080/15428119891010389>, vol. 59, no. 2, pp. 128–132, 2010, doi: 10.1080/15428119891010389.
- [12] A. Mahdavi, "Efficiency Measurement of N95 Filtering Facepiece Respirators against Ultrafine Particles under Cyclic and Constant Flows," Sep. 2013.

CHAPTER 6

- [13] “Principles of Physiology and Respirator Performance -- Occupational Health & Safety.” <http://www3.ohsonline.com/Articles/2003/06/Principles-of-Physiology-and-Respirator-Performance.aspx> (accessed Jan. 16, 2022).
- [14] C. Brochot, A. Bahloul, P. Abdolghader, and F. Haghghat, “Performance of mechanical filters used in general ventilation against nanoparticles”, doi: 10.1088/1757-899X/609/3/032044.
- [15] A. Richardson, J. Eshbaugh, K. Hofacre, and P. Garnder, “Respirator Filter Efficiency Testing against Particulate and Biological Aerosols under Moderate to High Flow Rates,” 2006.
- [16] S. Adanur and A. Jayswal, “Filtration mechanisms and manufacturing methods of face masks: An overview:,” <https://doi.org/10.1177/1528083720980169>, Dec. 2020, doi: 10.1177/1528083720980169.
- [17] W. Albrecht, H. Fuchs, and W. Kittelmann, *Nonwoven fabrics: raw materials, manufacture, applications, characteristics, testing processes*. 2006. Accessed: Jan. 17, 2022. [Online]. Available: https://books.google.com/books?hl=en&lr=&id=pvQwXBi3HwMC&oi=fnd&pg=PR5&dq=Wilhelm+A,+Hilmar+F+and+Walter+K.+Nonwoven+Fabrics:+Raw+Materials,+Manufacture,+Applications,+Characteristics,+Testing+Processes.+Weinheim:+Wiley+-VCH,+2002,+pp.+772.&ots=yAVAxpJLI2&sig=7T5pibqFL_6ABWt13s4TPQFc7KI
- [18] S. Backer and D. R. Petterson, “Some Principles of Nonwoven Fabrics1:,” <http://dx.doi.org/10.1177/004051756003000912>, vol. 30, no. 9, pp. 704–711, Jul. 2016, doi: 10.1177/004051756003000912.
- [19] S. Bhattacharjee *et al.*, “Experimental Evidence for the Optimal Design of a High-Performing Cloth Mask,” *ACS Biomaterials Science and Engineering*, vol. 7, no. 6, pp. 2791–2802, Jun. 2021, doi: 10.1021/ACSBMATERIALS.1C00368/SUPPL_FILE/AB1C00368_SI_003.MP4.
- [20] H. Lim, “A Review of Spunbond Process,” *Journal of Textile and Apparel, Technology and Management*, vol. 6, no. 3, Apr. 2010, Accessed: Jan. 17, 2022. [Online]. Available: <https://ojs.cnr.ncsu.edu/index.php/JTATM/article/view/513>

CHAPTER 7

UniBo laboratory tests and apparatus

In early 2020, Italy was the most affected European country by COVID-19 and the third in the world in terms of total number of cases, after China and USA, despite its smaller population [1, 2]. The pandemic outbreak heightened the pressure on the Italian healthcare system, as shown in figure 7.1, and the situation was further exacerbated by the severe shortage of DPIs, surgical masks above all, for the healthcare operators [3 – 5].

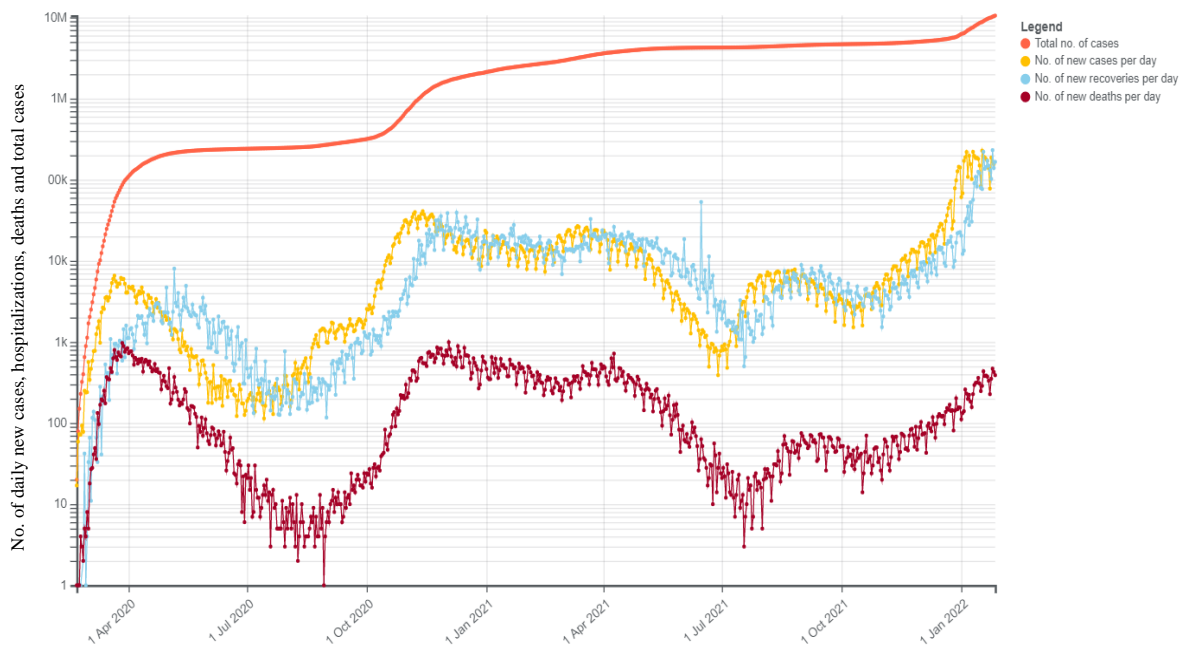


Figure 7.1: COVID-19 pandemic outbreak in Italy [5].

To address the shortage and to diversify their business, several companies and public organizations, mainly from the textile industry, started reconverting their production towards surgical masks [6]. Surgical masks dedicated to the European market, whether they are

produced or imported, should comply to the European standard EN 14683:2019, “*Medical face masks – Requirements and test methods*”, which specifies construction, design, performance requirements and test methods [7]. On 17 March 2020, a decree-law of the Italian government allowed the validation by the National Institute of Health (ISS), of non CE-marked surgical masks, produced or imported in the national territory. The ISS evaluates the masks quality on the basis of the results of any laboratory (even if not accredited) able to perform the tests required by the EN standard [1]. To support the industrial reconversion of the Italian industry, in late March 2020 a multidisciplinary group of the University of Bologna, headed by prof. Cristiana Boi (Associate professor at DICAM, University of Bologna) and prof. Francesco S. Violante (Full professor at DIMEC, University of Bologna, and Director of the unit of Occupational Medicine at Ospedale Sant’Orsola, Bologna, Italy), created the first Italian laboratory able to perform all the tests required for the evaluation and certification of surgical masks [8]. Figure 7.2 shows the team on 27 March 2020, the first day of activity of the laboratory.



Figure 7.2: Multidisciplinary team of the University of Bologna in a surgery room of the Sant’Orsola hospital, Bologna (Italy)

This chapter describes the different test lines set-up in the laboratory to evaluate the performance of the prototypes produced by public organizations and private companies, according to the European standard EN 14683:2019. In addition, the experimental procedures developed to achieve reliable results will be detailed, along with considerations and proposals of improvement regarding the apparatuses and the protocols indicated by the standard. Finally, the results obtained will be analyzed to provide useful correlation between the performance and the material of surgical masks.

7.1 Tests apparatus and protocols

According to the European standard EN 14683:2019, four different test lines to perform all the functional tests were set-up: breathability, bacterial filtration efficiency (BFE), splash test (for IIR type masks) and microbial cleanliness (bioburden) [7]. Bioburden is a measure of the cleanliness of a surgical mask rather than of its performance and a positive result could be obtained by a correct sanitization of the production process or of the final product [9]. Indeed, since the result of microbial cleanliness test is not correlated with the mask performances, it will not be considered in this work. A detailed analysis of the apparatuses and protocols for the other tests, indicated by the EN standard and aimed to evaluate the performance of surgical masks, is reported in chapter 2.1. The test lines are made of several specific pieces and equipment. Unfortunately, most of them were not readily available on the market, due to the emergency and the full lockdown enforced by the Italian government on March 9th 2020 [10].

Therefore, all the test lines were designed adapting components already present in the laboratories of the Department of Civil, Chemical, Environmental and Materials Engineering (DICAM) of the University of Bologna (Italy). Most of them were disassembled from other

test rigs. Other components were generously donated by companies, citizens, or other departments of the University of Bologna. After some months, the early versions of the bacterial filtration efficiency and breathability test lines were upgraded.

The masks delivered to the laboratory were analyzed in a specific order. The breathability was the simplest and fastest test to perform, indeed it was used to rapidly exclude those masks that were non-certifiable because of the poor breathability. The prototypes with a differential pressure (ΔP) below 60 Pa/cm^2 were then tested for the BFE, to discern cloth masks (BFE not sufficient) from Type I ($95 \% \leq \text{BFE} < 98 \%$ and $\Delta P < 40 \text{ Pa/cm}^2$) and Type II ($\text{BFE} \geq 98 \%$ and $\Delta P < 40 \text{ Pa/cm}^2$) surgical masks [7]. Type II surgical masks were finally tested for the resistance against splashes of synthetic blood, to be classified as type IIR in case of positive outcome.

All the tests were performed following the procedure indicated by the EN standard, with the addition of some experimental procedures aimed to reduce the error of the measures. Accordingly, before the tests all the samples were conditioned by exposure overnight to a room temperature of $(21 \pm 5)^\circ\text{C}$ and a relative humidity of $(85 \pm 5)\%$, to simulate the conditions of use when the wearer breaths through the mask [7]. The correct environment was created by placing a KCl saturated solution in a closed plastic box, where the masks were accommodated [11]. The EN standard also indicates that the number of samples per mask prototype to be tested should be high enough to achieve an acceptable quality limit (AQL) of 4% in all the tests. In the first stage of the pandemic outbreak, the number of masks prototype produced by the reconverted industrial productions was typically small, therefore 5 mask specimens per test were considered sufficient.

7.1.1 Breathability

For the set-up of the first apparatus, developed during the first Covid-19 outbreak, two different configurations, reported in figure 7.3, were compared. In the first configuration the airflow was generated by a vacuum pump placed downstream to the mask sample, in agreement with the standard, while in the latter it was generated by pushing the air in the section upstream the sample, by the means of an air compressor [7]. The two apparatus were compared by testing several samples and an average difference of $(1.6 \pm 0.8) \%$ was observed in the measured differential pressure. Since this difference was significantly lower than the relative standard deviation typically observed (equal to 6.9% and caused mainly by the differences between samples of the same prototype), the latter configuration was preferred

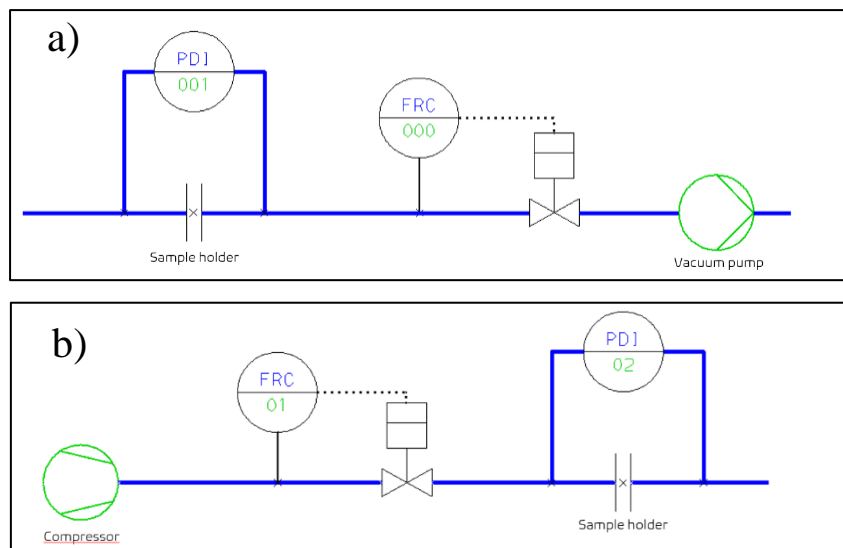


Figure 7.3: Layout of the breathability apparatus: a) configuration I, with vacuum pump downstream (not implemented); b) configuration II, with compressor upstream

because of the absence of regions with pressure under vacuum. This choice relied on the consideration that, in general, any possible leakage in a test rig is easily detectable when working under pressure, while it may go unnoticed under vacuum.

The first version of the breathability test rig, reported in figure 7.4, was installed at DICAM (University of Bologna, Italy). Compressed air, coming from the department supply-line,

was regulated by the means of a gate valve and its flow rate measured by a rotameter (range 0-500 L/h), before reaching the sample holder. The samples were clamped between the connections of two iron steel T-tubes, having an internal diameter of 25 mm and tri-clamp connections at all the extremities. Two flat, rubber ring gaskets, with an internal diameter of 25 mm, were placed above and below the specimen, to seal the sample holder and to ensure the correct sample cross-sectional area. The differential pressure was measured using

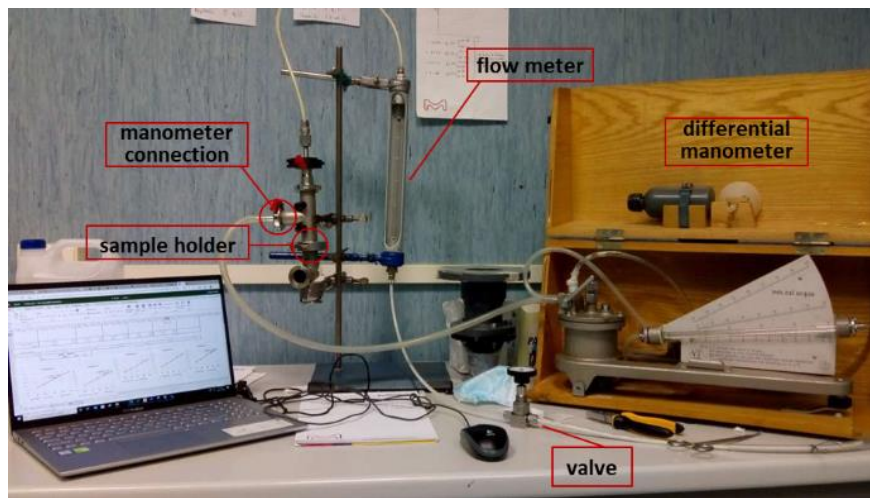


Figure 7.4: Representation of the first breathability apparatus

a U-tube differential manometer (maximum reading 2 kPa, accuracy 1 Pa) connected at the remaining branch of both the T-tubes, one upstream and the other downstream the sample holder.

All the samples were cut from the masks by punching with a hollow cutter (30 mm diameter) before being conditioned. According to the standard, the differential pressure should be measured when the sample is crossed by air at 8 L/min, corresponding to 480 L/h. However, an experimental procedure was developed in order to minimize the errors (both accidental and systematic) and to ensure the accuracy of the tests. The differential pressure was measured at least twice per each specimen at multiple flow rates, namely 100, 200, 300, 400, 450, 500 L/h. The values measured per each flow rate were used to determine a linear correlation, from which the final pressure drop at 480 L/h was calculated. Figure 7.5 shows

the linear correlation of a typical surgical mask sample. The final breathability reported for each specimen was the arithmetic mean of the different measurements (at list two), after its division by the sample area.

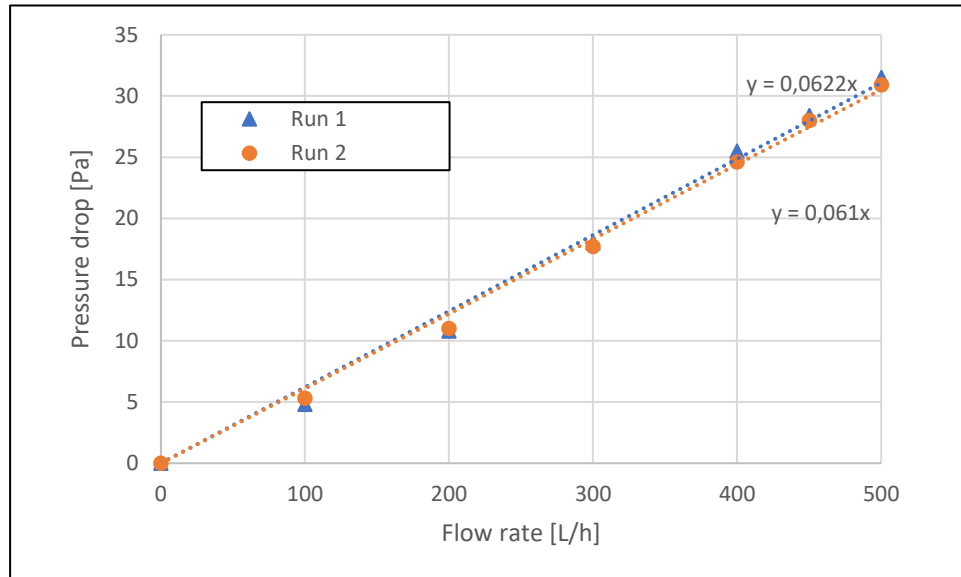


Figure 7.5: Results of a two-runs breathability test, reporting the linear correlations used for the calculation of the pressure drop at 8 L/min (480 L/h)

In late 2020, the apparatus has been upgraded:

- the gate valve and the rotameter were substituted by a digital flow meter and controller (Bronkhorst EL-FLOW, range 0 – 50 NL/min \pm 0.5%, Bronkhorst High-tech b. v., Netherlands);
- The U-tube differential manometer was replaced by a capacitance differential manometer (Baratron 226A, range 0 – 1000 Pa \pm 0.01%, accuracy 0.50 %, MKS Instruments, USA).

The upgraded rig led to a consistent reduction of the error affecting the single measure, corresponding to a specific flow rate. However, the original and the upgraded apparatus provided almost identical results in terms of final samples breathability, confirming the positive effects of the experimental protocol adopted. Indeed, this protocol was applied also

for the upgraded apparatus, since it makes easier the identification of accidental human errors.

7.1.2 Bacterial filtration efficiency

The first set-up of the BFE apparatus, whose layout is illustrated in figure 7.6 and figure 7.7, was installed in a disused surgery room at the University hospital, Policlinico Sant'Orsola (Bologna, Italy), to ensure the sterile conditions required for the procedure and the security for the operators.

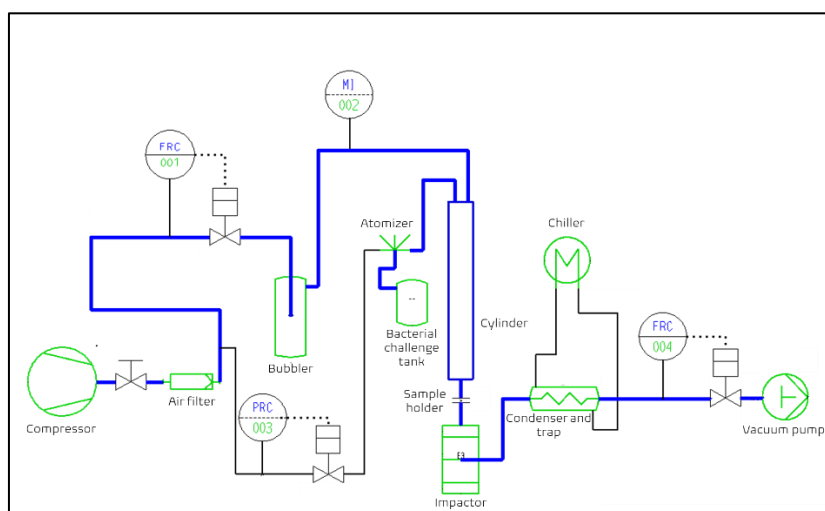


Figure 7.6: Layout of the BFE apparatus

The air, coming from the sterile room supply-line, was pulled by a vacuum pump (placed downstream of the process) into a 1.5 m, transparent, poly methyl methacrylate (PMMA) tube, with an internal diameter of 80 mm and flanged at both ends. The samples were placed between the bottom flange of the PMMA tube and the top flange of a polyethylene terephthalate (PET) cone. The cone was specifically designed by the software Autodesk Inventor 2019 and produced by a 3D printer (Prusa i3 MK3S+, Prusa Research a.s., Prague, Czech Republic) to hold the mask sample and to connect the PMMA chamber to the Andersen impactor below. Two flat, rubber ring gaskets with an internal diameter of 80 mm

were placed above and below the specimen, to seal the sample holder and to ensure the correct sample cross-sectional area. At half of the tube height (700 mm), a pressure-driven nebulizer (Collison single-jet nebulizer, CH technologies Inc., USA), was used to produce a *Staphylococcus aureus* ATCC6538 solution aerosol. To obtain an aerosol constituted by particles with a mean particle size (MPS) in the range $(3 \pm 0.3) \mu\text{m}$, as stated by the EN standard, the pressure was set at 0.4 barg [12]. The solution was prepared at an initial concentration of 5×10^5 colony forming units (CFU)/mL by diluting 7000 times a bacterial culture with 1.8 McFarland turbidity in 50 mL of modified peptone water (peptone 5 g/L, NaCl 5 g/L). The final inoculum concentration allowed to measure a number of CFU in the range $1.7 - 3 \times 10^3$ CFU in the positive control runs.

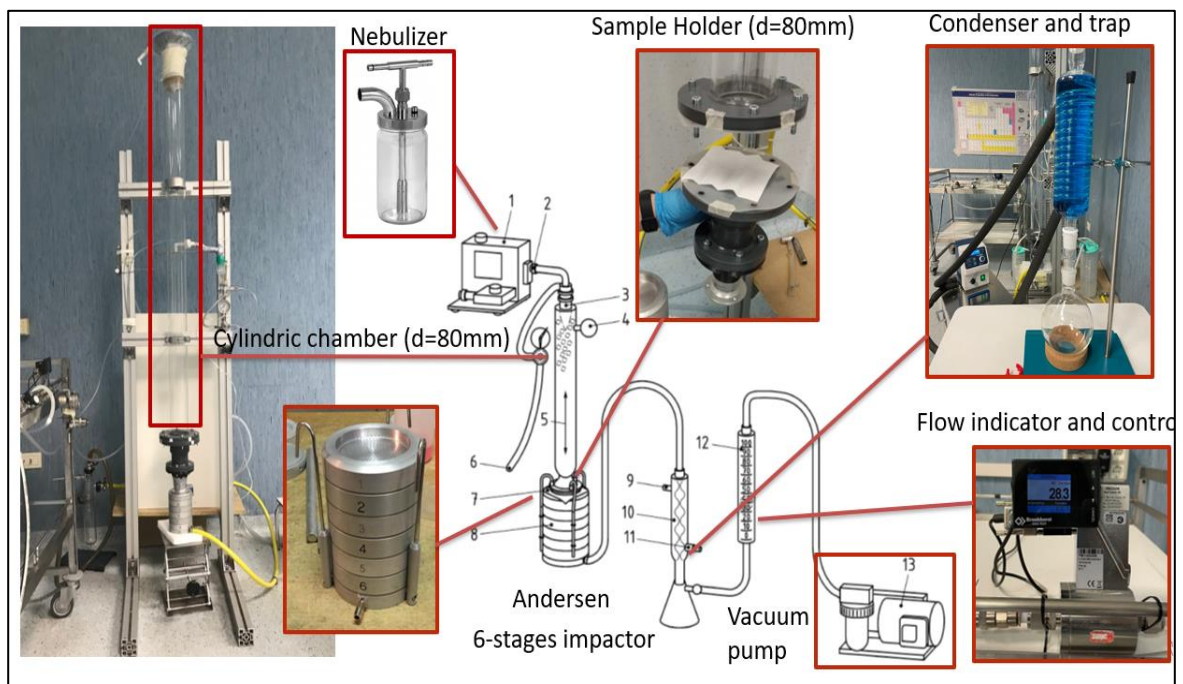


Figure 7.7: Representation of the first BFE apparatus

The EN standard requires a glass tube with an internal diameter of 80 mm and a height of 600 mm, from the top of which both the aerosol and the airstream enter [7]. The aim of this chamber is to provide a pathway long enough to obtain a uniform stream, resulting from the mixing the air and the bacteria aerosol, and to avoid the adhesion of infectious particles that may contaminate the instruments. About the material, no interaction between the aerosol and

the PMMA tube were observed. This was demonstrated by the absence of *S. Aureus* colony forming unit (CFU) in all the negative control runs (more than 400) executed during the entire period of investigation. About the excess height of the tube, the aerosol entered the tube at 70 cm from the bottom, indeed the above portion of the pipe was not involved in the aerosol flux and it was considered non influent from a fluid dynamic point of view. The 10 cm of additional pathway was not expected to negatively affect the uniformity of the stream delivered to the mask specimen.

Another difference involves the air fed to the system. The EN standard indicates that all the samples, before being tested, should be conditioned by exposure for at least 4 hours to a room temperature of $(21 \pm 5)^{\circ}\text{C}$ and a relative humidity of $(85 \pm 5)\%$, to simulate the conditions of use when the wearer breaths through the mask. However, there is no mention about the humidity of the air entering the apparatus. The atmosphere in the operating theatre was maintained at approximately 30% R.H. and the difference compared to the conditioning relative humidity was considered to affect the droplets evaporation rate. Therefore, the air entering the top of the cylinder was first humidified by bubbling in a polyvinyl chloride (PVC) tube filled with demineralized water. The height of the water column was adjusted to achieve 85% R.H., which was steadily measured by a digital thermo-hygrometer (XS UR 200, XS Instruments, Modena, Italy) inside the PMMA chamber. The bubbler was connected by a T-connection to the top of the PMMA pipe and to the atmosphere. The conditioned air was sent in excess to the system. This procedure ensured that all the air that was entering the apparatus (28.3 L/min) was conditioned, while the portion exceeding was wasted in the atmosphere.

The remaining equipment of the apparatus were chosen to meet the EN standard requirements. Downstream to the sample holder, the droplets larger than $0.65 \mu\text{m}$ permeating the masks were collected by a 6-stages Andersen impactor, generously donated by Cavazza

Anna SAS (Bologna, Italy), while those smaller were gathered in a vacuum trap, preceded by a glass, water cooled condenser. Finally, a flow indicator (Bronkhorst el-flow, range 0-100 L/min, generously donated by IMA SpA, Ozzano Emilia, Italy), a gate valve for the standard of the airstream and the vacuum pump (already available at DICAM, University of Bologna) were placed, in sequence, downstream.

At the end of the BFE test, the culture plates (provided by the Sant'Orsola hospital) were placed in an incubator at 37 °C and, after about 24 h, the CFU were counted and corrected using the positive hole conversion table. The BFE of each specimen was then calculated. Table 7.1 and table 7.2 report the value obtained for a non-compliant mask prototype before and after the positive hole correction, respectively. As can be observed from table 7.1, a total of about $3 \cdot 10^3$ CFU should be counted on the culture plates. This number can be higher or lower, depending on the filtration efficiency of the mask, but in general a total of about 10^3 CFU should be observed in each positive control run to achieve a mean value in the range $(1.7-3.0) \cdot 10^3$ CFU, after the correction with the positive hole conversion table, as indicated by the EN standard.

Table 7.1: Number of CFU counted per each stage and per each run, for a cloth mask.

	S1 [CFU]	S2 [CFU]	S3 [CFU]	S4 [CFU]	S5 [CFU]	S6 [CFU]	TOT [CFU]
PC1	4	15	177	392	284	99	913
1	0	0	5	64	96	90	255
2	2	1	6	52	84	69	214
3	1	0	4	66	120	64	255
4	0	0	4	92	94	99	289
5	0	0	5	42	95	71	213
PC2	6	12	168	383	271	125	828
NC	1	0	0	0	0	0	1

As expected, the highest number of CFU was usually observed in the stage 4, which collects particles with an aerodynamic diameter in the range 2.1 - 3.3 μm . In a typical working day,

especially during the first months, 8 mask prototypes per day were tested, turning in more than $25 \cdot 10^3$ CFU to be counted.

Table 7.2: Number of CFU per each stage and per each run, for a cloth mask, after the positive hole conversion.

	S1 [CFU]	S2 [CFU]	S3 [CFU]	S4 [CFU]	S5 [CFU]	S6 [CFU]	TOT [CFU]	PC MEAN [CFU]	BEF [%]
PC1	4	15	234	1565	495	114	2427	2265	
1	0	0	5	70	110	102	287		87.3
2	2	1	6	56	94	76	235		89.6
3	1	0	4	72	143	70	290		87.2
4	0	0	4	105	107	114	330		85.4
5	0	0	5	44	108	78	235		89.6
PC2	6	12	218	1263	453	150	2102		
NC	1	0	0	0	0	0	1		

To avoid errors in counting such high numbers, in particular for stage 4, an experimental apparatus for automatic CFU counting was set-up, as reported in figure 7.8. Culture plates were inserted in a box and imaged by a camera (GoPro Hero4, GoPro, San Mateo, USA) connected to a computer. The pictures were then analyzed by an open-source software (OpenCFU) and double-checked by an operator.

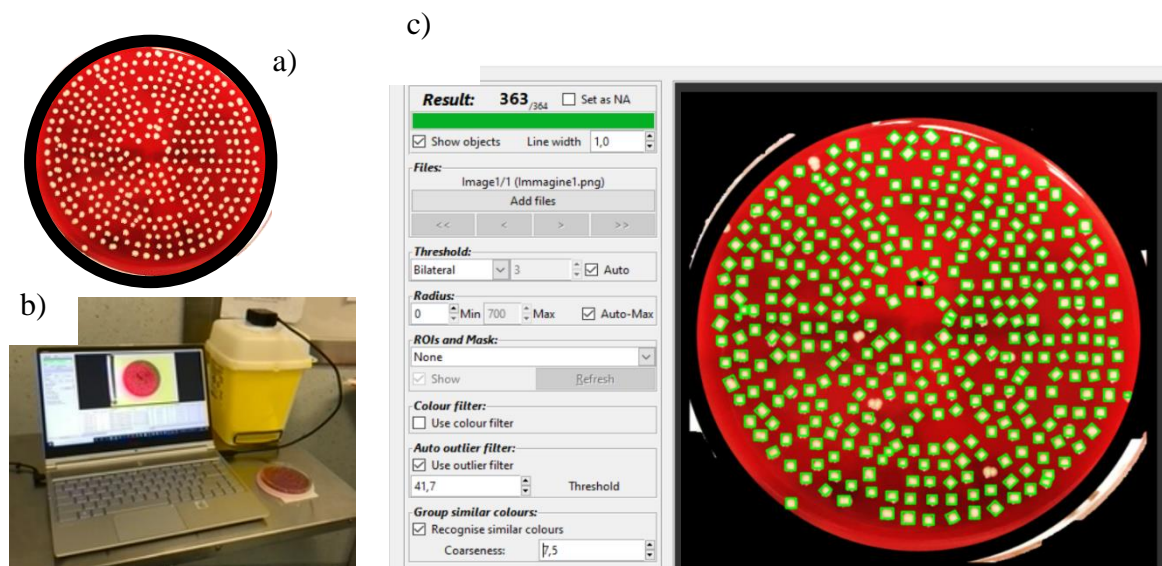


Figure 7.8: Experimental set-up for CFU counting: a) stage-4 culture plate from a positive control run after incubation; b) set-up for imaging and counting; c) open-source software OpenCFU

In late 2020, the BFE apparatus was completely re-designed and automated:

- The PMMA pipe was replaced by a glass tube, having an internal diameter of 80 mm and a length of 600 mm (FAVS s.r.l., Bologna, Italy);
- The cone connecting the tube to the impactor was re-designed by the software Autodesk Fusion 360 and produced by a M-SLA 3D printer (Prusa SL1, Prusa Research a.s., Prague, Czech Republic);
- All the valves were replaced by solenoid valves (mod. 20105, Fluid Precision Control s.r.l., Milano, Italy);
- The gate valve for the airflow control and the flowmeter donated by IMA were replaced by a mass flowmeter and controller (Bronkhorst EL-FLOW, range 0 – 50 $NL/min \pm 0.5\%$, Bronkhorst High-tech b. v., Netherlands);
- A mass flowmeter and controller (Bronkhorst EL-FLOW, range 0 – 50 $NL/min \pm 0.5\%$, Bronkhorst High-tech b. v., Netherlands) was added to the line for the air conditioning;
- A software for the automatization of the process, able to control all the solenoid valves and the mass flowmeter and controller) was developed in collaboration with FD Group (Bologna, Italy).

5 different surgical masks, already test with the original apparatus, were tested again with the upgraded one. The BFE efficiency measured by the two apparatus were almost identical and the same MPS was observed, indicating that the different material and length of the pipe of the original apparatus was not influent from a fluid dynamic point of view.

7.1.3 Splash test

The blood resistance test rig was assembled as indicated by the ISO 22609:2004 standard as it is shown in figure 7.9 [13]. The mask samples were accommodated onto a specimen-holding frame specifically designed by the software Autodesk Inventor 2019 and produced by a 3D printer (Prusa i3 MK3S+, Prusa Research a.s., Prague, Czech Republic). A syringe, equipped with a cylindrical needle 12.7 mm long and with a 0.83 mm diameter, was filled with synthetic blood and placed at (300 ± 10) mm from the sample. The syringe was then linked to a dosing system (Fisnar JB1113N, NJ, United States) which, connected to the department compressed air supply-line, allowed to set the required pressure and the splash time. The former was set at 16 kPa, while the latter at 0.8 s. The standard ISO 22609:2004 states that the splash test should be performed at three different pressures (namely 10.6, 16.0 and 21.3 kPa) and that, by calculation, the splash time at 16 kPa should be 0.66 s, to achieve a volume ejected equal to 2 mL. However, the main standard EN 14683:2019 states that type IIR surgical masks are compliant if they pass the test at a pressure equal or higher to 16.0 kPa. Indeed, all the samples were tested only at this pressure, that was double checked by an additional external manometer (Druck PTX-1400, UK). About the splash time, it was not possible to set 0.66 s the available dosing system. 0.8 s was identified as the value leading to the correct amount of blood delivered, by measuring the volume collected in a graduated Eppendorf tube at different times. Both, the air pressure and the volume of the blood sprayed, were checked before each test.

In addition to the velocity and volume, other key characteristics that govern the splash tests were the synthetic blood surface tension and density. The synthetic blood was prepared according to the following procedure. 5% w/v of poly(ethylene glycol)-b-poly(propylene glycol)-b-poly(ethylene glycol) (Pluronic® F-108, Merck, Italy) was added to 1 L of distilled water previously boiled for at least 5 min. The solution was kept under agitation for 1 h and

subsequently sonicated for 15 min. 30 g of Rhodamine (purity > 95%, Millipore-Sigma USA) was added to the solution with a further agitation for 40-60 min, using an orbital shaker. The surface tension of the obtained solution was measured in triplicate by the pendant drop method using a Theta Lite tensiometer (Biolin Scientific, Sweden). The density was measured in triplicate using a 1.0 mL Hamilton syringe and an AX224 Sartorius balance (Lab Instruments GmbH & Co. KG Goettingen Germany) with 0.0001 g precision. The synthetic blood obtained by following this procedure was characterized by a surface tension equal to 41.45 mN/m and a density of 1015 kg/m³.

After testing, the “pass/fail” evaluation of the samples was done by a simple visual inspection, to detect any trace of synthetic blood passed through the mask inner layer. In case of masks characterized by particular colors or draws, talcum powder was added to detect any trace of blood.

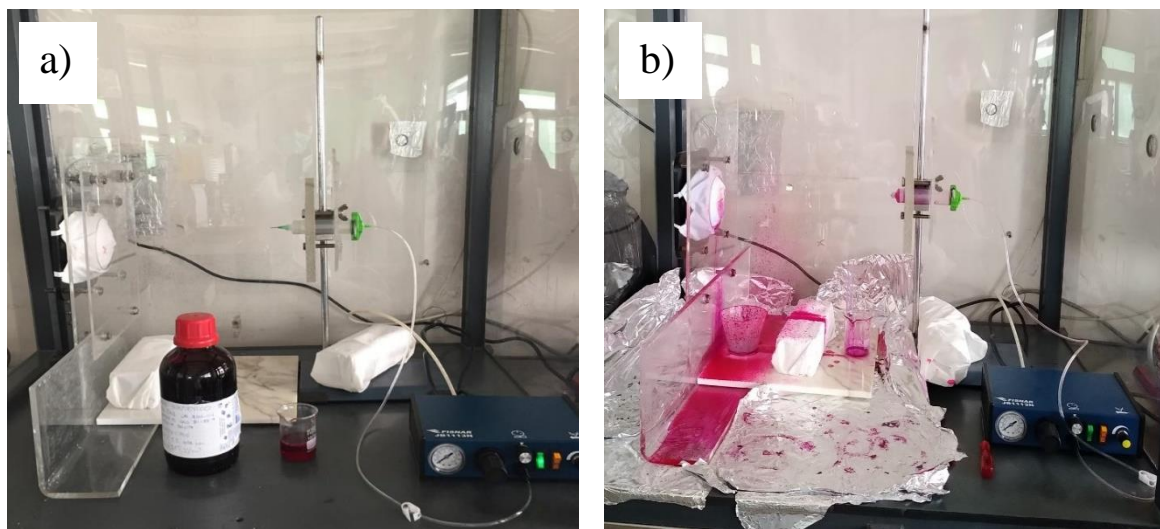


Figure 7.9: Splash test apparatus: before (a) and after (b) testing a set of five specimens

7.2 Results

The laboratory started the activity on the 24th of March 2020 and, until the 31st of July 2021, more than 600 prototypes were tested, with nearly 1200 tests performed in total. Most of the tests were performed for private companies, which intended to certify the masks for the Italian market, while others aimed to verify their compliance for internal use. Other tests were performed for public companies (such as hospitals) and, in particular, for the COVID-19 Italian task force, to select suitable fabrics for the production of surgical masks on a national scale between those commercially available at that moment.

Figure 7.10 shows the number of prototypes analyzed within 2020 on a by-monthly basis and the fraction that, succeeding in all the tests, were declared compliant. The highest workload was during the first 4 months, when nearly 350 prototypes were tested. Unfortunately, most of them were found to be not sufficiently performant. Only 6 (3.2%) succeeded in all the test within the end of April and 17 (8.64%) in the next two months. However, even if these numbers are impressive, they should not surprise.

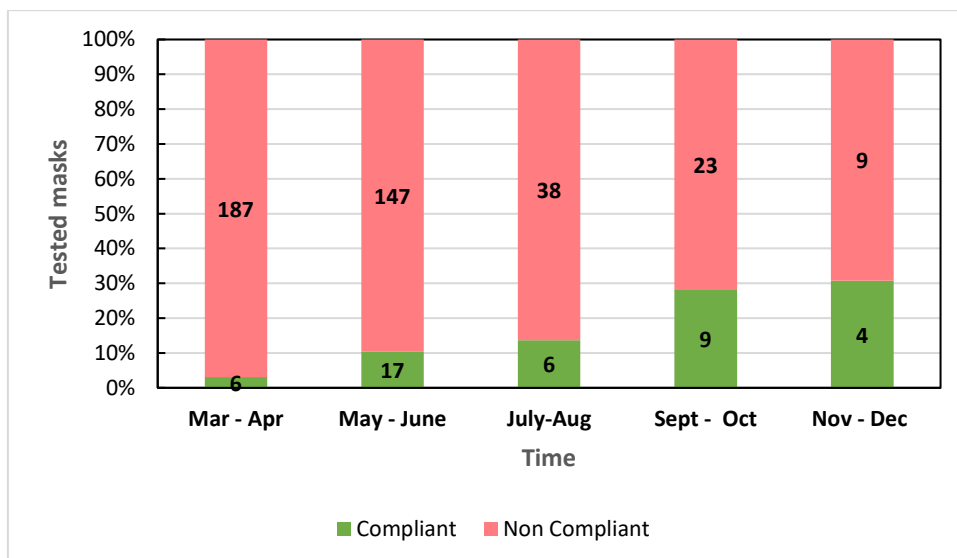


Figure 7.10: Number of prototypes tested on a by-monthly basis

Even if surgical masks are basic and relatively cheap products, their production requires specific raw materials that should be processed and assembled in a relatively sophisticated process [14]. The most important component is the internal filtering layer, that is responsible for most of the filtration efficiency [15]. This layer is typically a polypropylene, nonwoven, meltblown fabric with electrostatically charged fibers (electret) and its production requires expensive heavy machinery (such as hoppers, extruders and melt spinning systems)[16]. In the early months of the pandemic, several companies, mainly of the textile industry, tried to reconvert their production towards surgical masks without an appropriate technical knowledge [6]. Most of them simply reconverted their production lines (mainly for clothes, various types of fabric, but also sanitary pads, swim costumes) to create products with the shape of a surgical masks. Others tried to combine their raw materials with nonwoven fabrics available on the market that, in most of cases, were not appropriate due to the shortage of specialized materials. The result was a very broad spectrum of prototypes that were proposed for certification and were found to be inadequate, either due to their poor filtration ability or to a limited breathability (*i.e.*, too large pressure drop). However, thanks to an increasing knowledge of the main requirements, accompanied by the higher availability of specialized materials, the number of prototypes successfully passing all the tests steadily increased over the entire 2020 and 30.8 % were potentially ready to enter the market during November and December.

The screening of materials for the COVID-19 Italian task force was done by performing the tests on single nonwoven fabric layers or on a combination of them. Since they were not ready prototypes, they will not be considered in the following analysis. The breathability is the easiest and fastest test, for this reason it was performed first, as to rapidly discard all those masks that were not compliant to the EN standard because of too high resistance to the respiration. Of 435 prototypes, 194 (44.6%) showed a differential pressure equal or higher

than 60 Pa/cm^2 , that is the limit stated by the EN standard, and were indeed rejected. The remaining 241 (55.4%) were instead admitted to the bacterial filtration efficiency test, whose lower limit depends on the mask type and, therefore, on the breathability:

- 95% and 98% for, respectively, Type I and Type II surgical mask with a breathability below 40 Pa/cm^2 ;
- 98% for type IIR, whose breathability should be below 60 Pa/cm^2 .

About 60% of the 241 prototypes were identified as potential Type I and Type II surgical masks from the differential pressure analysis, but only 28 showed a BFE within the limits. For 8 of them a bacterial filtration efficiency in the range 95 – 98 % was measured and they were indeed classified as Type I, while the remaining 14 were classified as Type II. Concerning the potential Type IIR masks (about 40%), only 17 prototypes were found compliant in terms of both, breathability and bacterial filtration efficiency, and were indeed subjected to the splash test, considered the last step on the road to certification. Only 3 masks failed this last test. Figure 7.11 summarizes the results obtained. Of 435 prototypes only 42 were found to be compliant to the EN standard, while the remaining failed due to a too high resistance to the respiration or a low efficiency in retaining respiratory droplets and aerosols, highlighting the difficulties in finding a good compromise between these two parameters.

Figure 7.11 summarizes the results obtained. Of 435 prototypes only 42 were found to be compliant to the EN standard, while the remaining failed due to a too high resistance to the respiration or a low efficiency in retaining respiratory droplets and aerosols, highlighting the difficulties in finding a good compromise between these two parameters. Several prototypes that failed because of a poor breathability were, however, tested to evaluate the BFE, to measure their performance as community mask. The results, plotted in figure 7.12, shows that the performance of cloth masks vary across a wide range and that most of them offer a

good breathability at the expense of the BFE, that is in most cases below 70%. However, if it can be stated that, on average, to a higher resistance to the airflow corresponds a higher BFE, this is not always true, as several cloth masks with a differential pressure well above the limit were characterized by an insufficient filtration efficiency.

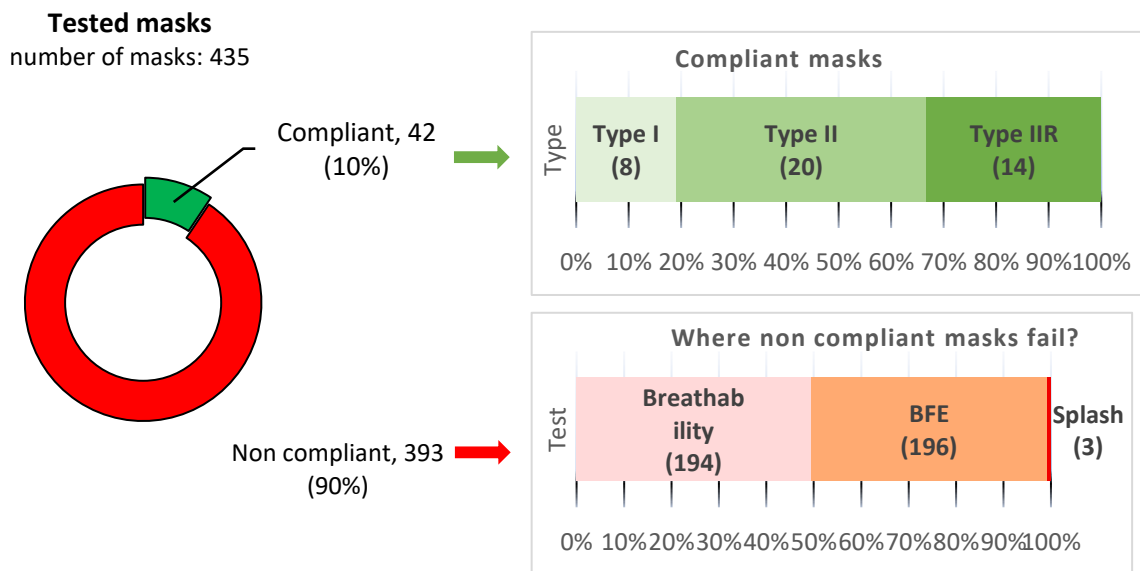


Figure 7.11: Analysis of compliant and non-compliant prototypes analysed with the indication of the test successfully passed or failed

This behavior is in agreement with the theory of mask filtration, according to which the physical interception alone is usually not sufficient to achieve the efficiency required by the standard [17]. To block at least 95% of the respiratory particles by physical filtration only, a high number of filters (or a high density of the fibers) would be necessary, causing in turn a low breathability [18]. This is the case, for example, of cloth masks composed by one or more cotton layers or that use common nonwoven fabric as filtering media (typically spunbond) [19]. Instead, it is possible to increase the breathability without affecting the BFE by taking advantage of the electrostatic attraction that allows to produce efficient filters with a high porosity and permeability to the airflow, as shown in figure 12 [20]. This phenomenon appears evident in figure 7.13, where SEM analysis of a cotton cloth mask and of a surgical mask are shown, and even more in figure 7.14, that reports the BFE and the breathability of

2 typical cotton masks made of a different number of layers compared to those of a 3-layers surgical masks.

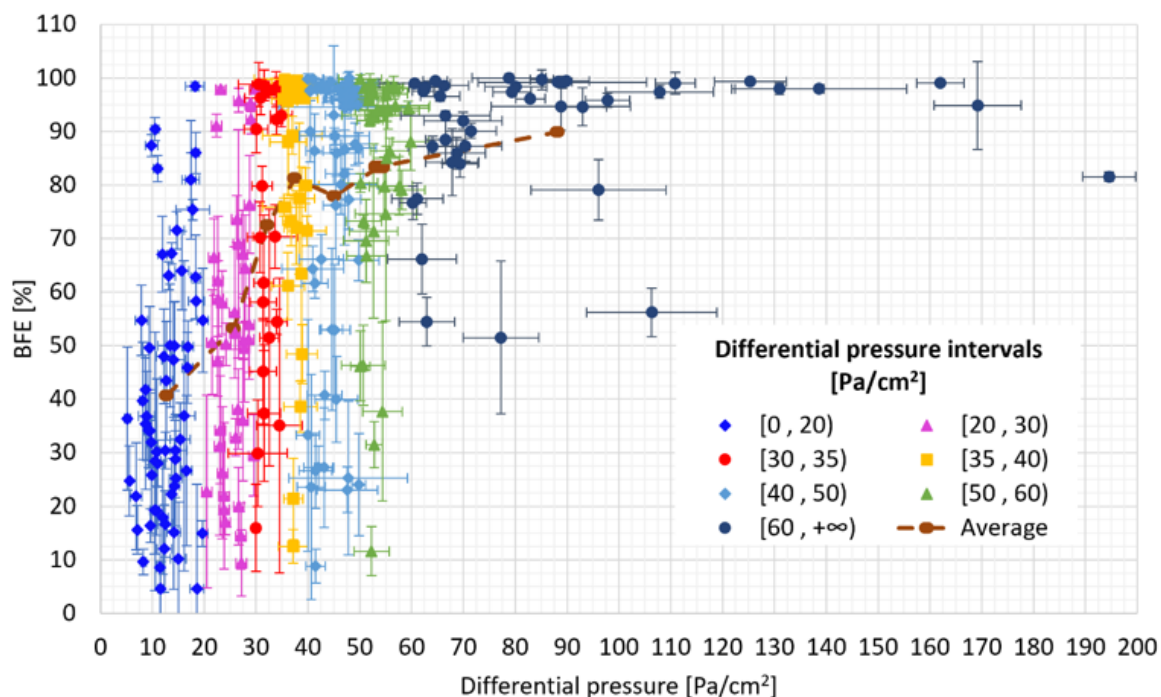


Figure 7.12: Relationship between breathability and bacterial filtration efficiency of all the masks on which both tests have been performed

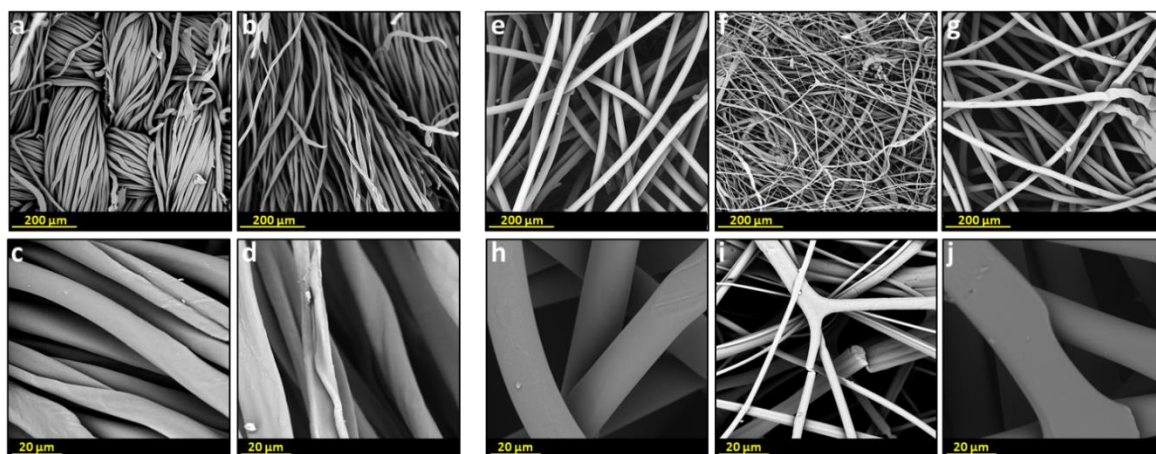


Figure 7.13: SEM analysis of a two layers cloth cotton mask and of a three layers surgical mask at different magnifications. External layer of a cloth mask at 400X (a) and at 3000X (c); internal layer of a cloth mask at 400X (b) and at 3000X (d); external layer of a surgical mask at 400X (e) and at 3000X (h); middle layer of a surgical mask at 400X (f) and at 3000X (i); internal layer of a surgical mask at 400X (g) and at 3000X (j)

Cloth masks made of 1 layer of cotton provide, in general, a very low protection, with a filtration efficiency typically below 40%. To achieve a higher efficiency, different companies unsuccessfully tried to add more layers, causing an excessive increase of the pressure drop that was not balanced by a sufficient filtration efficiency.

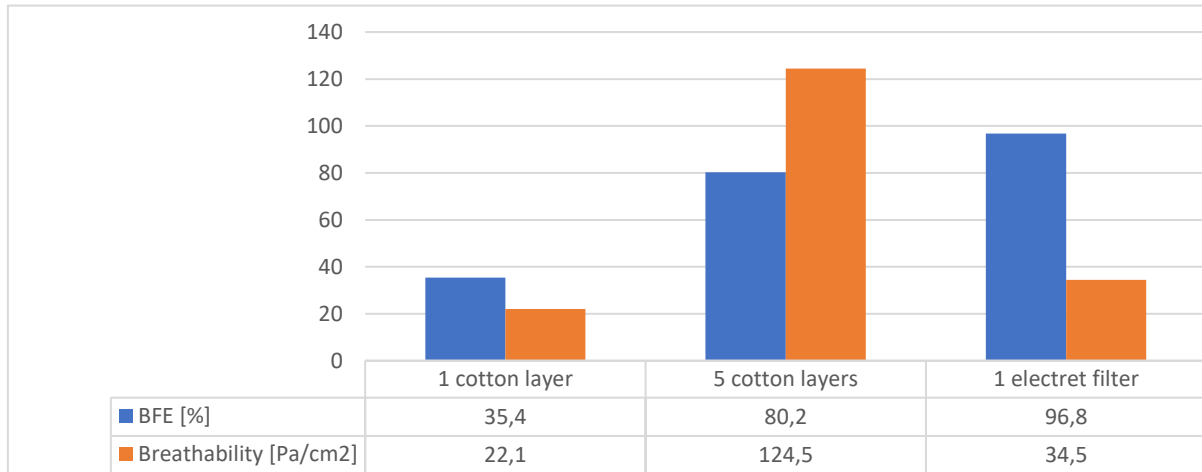


Figure 7.14 BFE and breathability of cotton and surgical masks.

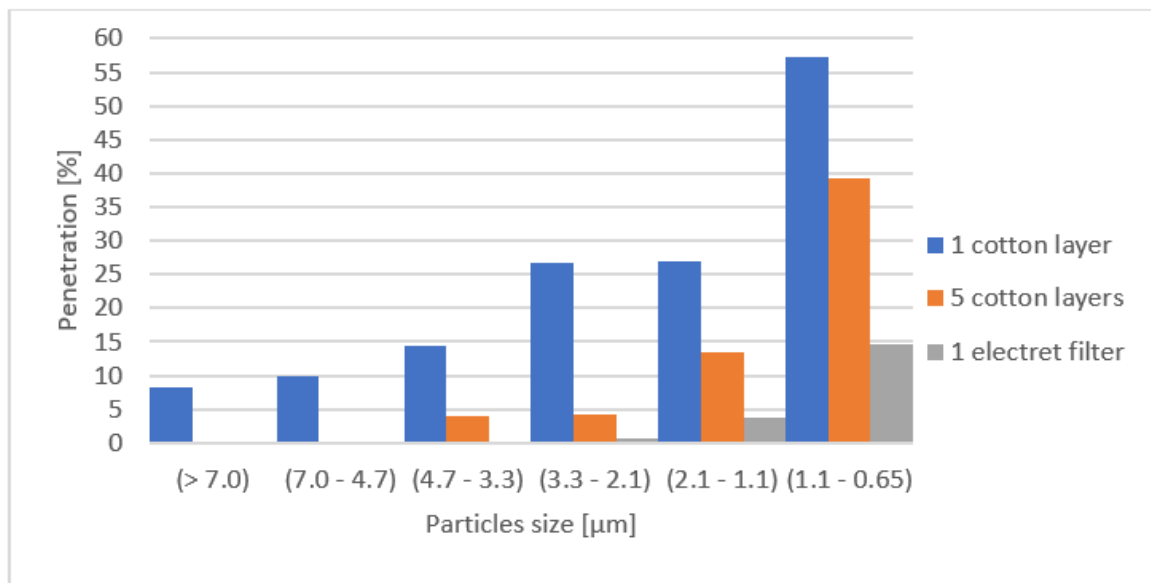


Figure 7.15: Penetration of respiratory particles of different size for two cloth masks and a surgical mask employing an electret.

Due to the absence of electrostatic attraction, cloth masks are only able to block large respiratory droplets and offer a poor protection against small droplets and aerosols, as shown in figure 7.15. The single cotton layer cloth mask is not even able to avoid the passage of all

the large respiratory droplets and is largely ineffective against aerosols. The addition of further layers increases the efficiency against large droplets, but not against aerosols, that have a similar penetration through the mask. Instead, surgical masks are very efficient against the droplets and are able to trap a large portion of the aerosols thanks to the presence of highly efficient filters, typically a meltblown or an SMS, as confirmed by the analysis of the materials of compliant masks, which demonstrated that 12% of the filters were SMS (mainly with a grammage of 70 g/m^2) and 88% were meltblown (with an average grammage of $26.2 \pm 2.5 \text{ g/m}^2$).

Notably, the use of meltblown or SMS with the correct grammage is essential but is not a guarantee for the production of a compliant face mask, since several prototypes made with a meltblown or a SMS filter failed the BFE, as shown in figure 7.16, thus highlighting the importance of the production process.

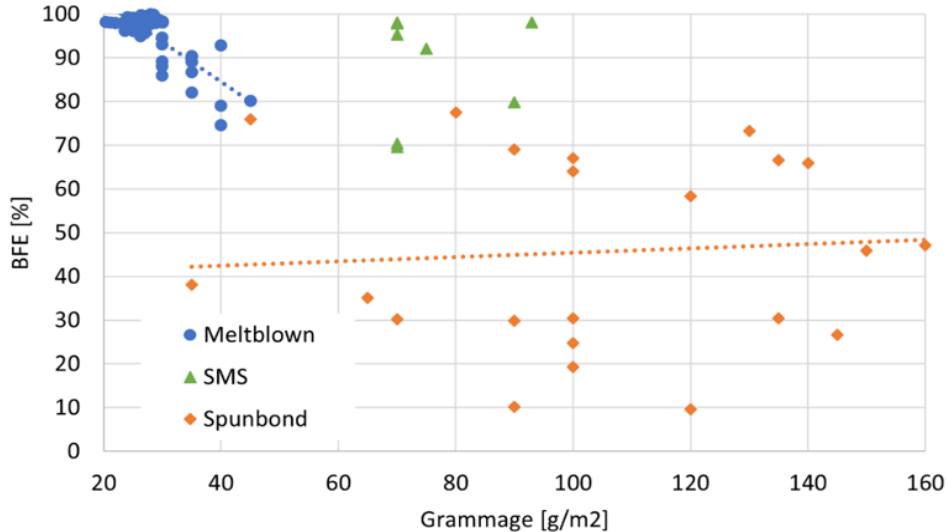


Figure 7.16: BFE as a function of the grammage for all the mask with materials indicated by the manufacturer

In addition, the analysis of the materials of all the prototypes for which a technical sheet was available confirmed that most frequently a surgical mask is composed by three layers (the filter sandwiched between two external nonwoven fabrics) and that the addition of further

layers does not increase the probability to obtain a performant device [21], as shown in figure 7.17.

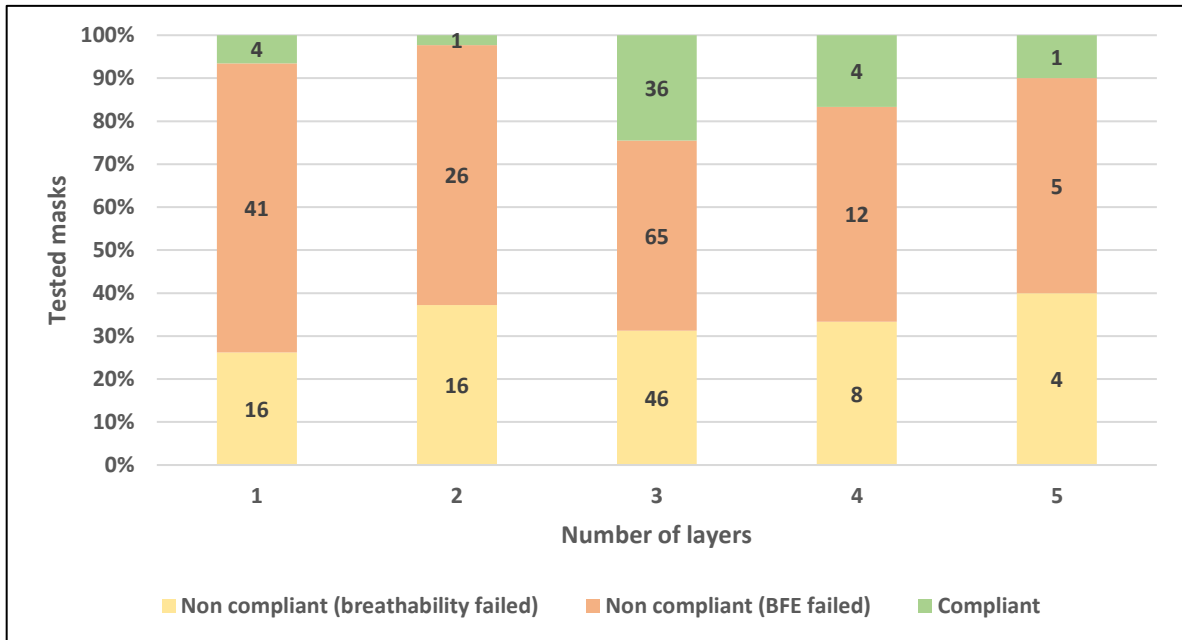


Figure 7.17: Results of the bacterial filtration efficiency and breathability according to the number of layers

The development of the apparatus and the high number of tests performed, led to identify possible critical points of the test procedures and to draw some considerations on the experimental protocols. About the breathability, the EN standard states that the samples should be tested at 8 L/min, after conditioning for at least 4 h at 85% R.H. and room temperature, to simulate the operative conditions. However, no information is provided about the humidity of the air that should be used in the breathability apparatus. In addition, the measurement at a single flowrate may led to experimental and accidental errors that can go unnoticed. Indeed, a different approach is suggested, consisting in measuring the breathability at several flow rates (including the one indicated in the EN standard), to derive a linear relationship from which the value at 8 L/min can be verified. Such approach allows to exclude possible errors due to instrument accuracy or in the execution of the test. The procedure developed considers five different flowrates (namely 100, 200, 300, 400, 500 L/h)

and was found appropriate, accurate, and not time consuming. However, a different range of flow rates can be chosen, but the linearity of the relationship in that range should be previously verified.

About the bacterial filtration efficiency, the efficiency measured by the apparatus is strongly affected by several parameters:

- Size distribution of the droplets;
- Humidity inside the glass cylinder;
- Dimension and number of the particles collected by the impactor;
- Correct calculation of the number of CFU on the culture plates.

The size distribution of the droplets delivered to the apparatus strongly depends on the nebulizer adopted and on the humidity inside the glass cylinder, that affect their evaporation rate. However, the EN standard provides information only about the mean particle size. Indeed, it would be recommended to specify the characteristic of the air that should be fed to the apparatus and of the nebulizer to obtain more reliable results. In addition, given the importance of surgical masks in protecting healthcare operators (and more generally, the whole population during pandemic situations) since the transmission of the virus occurs also via fine aerosols [22], the BFE test should provide more information about the filtration efficiency of smaller particles. Therefore, it would be recommended to extend the range of particle size collected by the impactor by the addition of stages with a lower cut-off. Last, the count of the CFU on the culture plate may lead to different results if not executed correctly. In particular, to obtain the number of CFU required by the EN standard in the positive control runs, a very high number of colonies should be present on the culture plates, especially those of stage 4, where a typical value is in the range 370-390 CFU [7]. Since this number is close to the limit (400), the difference between the number of CFU counted (after

the correction by the positive hole conversion table) and the real value could be substantially different, providing a wrong result. Moreover, high number of colonies are very difficult to count in absence of proper instrumentation and, since bacteria grow over time, the different colonies may join after several hours, making impossible the distinction and, indeed, the correct calculation. Therefore, it would be recommended to lower the value of the CFUs that should be measured in the positive control run. Several experiments were performed in this sense and a range 1000-1400 CFU was found appropriate and more accurate.

About the splash test, the measure of the resistance against splashes of synthetic blood is qualitative in nature and may undermine the reproducibility of splash test between different laboratories [13]. In particular, the adoption of more stringent standards for the synthetic blood formulation would be recommended, as to achieve similar fluid properties in any laboratory. In addition, the evaluation of the results through a digital image analysis should be encouraged, since it is totally dependent on the operator carefulness and thus is highly subjected to a human error.

References

- [1] A. Remuzzi and G. Remuzzi, “COVID-19 and Italy: what next?,” *The Lancet*, vol. 395, no. 10231, pp. 1225–1228, Apr. 2020, doi: 10.1016/S0140-6736(20)30627-9.
- [2] F. Ortenzi, E. Albanese, and M. Fadda, “A Transdisciplinary Analysis of COVID-19 in Italy: The Most Affected Country in Europe,” *International Journal of Environmental Research and Public Health*, vol. 17, no. 24, pp. 1–12, Dec. 2020, doi: 10.3390/IJERPH17249488.
- [3] “«Negli ospedali mancano mascherine e visiere»: c’è un’inchiesta in Procura - Corriere.it.” https://torino.corriere.it/cronaca/20_marzo_25/negli-ospedali-mancano-mascherine-visiere-procura-apre-un-inchiesta-2af05d78-6ecd-11ea-925b-a0c3cdbc1130.shtml (accessed Feb. 02, 2022).
- [4] “Coronavirus, gli infermieri: ‘Mancano guanti e mascherine per lavorare’ - la Repubblica.” https://www.repubblica.it/salute/medicina-e-ricerca/2020/02/24/news/coronavirus_gli_infermieri_chiedono_mezzi_di_protezione_e_individuali-249473258/ (accessed Feb. 02, 2022).
- [5] “Italy’s Health Care System Groans Under Coronavirus — a Warning to the World - The New York Times.” <https://www.nytimes.com/2020/03/12/world/europe/12italy-coronavirus-health-care.html> (accessed Feb. 02, 2022).
- [6] “La grande corsa alla riconversione: chi creava vestiti ora fa mascherine - La Stampa.” <https://www.lastampa.it/economia/2020/03/18/news/la-grande-corsa-alla-riconversione-chi-creava-vestiti-ora-fa-mascherine-1.38605102/> (accessed Feb. 02, 2022).
- [7] *BS EN 14683:2019: Medical face masks - Requirements and test methods*. European Committee for standardization.
- [8] “Il business delle mascherine e i laboratori che fanno i test: molte non sono a norma - Il Sole 24 ORE.” <https://www.ilsole24ore.com/art/il-business-mascherine-e-laboratori-che-fanno-test-molte-non-norma-ADqkm8F> (accessed Jan. 20, 2022).
- [9] “ISO - ISO 10993-1:2018 - Biological evaluation of medical devices — Part 1: Evaluation and testing within a risk management process.” <https://www.iso.org/standard/68936.html> (accessed Jan. 22, 2022).

- [10] “La storia del coronavirus dall’inizio.” <https://lab24.ilsole24ore.com/storia-coronavirus/> (accessed Jan. 18, 2022).
- [11] L. Greenspan, “Humidity Fixed Points of Binary Saturated Aqueous Solutions,” *JOURNAL OF RESEARCH of the National Bureau of Standards-A. Physics and Chemistry*, vol. 81, no. 1.
- [12] K. R. May, “The collision nebulizer: Description, performance and application,” *Journal of Aerosol Science*, vol. 4, no. 3, pp. 235–243, May 1973, doi: 10.1016/0021-8502(73)90006-2.
- [13] “ISO - ISO 22609:2004 - Clothing for protection against infectious agents — Medical face masks — Test method for resistance against penetration by synthetic blood (fixed volume, horizontally projected).” <https://www.iso.org/standard/35055.html> (accessed Jan. 22, 2022).
- [14] J. T. J. Ju, L. N. Boisvert, and Y. Y. Zuo, “Face masks against COVID-19: Standards, efficacy, testing and decontamination methods,” *Advances in Colloid and Interface Science*, vol. 292, p. 102435, Jun. 2021, doi: 10.1016/J.CIS.2021.102435.
- [15] “How Surgical Masks are Made, Tested and Used.” https://www.thomasnet.com/articles/other/how-surgical-masks-are-made/#_Types_of_Masks (accessed Jan. 15, 2022).
- [16] A. Tcharkhtchi, N. Abbasnezhad, M. Zarbini Seydani, N. Zirak, S. Farzaneh, and M. Shirinbayan, “An overview of filtration efficiency through the masks: Mechanisms of the aerosols penetration,” *Bioactive Materials*, vol. 6, no. 1, pp. 106–122, Jan. 2021, doi: 10.1016/J.BIOACTMAT.2020.08.002.
- [17] “Types of Masks and Respirators | CDC.” <https://www.cdc.gov/coronavirus/2019-ncov/prevent-getting-sick/types-of-masks.html> (accessed Jan. 15, 2022).
- [18] A. Podgórski, A. Bałazy, and L. Gradoń, “Application of nanofibers to improve the filtration efficiency of the most penetrating aerosol particles in fibrous filters,” *Chemical Engineering Science*, vol. 61, no. 20, pp. 6804–6815, Oct. 2006, doi: 10.1016/J.CES.2006.07.022.

- [19] H. Lim, “A Review of Spunbond Process,” *Journal of Textile and Apparel, Technology and Management*, vol. 6, no. 3, Apr. 2010, Accessed: Jan. 17, 2022. [Online]. Available: <https://ojs.cnr.ncsu.edu/index.php/JTATM/article/view/513>
- [20] A. Mahdavi, “Efficiency Measurement of N95 Filtering Facepiece Respirators against Ultrafine Particles under Cyclic and Constant Flows,” Sep. 2013.
- [21] K. P. Chellamani, D. Veerasubramanian, and R. S. Vignesh Balaji, “Surgical Face Masks: Manufacturing Methods and Classification,” *Journal of Academia and Industrial Research*, vol. 2, no. 6, p. 320, 2013.
- [22] K. Escandón *et al.*, “COVID-19 false dichotomies and a comprehensive review of the evidence regarding public health, COVID-19 symptomatology, SARS-CoV-2 transmission, mask wearing, and reinfection,” *BMC Infectious Diseases* 2021 21:1, vol. 21, no. 1, pp. 1–47, Jul. 2021, doi: 10.1186/S12879-021-06357-4.

CHAPTER 8

Durability of surgical masks

Surgical masks were designed in 1960s for healthcare settings to be single use: the operators wear them to avoid infecting patients with their respiratory droplets and splashes, mainly in the surgery room, and discard the devices after each operation or after 4 hours of usage [1]. The maximum duration of 4 hours derives from a WHO report that, based on experimental evidence, claims that the comfort and the tolerance of the masks by the healthcare personnel begins to decrease. As consequence, there is a tendency to touch the mask often with the hands, increasing the risk of direct contact and fomite infection or of inhaling infectious particles while repositioning the mask [2]. Under ordinary circumstances, this recommendation was blindly applied.

In early 2020, due to the COVID-19 pandemic outbreak, the use of these medical devices became essential to prevent infection of frontline healthcare workers, treating asymptomatic and symptomatic patients. and to enable the continued functioning of national healthcare systems. Their use was recommended also to symptomatic and vulnerable individuals (over 60 or with underlying health risks), but surgical masks were largely employed in the community for personal safety [3, 4]. The unprecedented demand and the consequent severe shortage of surgical masks led to extended use and re-use of disposable surgical masks by frontline health workers [5]. According to the survey performed by Selvaranjan et al., involving a total of 1033 individuals from different countries (mainly Australia, USA and

UK), this behaviour is even more pronounced in the community, where most of the people re-use the same mask for several days, some for an entire working week, as shown in figure 8.1.

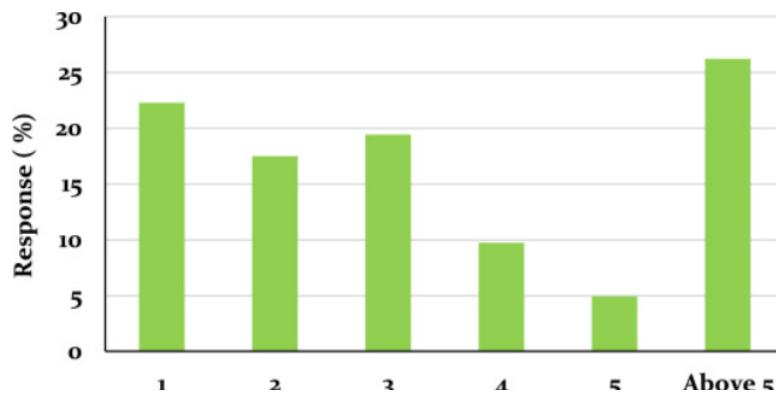


Figure 8.1: Number of masks used by an individual per week[4]

An additional problem caused by the large use of surgical mask is environmental pollution. Recent studies estimated a worldwide consumption of 129 billion surgical masks per month, equivalent to about 645 thousand tonnes of plastics that cannot be readily biodegraded and may, in addition, fragment into smaller micro- and nano-plastics that widespread in ecosystems if not wasted properly.

To address the shortage of surgical masks and to reduce their environmental pollution, several studies have been done about their disinfection, to allow a safe re-use. All these studies investigated the disinfection efficiency on bacteria (*Bacillus subtilis* and *Geobacillus stearothermophilus*) or on the influenza virus N1H1, none of them have data on SARS-CoV-2 [6]. However, the influenza virus belongs to the same group of lipid bilayer enveloped viruses and bacteria are more challenging to disinfect than viruses, thus the available data can be applied to the SARS-CoV-2 [7 – 9]. Ultraviolet light-C, with a primary wavelength of 254 nm, provides an efficient disinfection, it does not affect the filtration efficiency nor the physical structure, but reduces the strength of the device and requires several instruments to be performed [10 – 12]. Hydrogen peroxide vapor with a

concentration in the range 30-35% is another efficient method, providing an excellent decontamination and able to leave the filtration efficiency and the physical structure unchanged even after 50 cycles [13 – 15]. Heat decontamination has been mostly tested only on viruses with excellent results at 65°C for 30 minutes, but it partially reduces the filtration efficiency and, in some cases, the degradation of the physical structure of the mask has been observed [16], [17]. Instead, disinfection by alcohols or water and soap is not recommended, since it affects the filtration efficiency of the masks [18], [19]. According to Tsai, these methods cause the reduction of the electrostatic charge of the meltblown layer and, in turn, of the efficiency of the mask, as shown in figure 8.2.

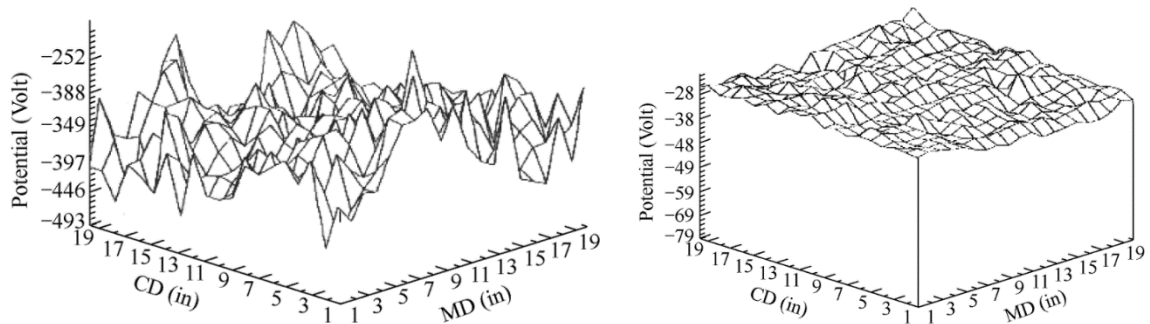


Figure 8.2: Surface charge potential of a meltblown filter: a) before washing; b) after washing

Nevertheless, some methods for the disinfection of a surgical mask able to preserve its filtration efficiency exist, allowing a potential re-use. However, there are no information about how the performance vary over time of usage and, indeed, how many hours a surgical mask can be worn without losing its properties. The knowledge of the durability is fundamental to understand if the extended use and re-use are possible and recommended.

In this chapter two different surgical mask types will be tested in different experiments and conditions, to determine how their bacterial filtration efficiency and breathability change over time of usage. The aim is to evaluate which are the factors that cause the variation of mask performance and to identify a process to simulate this behaviour. For these tests, two

surgical masks, namely Mask A and Mask B, already available in the laboratory and with known performance, were chosen. Table 8.1 shows the characteristics of these masks, calculated as the mean of the values obtained in previous tests.

Table 8.1: Characteristic of Mask A and Mask B

	Type	BFE [%]	Breathability [Pa/cm ²]	Outer layer	Filter	Inner layer
Mask A	II	99.7 ± 0.10	28.2 ± 2.14	Spunbond	Meltblown	Spunbond
				30 g/m ²	25 g/m ²	30 g/m ²
Mask B	II	99.8 ± 0.04	36.7 ± 1.77	Spunbond	Meltblown	Spunbond
				30 g/m ²	30 g/m ²	30 g/m ²

8.1 Real usage evaluation

To study the durability of surgical masks, the best solution would have been to wear a mask for a long time and to measure the bacterial filtration efficiency and the pressure drops over time on a regular basis. However, this procedure was not feasible, because the BFE test that requires an aerosol of *S. Aureus* would have contaminated the mask, hindering a further use. To circumvent this problem, the following experimental procedure was adopted.

4 operators working in the surgery room, where the BFE apparatus was placed, were selected as representative of a typical worker, gender included: 2 males (namely M1 and M2) and 2 females (namely F1 and F2). 5 specimens of both, Mask A and Mask B, were given to each operator, which worn the masks (one at time) 8 hours per day, reproducing the use over a typical working day. Masks A1 and B1 were worn for 1 day, A2 and B2 for 2 consecutive days, and so on. The samples were left in the surgery room at the end of each shift, to ensure the storage in a dry and ventilated environment. At the end of the respective scheduled time of usage, the masks were tested for the breathability and the bacterial filtration efficiency, stored overnight (about 16 h), tested again and then wasted, because contaminated by *S.*

Aureus. Their performance at time zero were supposed to be equal to the average ones, presented in table 8.2. Figure 8.3 provides a graphical representation of the protocol.

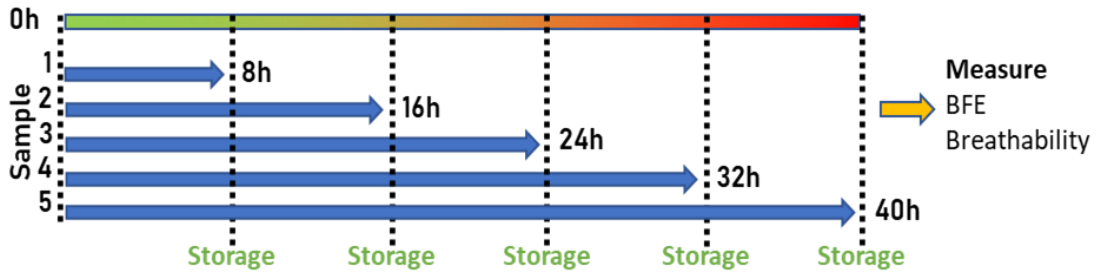


Figure 8.3: Real usage experiment protocol

This procedure was developed to measure the residual performance of the surgical masks after one or more working day of a typical employee and to observe if a portion of the lost performance was recovered during storage. To make the simulation as close to reality as possible, the samples were not conditioned before performing the tests, as typically requested by the EN standard [20].

Table 8.2: Name and time of usage of the masks provided to each operator

Sample name	Scheduled time of usage [h]	Working day [d]
A1, B1	8	1
A2, B2	16	2
A3, B3	24	3
A4, B4	32	4
A5, B5	40	5

For all the samples, no recovery was observed and the small differences in the BFE and the breathability before and after the storage (as shown in the paragraph 8.1.1) were ascribed to the intrinsic error of the measures. Therefore, to reduce this error, the BFE and the

breathability at the end of each scheduled time of usage were determined using equations 8.1 and 8.2, respectively.

$$BFE_i = \frac{BFE_{i,bs} + BFE_{i,as}}{2} \quad (8.1)$$

Where BFE_i is the average bacterial filtration efficiency at time of usage “i” (namely 8, 16, 24, 32 and 40 hours) and $BFE_{i,bs}$ and $BFE_{i,as}$ are the measured BFE value at time of usage “i” before and after storage, respectively.

$$\Delta P_i = \frac{\Delta P_{i,bs} + \Delta P_{i,as}}{2} \quad (8.2)$$

Where ΔP_i is the average breathability at time of usage “i” (namely 8, 16, 24, 32 and 40 hours) and $\Delta P_{i,bs}$ and $\Delta P_{i,as}$ are the measured breathability values at time of usage “i” before and after storage, respectively.

8.1.1. Results of real usage evaluation

Figure 8.4 and figure 8.5 show the values of the bacterial filtration efficiency and of the breathability, respectively, measured for all the Mask A samples worn by the operator F1. A slight constant decrease was observed in the filtration efficiency going from sample A1 (worn for 8 h) to sample A4 (worn for 32 h), meaning a decrease over time of usage of the BFE that, however, remained above the limit of 95%. Instead, a significant downfall was observed for sample A5 (worn for 40 hours), that resulted to be non-compliant to the EN standard. Notably, the efficiency seems to remain constant between 16 and 24 hours of usage. This behaviour might be due to a different value of the two samples at time zero, that were only supposed to be equal. Perhaps, the starting value of the sample tested for 3 days was higher than that of the sample worn for 2 days.

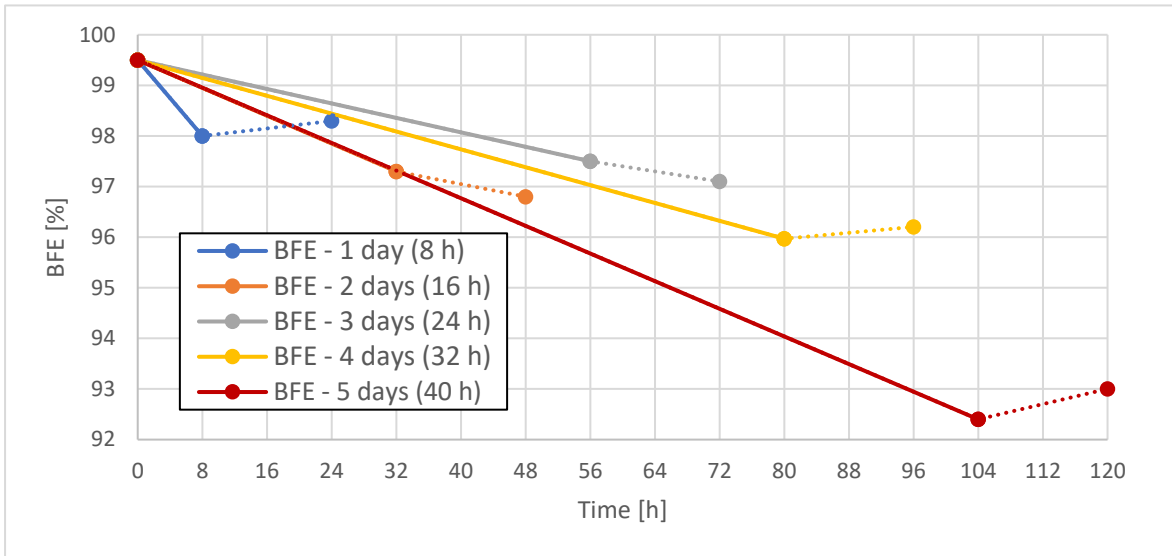


Figure 8.4: Variation of the BFE of surgical mask A after 8, 16, 24, 32 and 40 hours of usage, worn by operator F1. The dashed lines represent the variation of the after 16 h of storage in a dry and ventilated environment. Each usage time was tested on a different mask.

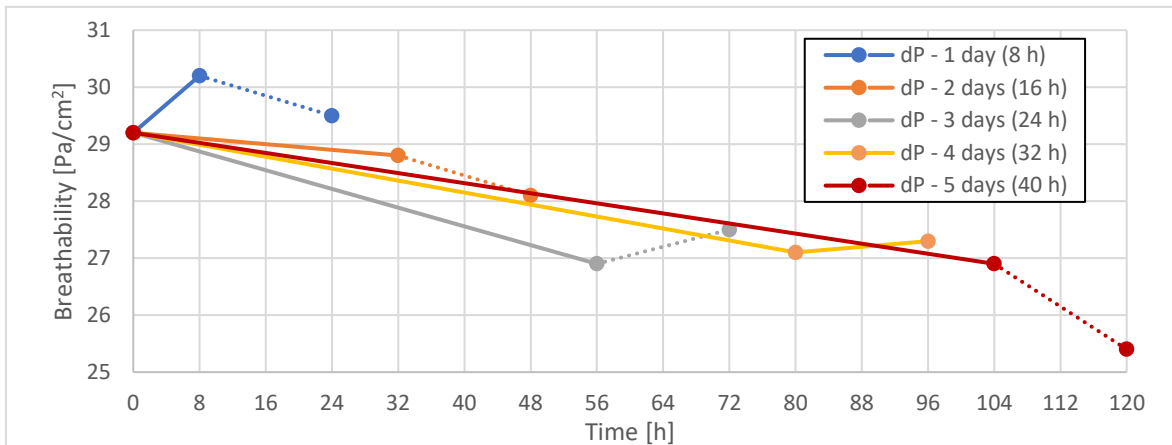


Figure 8.5: Variation of the breathability of surgical mask A after 8, 16, 24, 32 and 40 hours of usage, worn by operator F1. The dashed lines represent the variation of the efficiency after 16 h of storage in a dry and ventilated environment. Each usage time was tested on a different mask.

In addition, the storage overnight in a dry and ventilated environment resulted to be irrelevant, since only small positive and negative fluctuations were observed and were ascribed to the intrinsic error of the measures. About the breathability, the values measured seems to slightly decrease of about 2 Pa/cm² after 24 hours of usage. However, an increase was observed for sample A1 (worn for 8 h) and an equal value for sample A2. Perhaps the variations observed were ascribable to a different initial breathability value between the

samples. The results allowed to conclude that Mask A, worn by the operator F1, ceased to be compliant to the EN standard after 32 hours of usage due to a poor bacterial filtration efficiency.

A similar behaviour was observed for Mask B and for all the operators. Indeed, to reduce the error associated to the single measures, the BFE and the breathability at the end of each scheduled time of usage were calculated using equation 8.1 and equation 8.2. Figure 8.6 and figure 8.7 show the results obtained with this approach for Mask A and Mask B, respectively, for all the operators.

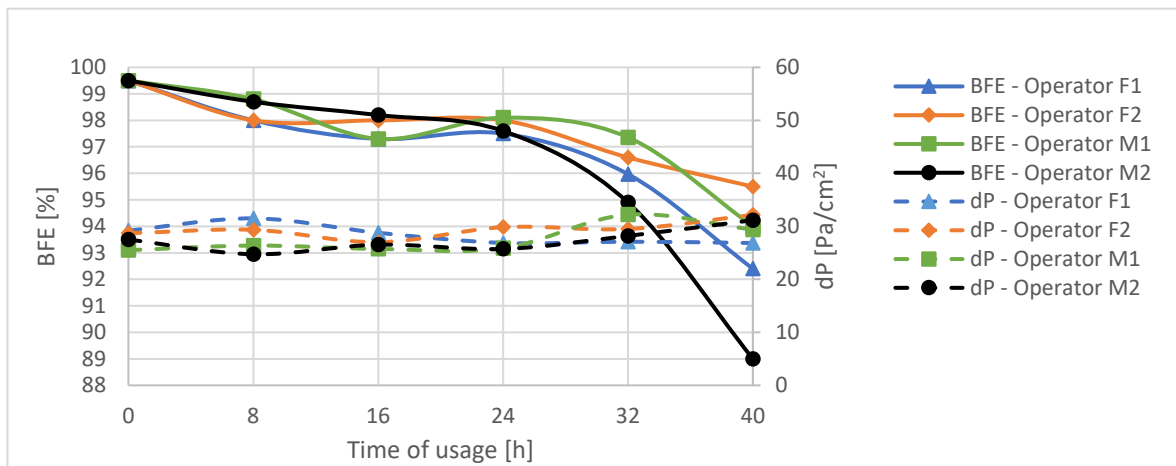


Figure 8.6: BFE and breathability variation over time of usage of Mask A.

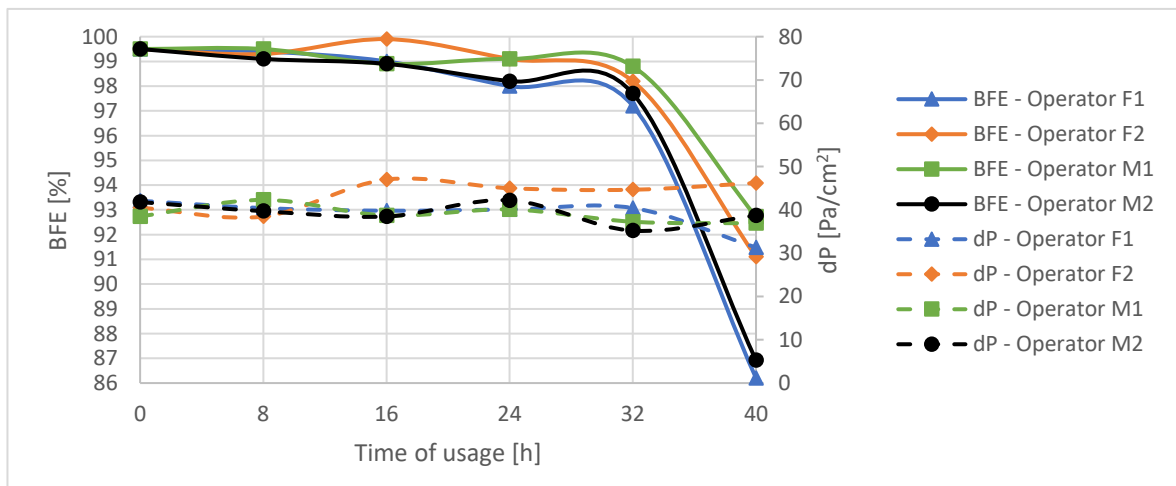


Figure 8.7: BFE and breathability variation over time of usage of surgical mask B.

In both cases, the approach used allowed to obtain consistent and reproducible results among all the operators, for which the behaviours were very similar. About Mask A, the results allowed to confirm the previous observations. The bacterial filtration efficiency of Mask A steadily decreases over time, showing excellent performance up to 32 hours of usage, time after which a fast decrease was observed and the mask ceases to be compliant to the EN standard. Instead, the breathability remains constant over the entire time of usage investigated, indicating that the reduction of the performance is not a consequence of a physical deterioration of the material. Similar consideration can be done for Mask B. In this case the bacterial filtration efficiency remains almost constant up to 32 hours of usage and then suddenly drops, while the breathability does not change and the small fluctuations observed could be ascribed to small and irrelevant errors of the measures.

About the bacterial filtration efficiency of both the masks, A and B, the values for the different operators are quite close in the compliant region, while they substantially diverge at the end, making difficult a precise estimation of the protection offered by these devices after 5 days. The different behaviour can be caused by the synergic combination of two factors:

- Due to the loss of a consistent portion of the electrostatic charge, the filtration efficiency of the devices mainly relies on the meltblown structure, unearthing minor unevenness that would be irrelevant in the presence of the electrostatic charge;
- The bacterial efficiency test provides replicable results for high-performing masks, but it becomes less precise when dealing with lower filtration efficiency, due to use of the positive hole conversion table.

The inhalation of aerosols has been recognized as a possible cause of SARS-CoV-2 transmission. As shown in chapter 3.2, surgical masks are effective against small particles,

thanks to the electrostatic charge present on the fibers surface. However, if the reduction of the bacterial filtration efficiency over time of usage observed for both, Mask A and Mask B, is partially caused by the loss of the electrostatic charge, it is important to verify the residual filtration efficiency of the re-used on the basis of the particles size. Figure 8.8a and figure 8.8b show the fraction of particles delivered to the system during the BFE tests that permeated through the Mask A and Mask B samples, respectively, worn by operator F1 and that were indeed collected by the impactor in each stage. Similar results were obtained for other operators (data not shown). About Mask A, as expected, the most penetrating particle size [MPPS] is in the range $0.65 - 1 \mu\text{m}$, corresponding to the smallest particles size that the impactor of the bacterial filtration efficiency apparatus is able to collect, in stage 6. The penetration of finer particles cannot be quantified, but it is expected to be higher. Notably, a new surgical mask A is able to filter almost all these small particles, but its efficiency rapidly decreases: after 8 h of usage about 6% of the droplets with a mean particle size (MPS) in the range $0.65 - 1 \mu\text{m}$ permeate and can be indeed potentially delivered in the immediate surroundings. This value steadily increases over time of usage and after 32 hours, when the bacterial filtration efficiency of the mask is still over 95%, only about 75% of these very small particles are retained. Similarly, the efficiency against particles with size in the range $(1.1 - 2.1) \mu\text{m}$ (collected in stage 5) decreases over time and after 32 h reduces from 100% to 90%. Instead, the efficiency against larger particles remains almost constant over the entire time of usage investigated. A similar behaviour was observed for Mask B, which shows a greater overall efficiency against particles in the range $(0.65 - 2.1) \mu\text{m}$ compared to Mask A, but higher penetration can be observed for larger particles.

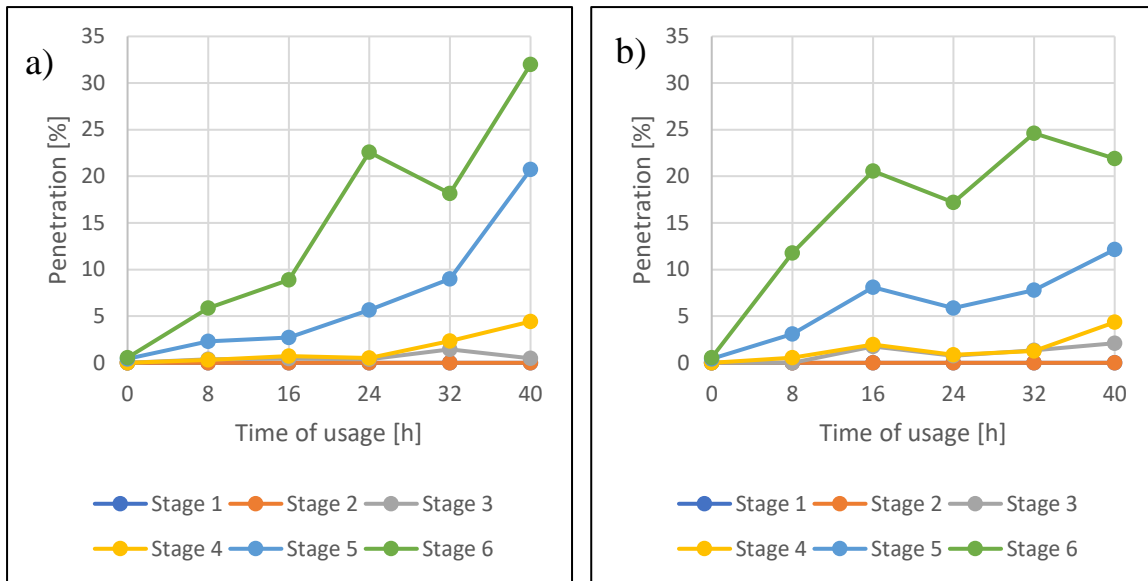


Figure 8.8: Variation of the penetration of the different particles sizes over time of usage: a) Mask A; b) Mask B.

4.2 Parameters affecting the durability

To investigate the main causes of the deterioration of the performance of surgical masks over time of usage, the bacterial filtration efficiency apparatus was used to recreate the operating conditions at which they are subjected when worn. 4 different conditions were examined to identify the most influent parameters involved during respiration:

- Bacteria contained in the respiratory droplets and aerosols exhaled (Condition I);
- Bacteria-free, demineralized, water droplets (Condition II);
- Air humidity (Condition III)
- Air flux (Condition IV).

In condition I, a Mask A specimen was accommodated in the BFE sample-holder and crossed by a constant flux of humid air at 28.3 L/min. During the entire test a *S. Aureus* solution was nebulized in the cylinder and forced through the mask by the airflow. However, the infectious particles were not collected in the impactor and were directly wasted in the

vacuum trap, since their collection was not of interest at this time. The apparatus and the bacterial solution used for this test were the same employed for the bacterial filtration efficiency test, reported in detail in chapter 2.1.2 and 3.1.2. At hourly intervals, the test was stopped to measure the bacterial filtration efficiency and the breathability and then launched again. This procedure was repeated for a total of 6 hours. The aim was to roughly simulate the emission of humid air, respiratory droplets and aerosols that are exhaled during respiration and to evaluate their effects on the mask performance over time. Indeed, the relative humidity of the airflow was set at 85 %, value indicated by the EN standard to simulate the use [20]. The concentration of the bacteria solution, the number of droplets and aerosols generated, the air flow rate and direction were obviously not representative of the real human respiration, but they were not a concern since the objective was the qualitative comparison with the other operative conditions.

In condition II, a surgical mask A specimen was tested as in condition I, except for the bacterial solution nebulization. In this case, the nebulizer was filled with only demineralized water. The aim was to verify if the absence of bacteria in the droplets and aerosols impacting the mask, positively or negatively, affected the variation of the performance over time.

In condition III, a Mask A specimen was accommodated in the BFE sample-holder and crossed only by a constant flux of humid air at 28.3 L/min, to observe if the bacterial filtration efficiency reduction was caused by only the humidity in the air.

Finally, in condition IV, a surgical mask A specimen was crossed by dry air (30 % R.H.), to rule out the degradation of the nonwoven fabrics due to the stress caused by the air flux.

The tests were performed on a total of 8 specimens, two per condition, as reported in table 3.

Table 8.3: Conditions for the determination of the influence of the different parameters

Condition	Specimens		Parameters		
	Mask type	N°	Air flow rate [L/min]	Air R.H. [%]	Atomizer
I	A	2	28.3	85	<i>S. Aureus</i> solution
II	A	2	28.3	85	Demineralized water
III	A	2	28.3	85	No
IV	A	2	28.3	30	No

8.2.1 Results of parameters affecting the durability

Figure 8.9 shows the variation of the bacterial filtration efficiency (BFE) and of the breathability over time per each condition. Since the values obtained for each couple of samples tested at the same condition were almost identical, only the mean value is reported. By comparing the BFE curves for conditions I and II, in which the only difference was the nebulization of the bacteria aerosol, it results that they follow a similar trend and that the small differences in terms of absolute value of each point are mainly related to the differences between the samples rather than the influence of the bacteria. Therefore, it was concluded that the bacteria enveloped in the respiratory droplets and aerosols did not considerably affect the performance of the surgical masks.

To an extent, this conclusion agrees with the results obtained by the test performed on the specimens worn by real operators, where any recovery was observed after storage. If the bacteria were the main cause, a certain recovery would be observed, since their concentration decreases over time during overnight storage in clean air [21]. On the contrary, the breathability curves substantially diverge over time. For condition II, pressure drops remain constant over time, as observed during the test of real usage, while they steadily and consistently increase for condition I. The different behaviour was ascribed to the high

concentration of NaCl (and to an extent, of bacteria) contained inside the inoculum that was nebulized and clogged the masks.

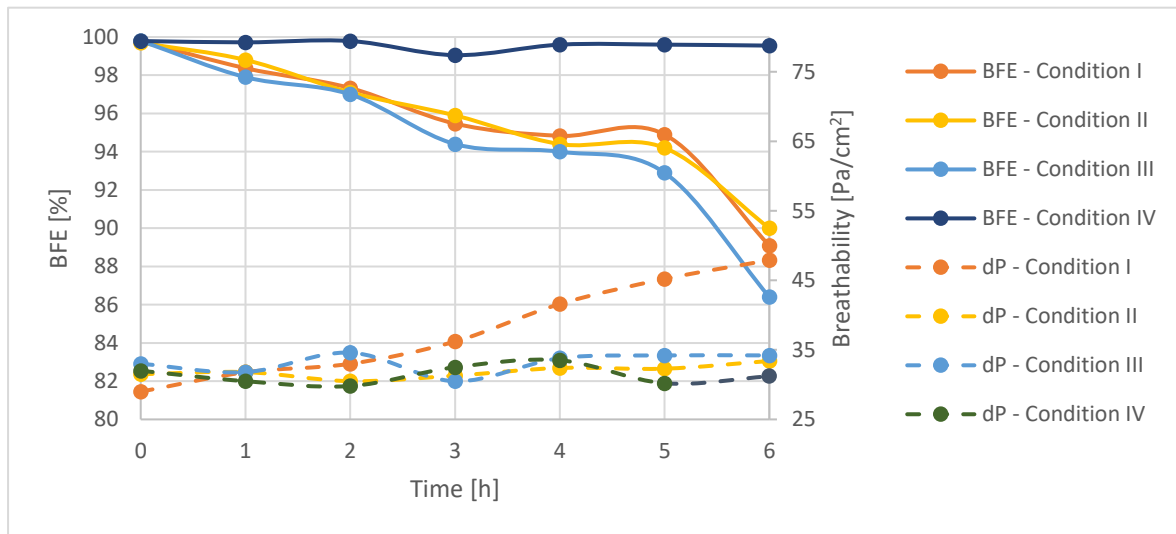


Figure 8.9: Variation of BFE (solid line) and breathability (dashed line) of Mask A under different conditions.

This statement is confirmed by the comparison of the curves for condition II and III. Only demineralized water was nebulized during the test for condition II, while no nebulization occurred in that of condition III. The pressure drops remained constant over time in both cases and the curves followed an almost identical trend. Similarly, the bacterial filtration efficiency was analogous and characterized by a constant decrease for the two conditions, ruling out an appreciable negative effect of the liquid respiratory droplets and aerosols impacting the meltblown fabric. Finally, conditions III and IV were compared, observing that the bacterial filtration efficiency remained constant in absence of high humidity in the airstream over the entire time of investigation. Indeed, it was concluded that the sole parameter that causes an appreciable reduction of the filtration efficiency of a surgical mask is humidity, which reduces the electrostatic charge of the meltblown (electret) filter. Instead, the breathability was not affected in any case, suggesting that the fibers and the fabric in general were not ruined by the airflow. To confirm this statement, a scanning electron microscopy (SEM) analysis was performed on one of the two sample tested for condition

III, revealing no differences in the structure of the fabrics, as shown in figure 8.10. As explained in detail in paragraph 6.3, surgical masks filter respiratory droplets and aerosols through several mechanisms. Most of them, such as interception and diffusion, successfully stop big droplets and fine aerosols, but are less effective against particles with a diameter around 300 nm. Indeed, the meltblown filters typically employed for surgical masks are charged to take advantage of the electrostatic interaction, that is able to trap a wide range of particles size. Thus, the loss of the electrostatic charge of the masks over time of usage due to the humidity contained in the exhaled air turns in a reduction of the filtration efficiency.

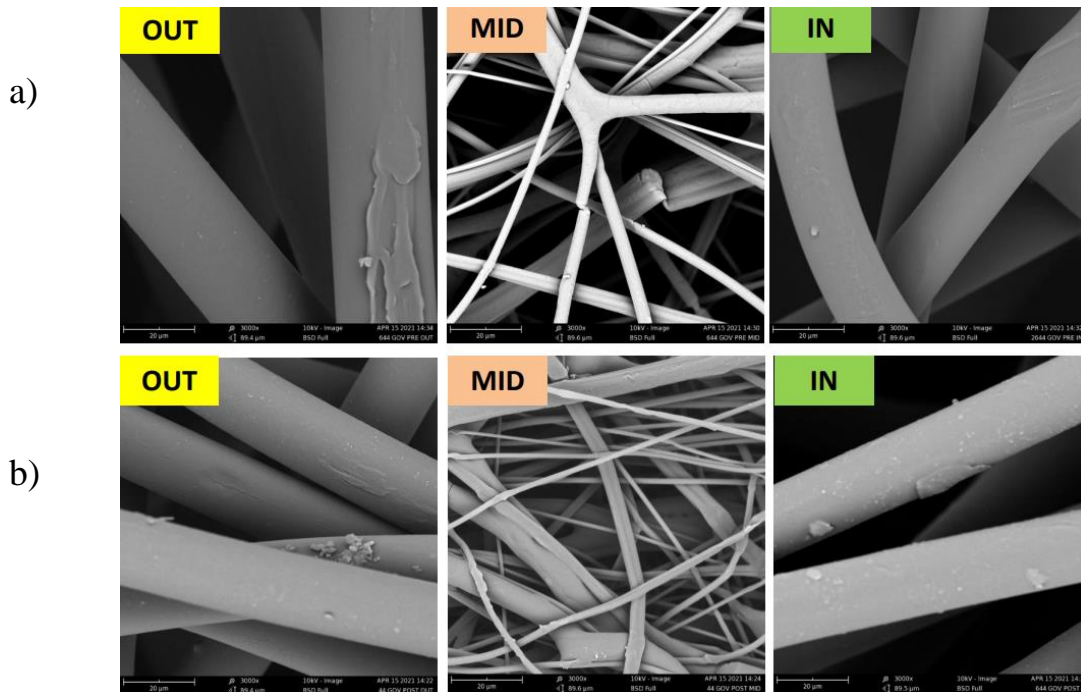


Figure 8.10: SEM analysis of a Mask A sample before and after the test at condition III: a) before the test; b) after the test.

4.3 Protocol for lifetime estimation

To wear and test an unknown surgical mask for long periods to investigate the variation of the performance over time can be dangerous if the procedure is not executed in a safe setting,

such as a surgery room in which an excellent ventilation is ensured. To this aim, an experimental protocol to simulate the use of a surgical mask by the means of the BFE apparatus was developed. The protocol is graphically represented in figure 8.11 and can be resumed as follows:

1. Take a mask from a batch and measure the breathability at time zero ($\Delta P_{t=0}$);
2. Place the mask specimen in the BFE sample-holder;
3. Measure the BFE at time zero ($BFE_{t=0}$);
4. Set the humidity of the air fed to the apparatus at 85% R.H. and set the most appropriate air flow rate;
5. Leave humid air flowing through the specimen for 4 hours;
6. Measure the BFE and the breathability after 4 hours ($BFE_{t=4}, \Delta P_{t=4}$);
7. Leave humid air flowing through the specimen for 4 hours
8. Measure the BFE and the breathability after 4 hours ($BFE_{t=8}, \Delta P_{t=8}$)
9. Leave the sample in a dry and ventilated environment overnight;
10. Measure the breathability after storage ($\Delta P_{t=8+st}$) and calculate the value after 1 day of usage using equation 8.3;

$$\Delta P_{1\ day} = \frac{\Delta P_{t=8} + \Delta P_{t=8+st}}{2} \quad (8.3)$$

11. Place the sample in the BFE apparatus, measure the BFE after storage and calculate the value after 1 day of usage using equation 8.4;

$$BFE_{1\ day} = \frac{BFE_{t=8} + BFE_{t=8+st}}{2} \quad (8.4)$$

12. Repeat the steps from 4 to 11 until the measured BFE or breathability result to be out of the limit prescribed by the EN standard.

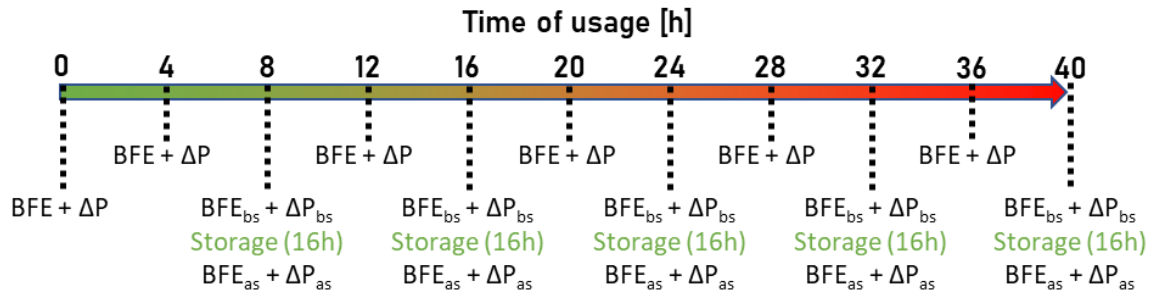


Figure 8.11: Protocol for the simulation of surgical masks durability

The relative humidity of the airflow was set at 85 %, value indicated by the EN as the most representative of the operative conditions, while several flow rates were investigated to identify the most appropriate to simulate the real use. The volume of air inhaled or exhaled by an individual per unit time is known as minute ventilation. Typical values are 6 L/min for an individual at rest and 20 - 30 L/min during relatively light work [22]. Therefore, starting from 8 L/min, additional flow rates were investigated, namely 10, 12, 14 and 28.3 L/min. The tests were performed on Mask A samples and one flow rate, 14 L/min, was tested also on Mask B. The results were compared to those obtained by real use.

Surgical masks are not always stored in a dry environment, especially in the community: it is not uncommon to see these devices left in a car overnight, for example. Indeed, to verify if the simulation performed can be affected by the storage in a humid and non-aerated environment, two samples of each type of mask were placed in two bottles, along with 100 mL of demineralized water and pieces of expanded polystyrene to avoid the direct contact between the masks and liquid water, as shown in figure 8.12. The bottles were placed on a hot plate at 40°C for 16 h, to force the evaporation of the water and the condensation on the masks (simulating the worst possible scenario) and then tested for the BFE and the breathability.

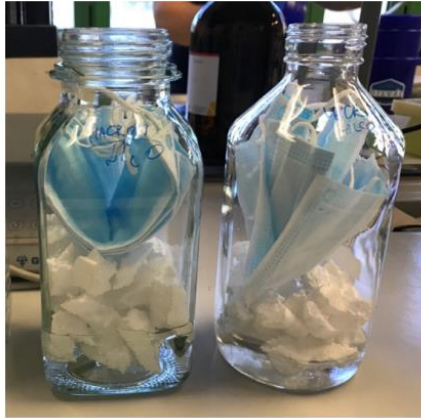


Figure 8.12: Bottles containing 100 mL of demineralized waters, pieces of polystyrene and two samples of Mask A (right) and Mask B (left)

8.3.1 Results of protocol for lifetime estimation

According to the protocol, 10 samples of Mask A were tested in total, 2 per each flow rate. The results obtained are shown in figure 8.13, where the variation of the bacterial filtration efficiency and of the breathability per each flow rate are reported and compared to the real use values. Each point is the average of the values obtained by the two samples at that specific flow rate. Similarly, the points of the real use curve are the average of the values obtained by each operator after a specific time of usage.

As expected by looking at the results shown in figure 8.9, where a similar flow rate was chosen, the procedure executed at 28.3 L/min (the value indicated by the EN standard to perform the BFE test) led to a quick downfall of the filtration efficiency well below 95% after only 4 hours. This did not surprise, since 28.3 L/min is close to the maximum minute respiration during relatively light work, while the operators in the laboratory, testing and elaborating data, were in a condition closer to rest. The test was extended for other 20 hours, to verify the existence of a minimum corresponding to the complete loss of the electrostatic

charge, and it was observed that the BFE stabilizes around 83% after 12 hours of usage. By contrast, the test executed at 8 L/min and 10 L/min provided a too conservative estimation of the variation of the BFE. In both the cases, a slight decrease over time was observed, but the loss of the electrostatic charge was lower compared to the real usage curve, resulting in a BFE still over 97% after 40 hours.

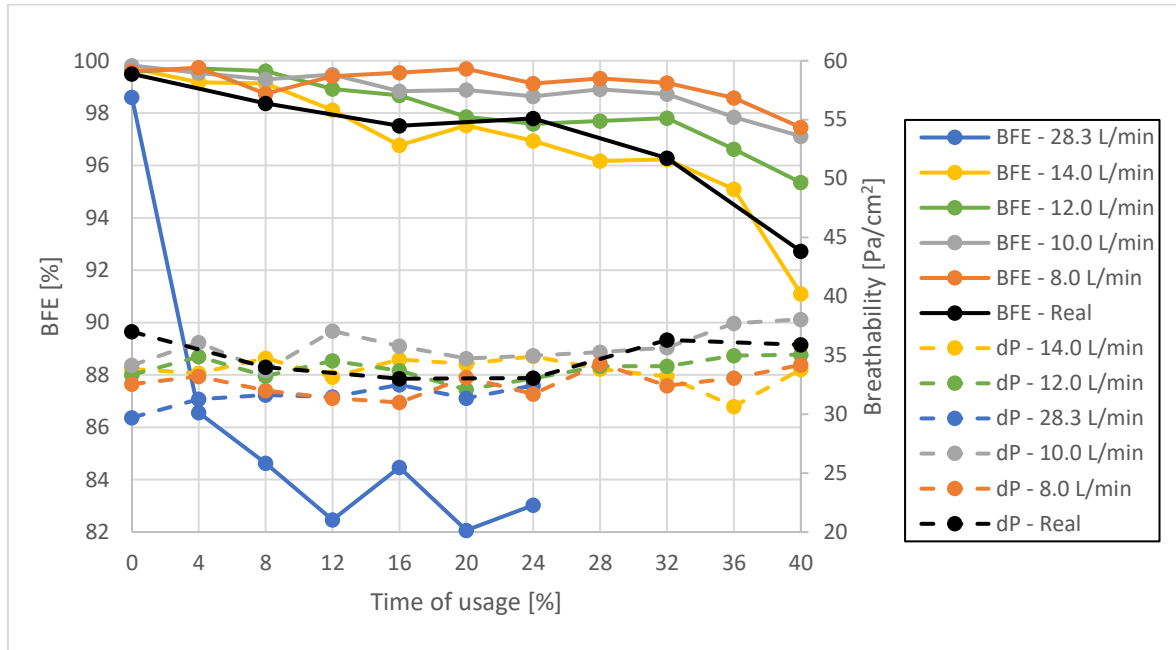


Figure 8.13: Simulated BFE and breathability variation over time of usage and flow rate for Mask A

As expected, in general the slope of the curves increases with the flow rate, since the higher the flow rate the higher the amount of water contained in the air that cross a sample per unit time. Unsurprisingly, it was observed that the curve obtained at 12 L/min and 14 L/min were much closer to the real one: on average, the former tends to slightly underestimate the variation of the BFE, while the latter overlaps the real usage curve in some point and overestimates in others. However, as observed in the real use experiments, the data significantly deviate after 32 hours and it is not possible to define precisely a final value. This phenomenon is caused by a low accuracy of the BFE test for low-efficiency samples and by minor differences in the fabric structure between the samples.

As expected, the breathability test resulted in no differences between the different flow rates and the real usage curve.

A conservative approach was adopted and 14 L/min was identified as the flow rate that, at the specific conditions indicated in the procedure, is able to best simulate the real use of surgical Mask A. These results are confirmed by the test performed at 14 L/min on surgical mask B, shown in figure 8.14.

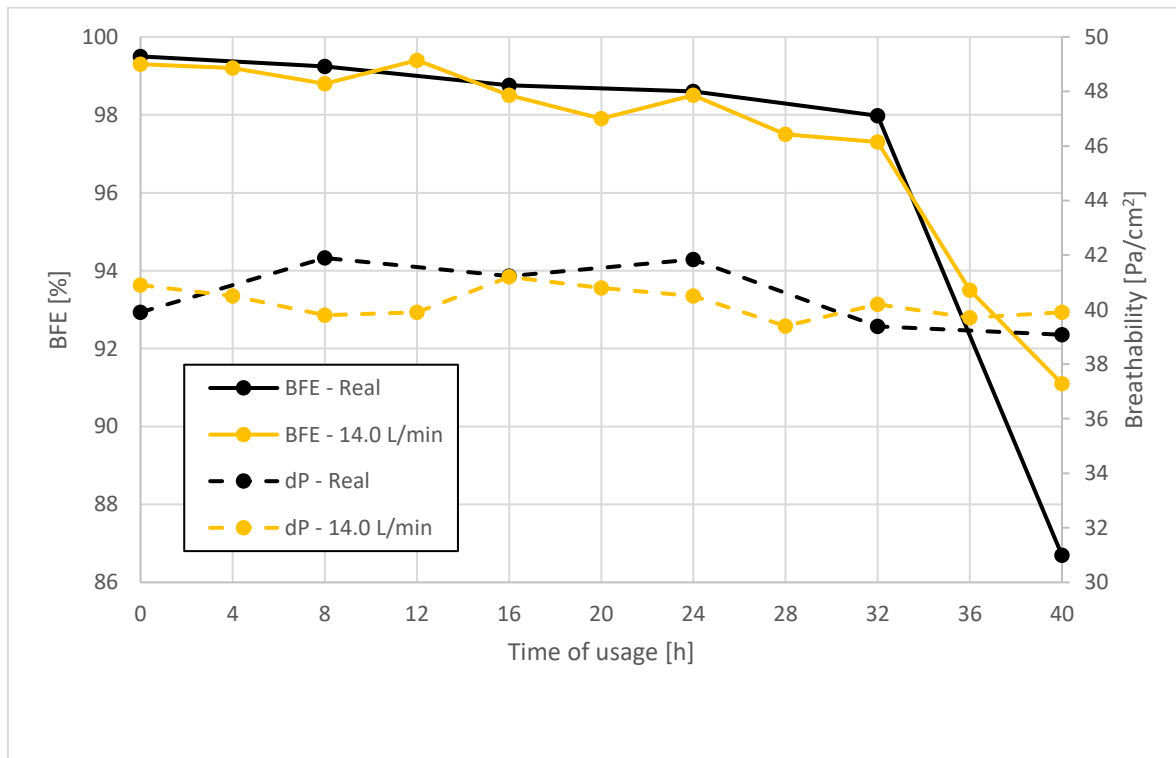


Figure 8.14: Simulated BFE and breathability variation over time of usage and flow rate for Mask B.

The two curves, simulated and real use, overlap frequently within the first 32 hours of usage but they are quite different at 40 hours, when the simulation estimates a BFE lower than the limit provided by the EN standard, but significantly higher than the real one. Again, this behaviour may depend on the BFE test accuracy and on minor differences between the samples.

The results obtained by the simulation at 14 L/min in both cases, Mask A and Mask B, indicated that the BFE apparatus, upgraded with the addition of a bubbler for the humidification of the air fed to the system, can be successfully used to simulate the variation of the performance of surgical masks over time of usage in every laboratory. In addition, the application of the proposed protocols allows to simulate the use (storage included) and to reduce the error that affects the single measures. For a relative humidity of 85%, an air flow rate that crosses the sample of 14.0 L/min appeared to be a sufficiently conservative choice. However, the real use of a surgical mask is strongly affected by the minute respiration of the wearer and, indeed, by the activity performed. Indeed, 14 L/min should be considered only to simulate surgical masks that are worn by individuals performing works that do not affect significantly their minute respiration, while for heavy works higher flow rates should be appropriately chosen.

About the negative effects of a possible storage in a humid environment, the result of the storage test at harsh conditions are reported in table 8.4, which shows the variation of the BFE and of the breathability before and after the test.

Table 8.4: BFE and breathability variation after 16 h of storage in a saturated environment.

	Sample	BFE variation [%]	breathability variation [Pa/cm ²]
Mask A	1	-0.7	+1.3
	2	+0.1	+0.4
Mask B	1	-0.2	+0.7
	2	-0.9	-0.1

The differences are not relevant and depend mainly on the error of the measures, indicating that the humidity in the air negatively affects the performance of a surgical mask only if it is forced to flow through the fibers, while it is irrelevant in static air because the external hydrophobic layers shield the internal filter.

References

- [1] “COVID: Can a surgical mask be used more than once? | Adios Corona.” <https://en.adioscorona.org/questions-reponses/2020-10-01-pollution-masque-chirurgical-plusieurs-fois-porter-utiliser-mer-ocean.html> (accessed Jan. 22, 2022).
- [2] “Rational use of personal protective equipment for coronavirus disease (COVID-19): interim guidance-2-Recommendations for optimizing the availability of PPE”.
- [3] “Advice on the use of masks in the context of COVID-19: interim guidance, 6 April 2020.” <https://apps.who.int/iris/handle/10665/331693> (accessed Jan. 20, 2022).
- [4] K. Selvaranjan, S. Navaratnam, P. Rajeev, and N. Ravintherakumaran, “Environmental challenges induced by extensive use of face masks during COVID-19: A review and potential solutions,” *Environmental Challenges*, vol. 3, p. 100039, Apr. 2021, doi: 10.1016/J.ENVC.2021.100039.
- [5] L. M. Kobayashi, B. R. Marins, P. C. D. S. Costa, H. Perazzo, and R. Castro, “Extended use or reuse of N95 respirators during COVID-19 pandemic: An overview of national regulatory authority recommendations,” *Infection Control and Hospital Epidemiology*, vol. 41, no. 11, pp. 1364–1366, Nov. 2020, doi: 10.1017/ICE.2020.173.
- [6] K. Seresirikachorn *et al.*, “Decontamination and reuse of surgical masks and N95 filtering facepiece respirators during the COVID-19 pandemic: A systematic review,” *Infection Control & Hospital Epidemiology*, vol. 42, no. 1, pp. 25–30, Jan. 2021, doi: 10.1017/ICE.2020.379.
- [7] J. S. M. Peiris, Y. Guan, and K. Y. Yuen, “Severe acute respiratory syndrome,” *Nature Medicine 2004 10:12*, vol. 10, no. 12, pp. S88–S97, Nov. 2004, doi: 10.1038/nm1143.
- [8] “Improving the performance of the office sterilizer - PubMed.” <https://pubmed.ncbi.nlm.nih.gov/1287400/> (accessed Jan. 23, 2022).
- [9] P. T. Ivanova, D. S. Myers, S. B. Milne, J. L. McClaren, P. G. Thomas, and H. A. Brown, “Lipid Composition of the Viral Envelope of Three Strains of Influenza Virus - Not All Viruses Are Created Equal,” *ACS Infectious Diseases*, vol. 1, no. 9, pp. 435–

- 442, Jan. 2016, doi: 10.1021/ACSINFECDIS.5B00040/SUPPL_FILE/ID5B00040_SI_001.PDF.
- [10] T. H. Lin, F. C. Tang, P. C. Hung, Z. C. Hua, and C. Y. Lai, “Relative survival of *Bacillus subtilis* spores loaded on filtering facepiece respirators after five decontamination methods,” *Indoor Air*, vol. 28, no. 5, pp. 754–762, Sep. 2018, doi: 10.1111/INA.12475.
- [11] W. G. Lindsley *et al.*, “Effects of Ultraviolet Germicidal Irradiation (UVGI) on N95 Respirator Filtration Performance and Structural Integrity,” *J Occup Environ Hyg*, vol. 12, no. 8, pp. 509–517, Aug. 2015, doi: 10.1080/15459624.2015.1018518.
- [12] D. Moher *et al.*, “Preferred reporting items for systematic reviews and meta-analyses: the PRISMA statement,” *PLoS Med*, vol. 6, no. 7, Jul. 2009, doi: 10.1371/JOURNAL.PMED.1000097.
- [13] P. A. Kenney *et al.*, “Hydrogen peroxide vapor sterilization of N95 respirators for reuse,” *medrxiv.org*, doi: 10.1101/2020.03.24.20041087.
- [14] A. Schwartz *et al.*, “Decontamination and reuse of N95 respirators with hydrogen peroxide vapor to address worldwide personal protective equipment shortages during the SARS-CoV-2,” *liebertpub.com*, vol. 25, no. 2, pp. 67–70, Jun. 2020, doi: 10.1177/1535676020919932.
- [15] “Investigating Decontamination and Reuse of Respirators in Public Health Emergencies | FDA.” <https://www.fda.gov/emergency-preparedness-and-response/mcm-regulatory-science/investigating-decontamination-and-reuse-respirators-public-health-emergencies> (accessed Jan. 23, 2022).
- [16] M. S. Bergman, D. J. Viscusi, Z. Zhuang, A. J. Palmiero, J. B. Powell, and R. E. Shaffer, “Impact of multiple consecutive donnings on filtering facepiece respirator fit,” *Am J Infect Control*, vol. 40, no. 4, pp. 375–380, May 2012, doi: 10.1016/J.AJIC.2011.05.003.
- [17] M. S. Bergman, D. J. Viscusi, B. K. Heimbuch, J. D. Wander, A. R. Sambol, and R. E. Shaffer, “Evaluation of multiple (3-Cycle) decontamination processing for filtering facepiece respirators,” *Journal of Engineered Fibers and Fabrics*, vol. 5, no. 4, pp. 33–41, 2010, doi: 10.1177/155892501000500405.

- [18] T. H. Lin, C. C. Chen, S. H. Huang, C. W. Kuo, C. Y. Lai, and W. Y. Lin, “Filter quality of electret masks in filtering 14.6-594 nm aerosol particles: Effects of five decontamination methods,” *PLoS One*, vol. 12, no. 10, Oct. 2017, doi: 10.1371/JOURNAL.PONE.0186217.
- [19] “Viscusi: Effect of decontamination on the filtration... - Google Scholar.” https://scholar.google.com/scholar_lookup?title=Effect+of+decontamination+on+the+filtration+efficiency+of+two+filtering+facepiece+respirator+models&author=Viscusi+DJ&author=King+WP&author=Shaffer+RE.&publication+year=2007&journal=J+Int+Soc+Respir+Prot&volume=24&pages=93-107 (accessed Jan. 23, 2022).
- [20] *BS EN 14683:2019: Medical face masks - Requirements and test methods*. European Committee for standardization.
- [21] N. Bedrosian *et al.*, “A Systematic Review of Surface Contamination, Stability, and Disinfection Data on SARS-CoV-2 (Through July 10, 2020),” *Environmental Science and Technology*, vol. 55, no. 7, pp. 4162–4173, Apr. 2021, doi: 10.1021/ACS.EST.0C05651/SUPPL_FILE/ES0C05651_SI_004.XLSX.
- [22] I. Holmér, K. Kuklane, and C. Gao, “Minute Volumes and Inspiratory Flow Rates During Exhaustive Treadmill Walking Using Respirators,” *The Annals of Occupational Hygiene*, vol. 51, no. 3, pp. 327–335, Apr. 2007, doi: 10.1093/ANNHYG/MEM004.

CHAPTER 9

Conclusions of Part II

The velocity and the routes of transmission of COVID-19 caused an unpredicted immediate worldwide demand of personal protective equipment (PPE) in early 2020, in particular of surgical face masks for the protection of the healthcare workers facing the disease in the hospitals. China, the world's leading manufacturer, was overwhelmed with orders [1]. This situation, further exacerbated by the absence of sufficient strategic stocks and secure supplies, led to a dramatic shortage of these medical devices. To address the shortage of surgical masks among healthcare operators and to support the industrial reconversion of the Italian industry, in late March 2020 a multidisciplinary group of the University of Bologna created the first Italian laboratory able to perform all the test required for the evaluation and certification of this medical devices [2]. To this aim several lines were set-up, according to the European regulation EN 14683:2019, namely breathability, bacterial filtration efficiency, microbial cleanliness and splash test. The highest workload was during the first 4 months, when nearly 350 prototypes were tested. Unfortunately, most of them were found to be not sufficiently performant: only 6 (3.2%) succeeded in all the tests within the end of April and 17 (8.64%) in the next two months. From the analysis of the results of all the prototypes analysed, it resulted that, even if surgical masks are basic and relatively cheap products, their production requires specific raw materials that should be processed and assembled in a relatively sophisticated process [3]. The most important component is the internal filtering layer, that is responsible for most of the filtration efficiency [4]. Of the compliant masks for which a technical sheet was available, 88% employed a meltblow filter and 12% a SMS filter. These nonwoven fabrics, by taking advantage of

the electrostatic attraction, are able to trap all the respiratory droplets and a large portion of aerosols. On the contrary, cloth masks, usually made of cotton or common nonwoven fabrics, are effective only against large particles. Notably, the use of meltblown or SMS filters with the correct grammage is essential but is not a guarantee for the production of a compliant face mask, since several prototypes made with a meltblown or a SMS filter failed the BFE, thus highlighting the importance of the production process.

Currently, more than 1200 test have been performed on more than 600 prototypes and only 42 masks have been found to compliant to the EN standard: 8 masks of Type I, 20 of Type II and 14 of Type IIR.

Surgical masks were designed for healthcare settings to be single use and their maximum duration is set at 4 hours for comfort reasons [5, 6], but the severe shortage led to extended use and re-use of single-use surgical masks by frontline health workers [7]. According to the survey performed by Selvaranjan et al., this behaviour is even more pronounced in the community. Several studies have demonstrated that the disinfection of surgical masks to allow a safe re-use is possible, but there are no information about how the performance vary over time of usage and, indeed, how many hours a surgical mask can be worn without loosing its properties [8, 22]. However, the knowledge of the durability is fundamental to understand if the extended use and re-use are possible and recommended. To answer this question two different surgical masks, namely Mask A and Mask B, were tested in different processes and conditions.

In the first test, the surgical masks were worn by 4 operators for a week, 8 h per day, and tested on a regular basis for the BFE and breathability. The results showed that the surgical tested remain complaint to the EN standard within 32 hours of use, time after which their bacterial filtration efficiency quickly downfall. However, even if compliant, a higher penetration of fine particles was observed. To investigate the cause of this behaviour, the same masks were processed in different conditions, finding out that the only responsible of the deterioration of the performance over time of

usage is the humidity of the air exhaled during respiration. This information allowed to set-up a protocol for the estimation of the durability of surgical masks in any laboratory equipped with a BFE apparatus. However, the results obtained have been validated only for an individual at rest or during very light work, since the minute respiration and, indeed, the amount of humid air flowing through a mask strongly depends on the activity an individual is performing.

The experience done in setting-up the apparatus and performing the tests allowed to develop some protocols to reduce the experimental errors and to identify possible critical points of the test procedures.

About the breathability, the measurement at a single flowrate may lead to experimental and accidental error that can go unnoticed. Indeed, a different approach is suggested, consisting in scanning the breathability at a several flow rates (including the one indicated in the EN standard) to derive a linear relationship from which the value at 8 L/min can be verified. The procedure developed considers five different flowrates (namely 100, 200, 300, 400, 500 L/h) and was found appropriate, accurate, and not time consuming.

About the bacterial filtration efficiency, it would be recommended to specify the characteristic of the air that should be fed to the apparatus and of the atomizer to obtain more reliable results. In addition, given the importance of surgical masks in protecting the healthcare operators (and the whole population in general) and the transmission of the virus also via fine aerosols [23], the BFE test should provide more information about the separation of smaller particle. Therefore, it would be recommended to extend the range of particle size collected by the impactor by the addition of stages with a lower cut-off. Last, the count of the CFU on the culture plate may lead to different results if not executed correctly. In particular, to obtain the number of CFU required by the EN standard in the positive control runs, a very high number of colonies should be present on the culture plates. Therefore, it would be recommended to lower the range of the number of CFU that should be

measured in the positive control run. Several experiments were performed in this sense and a range 1000-1400 CFU was found appropriate and more accurate.

About the splash test, the measure of the resistance against splashes of synthetic blood is qualitative in nature and may undermine the reproducibility of splash test between different laboratories [24]. It results the need of more stringent standards for the synthetic blood formulation, to achieve similar fluid properties in any laboratory.

Reference

- [1] “The face mask global value chain in the COVID-19 outbreak: Evidence and policy lessons.” <https://www.oecd.org/coronavirus/policy-responses/the-face-mask-global-value-chain-in-the-COVID-19-outbreak-evidence-and-policy-lessons-a4df866d/> (accessed Jan. 20, 2022).
- [2] “Il business delle mascherine e i laboratori che fanno i test: molte non sono a norma - Il Sole 24 ORE.” <https://www.ilsole24ore.com/art/il-business-mascherine-e-laboratori-che-fanno-test-molte-non-norma-ADqkm8F> (accessed Jan. 20, 2022).
- [3] J. T. J. Ju, L. N. Boisvert, and Y. Y. Zuo, “Face masks against COVID-19: Standards, efficacy, testing and decontamination methods,” *Advances in Colloid and Interface Science*, vol. 292, p. 102435, Jun. 2021, doi: 10.1016/J.CIS.2021.102435.
- [4] “How Surgical Masks are Made, Tested and Used.” https://www.thomasnet.com/articles/other/how-surgical-masks-are-made/#_Types_of_Masks (accessed Jan. 15, 2022).
- [5] “COVID: Can a surgical mask be used more than once? | Adios Corona.” <https://en.adioscorona.org/questions-reponses/2020-10-01-pollution-masque-chirurgical-plusieurs-fois-porter-utiliser-mer-ocean.html> (accessed Jan. 22, 2022).
- [6] “Rational use of personal protective equipment for coronavirus disease (COVID-19): interim guidance-2-Recommendations for optimizing the availability of PPE”.
- [7] L. M. Kobayashi, B. R. Marins, P. C. D. S. Costa, H. Perazzo, and R. Castro, “Extended use or reuse of N95 respirators during COVID-19 pandemic: An overview of national regulatory authority recommendations,” *Infection Control and Hospital Epidemiology*, vol. 41, no. 11, pp. 1364–1366, Nov. 2020, doi: 10.1017/ICE.2020.173.
- [8] “Viscusi: Effect of decontamination on the filtration... - Google Scholar.” https://scholar.google.com/scholar_lookup?title=Effect+of+decontamination+on+the+filtration+efficiency+of+two+filtering+facepiece+respirator+models&author=Viscusi+DJ&author=King+WP&author=Shaffer+RE.&publication+year=2007&journal=J+Int+Soc+Respir+Prot&volume=24&pages=93-107 (accessed Jan. 23, 2022).

- [9] P. A. Kenney *et al.*, “Hydrogen peroxide vapor sterilization of N95 respirators for reuse,” *medrxiv.org*, doi: 10.1101/2020.03.24.20041087.
- [10] A. Schwartz *et al.*, “Decontamination and reuse of N95 respirators with hydrogen peroxide vapor to address worldwide personal protective equipment shortages during the SARS-CoV-2,” *liebertpub.com*, vol. 25, no. 2, pp. 67–70, Jun. 2020, doi: 10.1177/1535676020919932.
- [11] “Investigating Decontamination and Reuse of Respirators in Public Health Emergencies | FDA.” <https://www.fda.gov/emergency-preparedness-and-response/mcm-regulatory-science/investigating-decontamination-and-reuse-respirators-public-health-emergencies> (accessed Jan. 23, 2022).
- [12] M. S. Bergman, D. J. Viscusi, Z. Zhuang, A. J. Palmiero, J. B. Powell, and R. E. Shaffer, “Impact of multiple consecutive donnings on filtering facepiece respirator fit,” *American journal of infection control*, vol. 40, no. 4, pp. 375–380, May 2012, doi: 10.1016/J.AJIC.2011.05.003.
- [13] M. S. Bergman, D. J. Viscusi, B. K. Heimbuch, J. D. Wander, A. R. Sambol, and R. E. Shaffer, “Evaluation of multiple (3-Cycle) decontamination processing for filtering facepiece respirators,” *Journal of Engineered Fibers and Fabrics*, vol. 5, no. 4, pp. 33–41, 2010, doi: 10.1177/155892501000500405.
- [14] B. K. Heimbuch *et al.*, “A pandemic influenza preparedness study: use of energetic methods to decontaminate filtering facepiece respirators contaminated with H1N1 aerosols and droplets,” *American journal of infection control*, vol. 39, no. 1, Feb. 2011, doi: 10.1016/J.AJIC.2010.07.004.
- [15] T. H. Lin, F. C. Tang, P. C. Hung, Z. C. Hua, and C. Y. Lai, “Relative survival of *Bacillus subtilis* spores loaded on filtering facepiece respirators after five decontamination methods,” *Indoor Air*, vol. 28, no. 5, pp. 754–762, Sep. 2018, doi: 10.1111/INA.12475.
- [16] W. G. Lindsley *et al.*, “Effects of Ultraviolet Germicidal Irradiation (UVGI) on N95 Respirator Filtration Performance and Structural Integrity,” *Journal of occupational and environmental hygiene*, vol. 12, no. 8, pp. 509–517, Aug. 2015, doi: 10.1080/15459624.2015.1018518.
- [17] D. Moher *et al.*, “Preferred reporting items for systematic reviews and meta-analyses: the PRISMA statement,” *PLoS medicine*, vol. 6, no. 7, Jul. 2009, doi: 10.1371/JOURNAL.PMED.1000097.

- [18] J. S. M. Peiris, Y. Guan, and K. Y. Yuen, “Severe acute respiratory syndrome,” *Nature Medicine* 2004 10:12, vol. 10, no. 12, pp. S88–S97, Nov. 2004, doi: 10.1038/nm1143.
- [19] “Improving the performance of the office sterilizer - PubMed.” <https://pubmed.ncbi.nlm.nih.gov/1287400/> (accessed Jan. 23, 2022).
- [20] P. T. Ivanova, D. S. Myers, S. B. Milne, J. L. McClaren, P. G. Thomas, and H. A. Brown, “Lipid Composition of the Viral Envelope of Three Strains of Influenza Virus - Not All Viruses Are Created Equal,” *ACS Infectious Diseases*, vol. 1, no. 9, pp. 435–442, Jan. 2016, doi: 10.1021/ACSINFECDIS.5B00040/SUPPL_FILE/ID5B00040_SI_001.PDF.
- [21] K. Seresirikachorn *et al.*, “Decontamination and reuse of surgical masks and N95 filtering facepiece respirators during the COVID-19 pandemic: A systematic review,” *Infection Control & Hospital Epidemiology*, vol. 42, no. 1, pp. 25–30, Jan. 2021, doi: 10.1017/ICE.2020.379.
- [22] K. Selvaranjan, S. Navaratnam, P. Rajeev, and N. Ravintherakumaran, “Environmental challenges induced by extensive use of face masks during COVID-19: A review and potential solutions,” *Environmental Challenges*, vol. 3, p. 100039, Apr. 2021, doi: 10.1016/J.ENVC.2021.100039.
- [23] K. Escandón *et al.*, “COVID-19 false dichotomies and a comprehensive review of the evidence regarding public health, COVID-19 symptomatology, SARS-CoV-2 transmission, mask wearing, and reinfection,” *BMC Infectious Diseases* 2021 21:1, vol. 21, no. 1, pp. 1–47, Jul. 2021, doi: 10.1186/S12879-021-06357-4.
- [24] “ISO - ISO 22609:2004 - Clothing for protection against infectious agents — Medical face masks — Test method for resistance against penetration by synthetic blood (fixed volume, horizontally projected).” <https://www.iso.org/standard/35055.html> (accessed Jan. 22, 2022).